Variability analysis of renewable power generation in complex terrain and the contribution of the spatio-temporal synergies for a resilient power supply. Methodology development and Ecuador case study

Vom Fachbereich Produktionstechnik

der

UNIVERSITÄT BREMEN

zur Erlangung des Grades

Doktor der Ingenieurwissenschaften (Dr.-Ing.)

genehmigte

Dissertation

von

M.Sc. Mariela Angélica Tapia Hinojosa

Gutachter:

Prof. Dr. ir. Edwin Zondervan (University of Twente)

Prof. Dr. Carsten Agert (Carl von Ossietzky Universität Oldenburg)

Tag der mündlichen Prüfung: 27.06.2023

In memory of Stefan,
an inspiring mentor and supportive friend.

Acknowledgments

Foremost, I would like to thank Prof. Dr. Stefan Gößling-Reisemann, our esteemed and greatly missed supervisor. Thank you for believing in me and for paving the way that led to the development of this work. I also express my sincere gratitude to Prof. Dr. Edwin Zondervan for taking over the role as supervisor. Thank you for your great support and valuable guidance along the way. I am also thankful to Prof. Dr. Carsten Agert for agreeing to be the second assessor and for taking the time to review this dissertation.

This work would not have been possible without the exceptional support from Dr. Detlev Heinemann. Thank you for being there from the beginning of this research project, and even much earlier, during the Energy Meteorology lectures, which shaped the ideas of what was going to be my future venture. I deeply appreciate your guidance and outstanding feedback.

Special thanks to Prof. Dr. Arnim von Gleich for the insightful discussions on the intricate world of resilience. Thanks also to my colleagues from the research group Resilient Energy Systems, especially to Torben Stührmann for enhancing the capabilities of the group to overcome the challenging situation we faced and for leading us to successfully *bounce forward*. Thanks to Martin Dörenkämper and the NEWA team for their assistance on the configuration of the wind mesoscale model. Thanks to the High-Performance Computing Team from the University of Oldenburg for their computing facilities. Many thanks to all the students who took part of this work for their interest and support. Thanks to Jon Chu and Leonard Ramos for the great effort put into your theses. Likewise, to Manuel Ariza, Rangelys Sorrentino, Fabio Dominguez, and Alejandro Reyes for helping with the data processing. Thanks also to my former colleagues Maria Sofia, Leo, Chris, Anton, and Pablo for the good times.

Lastly, thanks to Hannu for being truly supportive. Like the song says "*if not for you*" this journey would not have been the same. Special thanks to my parents and sisters, who despite the distance have always been there for me, encouraging me to pursue my goals. And to my lovely nephew and nieces Maty, Pau, and Nae. This work has been carried out believing that a more sustainable future for you is possible.

Summary

South American countries highly rely on hydropower for their electricity supply and the deployment of remaining untapped hydropower potential is the cornerstone of national generation capacity expansion plans. However, given the dependency of hydropower on water availability, risks associated with weather and climate variability could jeopardize the security of electricity supply of these countries.

In the case of Ecuador, according to government plans, fossil fuel thermal power plants will continue playing an important role in meeting the demand during the dry periods. A more sustainable and resilient strategy would be to diversify the power mix focusing on exploiting the complementarities between hydropower and other variable renewable energies, such as wind and solar. However, the deployment of these technologies in the country is still at a very early stage and there are some challenges to be tackled.

Due to the varying nature of solar and wind resources, the optimal planning and deployment of solar and wind power that could potentially complement hydropower requires detailed knowledge of the spatial and temporal variability of the resources. Unfortunately, long-term, high-quality solar irradiance and wind speed measurements are generally scarce and sparsely distributed, challenging the characterization of solar and wind resources at a country level. The complex climatic characteristics and topography of Ecuador represent another challenge to better understand the spatio-temporal dynamics between renewable resources, as well as the potential synergies of solar and wind power generation to compensate hydropower during the dry periods.

The main research goal of this dissertation is to develop tools and data to support the optimal planning of a more sustainable and resilient power system in Ecuador by systematically investigating the spatio-temporal variabilities and synergies of renewable resources in the complex terrain of Ecuador. For this purpose, climate data, machine learning techniques, and power system modeling tools are used.

The lack of solar and wind resource data is addressed by processing satellite-derived solar irradiance data and by using numerical weather prediction models to simulate wind resources. The generated meteorological datasets for Ecuador have a temporal resolution

of one hour and a spatial resolution of 3 × 3 km. They comprise 21 years (1998–2018) of solar irradiance data and 14 years (2005–2018) of bias-corrected wind speed and wind direction data at a turbine hub heigh of 80 m.

A novel methodology to characterize the spatio-temporal variability of gridded solar and wind resource datasets is proposed and demonstrated. Spatial functional data analysis (sFDA) is used to identify spatial subregions with similar intra-annual variability patterns of solar radiation and wind speed. Finally, the ability of geographically-dispersed photovoltaic (PV) and wind power systems to reduce the power output variability and provide reliable power generation is assessed by using power system performance models.

This dissertation provides the first comprehensive spatio-temporal characterization of solar radiation and wind speed in Ecuador. The identified subregions from the sFDA regionalization approach are the basis for the assessment of the complementarity between solar and wind to water resources of existing and planned hydropower plants. One of most important finding is that solar and wind resources have a strong spatio-temporal complementary behavior with water resources from both the Amazon and Pacific basins. This demonstrates that the seasonal variability of hydropower can be compensated by geographically-dispersed PV and wind power systems.

Another important finding is that the joint operation of PV and wind power systems from different subregions reduces the intrinsic variability of each resource. Wind power at a high-resource site (52% capacity factor) paired with PV from different subregions can provide the highest level of firm capacity (up to 5.5% of the combined capacity) for 87.5% of the time in a year. Furthermore, wind power from subregions with high resources stabilizes PV power output at diurnal timescales during the windy months (June–September), suggesting that both technologies could serve as baseload during this period, thus reducing the requirements for energy storage. The identified operational benefits of the spatio-temporal synergies among renewable power generation may provide economic incentives to increase the participation of PV and wind power in the Ecuadorian power mix.

These findings demonstrate that solar and wind power can play an important role in shaping a more sustainable and resilient power system in the country. The insights gained in this dissertation, as well as the provided data and tools, will support power sector planners and decision-makers in the development of strategies for the optimal expansion of solar and wind power technologies to complement hydropower and to reduce the dependencies on fossil fuel thermal power.

This dissertation contributes to the ongoing discussion on renewable energy complementarities in the region and the proposed methodology can be transferred to other countries to support optimal capacity expansion planning. Furthermore, the methods and data developed in this dissertation provide the groundwork for further research into energy system modeling.

Keywords: spatio-temporal variability, solar irradiance, wind speed, hydropower, PV, wind power, resilient energy systems, complementarity, energy meteorology, functional data analysis, clustering, Ecuador.

Zusammenfassung

Die Stromversorgung der Länder Südamerikas basiert in hohem Maße auf Wasserkraft und die Erschließung noch ungenutzter Wasserkraft-Potenziale ist der Eckpfeiler der nationalen Ausbaupläne zur Stromerzeugung. Da die Wasserkraftwerke jedoch von der Verfügbarkeit von Wasser abhängig sind, können durch Wetter- und Klimavariabilität entstehende Risiken die Sicherheit der Stromversorgung in diesen Ländern gefährden.

In Ecuador werden nach den Plänen der Regierung thermische Kraftwerke auf der Basis fossiler Brennstoffe weiterhin eine wichtige Rolle in der Stromversorgung während der Trockenperioden einnehmen. Eine nachhaltigere und resilientere Strategie wäre die Diversifizierung des Strommixes unter Nutzung der Komplementarität von Wasserkraft und anderen erneuerbaren Energien wie Wind- und Solarenergie. Allerdings befindet sich der Ausbau dieser Technologien im Land noch in einer sehr frühen Phase und einige Herausforderungen sind hierbei zu bewältigen.

Aufgrund des fluktuierenden Charakters der Solar- und Windressourcen erfordert die optimale Planung und Nutzung von Sonnen- und Windenergie zur Ergänzung von Wasserkraft detaillierte Kenntnisse über die räumliche und zeitliche Variabilität dieser Ressourcen. Leider sind qualitativ hochwertige Langzeitmessungen der Solarstrahlung und der Windgeschwindigkeit häufig kaum oder nur für wenige Messpunkte verfügbar, was die Charakterisierung der Solar- und Windressourcen auf Landesebene erschwert. Die komplexen klimatischen Bedingungen und die Topografie Ecuadors stellen eine weitere Herausforderung für das Verständnis der räumlich-zeitlichen Dynamik zwischen den erneuerbaren Ressourcen sowie der Möglichkeiten der Solar- und Windenergieerzeugung zur Kompensation des geringeren Outputs von Wasserkraftwerken während der Trockenperioden dar.

Das Hauptziel dieser Dissertation ist die Entwicklung von Tools und Daten, um die Planung eines nachhaltigeren und resilienten Stromversorgungssystems in Ecuador zu unterstützen, durch die systematische Untersuchung der räumlich-zeitlichen Variabilität und der Synergien zwischen erneuerbaren Ressourcen im komplexen Terrain

Ecuadors. Zu diesem Zweck werden Klimadaten, Techniken des maschinellen Lernens und Modellierungstools für Stromversorgungssysteme eingesetzt.

Der Mangel an Daten über Solar- und Windressourcen wird durch die Verarbeitung der von Satellitendaten abgeleiteten Solarstrahlungsdaten und durch die Verwendung numerischer Wettervorhersagemodelle zur Simulation der Windressourcen behoben. Die erzeugten meteorologischen Datensätze für Ecuador haben eine stündliche zeitliche Auflösung und eine Rasterauflösung von 3×3 km. Die Datensätze umfassen 21 Jahre (1998–2018) Solarstrahlungdaten und 14 Jahre (2005–2018) bias-korrigierter Windgeschwindigkeits- und Windrichtungsdaten auf einer Nabenhöhe von 80 m.

Zur Charakterisierung der räumlich-zeitlichen Variabilität von gerasterten Solar- und Windressourcendatensätzen wird eine neue Methodik vorgeschlagen und demonstriert. Mit Hilfe der *spatial functional data analysis* (sFDA) werden räumliche Teilregionen mit ähnlichen unterjährigen Variabilitätsmustern in der Sonneneinstrahlung und Windgeschwindigkeit identifiziert. Schließlich wird die Fähigkeit geografisch verteilter Photovoltaik- (PV) und Windkraftanlagen, die Variabilität der Leistungsabgabe zu verringern und eine zuverlässige Stromerzeugung zu gewährleisten, mit Hilfe von Stromversorgungsmodellen bewertet.

Diese Dissertation stellt die erste umfassende räumlich-zeitliche Charakterisierung der Solarstrahlung und der Windgeschwindigkeit im Gebiet Ecuadors dar. Die mit dem sFDA-Regionalisierungsansatz identifizierten Teilregionen bilden die Grundlage für die Bewertung der Komplementarität zwischen Solar- und Windressourcen und den Wasserressourcen bestehender und geplanter Wasserkraftwerke. Eines der wichtigsten Ergebnisse ist, dass Solar- und Windressourcen ein starkes räumlich-zeitliches Komplementärverhalten zu den Wasserressourcen des Amazonas- und Pazifikbeckens aufweisen. Dies zeigt, dass die saisonalen Schwankungen der Wasserkraft durch geografisch verteilte PV- und Windkraftanlagen kompensiert werden können.

Ein weiteres wichtiges Ergebnis ist, dass der gemeinsame Betrieb von PV- und Windkraftanlagen in räumlich getrennten Teilregionen die inhärente Variabilität jeder einzelnen Ressource reduziert. Windkraft an dem Standort mit den stärksten Ressourcen (52% Kapazitätsfaktor) kann zusammen mit PV-Anlagen in verschiedenen Teilregionen während 87,5% der Zeit im Jahr eine hohe Grundleistung (bis zu 5,5% der kombinierten Kapazität) bereitstellen. Darüber hinaus stabilisiert die Windenergie aus Teilregionen mit hohen Ressourcen die PV-Energieproduktion in den windreichen Monaten (Juni–September) auf der täglichen Zeitskala, was darauf hindeutet, dass beide

Technologien in diesem Zeitraum als Grundlast dienen können, wodurch sich der Bedarf an Energiespeichern verringert. Die festgestellten operativen Vorteile der räumlich-zeitlichen Synergien bei der Stromerzeugung aus erneuerbaren Energien können wirtschaftliche Anreize für einen Ausbau des Anteils von PV und Windenergie am ecuadorianischen Strommix bieten.

Diese Ergebnisse zeigen, dass Solar- und Windenergie eine wichtige Rolle bei der Gestaltung eines nachhaltigeren und resilienteren Stromversorgungssystems in Ecuador einnehmen können. Die in dieser Dissertation gewonnenen Erkenntnisse werden Planern und Entscheidungsträgern im Energiesektor bei der Entwicklung von Strategien für den optimalen Ausbau dieser Technologien zur Ergänzung von Wasserkraft und zur Reduktion der Abhängigkeit von fossilen Brennstoffen unterstützen. Damit wird ein Beitrag zur laufenden Diskussion über die Komplementarität erneuerbarer Energien in dieser Region geleistet, wobei die vorgeschlagene Methodik auf andere Länder übertragen werden kann, um eine optimale Planung des Kapazitätsausbaus zu unterstützen. Darüber hinaus bilden die in dieser Dissertation entwickelten Methoden und Daten eine wertvolle Grundlage für weitere Forschungsarbeiten in der Energiesystemmodellierung.

Schlagwörter: räumlich-zeitliche Variabilität, Solarressourcen, Windressourcen, Wasserkraft, Photovoltaik, Windkraft, resiliente Energiesysteme, Komplementarität, Energiemeteorologie, Clustering, Ecuador.

Table of content

List of Figures

List of Tables

List of Abbreviations

AGL	Above Ground Level
AOS	Andes-Occurring System
API	Application Programming Interface
ASW	Average Silhouette Width
CDO	Climate Data Operators
CHIRPS	Climate Hazards Infrared Precipitation with Stations
DHI	Diffuse Horizontal Irradiance
DNI	Direct Normal Irradiance
ENSO	El Niño-Southern Oscillation
ERA5	European Centre for Medium-Range Weather Forecasts Reanalysis V5
GHI	Global Horizontal Irradiance
GIS	Geographic Information System
GRDC	Global Runoff Data Centre
GWA	Global Wind Atlas
ITCZ	Intertropical Convergence Zone
KG	Köppen-Geiger Climate Classification
MBA	Mean Bias Absolute
MBE	Mean Bias Error
NCAR	National Center for Atmospheric Research
netCDF	Network Common Data Form
NEWA	New European Wind Atlas
NSRDB	National Solar Radiation Database
PCA	Principal Component Analysis
PSM	Physical Solar Model
PV	Photovoltaic
RMSE	Root Mean Square Error
SAPM	Sandia Array Performance Model
sFDA	Spatial Functional Data Analysis
TMY	Typical Meteorological Year
VRE	Variable Renewable Energy
WRF	Weather Research and Forecast

List of Symbols

CF_H	hydropower capacity factor
CF_{PV}	PV capacity factor
CF_W	wind capacity factor
Cov	covariance
C_{stab}	stability coefficient
CV_m	monthly coefficient of variation
CV_y	yearly coefficient of variation
$d\omega$	dissimilarity matrix
f_{loss}	factor for PV system losses
N_m	number the PV modules
P_{mpp}	power at maximum power point
P_{PV}	PV power output
P_W	wind power output
Q	river discharge
r_P	Pearson correlation coefficient
r_S	Spearman correlation coefficient
t	time-step
WD	wind direction
WS	wind speed
Z_0	surface roughness length
γ	trace-variogram function
σ	standard deviation
χ	functional process

Chapter 1 Introduction

1.1. Background

Hydropower is a low greenhouse gas emitting renewable energy that plays an important role in today's electricity mix, sharing 16% of electricity generation worldwide and about 45% of the total renewable capacity (IEA, 2021a). South American countries have important untapped potentials for hydropower generation and its deployment is at the core of the national energy strategies of countries like Bolivia, Ecuador, Paraguay, Chile and Brazil (IHA, 2017).

In the case of Ecuador, the natural geographic distribution of the Andes divides the country into two drainage basins: the Amazon and the Pacific, which together represent a technical potential for hydropower generation of 91 GW, from which 22 GW are assumed to be technically and economically feasible (CONELEC, 2013). The Ecuadorian government made targeted investments for hydropower infrastructure development in the Amazon basin during the 70's and 80's; however, this development was considerably diminished due to political and financial instabilities, especially between 1996 and 2008. During this time the country tried and failed to create a decentralized energy market, which was intended to provide economic incentives for private investors to develop new hydropower generation capacity (CONELEC, 2012; Zambrano-Barragan, 2012).

This situation led to a crisis in the energy sector that reached a critical point by the end of 2009, when the Amazon basin had the lowest river inflow in the last 46 years (47% lower than the November average) and the country faced several electricity shortages until the beginning of 2010 (Schaeffer et al., 2013). At that time, to compensate the lack of generation, the government expanded the fossil fuel thermal power portfolio and the amount of electricity imports from neighboring countries (Fig. 1-1). As a consequence, Ecuador's power mix increased in carbon intensity and was further exposed to the risks of energy imports, both with respect to fuel price volatility and uncertain electricity supply from neighboring countries (Zambrano-Barragan, 2012).

To achieve electricity self-sufficiency and reduce the expenditure on fuels for the power sector, the Ecuadorian government, based on the legal framework in place since 2008 that

allowed the recovery of the state control in the energy sector, established strategic generation capacity expansion plans focused on the construction of eight flagship hydropower projects with a total installed capacity of 2832 MW (CONELEC, 2013). Most of the new capacity consisted of five hydropower projects in the Amazon basin, of which the largest projects *Coca Coda Sinclair* (1500 MW) and *Sopladora* (487 MW) started operating in 2016. The remaining three projects are located in the Pacific basin, two of which already started operations: *Manduriacu* (50 MW) in 2016 and *Minas San Francisco* (275 MW) in 2018 (ARCERNNR, 2020).

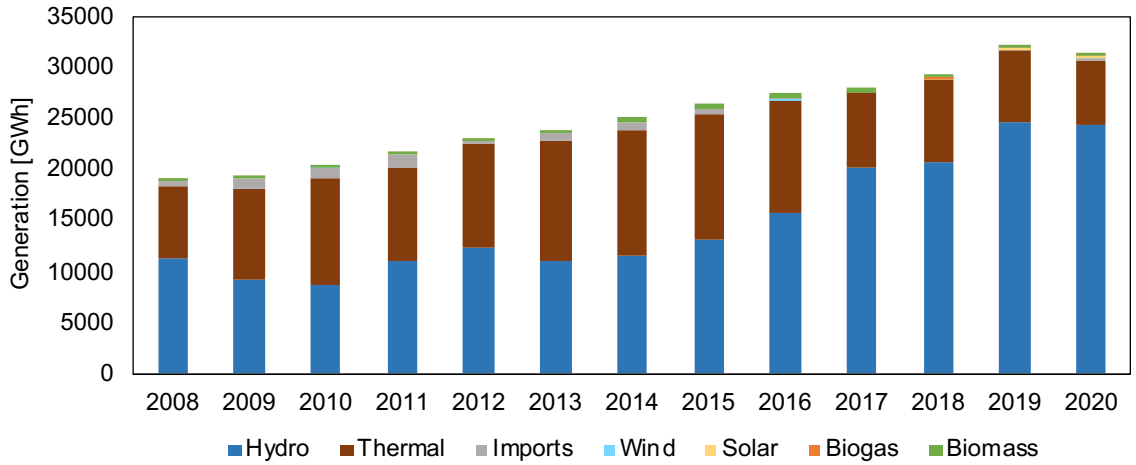

Fig. 1-1. Annual electricity generation in Ecuador during 2008–2020 disaggregated by supply source. Source: Own representation, data from ARCERNNR (2022a).

By 2020, the total installed generation capacity in Ecuador reached 8095.25 MW (ARCERNNR, 2022a), comprised by a large share of hydro and thermal power (62.56% and 35.09%, respectively), with a negligible participation of solar, wind, and other non-hydro renewables (Fig. 1-2).

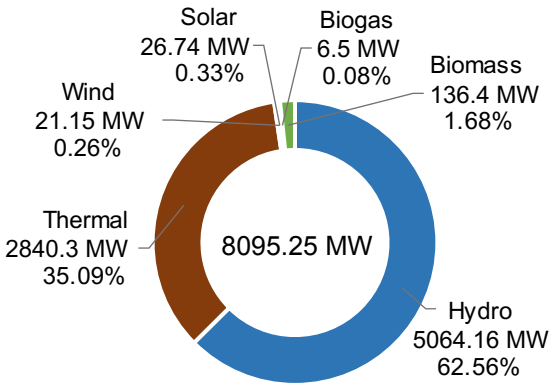

Fig. 1-2. Ecuadorian power mix in 2020. Source: Own representation, data from ARCERNNR (2022a).

Ecuador is planning to continue with this hydro-thermal configuration to meet the country's electricity demand in the mid- and long-term. By 2027, new large-scale hydropower projects in the Amazon basin are planned to add about 3000 MW of generation capacity, while fossil fuel thermal power will account for 12% of the power mix (MERNNR, 2018). Until 2040, it is planned that hydropower will be the main electricity supply source, maintaining at least a 70% share of the annual electricity production (MICSE, 2016).

1.2. Problem definition

The Ecuadorian government's strategy highly relies on hydropower and fossil fuel thermal power to meet the country's electricity demand. However, given the dependency of hydropower on water availability and the negative effects of fossil fuels, risks associated with weather and climate variability could jeopardize the security of the electricity supply in the country.

The Amazon and Pacific basins have a quasi-complementary energy production regime from February to April in the Pacific basin and from May to August in the Amazon basin (CONELEC, 2013). Nevertheless, between November and February, water resources are limited on both sides. Therefore, the vulnerability of the Ecuadorian power system grows proportionally with the increased probability of simultaneous critical hydrological scenarios in both basins (Schaeffer et al., 2013).

Another significant threat in the region is the cyclical climate period known as El Niño-Southern Oscillation (ENSO), which has an impact on the precipitation patterns in the tropical Pacific and could represent severe floods or droughts in timescales of two to about seven years (A. Bendix et al., 2006; Chiew et al., 2002; Trenberth, 2019). The ENSO driven variability in global and regional hydropower generation was investigated by Ng et al. (2017), who found from simulations that more than one third of the dams exhibit statistically significant annual energy production anomalies during ENSO events.

Furthermore, global climate change could add a significant amount of uncertainty to the natural climate variability, increasing the frequency and intensity of critical hydrological periods (Schaeffer et al., 2013). According to a recent study, hydropower generation in Ecuador is highly uncertain and sensitive to climate change, as variations in inflow to hydropower plants would directly lead to changes in the expected hydropower annual output (Carvajal et al., 2017).

To mitigate the aforementioned risks, a number of strategies have been suggested to help hydropower plants cope with weather and climate related variabilities. One strategy is to invest in reservoir capacity in order to compensate for seasonal variation of river inflow (Schaeffer et al., 2013). However, most of the existing hydropower plants in Ecuador do not have reservoirs and the planned projects are run-of-river plants located in the Amazon basin with small regulation reservoirs, which would not provide seasonal regulation. Furthermore, despite the fact that hydropower plants with reservoirs are less sensitive to inflow changes than run-of-river plants, any storage capacity would be ineffective under extremely dry climate change scenarios (Carvajal et al., 2017).

Another strategy is to rely on the use of existing and new fossil fuel thermal power plants to increase the margin of reserve (Schaeffer et al., 2013), which is the approach of the Ecuadorian government for the cases of low hydrological scenarios (MERNNR, 2018). However, the increase of fossil fuel thermal power generation will correspondingly increase the production of greenhouse gas emissions, causing environmental impacts and strengthening the effects of climate change.

This dissertation explores a more sustainable and resilient strategy that involves leveraging the complementarity behavior that the generation profiles of variable renewable energy (VRE), namely, solar and wind, might have to the hydrological regime. The positive impacts of the VRE–hydro synergies on the economic performance and reliability of the power systems, as well as their contribution to the energy security of countries in South America, have been highlighted in recent studies (e.g., IRENA (2016), Paredes and Ramírez (2017)). Furthermore, this strategy is more aligned to the guiding concept ‘resilient systems’ that aims at describing design principles to prepare energy systems to the unexpected (Gleich et al., 2019; Gößling-Reisemann, 2016). Resilience is understood as a (socio-technical) system’s ability to maintain its services under stress and in turbulent conditions (Gleich et al., 2010). Diversity, redundancy, decentralization, and geographical dispersion of power supply sources are all key resilience-enhancing design principles, which aim at helping the power supply system to be prepared for and to cope with the aforementioned weather and climate related variabilities, as well as to other uncertain stressors (Brand et al., 2017; Gleich et al., 2019; Gößling-Reisemann, 2016; Gößling-Reisemann et al., 2019).

There are, however, some challenges that need to be tackled to scale up the share of solar and wind technologies in the Ecuadorian power mix. A key question for capacity generation expansion planning is where to install new wind and/or solar power plants that could potentially complement hydropower during the dry periods. This is a relevant issue

in countries such as Ecuador where the deployment of these technologies is still at a very early stage. An increase of the solar installed capacity occurred in 2014 (from 3.9 to 26.4 MW) (ARCERNNR, 2020); however, there have been no major new capacity additions since that time. The same is true for wind power capacity since 2013, when the only wind farm in Ecuador's mainland, *Villonaco* (16.5 MW), started operations (ARCERNNR, 2020).

According to the latest Ecuadorian generation capacity expansion strategy, *Plan Maestro de Electricidad 2018–2027*, the planned non-hydro renewable energy capacity is estimated based on resource atlases and described as two blocks of 900 MW total, which was expected to be commissioned sequentially by 2023 (MERNNR, 2018). From this total capacity, only 310 MW correspond to specific on-going projects (two wind farms of 110 MW total and one utility-scale photovoltaic (PV) farm of 200 MW), while the technology and location of the remaining planned capacity is still to be defined (MERNNR, 2018).

However, due to the varying nature of solar and wind resources, the optimal planning and deployment of solar and wind power that could potentially complement hydropower requires more comprehensive resource variability assessments. Such assessments will provide relevant information to decision-makers for solving the optimal siting and sizing problem. Beside the magnitude of solar radiation that resource atlases provide, a complete characterization of the solar resource should also include the analysis of the variability of the solar radiation over time and space, at different timescales and distance ranges (Gueymard et al., 2011). The same applies for the characterization of the wind resource (Watson, 2014). Unfortunately, the lack of long-term and high-resolved measurements of solar irradiance and wind speed hinders such assessments, representing a significant hurdle not only for Ecuador, but also for many South American countries (IRENA, 2017).

An additional challenge to better understand the variability of solar and wind resources in Ecuador is the complex climate and topography of the country. From a climatic point of view, the country is influenced by the displacement of the Intertropical Convergence Zone (ITCZ), the Pacific Ocean sea surface temperature fluctuations, the trade winds, the influence of Hadley and Walker circulation cells, and moisture advection from the Amazon (Ballari et al., 2018). From a topographic point of view, Ecuador includes a wide variety of terrain, ranging from flat coastal plains, rugged complex mountains in the Andes, rain forest lowlands in the Amazon, and volcanic origin islands in the Galapagos (Fig. 1-3).

The assessment of the contribution of solar and wind power to reduce the power output variability in such a complex terrain is another challenge to be tackled. Previous studies

have highlighted that the jointly operation of geographically-dispersed renewable power plants can significantly smooth out the power output and contribute to baseload power (e.g., Archer and Jacobson (2007), Santos-Alamillos et al. (2015)). However, the lack of wind and solar resource data at a high spatial and temporal resolution has hindered the evaluation of these potential benefits for the power supply system.

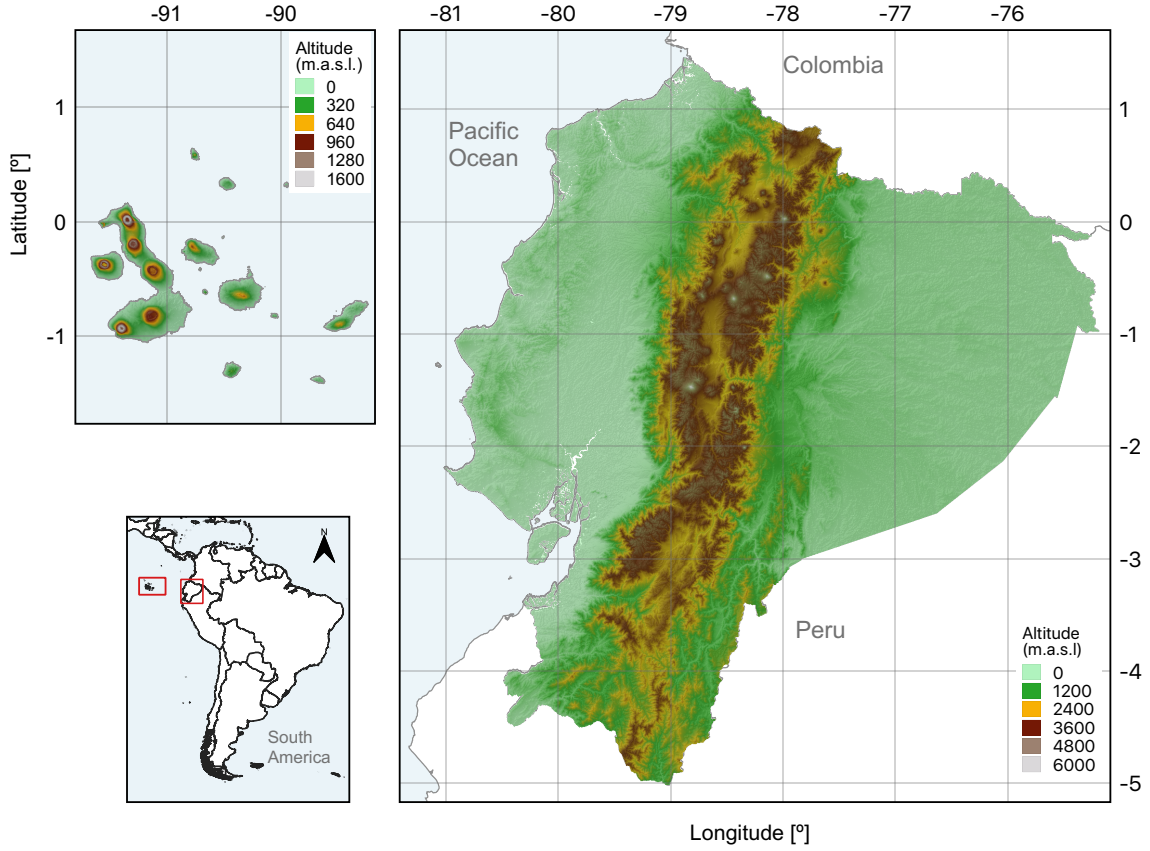

Fig. 1-3. Digital elevation map of Ecuador's mainland and the Galapagos Islands. Source: Own representation, data from IGM (2021), Watkins (2021).

Altogether, the Ecuadorian power planning sector encounters four central challenges to increase the share of solar and wind technologies that could complement hydropower: (i) the lack of historical, long-term, high-resolved, and validated meteorological datasets; (ii) the lack of an accurate characterization of the spatio-temporal variability of solar and wind resources in complex terrain; (iii) the lack of a comprehensive analysis of the spatio-temporal dynamics between solar, wind, and water resources; and (iv) the lack of a comprehensive analysis of the spatio-temporal synergies of geographically-dispersed PV and wind power generation to reduce the power output variability and provide reliable power generation.

1.3. Research objectives and scope

Based on the background and the problem statement described above, the main research goal of this dissertation is to develop tools and data for the optimal planning of a more sustainable and resilient power system in Ecuador by systematically investigating the spatio-temporal variabilities and synergies of renewable resources in the complex terrain of Ecuador.

To accomplish this research goal, four research objectives are defined:

1. To generate long-term and high-resolved solar and wind resource datasets for Ecuador.
2. To develop a new methodology based on spatial functional data analysis for the characterization of the spatio-temporal variability of solar and wind resources.
3. To analyze the spatio-temporal correlation between solar, wind, and water resources in Ecuador based on long-term and high-resolved meteorological datasets.
4. To analyze the opportunity of wind and solar power to enhance the resilience of the Ecuadorian power supply system by accounting the spatio-temporal synergies of renewable power generation.

This is the first study to undertake a systematic investigation from an energy meteorology perspective that addresses the aforementioned challenges confronting the Ecuadorian power planning sector. The findings of this dissertation represent the first comprehensive assessment of renewable power generation in Ecuador, which aims at supporting a sustainable energy transition in the country.

The study area comprises Ecuador's mainland and the Galapagos Islands, which are located 1000 km west from the Ecuadorian coast (Fig. 1-3). Although there is no hydropower in Galapagos, the islands rely heavily on diesel fuel imported from the mainland to generate electricity (Apolo et al., 2019). Considering the importance of the conservation of the marine and terrestrial ecosystems in Galapagos, this area is also included in the study to support the transition towards 100% renewable energy in the islands.

This dissertation is exclusively focused on the generation side of the power supply system. The analysis of transmission and distribution grid, as well as the economic aspects of solar and wind technologies are outside the scope of this study. Ecuador is chosen as a case study due to its complex climatic characteristics and topography, as well as the power sector particularities. Nevertheless, the proposed methodology can be transferred to other countries or regions to support the optimal planning of generation capacity expansion.

1.4. Dissertation outline

The schematic overview of the structure of this dissertation is depicted in Fig. 1-4, where the colored blocks represent the approaches used to address the research objectives. These approaches are explained in detail in the remaining part of this dissertation as follow.

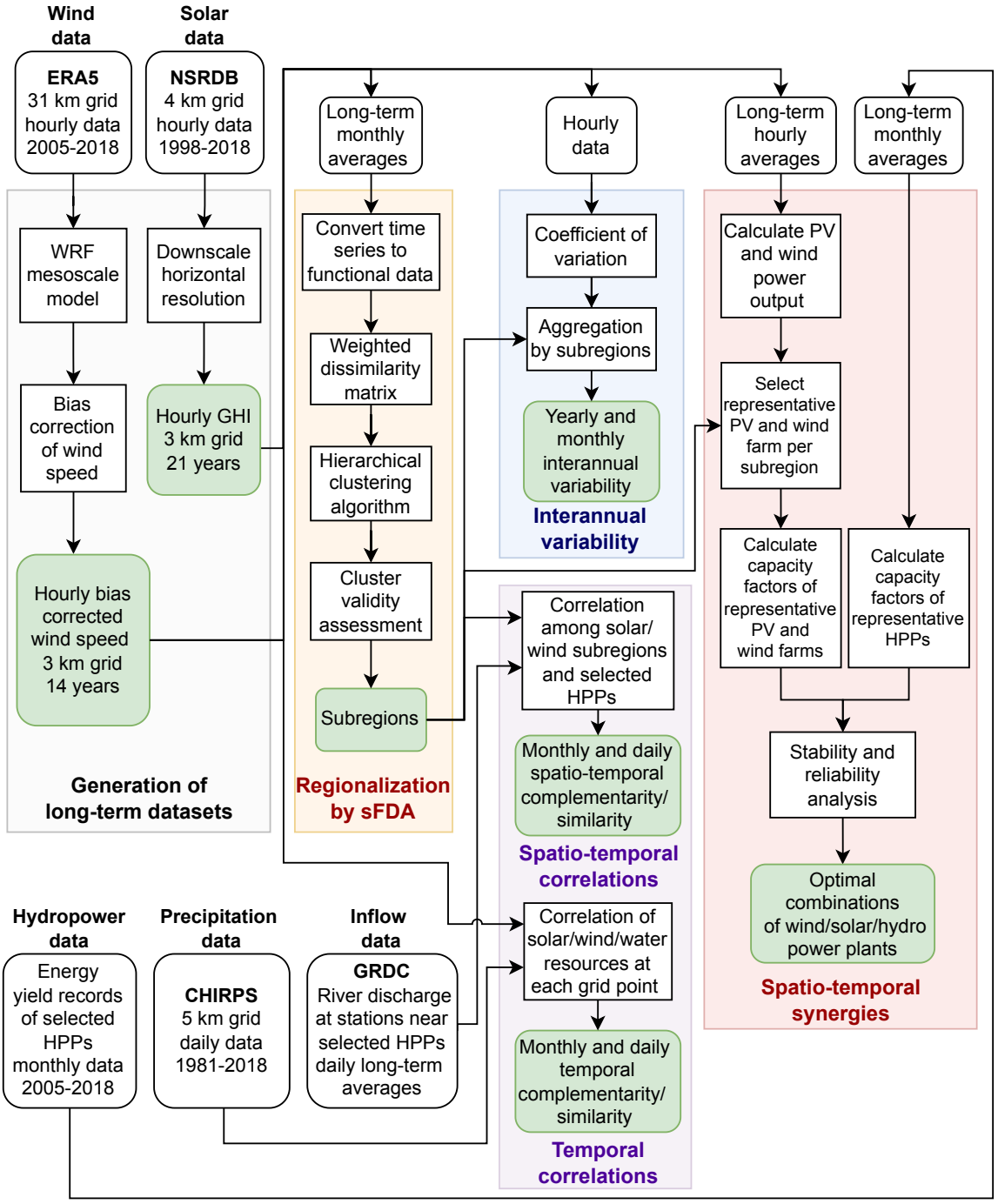

Fig. 1-4. Schematic overview of the structure of this dissertation. Each colored block represents the approaches used to address the research objectives, which are explained in detail in the corresponding chapters. Abbreviations: ERA5: European Centre for Medium-Range Weather Forecasts Reanalysis v5; NSRDB: National Solar Radiation Database; WRF: Weather and Research Forecast; HPP: Hydropower plant; CHIRPS: Climate Hazards Infrared Precipitation with Stations; GRDC: Global Runoff Data Center. Source: Own representation.

In Chapter 2, the new methodology to characterize the spatio-temporal variability of long-term and gridded meteorological datasets using spatial functional data analysis (sFDA) is described (*Research Objective 2*). The feasibility of the methodology is demonstrated by using a solar irradiance dataset of Ecuador's mainland and the Galapagos Islands. This dataset consists of a 21-year period of hourly solar resource data at 3×3 km grid resolution, which is generated by processing satellite-derived data retrieved from the National Solar Radiation Database (NSRDB) (*Research Objective 1 – solar resource dataset*).

Chapter 3 describes the configuration and validation of the Weather Research and Forecast (WRF) mesoscale model, which is used to generate a 14-year period of hourly wind resource data at a 3×3 km horizontal grid resolution for Ecuador's mainland and the Galapagos Islands (*Research Objective 1 – wind resource dataset*). This chapter also presents and discusses the results of the spatio-temporal variability analysis of wind speed over the study area, which is characterized by using the methodology proposed in Chapter 2.

Chapter 4 is concerned with the temporal and spatio-temporal correlation analysis between solar, wind, and water resources in the study area (*Research Objective 3*). First, this chapter investigates to which extent solar and wind resources are complementary in time and space to water resources in existing and planned hydropower plants. Next, the pairwise temporal correlations between solar, wind, and water resources at each grid point are assessed. The results from the sFDA regionalization and the long-term, gridded datasets of solar and wind resources generated in the previous chapters are used for the analysis. For water resources, historical measurements of river discharge near six representative hydropower plants, as well as a gridded precipitation dataset are used for the spatio-temporal and temporal correlation analysis, respectively.

In Chapter 5, the hourly time series of solar and wind resource datasets are converted into power output to analyze the complementarity of renewable power generation. The analysis focuses on the benefits that the spatio-temporal synergies between PV, wind, and hydropower could provide to enhance the resilience of the Ecuadorian power supply system. (*Research Objective 4*). This chapter describes the methodology to assess the benefits in terms of reliability and stability, and discusses the findings.

This dissertation finishes with Chapter 6 that summarizes the main findings related to each research objective, highlights the significance and contributions of this dissertation, and gives recommendations for further research work.

Chapter 2 Spatio-temporal characterization of long-term solar resource using spatial functional data analysis[1]

This chapter presents a new methodology to characterize the spatio-temporal variability of long-term and gridded meteorological datasets. Spatial functional data analysis (sFDA) is used to identify spatial areas with similar intra-annual variability patterns. The feasibility of the methodology is demonstrated by using a 21-year period of global horizontal irradiance (GHI) data on Ecuador's mainland and the Galapagos Islands, which is retrieved from the National Solar Radiation Database (NSRDB). This is the first time that the sFDA regionalization method is used for the characterization of solar resources and the results indicate that it provides a suitable basis for the interannual variability and complementarity analyses. In Ecuador's mainland, twenty-two subregions with four seasonal patterns are identified. The Inter-Andean valleys have the highest long-term annual mean GHI (5.4 $kWhm^{-2}d^{-1}$) with the lowest mean interannual variability (3.4%). In Galapagos, high values are found over all islands (≥ 4.8 $kWhm^{-2}d^{-1}$), characterized by three subregions with one seasonal pattern. The proposed methodology is applied in the next chapter for the characterization of wind resources and constitutes the basis for the achievement of the remaining research objectives of this dissertation.

2.1. Introduction

Solar energy plays a leading role in the global renewable capacity expansion. In 2020, there was an annual increase of solar capacity of 127 GW (+22%) (IRENA, 2021). This growing expansion is a key component that supports the energy transition towards decarbonization in many countries worldwide. However, due to the varying nature of the solar resource, the optimal planning and deployment of solar power applications requires detailed knowledge of the spatial and temporal variability of solar irradiance.

[1] This chapter is based on Tapia, M., Heinemann, D., Ballari, D., and Zondervan, E. (2022). Spatio-temporal characterization of long-term solar resource using spatial functional data analysis: Understanding the variability and complementarity of global horizontal irradiance in Ecuador. *Renewable Energy*, *189*, 1176–1193. https://doi.org/10.1016/j.renene.2022.03.049

Long-term variability analyses of solar irradiance provide essential information to decision-makers for a valid selection of suitable locations and optimal system design, as well as for the assessment of risk and the financial viability of solar energy projects (Fernández Peruchena et al., 2016; Gueymard et al., 2011; Lohmann et al., 2006; Rodríguez-Benítez et al., 2018; Sengupta et al., 2018; Vignola et al., 2012). Historical datasets covering 30 years or longer are needed to statistically characterize the solar irradiance at any location (Vignola et al., 2012). Unfortunately, such long-term, high-quality solar irradiance measurements are generally scarce and sparsely distributed, which challenges the spatial characterization at a country or regional level, especially over complex terrain. To overcome this limitation, satellite-derived datasets are considered a reliable and practical option that cover a wide spectrum of spatial scales and are available for long time periods (Sengupta et al., 2018).

Previous studies have explored the spatio-temporal variability of the solar resource at a regional scale using gridded satellite datasets (Gutiérrez et al., 2017; Habte et al., 2020; Laguarda et al., 2020; Vindel et al., 2020; Zagouras et al., 2013; Zagouras, Inman, et al., 2014; Zagouras, Pedro, et al., 2014)[2]. Some authors used climatological classifications to condense the large number of grid points into smaller groups (Habte et al., 2020), while other studies applied data-driven methods based on regionalization techniques to identify areas with similar solar radiation variability (Gutiérrez et al., 2017; Laguarda et al., 2020; Vindel et al., 2020; Zagouras et al., 2013; Zagouras, Inman, et al., 2014; Zagouras, Pedro, et al., 2014). A common approach used in the latter is the k-means algorithm applied to a dimension-reduced dataset by Principal Component Analysis (PCA). Reducing the data dimensionality lowers the computational complexity; however, it might not consider the inherent spatio-temporal dependencies of the data (Ballari et al., 2018; Jacques et al., 2014).

Spatial functional data analysis (sFDA) represents an alternative for analyzing high-dimensional gridded satellite-derived data, which considers the spatio-temporal dependencies of each grid point by means of spatial autocorrelation and complete time functions (Ballari et al., 2018; Giraldo et al., 2018). Although a spatial functional regionalization method was previously applied to gridded satellite precipitation data by Ballari et al. (2018), no studies have been found that applied spatial functional regionalization methods to gridded satellite GHI data to analyze the spatio-temporal variability of solar radiation.

[2] An overview of these studies can be found in Table A-1 in Appendix A.1.

In this chapter, a new methodology to characterize the spatio-temporal variability and complementarity of long-term gridded satellite-derived GHI data using sFDA is proposed. The methodology comprises multiple steps. First, a hierarchical regionalization method for spatial functional data is used to identify homogeneous areas with similar intra-annual variability patterns. Second, the characterization of the interannual GHI variability is performed using the coefficient of variation. Finally, the spatio-temporal complementarity between the resulting areas from the regionalization is analyzed through correlation coefficients.

As a case study, this methodology is applied to a 21-year period of gridded satellite-derived GHI data on Ecuador's mainland and the Galapagos Islands, which is retrieved from the National Solar Radiation Database (NSRDB). This region features complex climatic characteristics and topography (Morán-Tejeda et al., 2016; Pourrut, 1995), which may cause significant spatio-temporal GHI variability (Gueymard et al., 2011; Sengupta et al., 2015; Vignola et al., 2012), thus representing a relevant case for the application of the proposed methodology. Furthermore, Ecuador has an important solar energy potential, since almost 55% of its territory shows solar radiation levels above 4.1 $kWhm^{-2}d^{-1}$ (Ordoñez et al., 2019). However, the share of solar technology in the Ecuadorian power mix is still marginal. In 2020, the installed capacity of solar PV was 26.74 MW, representing only 0.33% of the total installed capacity in the country (see Fig. 1-2 in Chapter 1).

Therefore, the relevance of this chapter is twofold. First, its novelty lies in the use of the sFDA method for the regionalization of long-term gridded satellite-derived GHI data applied to a region characterized by complex climate and terrain. Second, the case study provides the first comprehensive spatio-temporal characterization of GHI in Ecuador that aims at supporting the Ecuadorian energy sector for the optimal planning and deployment of solar power systems in the country.

This chapter is structured as follows. Section 2.2 presents the data used and describes the proposed methodology. Section 2.3 presents the results of the case study in different subsections: (2.3.1) GHI regionalization, (2.3.2) interannual spatio-temporal variability, and (2.3.3) seasonal complementarity. Section 2.4 discusses the methodological approach and the practical contribution of the findings. Finally, Section 2.5 presents the conclusions of this chapter.

2.2. Methods and data

2.2.1. Solar resource data

For this chapter, the satellite-derived GHI data of the Physical Solar Model (PSM) version 3 from the NSRDB (Sengupta et al., 2018) is used. The NSRDB is produced and disseminated by the National Renewable Energy Laboratory (NREL) and provides solar irradiance and other meteorological data at a high spatio-temporal resolution (4×4 km grid at hourly and half-hourly intervals) covering a large part of the American continent (Sengupta et al., 2018). The comparison between GHI satellite estimations from the NSRDB and ground measurements from 53 stations across Ecuador's mainland was performed by Ordoñez et al. (2019). According to their results, the hourly mean bias error (MBE) for clear sky conditions was less than 5%, while for cloudy sky conditions the MBE was found to be less than 10%, suggesting a good agreement between measured and satellite-estimated data (Ordoñez et al., 2019). Those results were aligned with the findings from other comparisons at locations throughout the continental United States (Habte et al., 2018; Sengupta et al., 2018).

A 21-year period of hourly solar irradiance and meteorological data from 1998 to 2018 corresponding to the study area was downloaded through the Application Programming Interface (API)[3] provided by NREL. Two preprocessing steps were performed before applying the methodology described in Section 2.2.2. First, the dataset was statistically checked to search for possible data anomalies that could be related to satellite artifacts. This analysis revealed that grid points at longitudes 78.02°W and 77.98°W between latitudes 0.13°N and 1.71°S showed anomalies from 24-11-2008 to 31-12-2017, which might be attributed to satellite artifacts (See Fig A-1 in Appendix A). The nearest-neighbor interpolation method was applied to the identified grid points to reduce the anomalies. Second, the spatial resolution of the dataset was increased from the native NSRDB resolution to 3×3 km, applying the first order conservative remapping method. The change in resolution was required for the assessment of complementarities between solar and wind resources for the study area, which uses wind resources at a 3×3 km resolution simulated by the WRF mesoscale model (see Chapter 3). The processed solar resource dataset is stored as a netCDF file (network Common Data Form) with the variables listed in Table A-2 in Appendix A.3. The long-term monthly mean daily total GHI dataset for Ecuador and the Galapagos Island used in this chapter is displayed in Fig. 2-1.

[3] https://developer.nrel.gov/docs/solar/nsrdb/psm3-download/

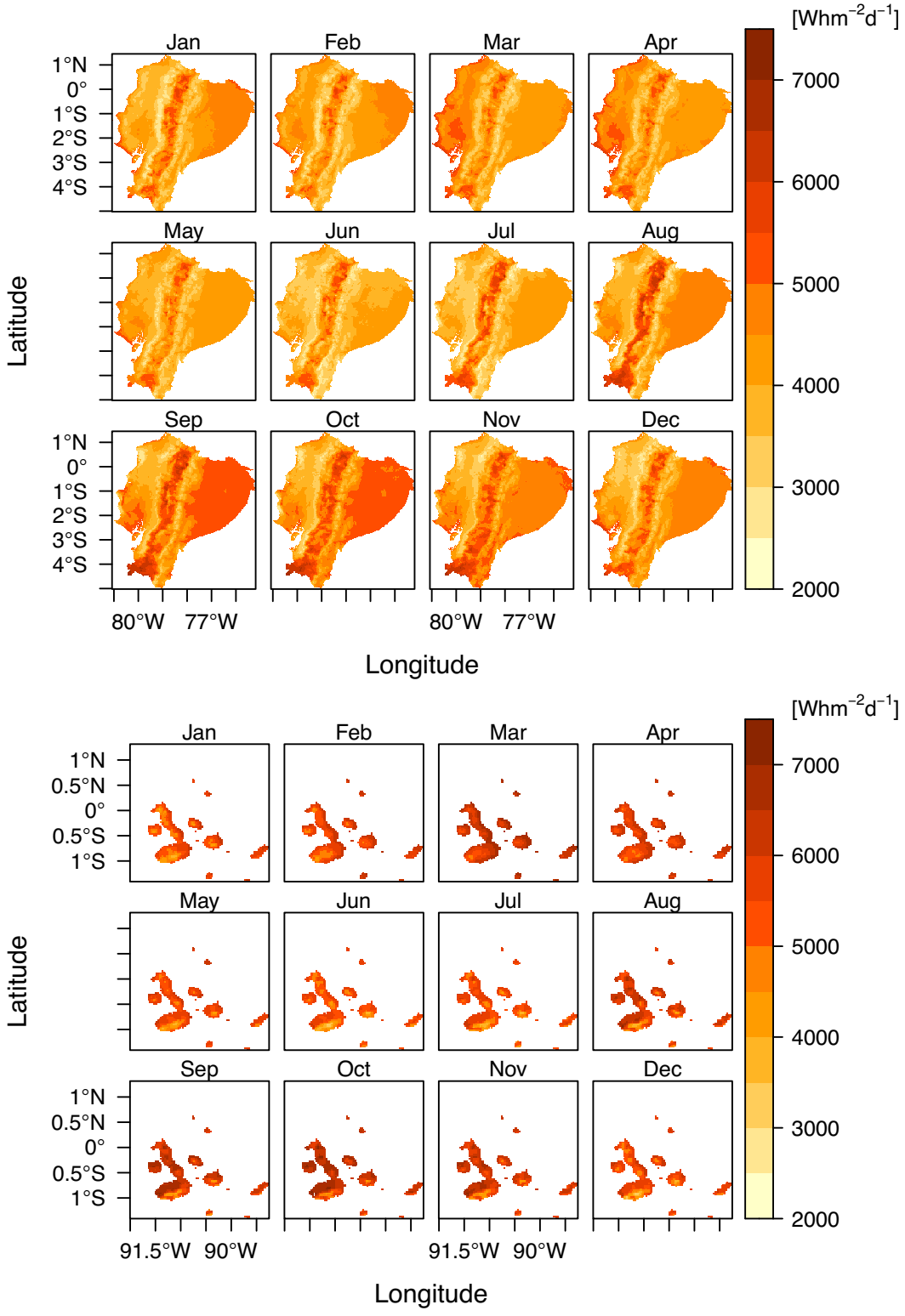

Fig. 2-1. Long-term monthly mean daily total GHI from 1998 to 2018 at a 3 × 3 km resolution on Ecuador's mainland (top) and the Galapagos Islands (bottom). Source: Own representation, data retrieved from the NSRDB.

2.2.2. Characterization of the spatio-temporal variability of gridded data

Fig. 2-2 provides an overview of the proposed methodology. Each block represents one of the different steps: regionalization, interannual variability, and complementarity analyses, which are explained in detail in the following subsections.

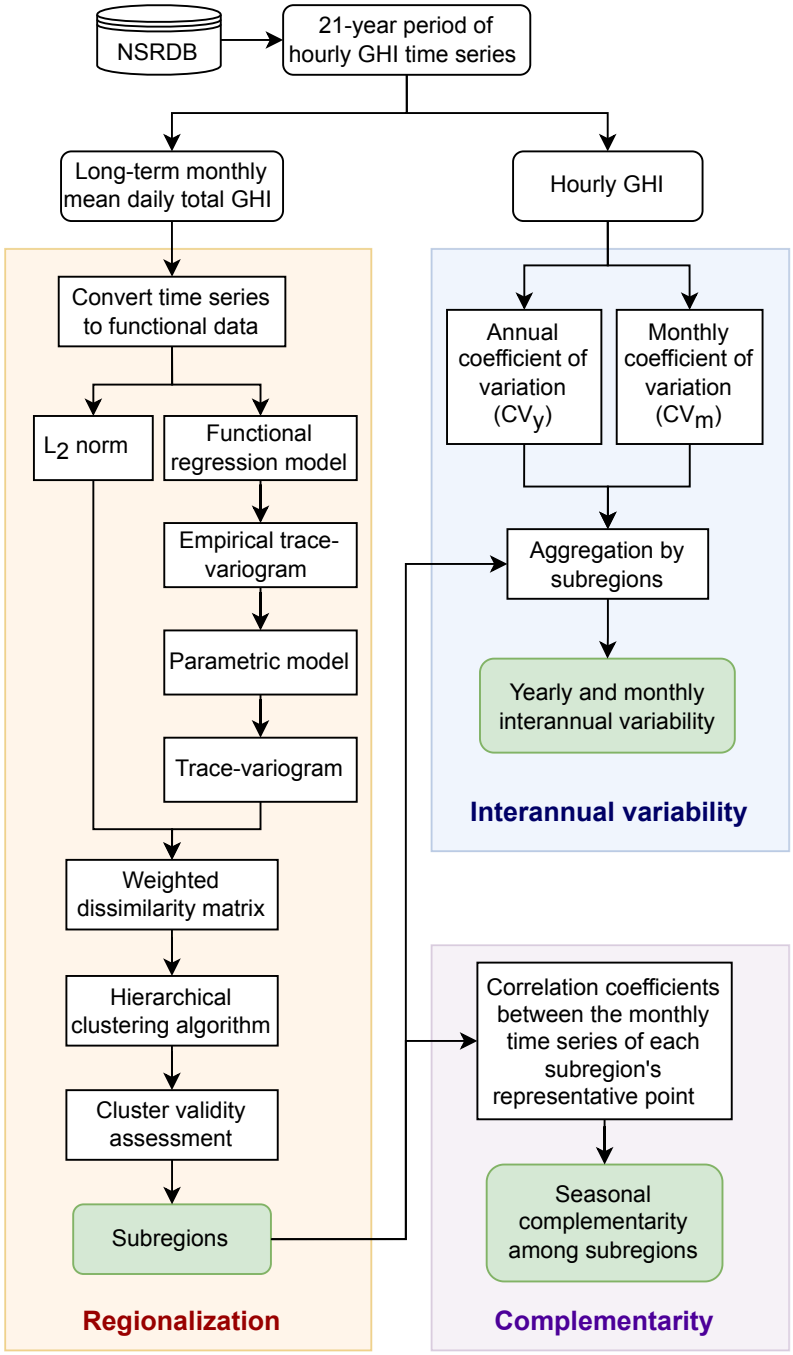

Fig. 2-2. Flowchart of the proposed methodology to characterize the spatio-temporal variability and complementarity of long-term gridded satellite-derived GHI data.

2.2.2.1. Regionalization

The hierarchical regionalization methodology for spatial functional data described in Giraldo, et al. (2012) is applied to the GHI dataset in order to identify homogeneous spatial areas with similar intra-annual variability patterns. This method combines hierarchical clustering algorithms for both geographically referenced and functional data to classify spatially correlated curves (Giraldo, Delicado, et al., 2012). It requires a weighted dissimilarity matrix based on the L_2 norm, which accounts for the dissimilarities among curves, and the so-called trace-variogram function (Giraldo et al., 2011), which accounts for their spatial correlation. A detailed description of the method can be found in Ballari et al., (2018) and Giraldo, et al. (2012). The following is a summary of the required steps that are displayed in the regionalization block of Fig. 2-2.

- ***Convert time series to functional data:*** The discrete time series of monthly mean daily total GHI (12-dimension vectors per grid point) are converted into functional curves using a Fourier basis with 11 functions. The Fourier basis system is chosen as the smoothing method assuming the periodicity of the GHI time series (Ramsay et al., 2005). The resulting dataset comprises the functional curves $\chi_{s_i}(t), \dots, \chi_{s_n}(t)$ at s_n geographical locations (27,175 in Ecuador's mainland and 874 in the Galapagos Islands).
- ***Weighted dissimilarity matrix:*** The weighted dissimilarity measure is expressed as:

$$d\omega\left(\chi_{s_i}(t), \chi_{s_j}(t)\right) = d\left(\chi_{s_i}(t), \chi_{s_j}(t)\right)\gamma_{s_i s_j}(h) \qquad (2.1)$$

  where $d\left(\chi_{s_i}(t), \chi_{s_j}(t)\right) = \sqrt{\int_T (\chi_{s_i}(t) - \chi_{s_j}(t))^2 dt}$ is the L_2 norm of the distance between two functional curves, and $\gamma_{s_i s_j}(h)$ is the trace-variogram function (Giraldo et al., 2011), which is calculated according to the spatial distance between geographical locations s_i and s_j (Ballari et al., 2018).

  The method assumes that the spatial functional process is second-order stationary (Giraldo, Delicado, et al., 2012); however, this assumption no longer holds true when there is a pronounced geographic trend in the dataset (Oliver et al., 2015), which is the case with solar radiation. For this reason, it is necessary to remove the spatial trend before calculating the trace-variogram function (Giraldo, Delicado, et al., 2012). This is done by using a functional regression model (Ramsay et al., 2005) with functional response (smoothed

GHI curves) and three scalar covariates (longitude, latitude and altitude). Once the regression model is estimated, the functional residuals are calculated to compute the empirical trace-variogram function. Then, a parametric model is fitted to the empirical trace-variogram following classical geostatistical estimation procedures (Giraldo, Delicado, et al., 2012). Finally, the trace-variogram $\gamma_{s_i s_j}(h)$ is calculated by subtracting the covariance function $C(h)$ for the distance between each pair of geographical locations from the variance $C(0)$ obtained from the fitted parametric model (Ballari et al., 2018).

- ***Hierarchical clustering algorithm:*** Once the weighted dissimilarity matrix is calculated, the Ward hierarchical agglomerative clustering method is applied. This method forms hierarchical groups of mutually exclusive subsets on the basis of their similarity with respect to specified characteristics (Ward, 1963).

- ***Cluster validity assessment:*** The optimal number of clusters is selected based on both the analysis of the average silhouette width (ASW) (Rousseeuw, 1987) and the analysis of the functional boxplots of the resulting clusters. The ASW provides a score based on how similar a curve is to all the curves in its respective cluster compared to curves in other clusters (Ballari et al., 2018), whereas the functional boxplots provide a visual comparison of the similarities/dissimilarities of the curves grouped in each cluster.

2.2.2.2. Interannual spatio-temporal variability

The coefficient of variation (CV) is used to analyze the interannual GHI variability during the 21-year period at yearly and monthly timescales. The CV is defined as the ratio of the standard deviation to the mean value (Gutiérrez et al., 2017). The results are expressed as percentages and represent a measure of the GHI variability over time at the cell's geographical location (Gueymard et al., 2011). For the analysis of the yearly interannual variability, the annual coefficient of variation (CV_y) is calculated as:

$$CV_y(\%) = \frac{\sqrt{\frac{1}{N}\sum_{i=1}^{N}(GHI_{y_i} - \overline{GHI}_y)^2}}{\overline{GHI}_y} \times 100 \qquad (2.2)$$

where N is the number of years; GHI_{y_i} is the annual mean daily total GHI of each individual i year; and $\overline{GHI}_y$ is the mean of the mean daily total GHI during the 21-year period (Habte et al., 2020).

Similarly, for the analysis of the monthly interannual variability, the monthly coefficient of variation (CV_m) is calculated based on monthly bins of data (e.g., Januaries, Februaries, etc.) as:

$$CV_m(\%) = \frac{\sqrt{\frac{1}{N}\sum_{i=1}^{N}(GHI_{m_i} - \overline{GHI}_m)^2}}{\overline{GHI}_m} \times 100 \quad (2.3)$$

where N is the number of years; GHI_{m_i} is the monthly mean daily total GHI of each individual i year; and $\overline{GHI}_m$ is the 21-year monthly mean daily total GHI for the corresponding month (Gueymard et al., 2011; Habte et al., 2020).

Both CV_y and CV_m are aggregated by the resulting clusters from the regionalization to facilitate the intercomparison among the spatial areas.

2.2.2.3. Complementarity

The Pearson product-moment correlation coefficient (r_P) is used to assess the spatio-temporal complementarity among different spatial areas and is calculated as:

$$r_{P_{ij}} = \frac{Cov(i,j)}{\sigma_i\, \sigma_j} \quad (2.4)$$

where $Cov(i,j)$ is the covariance between the monthly time series corresponding to the representative points of the clusters i and j; and σ_i, σ_j is the standard deviation of the monthly time series of the representative point of cluster i and j, respectively. The correlation coefficient can range from −1 to 1. Complementarity is associated to the negative values, whereas similarity is related to the positive values.

The level of complementarity and similarity is evaluated according to the interpretation given in Table 2-1 (Cantão et al., 2017).

Table 2-1. Interpretation of correlation coefficient values for the analysis of complementarity and similarity of renewable resources (Based on Cantão et al. (2017)*)*

Behavior	Correlation coefficient	Interpretation
Similarity	$0.9 \leq r_P \leq 1.0$	Very strong similarity
	$0.6 \leq r_P < 0.9$	Strong similarity
	$0.3 \leq r_P < 0.6$	Moderate similarity
	$0.0 \leq r_P < 0.3$	Weak similarity
Complementarity	$-0.3 < r_P < 0.0$	Weak complementary
	$-0.6 < r_P \leq -0.3$	Moderate complementary
	$-0.9 < r_P \leq -0.6$	Strong complementary
	$-1.0 \leq r_P \leq -0.9$	Very strong complementary

2.2.2.4. Implementation

The described methodology was implemented in R (R Core Team, 2020), using the packages *fda* (Ramsay et al., 2020) and *geofd* (Giraldo, Mateu, et al., 2012), among others.

2.3. Results

2.3.1. Regionalization results

This section presents the regionalization of GHI in Ecuador's mainland and the Galapagos Islands, described and analyzed in relation to the climate characteristics of the resulting spatial areas.

2.3.1.1. Regionalization of GHI in Ecuador's mainland

Twenty-two clusters are selected as the optimal partition for Ecuador's mainland according to the cluster validity assessment explained in Appendix A.4. These clusters (hereafter called subregions) represent spatially homogeneous areas featured with similar intra-annual GHI variability. From the functional boxplots of the subregions (see Appendix A.5), four main seasonal patterns are identified; consequently, the subregions are grouped into four spatial areas (hereafter called regions) according to the corresponding seasonal pattern.

The spatial distribution of the four regions and their respective subregions is shown in Fig. 2-3, where it can be seen that the regions are spatially contiguous and compact areas, which are distributed longitudinally through Ecuador's mainland. From east to west, region A is located in the Ecuadorian Amazon, regions EH and WH are located in the eastern and the western side of the Andean highlands, respectively, and region C is located in the coastal area.

The Ecuadorian Andes consist of two parallel mountain ranges (the Eastern and Western Cordilleras) separated by the tectonic Inter-Andean Depression (Coltorti et al., 2000). They are the major climate divide that separates the humid lowland forests of the Amazon basin from the coastal areas (Rollenbeck et al., 2011). These topographical and climate characteristics are reflected in the spatial distribution of the four regions, where the borders of regions C and A closely match the contour of the highlands. Furthermore, the spatial location of regions EH and WH resembles the distribution of the Andean highlands.

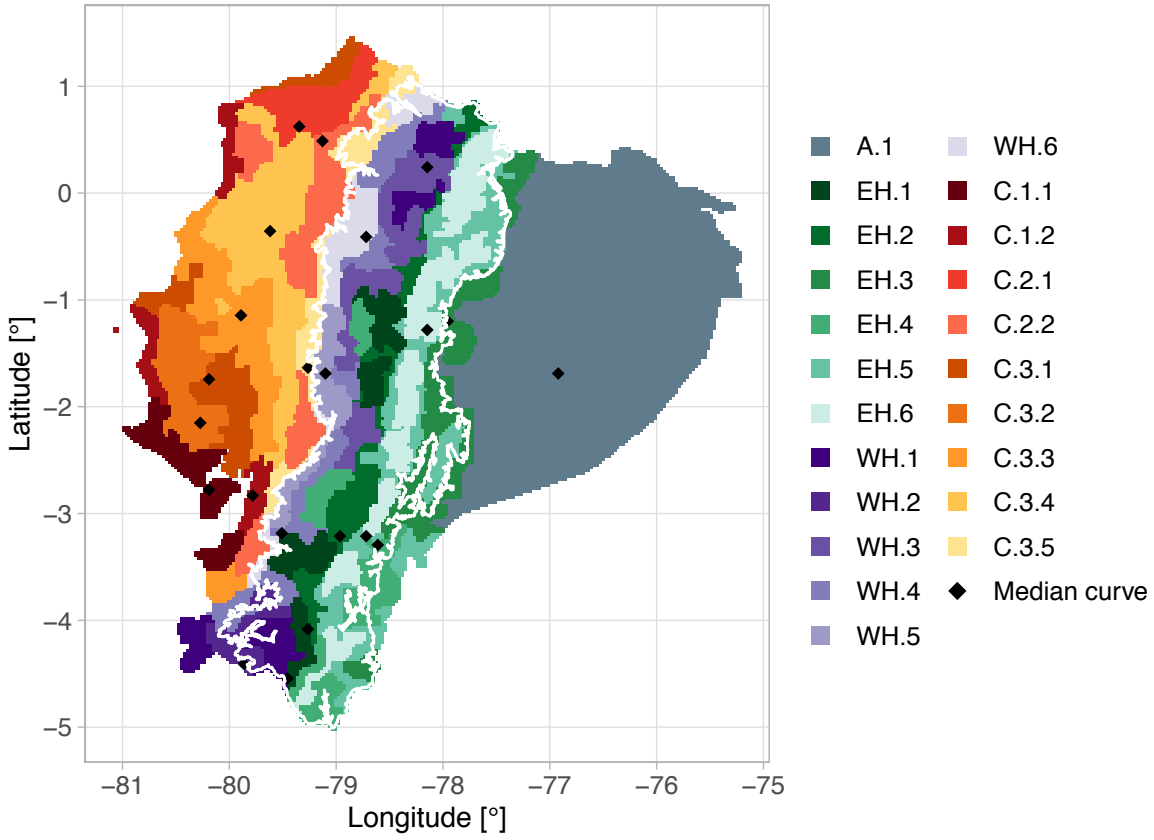

Fig. 2-3. Spatial distribution of the 22 solar subregions in Ecuador's Mainland after applying the sFDA regionalization method. The subregions are grouped and named according to their corresponding region: Amazon (A), Eastern highlands (EH), Western highlands (WH) and Coast (C). The white line depicts the altitudinal contour at 1000 meters above sea level (m.a.s.l.). The black points represent the location of the median curve of each subregion.

Fig. 2-4 shows the intra-annual GHI variability of each region. Fig. 2-4a shows the dispersion of the functional curves per region, whereas Fig. 2-4b compares their monthly and annual means. High GHI values are found in region WH, which shows a unimodal pattern with a peak in September. Region A displays a bimodal pattern with the annual maxima occurring in September–October and a peak of smaller magnitude in April. Region EH shows a similar seasonal pattern as region A but of smaller GHI magnitude, with the annual maxima occurring in October. In contrast to the previous regions, region C shows a bimodal pattern with a high peak in March and another of smaller magnitude in September. The annual minima of GHI in all regions (except for WH) occur in June–July, following the mid-year low sun elevation that corresponds to the austral winter. From Fig. 2-4b (left) it is evident that seasonal complementarity exists between region C and the other regions.

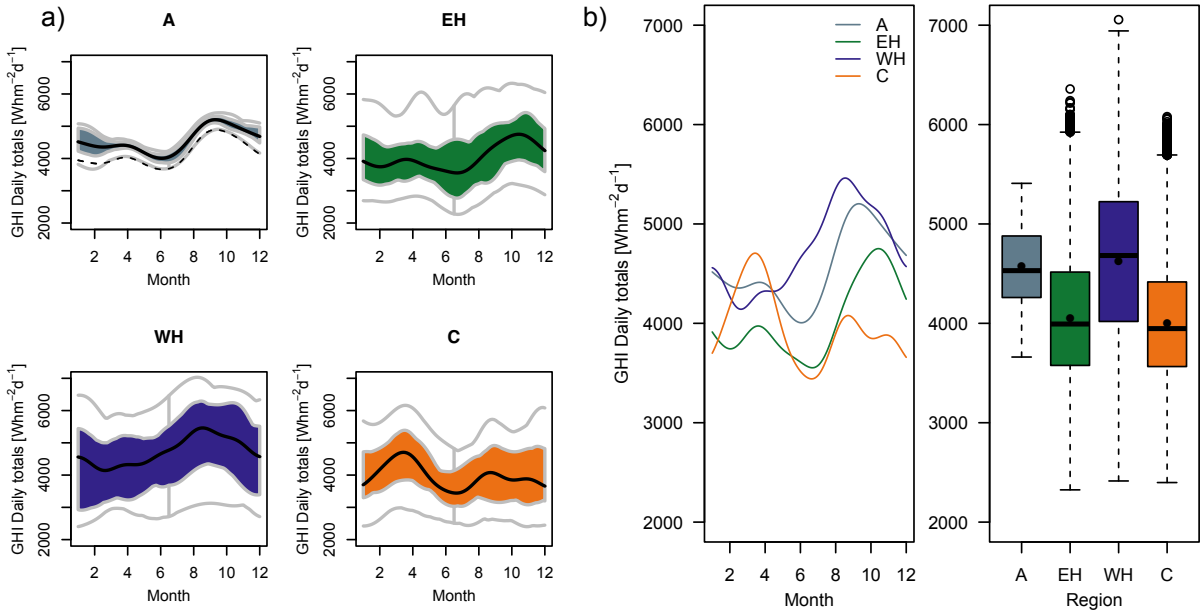

Fig. 2-4. Intra-annual variability of GHI in the four regions in Ecuador's mainland: Amazon (A), Eastern highlands (EH), Western highlands (WH) and Coast (C). The functional boxplots on a) show the monthly dispersion of the functional curves per region, where the colored shapes represent the interquartile range, the gray external lines depict the minimum and maximum curves, and the black lines are the median curves interpreted as the main seasonal patterns in each region. The black dotted line in region A represents the outlier curves in the region. The left side of b) shows the comparison of the four main seasonal patterns. The right side of b) shows the dispersion of the annual mean daily total GHI per region, where the black points represent the values of the median curve for each region, and the black circles are the outliers.

Fig. 2-5 and Fig. 2-6 show the spatial distribution and the intra-annual GHI variability of the 22 subregions grouped by their corresponding region. Here it is noticeable that the subregions in the corresponding region share similar seasonal patterns, but they differ in the magnitude of GHI. This can also be seen in Table 2-2, which summarizes the long-term annual mean daily total GHI per subregion.

Similar to the spatial variability, the intra-annual GHI variability may be explained by the climate characteristics – mainly cloud and rainfall dynamics – occurring in the different subregions that can affect GHI in complex ways.

In Ecuador's mainland, the climatic regimes closely depend on the characteristics of the air masses, which in turn are influenced or produced by three main factors: (i) the seasonal displacement of the ITCZ towards the north or south that determines the input of air masses with different temperature and humidity conditions; (ii) the mountain ranges that play a fundamental role in the formation, displacement, and isolation of local or regional air

masses; and (iii) the Pacific Ocean currents and the maritime air masses that influence the rainfall patterns in the Coast and the Andes region (Celleri et al., 2007; Pourrut, 1995).

The influence of these factors on the spatio-temporal GHI variability will become more evident when describing the subregions of each region in the following subsections.

Table 2-2. Long-term annual mean daily total GHI, yearly coefficient of variation (CV_y), and mean elevation in each solar subregion. Note that subregions are named and sorted in decreasing order according to the GHI value in their respective region.

Solar Subregion	GHI [$kWhm^{-2}d^{-1}$]	CV_y [%]	Mean elevation [m.a.s.l.]
A.1	4.6	3.8	312.3
EH.1	5.0	4.0	2645.5
EH.2	4.5	4.9	3186.4
EH.3	4.2	4.8	951.7
EH.4	4.1	5.4	2120.0
EH.5	3.8	6.2	2016.7
EH.6	3.4	8.0	2685.9
WH.1	5.4	3.4	1763.1
WH.2	5.1	4.5	1148.2
WH.3	5.1	4.7	3414.7
WH.4	4.5	5.3	2546.0
WH.5	4.0	6.1	2243.8
WH.6	3.7	6.0	1790.8
C.1.1	4.8	4.4	31.2
C.1.2	4.1	6.0	101.5
C.2.1	4.0	4.9	140.0
C.2.2	3.6	6.2	319.2
C.3.1	4.6	4.0	52.0
C.3.2	4.3	4.2	246.3
C.3.3	4.2	4.5	98.7
C.3.4	3.8	5.5	176.9
C.3.5	3.3	7.0	956.4
G.1.1	6.0	3.9	259.1
G.1.2	5.5	5.7	212.8
G.1.3	4.8	7.3	292.2

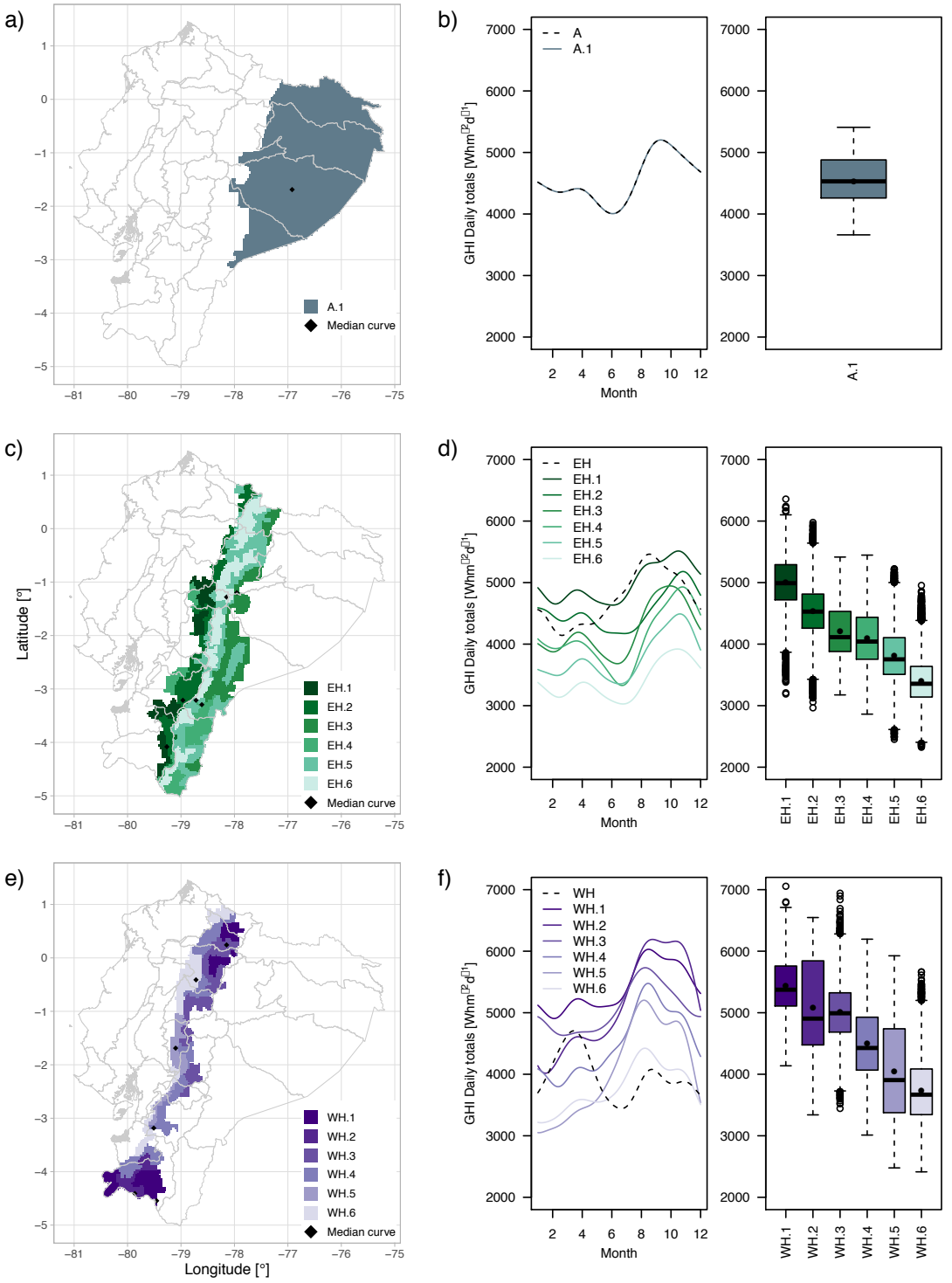

Fig. 2-5. Spatial and temporal variability of GHI per subregions in regions: Amazon (A), Eastern highlands (EH) and Western highlands (WH). The maps on a), c) and e) show the spatial distribution of subregions within each region (gray polygons depict the province boundaries. See Appendix D for provinces' names). The left sides of b), d) and f) show the comparison of the main GHI seasonal patterns for the corresponding region (dotted black lines) and the median curves in each subregion. The right sides of b), d) and f) show the dispersion of the annual mean daily total GHI for each subregion, where the black points represent the values of the median curve of each subregion.

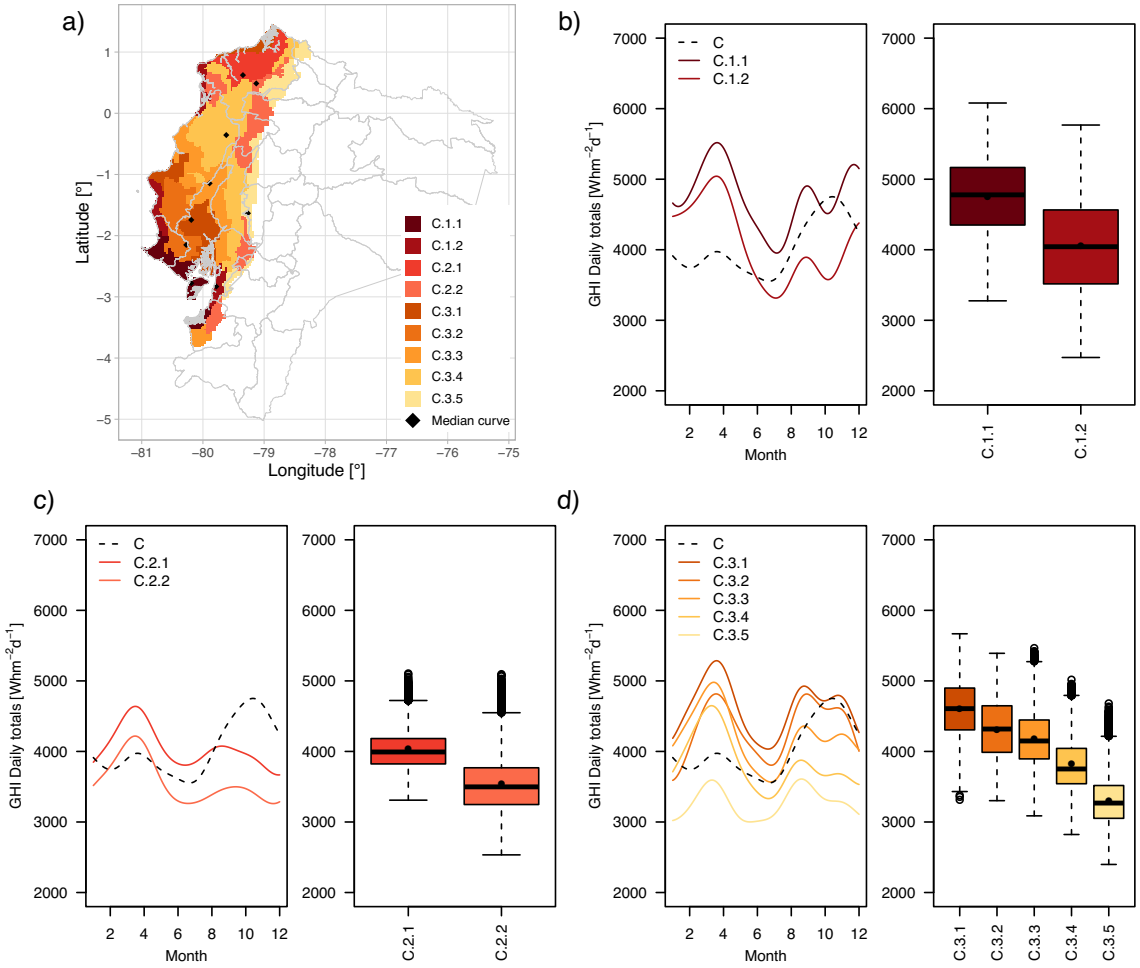

Fig. 2-6. Spatial and temporal variability of GHI per subregions in the coast region (C). The map on a) shows the spatial distribution of the subregions (gray polygons depict the province boundaries. See Appendix D for provinces' names). The left sides of b) – d) show the comparison of the main GHI seasonal pattern of region C (dotted black lines) and the median curves in each subregion. The right sides of b) – d) show the dispersion of the annual mean daily total GHI for each subregion, where the black points represent the values of the median curve of each subregion.

2.3.1.1.1. Amazon

One subregion (A1) is identified over the Amazon lowlands (Fig. 2-5a). Interestingly, this homogeneous subregion covers an extended geographical area and it is characterized by high annual mean values (4.6 $kWhm^{-2}d^{-1}$) and low intra-annual variability (Fig. 2-5b). This may be attributed to the high specific humidity and convective activity throughout the year in the area (Laraque et al., 2007), which results in low total annual sunshine hours (Pourrut, 1995).

2.3.1.1.2. Eastern Andean Highlands

Six subregions (EH.1–EH.6) are identified along the eastern Andean highlands and partly over the inter-Andean valleys (Fig. 2-5c). The highest annual mean values are found in EH.1, followed by EH.2 and EH.4 (5.0, 4.5, 4.1 $kWhm^{-2}d^{-1}$, respectively) (Fig. 2-5d), which are located along the Inter-Andean valleys. In contrast, the lowest annual values are found in EH.6, followed by EH.5 (3.4, 3.8 $kWhm^{-2}d^{-1}$, respectively), located along the eastern Andean flanks.

The low GHI values and low intra-annual variability found in EH.5 and EH.6 may be explained by the influence of a high cloudiness and precipitation band called Andes-Occurring System (AOS) (J. Bendix et al., 2006). This area is dominated by moisture bearing easterlies that originate over the tropical Atlantic and Amazon basin (Buytaert et al., 2006; Vuille et al., 2000). Most of the moisture is precipitated in the form of long duration drizzle due to orographic lifting (Rollenbeck et al., 2011).

The higher values of GHI seen in EH.1 and EH.2 may be attributed to lower rainfall amounts occurring in the Inter-Andean valleys because air masses transported from the Amazon and the Pacific lose much of their humidity on the eastern and western flanks of the Andes (Vuille et al., 2000). EH.3 is partly located along the outer eastern Andean flanks, and therefore shows a similar seasonal pattern as EH.5 and EH.6, but of higher GHI magnitude, since EH.3 covers part of the Amazon lowlands.

All the EH subregions depict annual maxima in October-November. This is aligned to ground measurements from stations located in southern Ecuador that found November as the month with the greatest clear sky probability (Emck, 2007). The annual minima occur in June-August, which coincides with the lowest sun elevation of the year and more persistent overcast skies brought in by the strong easterlies (Emck, 2007).

2.3.1.1.3. Western Andean Highlands

Six subregions (WH.1–WH.6) are identified along the western Andean highlands and the Inter-Andean valleys (Fig. 2-5e). Subregion WH.1 shows the highest annual mean GHI values (5.4 $kWhm^{-2}d^{-1}$) and low intra-annual variability. Subregion WH.2 shows high annual mean GHI values (5.1 $kWhm^{-2}d^{-1}$) as well; however, the intra-annual variability is higher compared to WH.1 (Fig. 2-5f). Subregion WH.3 is located at high elevations of the western and eastern Cordillera and shows a similar seasonal pattern to WH.1, but of lower GHI magnitude (Fig. 2-5f).

Subregions WH.4, WH.5 and WH.6 are spatially distributed along the western Andean slopes towards the coastal area (Fig. 2-5e) and show lower annual mean GHI values

(4.5, 4.0, and 3.7 $kWhm^{-2}d^{-1}$, respectively) (Fig. 2-5f). The reduced GHI magnitude in this area may be attributed to the influence of the ITCZ over the eastern Pacific, which is responsible for continuous moisture in the form of rainfall, clouds, and fog due to orographic uplift (Buytaert et al., 2006). These aspects are especially reflected in the lower intra-annual GHI variability of subregion WH.6 (Fig. 2-5f).

As mentioned above, the annual minima in the WH region do not match the lowest sun elevation of the year and vary from December to March among the subregions. This singularity was analyzed by Emck (2007) using measured data from stations located in southern Ecuador. The author concluded that the barrier effect produced by the eastern mountains benefits the leeward flanks, because in June–August the share of the water vapor and the clouds retained by the mountain range increases. Consequently, extended times of direct insolation compensate for the lowest annual solar radiation (Emck, 2007).

2.3.1.1.4. Coast

Nine subregions with three slightly different seasonal patterns are identified in the coastal area and grouped accordingly as C.1.1, C.1.2, C.2.1, C.2.2, C.3.1–C.3.5 (Fig. 2-6). In general, all the subregions show annual maxima in March-April and another peak of reduced intensity in September–October. Fig. 2-6b shows the first type of seasonal pattern found in C.1.1 and C.1.2. The highest annual mean GHI value is found in subregion C.1.1 (4.8 $kWhm^{-2}d^{-1}$) located in the lowlands near the coastline. This area is particularly dry with low rainfall rates (in the form of drizzle) due to the influence of the cold Humboldt current (Pourrut, 1995). C.1.2 has a similar seasonal pattern to C.1.1, but of lower GHI magnitude due to the spatial dispersion and the humidity level of the three partitions that comprise this subregion (ranging from arid and dry to super-humid and sub-humid (Moya, 2006)).

Fig. 2-6c shows the second type of seasonal pattern that is found in C.2.1 and C.2.2, characterized by low intra-annual variability and low GHI values. This may be attributed to the influence of the ITCZ (Ilbay-Yupa et al., 2021) and the location of the subregions along the lower slopes of the western Andean, where orographic rainfall occurs.

Fig. 2-6d shows the third seasonal pattern that is found in C.3.1–C.3.5, where a gradual decrease of GHI magnitude can be seen. From Fig. 2-6a, it is noticeable that this gradient occurred from west to east and is related to the geographical location and altitude of the subregions, since rainfall increases between the low-altitude coastal cordillera and the Andean foothills (Erazo et al., 2018).

2.3.1.2. Regionalization of GHI in the Galapagos Islands

Three subregions are selected as the optimal partition for the Galapagos Islands according to the cluster validity assessment explained in Appendix A.4. Fig. 2-7a shows the spatial distribution of the subregions (G.1.1, G.1.2, and G.1.3), which depict a bimodal pattern, but they differ in GHI magnitude (Fig. 2-7b). G.1.1 shows the highest annual mean value (6.0 $kWhm^{-2}d^{-1}$) with the annual maxima in October. G.1.2 and G.1.3 show lower values (5.5 and 4.8 $kWhm^{-2}d^{-1}$, respectively) with the annual maxima in March. The minima of all subregions occur in June-July.

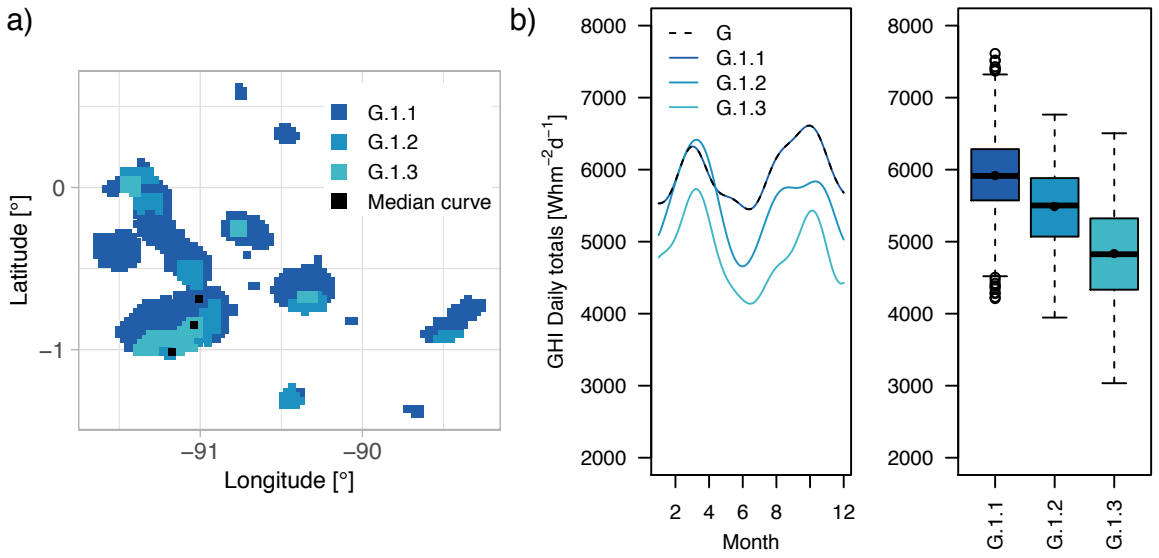

Fig. 2-7. Spatial and temporal variability of GHI in the Galapagos Islands (region G) per subregions after applying the sFDA regionalization method. The map on a) shows the spatial distribution of subregions (See Appendix D for islands' names). The left side of b) shows the comparison of the main GHI seasonal pattern of region G (dotted black lines) and the median curves in each subregion. The right side of b) shows the dispersion of the annual mean daily total GHI for each subregion, where the black points represent the values of the median curve of each subregion.

Similar to Ecuador's mainland, the spatio-temporal variability of GHI in Galapagos may be explained by the climate characteristics in this area, which result from a complex interaction of oceanic currents that surround the islands and the predominant trade winds from the southeast (Trueman et al., 2010). During January to May (hot season), G.1.1 and G.1.2 show similar patterns and high GHI values. In contrast, from June to December (cool season) a difference in GHI magnitude can be seen (Fig. 2-7b). On the one hand, G.1.2 is located along the windward side of both the islands and the volcanoes, which are more humid during the cool season (Trueman et al., 2010), thus reducing the incoming radiation in these areas. On the other hand, G.1.1 comprises the lowlands and the tops of higher volcanoes, areas that remain dry during the cool season (Trueman et al., 2010), thus showing higher GHI values. G.1.3 shows lower GHI values throughout the year compared

to the other subregions. This may be attributed to its location over the highlands and south-facing slopes, since humidity and rainfall increase considerably with altitude due to the influence of the Humboldt Current (Pourrut, 1995).

2.3.2. Interannual spatio-temporal variability of GHI

Fig. 2-8 shows the annual coefficient of variation CV_y, where it can be seen that the highest yearly interannual variabilities are along the eastern and western flanks of the Andes, the northwest coastline, and over the south-facing slopes of the Galapagos Islands. In contrast, the Amazon lowlands and the Inter-Andean valleys show the lowest variabilities.

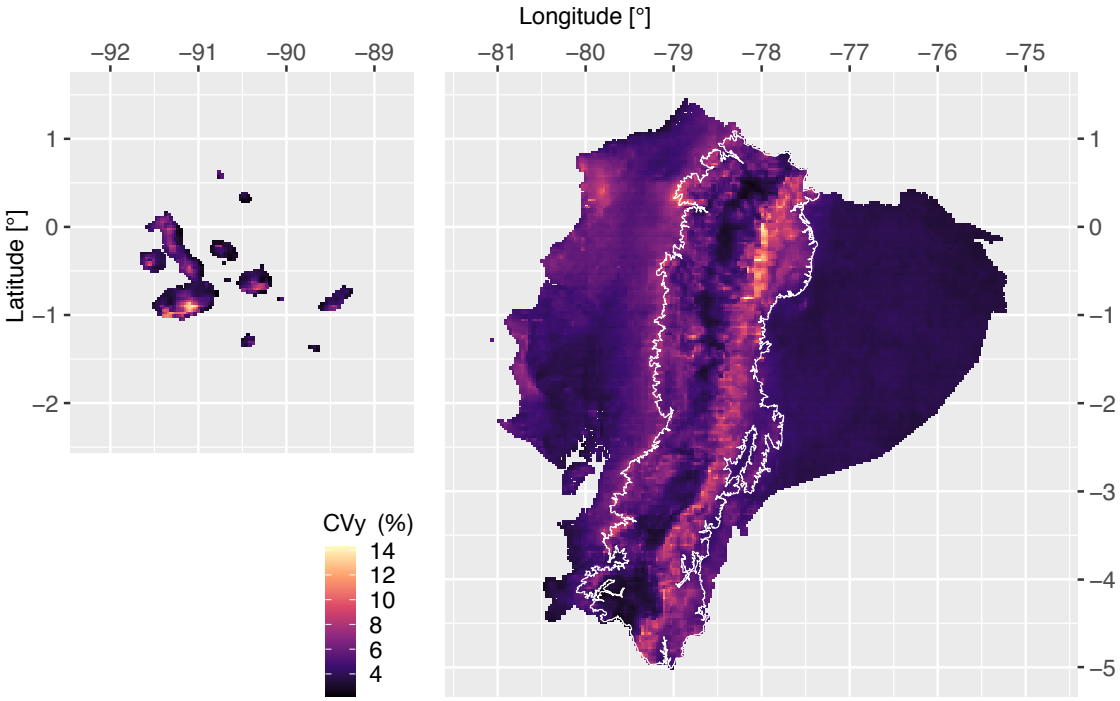

Fig. 2-8. Annual coefficient of variation CV_y (%) of mean daily total GHI during 1998–2018 over Ecuador's mainland and the Galapagos Islands. The white line over the continental part depicts the altitudinal contour at 1000 m.a.s.l.

Table 2-2 and Fig. 2-9 show the variability per subregion in detail. The highest mean CV_y values (> 6.0 %) are found in EH.6, G.1.3, C.3.5, EH.5, and C.2.2, while the lowest mean values (< 4.0 %) are found in WH.1 and A.1. Fig. 2-9 also reveals a clear trend of increasing variability among the subregions within their corresponding regions, meaning that the subregions that show higher CV_y values are those with lower GHI magnitude in their respective region.

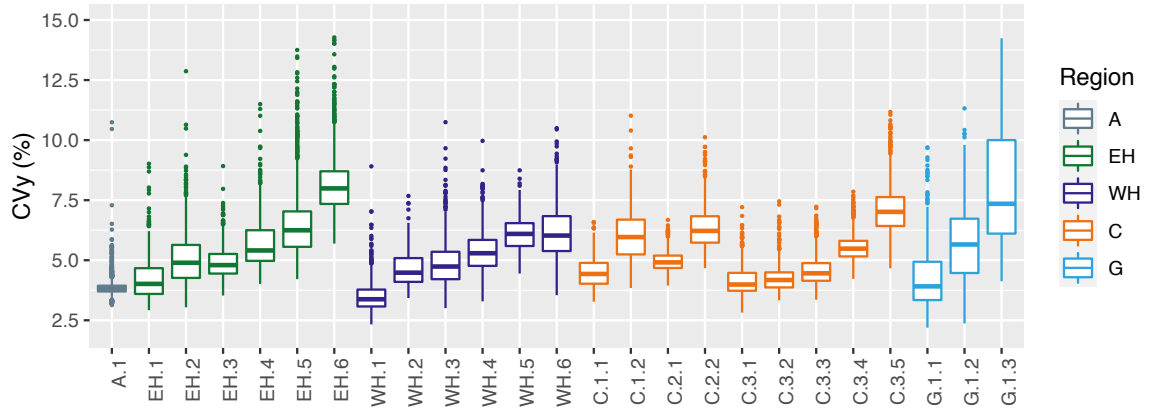

Fig. 2-9. Annual coefficient of variation CV_y (%) of mean daily total GHI during 1998–2018 per subregion and grouped by region: Amazon (A) Eastern highlands (EH), Western highlands (WH), Coast (C), Galapagos (G).

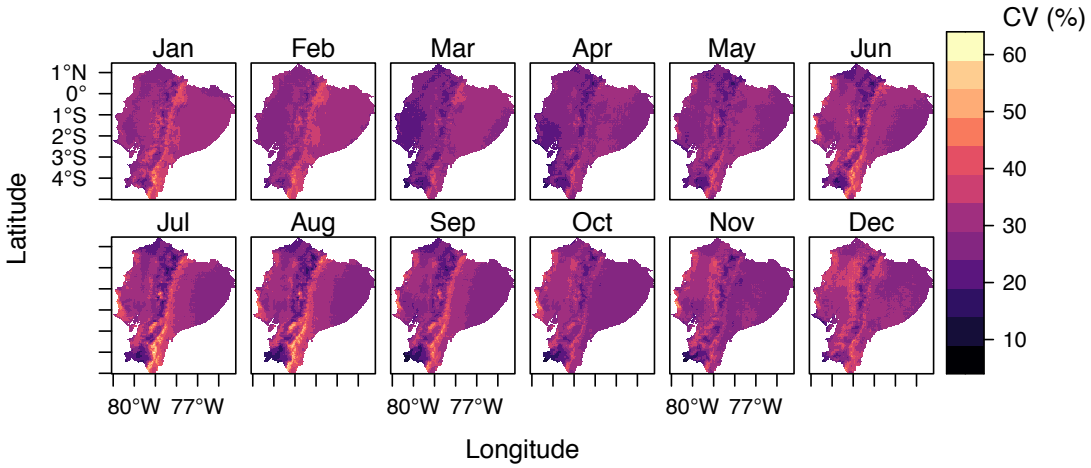

Fig. 2-10. Monthly coefficient of variation CV_m (%) of mean daily total GHI during 1998–2018 over Ecuador's mainland.

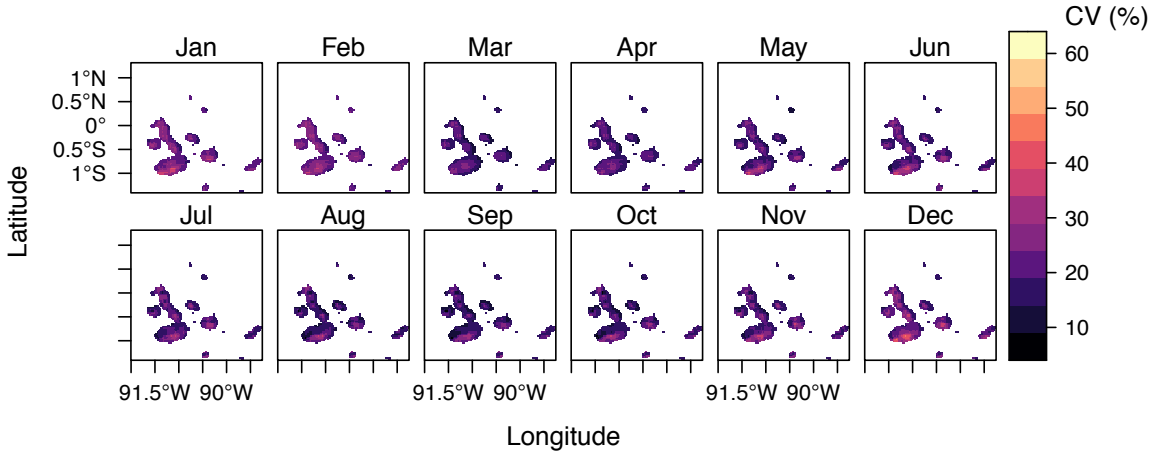

Fig. 2-11. Monthly coefficient of variation CV_m (%) of mean daily total GHI during 1998–2018 over the Galapagos Islands.

Fig. 2-10 and Fig. 2-11 show the monthly coefficient of variation CV_m, where it is notable that the highest monthly interannual variabilities are along the eastern flanks of the Andes, the western coastline, and over the south-facing slopes of the Galapagos Islands.

Fig. 2-12 takes a more detailed look at these findings, aggregated per subregions. The highest mean CV_m values are in the EH region (especially in EH.6) during two intervals: December to February and July to September. On the coast, C.1.2 shows high variabilities from May to December. Further, in Galapagos, G.1.3 shows the highest variabilities from December to January. In contrast, the lowest variabilities with minimum changes during the twelve months are in WH.1, located in the Inter-Andean valleys.

The high variability in EH.6 is associated with the AOS band of clouds and precipitation, as mentioned in Section 2.3.1.1.2. However, from Fig. 2-8 it can be inferred that this variability may also be attributed to the satellite image artifacts (see Appendix A.2), which particularly affects this subregion.

The high variability in subregions C.2.2, C.3.5, WH.4, WH.5, WH.6 and G.1.3 may be attributed to the effect of climatic phenomena occurring in the area, such as ENSO. This phenomenon, recognized in its cold phase as La Niña and its warm phase as El Niño, influences the rainfall interannual variability on the Pacific coast (Trenberth, 2019). El Niño triggers convection that leads to large rainfall events along the coast of Ecuador and Peru (A. Bendix et al., 2006; Morán-Tejeda et al., 2016) and the western Andean slopes between 1°–3°S (Vuille et al., 2000). Similarly, the surface ocean around the Galapagos Islands warms substantially during El Niño events, producing significantly more rainfall compared to normal years (Sachs et al., 2002).

Studies regarding the effects of ENSO on solar radiation in Ecuador were not found in the literature. Nevertheless, Henao et al. (2020) found that solar radiation anomalies in Colombia increase during El Niño and decrease during La Niña, which are related to the absence and excess of convective clouds. Similar dynamics might be expected in Ecuador; however, further investigation is needed to determine the underlying factors of the interannual GHI variability in Ecuador.

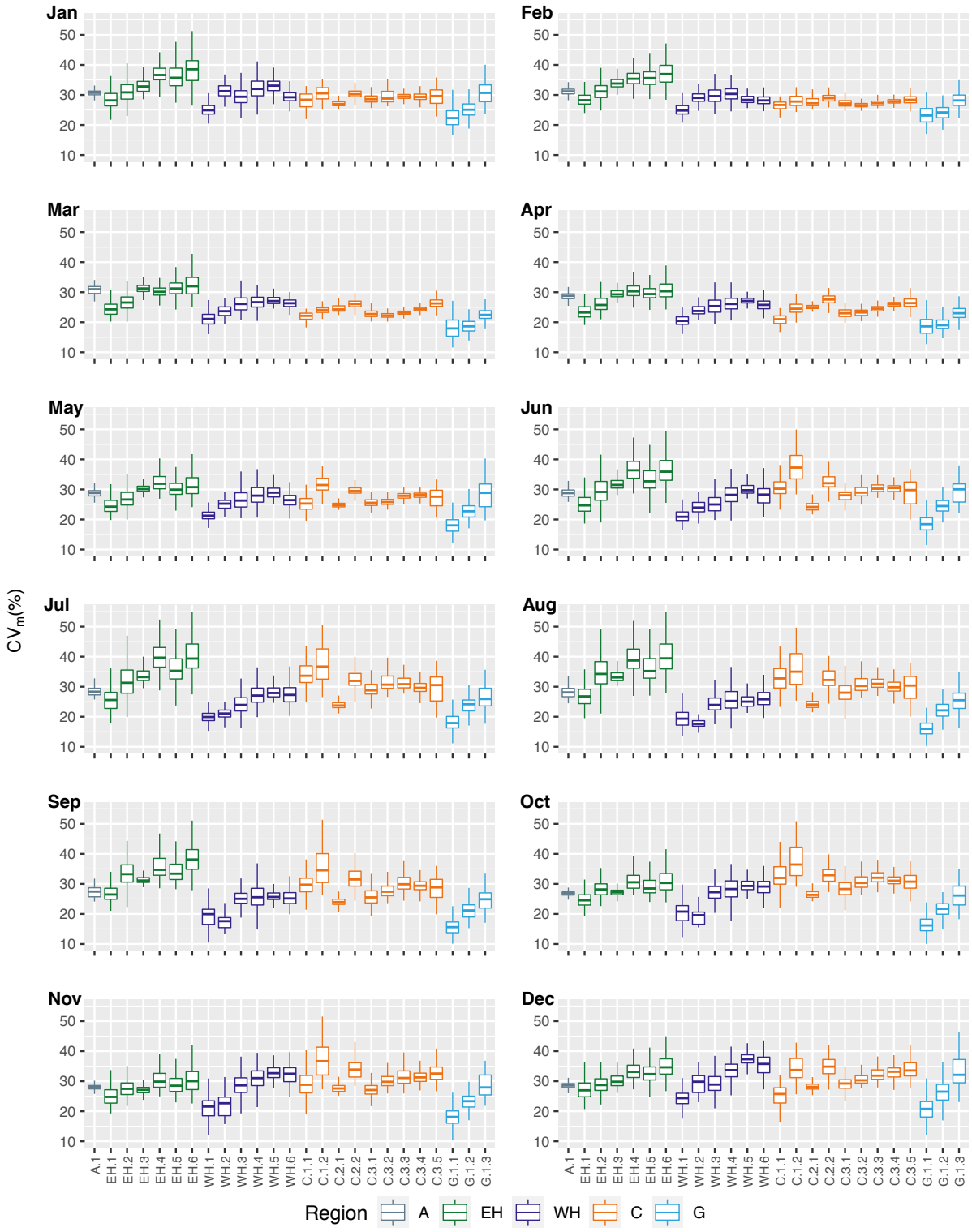

Fig. 2-12. Boxplots of the monthly coefficient of variation CV_m (%) of mean daily total GHI during 1998–2018 per subregion and grouped by region: Amazon (A) Eastern highlands (EH), Western highlands (WH), Coast (C), and Galapagos (G). The outliers are excluded for clarity.

2.3.3. Seasonal complementarity

The correlation matrix for all the pairs of subregions in Ecuador's mainland and the Galapagos Islands is shown in Fig. 2-13. The negative coefficients highlight that region C and the other regions are complementary, since their seasonal patterns are opposite (Fig. 2-4). Different levels of complementarity are identified: (i) strong complementarity between C.1.2 and all WH subregions, as well as between C.2.2 and WH.3, WH.4 and WH.5; (ii) moderate complementarity between subregions in C (except C.3.1 and C.3.2) and E.1 and WH subregions; and (iii) weak complementarity between C and A, and the other subregions in EH and WH. From the positive correlation coefficients, it is also evident that all subregions within each respective region show high similarities, thus highlighting the ability of the sFDA regionalization method to find groups with similar temporal patterns.

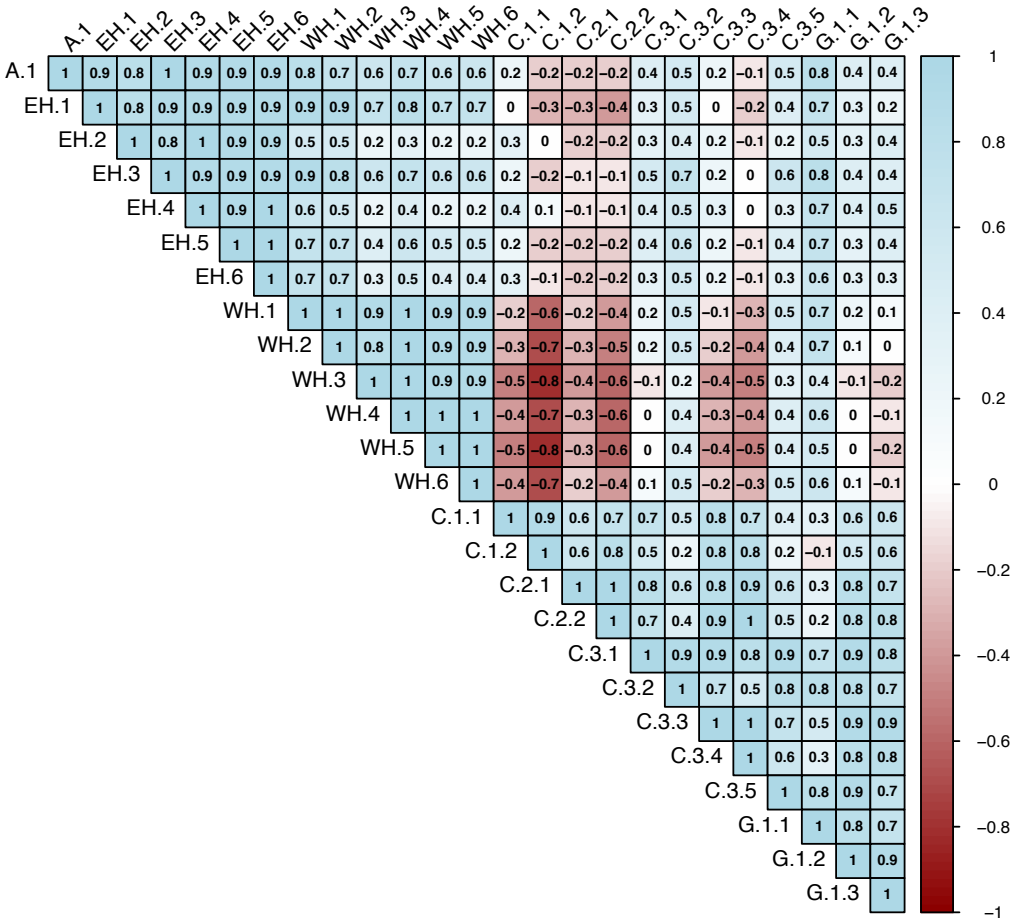

Fig. 2-13. Pearson correlation coefficient matrix of monthly mean daily total GHI time series of the median curves of each subregion.

2.4. Discussion

The results from the case study indicate that the sFDA regionalization method applied to gridded satellite-derived GHI data effectively identifies spatially homogeneous areas featured by similar GHI intra-annual variability patterns. The variation of the magnitude of GHI among areas that share similar patterns can also be identified. This approach differs from previous studies dealing with the analysis of the spatio-temporal variability of solar resource in a number of respects.

Firstly, the sFDA regionalization is a data-driven method that allows for the classification of the dataset considering its inherent spatio-temporal characteristics. This objective classification differs from classical climatological classifications based on temperature and precipitation. Habte et al. (2020) used the Köppen-Geiger (KG) climate classification (Kottek et al., 2006) to analyze the variability of the solar resource over America. Other studies used also the KG classification in various solar applications at a global scale (Ascencio-Vásquez et al., 2019; Sun et al., 2019). Such an approach may be appropriate for the analysis over large geographical areas; however, misclassifications could be expected due to the global focus and coarser resolution of the KG (Giler-Ormaza, 2018), or because misclassifications in mountainous regions in South America could not be corrected due to lack of data (Peel et al., 2007). Therefore, the KG classification might not be suitable for the analysis over smaller areas, since solar irradiance can vary significantly over relatively small distances due to microclimate effects of topography and the general behavior of regional weather patterns (Gueymard et al., 2011; Sengupta et al., 2015; Vignola et al., 2012).

Secondly, unlike previous GHI regionalization approaches that applied clustering algorithms after reducing the dimensionality of the satellite-derived datasets (Gutiérrez et al., 2017; Laguarda et al., 2020; Vindel et al., 2020; Zagouras et al., 2013; Zagouras, Inman, et al., 2014; Zagouras, Pedro, et al., 2014), the sFDA method classifies the dataset based on the dissimilarities between the curves from each grid point weighted by the dissimilarities throughout space. By considering the existing spatial correlation, the method is able to find groups of curves that are spatially homogeneous, since the weighting function increases the dissimilarities among distant points (Romano et al., 2015). In addition, the sFDA method provides tools such as functional boxplots in which the dispersion of the curves within each subregion can be explored in both spatial and temporal dimensions (Ballari et al., 2018).

Thirdly, the regionalization results from this case study indicate that the sFDA method captures the GHI variability due to microclimate effects. This ability is reflected for example in the spatial classification of the subregions along the Andes (Section 2.3.1.1.2). This outcome is contrary to that of Ballari et al. (2018), who applied the same regionalization approach for precipitation data but local variabilities along the eastern Andes were not captured. The authors attributed this limitation to the low resolution of the input satellite-derived dataset, which is confirmed by the findings of this study, since data at higher resolution is used (3 $\times$ 3 km grid resolution instead of 27 $\times$ 27 km used in Ballari et al. (2018)).

Finally, the variabilities due to the topographic effects are also captured by the sFDA. The interannual variability results of this case study are in line with those of Habte et al. (2020), who found high spatial variabilities over western South America. The authors attributed this finding to the complex topography and large ranges of elevation change over small areas. The results of this case study support this association; however, it is further identified that the variabilities not only account for the change of elevation, but also the microclimate effects in the different subregions. In addition, the high variabilities in the eastern Andes may also be attributed to the satellite image artifacts (see Appendix A.2).

The findings from this chapter contributes to the better understanding of the availability and variability of GHI in Ecuador. Previous studies have only provided information regarding the magnitude of the solar resource in Ecuador (Cevallos-Sierra et al., 2018; Echegaray-Aveiga et al., 2018; Ordoñez et al., 2019), but not a comprehensive analysis about its spatio-temporal variability. Ordoñez et al. (2019) built an updated solar atlas using the typical meteorological year (TMY) dataset from the NSRDB and highlighted those provinces with good solar potential. However, TMY datasets represent typical rather than extreme conditions, therefore they are not suitable to completely understand the resource variability (Vignola et al., 2012). In contrast, this study uses a 21-year period dataset from the NSRDB that enables both the identification of spatial areas with the best potential, and the evaluation of the variability of GHI over time, which is highly relevant for the design and financial feasibility assessment of solar energy projects (Gueymard et al., 2011).

Another important finding is that the subregions on the coast and the western Andean highlands show significant seasonal complementarities. This aspect raises the possibility for exploring planning and operation strategies, known as geographical smoothing effect (Lave et al., 2012; Marcos et al., 2012; Mills et al., 2009; Zagouras, Pedro, et al., 2014), to smooth out the intra-annual GHI variability and consequently the solar production in these areas. Nevertheless, according to the statistical analysis of the interannual variability, high

variabilities from May to December are found in C.1.2 and C.2.2. Since these subregions show strong complementarity to the WH region, further investigation is needed for assessing the complementarities during ENSO events, which could have an effect on the solar resource, as previously investigated in Colombia (Henao et al., 2020; Parra et al., 2020).

The validation of the NSRDB dataset over the study area was beyond the scope of this dissertation. In that respect, Ordoñez et al. (2019) found a good agreement between the satellite estimates and ground-measured solar radiation data from 53 stations in Ecuador's mainland. However, due to the sparse monitoring systems across the country, no measurements from the eastern and southern Ecuadorian Amazon, nor from the Galapagos Islands were used in the mentioned study. Therefore, it is recommended to perform further validations supported by the findings from this study. The geographical location of the median curves of each subregion, which is considered the most representative temporal pattern of the subregion, could be used for the placement of ground-based sensors and thus establish an optimal measurement network. The subregions with low interannual variability would require shorter measurement periods to characterize the solar resource (Gueymard et al., 2011).

The regionalization of GHI in this case study is performed using monthly averaged data to understand the intra-annual variabilities and seasonal complementarities. Nevertheless, the proposed methodology can be used at different temporal scales (e.g., daily or hourly), as well as to analyze other renewable resources, or energy production data. This case study uses the Fourier basis system as the smoothing method assuming that the monthly time series are periodic, however, for nonperiodic data (e.g., hourly wind speed data), the spline basis would be recommended (further details can be found in (Ramsay et al., 2009)). A practical limitation for using the sFDA regionalization method might be, however, the high computation cost in the case of a larger number of grid points or data at a high temporal resolution.

2.5. Conclusions

In this chapter a new methodology to characterize the spatio-temporal variability of long-term gridded satellite-derived GHI data using spatial functional data analysis is proposed. The methodology is implemented over Ecuador's mainland and the Galapagos Islands to demonstrate its applicability over a region characterized by complex climate and terrain.

The results indicate that the regionalization method identifies coherent areas with similar intra-annual variability patterns and effectively captures the GHI variations influenced by microclimate and topographic effects. Furthermore, the resulting subregions provide an appropriate basis for the analysis of the interannual variability and complementarity. In general, it is concluded that the proposed methodology can be applied to other regions or countries and adapted to analyze the spatio-temporal variability of other renewable resources or energy yield.

This chapter provides the first comprehensive spatio-temporal characterization of GHI in Ecuador, which is of particular relevance to support the optimal planning and deployment of solar power systems in the country. The regionalization map and the variability statistics provide explicit information to identify optimal sites for the deployment of irradiance measurement networks and solar power plants.

In Ecuador's mainland, WH.1 is one of the most suitable subregions, since it shows the highest annual mean values (5.4 $kWhm^{-2}d^{-1}$) and the lowest annual coefficient of variation (3.4%). Further areas with high potential (≥ 4.5 $kWhm^{-2}d^{-1}$) are located in the Inter-Andean valleys, the Amazon lowlands and along the coastline. In Galapagos, all islands show great potential (≥ 4.8 $kWhm^{-2}d^{-1}$), especially the subregion G.1.1, which has the highest annual mean values (6.0 $kWhm^{-2}d^{-1}$) and the lowest annual coefficient of variation (3.9%).

Moreover, the newly identified seasonal complementary behavior between the coast and the Andean Highlands lays the foundation for planning geographically-dispersed solar power plants, with the goal of smoothing the solar resource variability. This aspect is further explored in Chapter 4 and Chapter 5. The proposed methodology, the generated solar resource dataset, and the findings reported in this chapter represent the basis for the achievement of the remaining research objectives of this dissertation.

Chapter 3 Mesoscale modeling and characterization of wind resources over complex terrain in Ecuador

In this chapter, the newly developed 14-year period dataset of hourly wind speed and wind direction at a 3 × 3 km grid resolution for Ecuador's mainland and the Galapagos Islands is presented. The configuration and validation of the Weather Research and Forecast (WRF) mesoscale model used to generate this dataset is discussed in detail. The systematic deviations found between simulated wind speed at 80 m above ground level (AGL) with respect to observations at four sites located along the Andean highlands are then corrected using a linear scaling correction combined with the sFDA regionalization method. Next, the intra-annual and interannual spatio-temporal variability of wind speed is characterized applying the methodology proposed in Chapter 2. Results show that the key area for wind energy development is located over the Andean highlands that shows high long-term annual mean wind speeds (8.3 m s^{-1}) and stronger winds (up to 19.2 m s^{-1}) between June and September.

3.1. Introduction

A remarkable growth in the global wind energy installed capacity has been seen in the last decade. From 2010 to 2021, the global cumulative onshore wind capacity increased by more than four times, from 178 to 769 GW (IRENA, 2022). Driven by ambitious decarbonization targets set by governments around the world, as well as due to cost reductions, wind capacity is expected to further increase to double its current capacity by 2030 (IEA, 2021b).

In the case of Ecuador, the country has no policies that establish mechanisms and goals to promote non-hydro renewable energies (García de Fonseca et al., 2019). As a consequence, wind energy deployment is still at an early stage in the country. The total installed wind power capacity in the country is 21.15 MW, (16.5 MW in Ecuador's mainland and 4.65 MW in the Galapagos Islands), which represented only 0.26% of the share in the Ecuadorian power mix in 2020 (ARCERNNR, 2021).

The only existing wind farm in Ecuador's mainland, *Villonaco*, reached in 2015 an impressive capacity factor of 64%, generating 52% more than the estimated energy yield from the feasibility study (CELEC, 2016). While this highlights the significant wind potential in the country, it also shows the need for more reliable wind power assessments for the optimal planning and operation.

The output power of a wind turbine is given by the expression: $P = 0.5\, C_p\, \rho\, A\, U^3$; where, ρ is the air density; C_p is the power coefficient, which describes the fraction of power in the wind that may be converted by the turbine into mechanical work; A is the rotor swept area; and U is the average wind speed over the rotor area (Burton et al., 2021). Given the cubic dependence of a wind turbine's power output on wind speed, even small errors in wind speed translate into large errors in predicted power output. Therefore, accurate and reliable long-term wind resource data is required. Key sources of historical meteorological data to conduct wind power assessments include: ground observations, wind atlases, global reanalyses, and regional reanalyses (McKenna et al., 2022).

In Ecuador, wind resources are sparsely monitored and measurements are usually available at 10 m AGL, which is the standard meteorological measurement height; however, not relevant for wind energy applications (Jung et al., 2019). Recently installed high masts (50+ m) observation stations are only available at a few geographical locations over the Andean highlands. To identify sites with high wind resource potential, the country relies since 2013 on a tailored wind atlas at a 200 × 200 m spatial grid resolution covering Ecuador's mainland and the Galapagos Islands (MEER, 2013). Previous studies on wind resource assessment in the country used the raster layers of annual average wind speeds from this wind atlas (Cevallos-Sierra et al., 2018; Jijón et al., 2018; Villacreses et al., 2017). The Global Wind Atlas (GWA) (Global Wind Atlas, 2022) is another source at a spatial grid of 250 × 250 m, which covers onshore and offshore areas.

Wind atlases provide long-term mean wind speed and/or power density at a high spatial resolution (McKenna et al., 2022) and they are useful for identifying high-resource sites and for the design of measurement campaigns (Mortensen et al., 2017). However, wind atlases are static products and do not provide information for the assessment of the temporal variability of wind resources.

Global reanalysis datasets, which interpolate meteorological observations in space and time using numerical weather prediction models (Rose et al., 2015), represent an alternative for such assessments. Reanalyses provide long-term meteorological data on a global regular grid with information considered representative for the entire grid cell

(McKenna et al., 2022). Currently used global reanalysis datasets are, for instance, ERA5 (31 km horizontal grid, at hourly intervals) (Hersbach et al., 2018) and MERRA2 (~50 km horizontal grid, at hourly intervals) (Gelaro et al., 2017).

Previous studies on energy system models for Ecuador used reanalysis data as feed-in time series to simulate wind farms located in high potential sites selected according to the Ecuadorian wind atlas (Carvajal et al., 2019; Godoy et al., 2021). However, using data from global reanalyses for simulating wind power output can lead to a severe underestimation of the wind energy technical potential, specially over complex terrain (Pickering et al., 2020). Thus, global reanalyses should only be relied upon after they have been thoroughly validated (Staffell et al., 2016), which has not been performed for Ecuador yet.

Regional reanalyses provide the higher resolution required to resolve wind patterns in complex terrain and perform better than global reanalyses (Pickering et al., 2020). Although such datasets are available for Europe, Australia, China, and North America (McKenna et al., 2022), there are no datasets available for South America or for the Andean Region.

Due to these limitations and needs, this chapter aims to produce a consistent long-term and high-resolved wind resource dataset for Ecuador using numerical weather prediction models. This dataset is a core element of this dissertation and necessary for the characterization of the spatio-temporal variability of wind resources in Ecuador, as well as for the subsequent analysis of the correlation with solar and hydro resources.

The Weather Research and Forecast (WRF) mesoscale model is selected to produce a 14-year period dataset (2005–2018) of hourly wind resource data at a 3×3 km spatial resolution. The ERA5 reanalysis dataset is used as input data for the WRF model. Then, the simulated wind speed and wind direction at 80 m AGL are validated using measured data from four tall meteorological masts located over the Andes. This comparison allows the definition of correction factors that are applied to the complete dataset for correcting systematic biases. Finally, the long-term, bias-corrected simulated dataset is used to characterize the spatio-temporal variability of the wind resource applying the methodology explained in Chapter 2, Section 2.2.2.

This chapter is structured as follows. Section 3.2 describes the configuration of the mesoscale model, presents the data and methods for the validation of the simulations, as well as the methodology for the bias correction. Section 3.3 presents the results in different subsections: (3.3.1) the evaluation of the performance of simulated wind speed; (3.3.2) the evaluation of the performance of simulated wind direction; (3.3.3) the evaluation of the wind

speed bias correction; and (3.3.4) the spatio-temporal variability analysis of wind resources. Section 3.4 discusses the main findings and contributions, and finally Section 3.5 presents the conclusions of this chapter.

3.2. Methods and data

3.2.1. Mesoscale model

The selected mesoscale model to perform the simulations is the Advanced Research WRF (ARW), a widely used open-source community model developed by the National Center for Atmospheric Research (NCAR) and other institutes (Skamarock et al., 2019). WRF is a state-of-the-art atmospheric modeling system designed for both meteorological research and numerical weather prediction (Skamarock et al., 2019). The WRF mesoscale model has been previously used for wind energy applications (e.g., Carvalho et al. (2014), Santos-Alamillos et al. (2014), Salvação and Guedes Soares (2018), Dörenkämper et al. (2020)).

This study uses the WRF-ARW version 4.0.2 to produce 14 years (2005–2018) of atmospheric data with an hourly temporal resolution. A detailed description of the model can be found in Skamarock et al. (2019). The spatial configuration of the model (Fig. 3-1) comprises one outer coarse-resolution (parent) domain (named d01) and two nested (child) domains (named d02 and d03), which cover the Galapagos Islands and Ecuador's mainland, respectively.

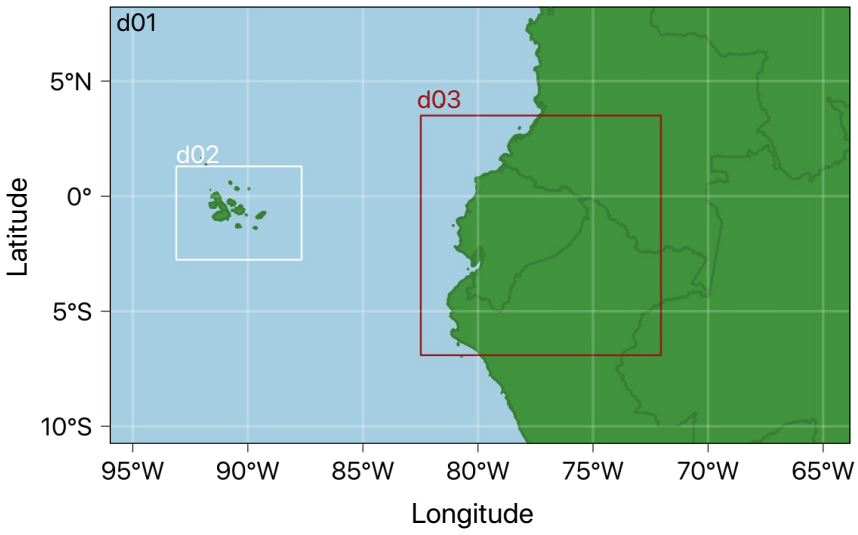

Fig. 3-1. Spatial configuration of the WRF mesoscale model, where d01 represents the parent domain, d02 covers the Galapagos Islands and d03 covers Ecuador's mainland.

The WRF model setup parameters are listed in Table 3-1. The physics parametrization schemes follow the model configuration used for the production of the New European Wind Atlas (NEWA) (Dörenkämper et al., 2020). The sensitivity analysis and evaluation procedures for choosing the NEWA model setup can be found in Hahmann et al. (2020).

Table 3-1. WRF model setup configuration used for the production of a 14-year period wind resource dataset for Ecuador

WRF version	4.0.2
Period	00:00 UTC 01-01-2005 23:00 UTC 31-12-2018
Domain	d01: 9 km parent (400 x 220 grid) d02: 3 km child (202 x 151 grid) d03: 3 km child (385 x 385 grid)
Vertical levels	61 levels (surface to 50 hPa)
Dynamical forcing	ERA5 reanalysis (hourly, 31 x 31 km)
Nudging	Spectral nudging in d01 only, above PBL and level 20
Physics schemes	Rapid radiative transfer model for global applications (RRTMG) longwave and shortwave radiation schemes WRF Single-Moment five-class micro-physics Noah land surface model Eta Similarity surface layer Mellor–Yamada–Nakanishi–Niino level 2.5 Planetary boundary layer (PBL) scheme Kain-Fritsch cumulus convection scheme

The initial and boundary conditions for the WRF simulations are obtained from ERA5 reanalysis data. ERA5 is the most recent global reanalysis produced by the European Centre for Medium-Range Weather Forecasts (ECMWF), which includes a detailed record of the global atmosphere, land surface and ocean waves with a horizontal resolution of 31 km, 137 vertical layers, and an hourly data output from 1950 onwards (Hersbach et al., 2020).

The simulations are performed month by month for the 14-year period (2005–2018). Each month is split into four runs and a 24-hour spin-up period is added at the beginning of each run, which guarantees that the mesoscale flow is in full equilibrium with the mesoscale aerodynamic characteristics of the terrain (Dörenkämper et al., 2020). Nudging in domain d01 is used to prevent the model solution to diverging from the large-scale circulation patterns (Dörenkämper et al., 2020; Vincent et al., 2015).

The post-processing of the WRF simulations follows the procedure described in Dörenkämper et al. (2020). The resulting hourly time series are stored as netCDF files with the variables listed in Appendix B.1.

3.2.2. Observational data

The wind speed and wind direction simulated by the WRF model is compared to observations from four tall meteorological masts located along the Andean highlands, which are referred to as Site A–D in this dissertation. Due to the sensitive nature of the data, the coordinates of the sites are not disclosed and normalized wind speed values are shown in the results section.

The observations consist of 10-minute averages of wind speed and direction at 80 m AGL for twelve months (November 2016 to October 2017). Site D has additional data for nine months (January to September 2015), which is used for the bias-correction validation (which will be discussed in Section 3.2.5). Preprocessing steps were performed before using the observation data for the comparison, which included data quality control and converting the 10-minute data to hourly averages.

3.2.3. ERA5 data

To evaluate the pairwise agreement between ERA5, WRF simulations, and observations, wind speed and direction at 100 m AGL are retrieved from ERA5 (Hersbach et al., 2018). The bilinear interpolation method is used to horizontally interpolate from the four closest grid points to each observation site. Then, wind speed at 80 m AGL is estimated using the logarithm profile according to Equation (3.1) (Sathyajith, 2006):

$$WS_{Z_2} = WS_{Z_1} \frac{\ln (Z_2/Z_0)}{\ln (Z_1/Z_0)} \quad (3.1)$$

where, WS_{Z_1} and WS_{Z_2} is ERA5 wind speed at 100 and 80 m AGL, respectively; Z_1 is 100 m; Z_2 is 80 m; and Z_0 is the surface roughness length at each observation site, which is obtained by interpolating the Z_0 simulated by WRF from the four closest grid points to each observation site.

3.2.4. Performance metrics

A statistical approach is used to describe the degree of the agreement between simulated and observed wind data. Simulated wind data refers to either WRF simulations or ERA5 data. The three selected statistical metrics for wind speed are: mean bias error (MBE), root mean square error (RMSE) and Pearson correlation coefficient r_P, calculated according to Equations (3.2)–(3.4) (Wilks, 2006), respectively:

$$MBE = \frac{1}{n}\sum_{i=1}^{n}(WS_{SIM_i} - WS_{OBS_i}) \quad (3.2)$$

$$RMSE = \sqrt{\frac{\sum_{i=1}^{n}(WS_{SIM_i} - WS_{OBS_i})^2}{n}} \quad (3.3)$$

$$r_P = \frac{Cov(WS_{SIM}, WS_{OBS})}{\sigma_{SIM}\sigma_{OBS}} \quad (3.4)$$

where, n is number of data points in the considered time series; WS_{SIM_i} and WS_{OBS_i} refer to the i-th value of the simulated and observed wind speed, respectively; $Cov(WS_{SIM}, WS_{OBS})$ is the covariance between simulated and observed wind speed; and σ_{SIM} and σ_{OBS} are the standard deviation of the simulated and observed wind speed, respectively.

The performance of the WRF model is evaluated by comparing simulations and observations from the four observation sites (A–D) during the control period (November 2016 to October 2017). ERA5 data is also compared to observations for the same period. For the comparison, the hourly time series of WRF simulated wind speed and direction for each site are extracted from the WRF output at 80 m AGL using bilinear interpolation from the four closest grid points to each site. ERA5 wind speed and direction at 80 m AGL are extracted according to the procedure described in Section 3.2.3.

In the case of wind direction, the difference between simulations and observations ΔWD in Equation (3.5) is evaluated following the methodology described in Jiménez and Dudhia (2013) and Salvação and Guedes Soares (2018) in which:

$$\Delta\text{WD} = \begin{cases} WD_{SIM} - WD_{OBS} & \text{if } WD_{SIM} - WD_{OBS} \leq |180| \\ WD_{SIM} - WD_{OBS} - 360 & \text{if } WD_{SIM} - WD_{OBS} > 180 \\ WD_{SIM} - WD_{OBS} + 360 & \text{if } WD_{SIM} - WD_{OBS} < -180 \end{cases} \quad (3.5)$$

where, WD_{SIM} and WD_{OBS} are the simulated and observed wind direction, respectively. Using this formulation, counterclockwise rotations occur when ΔWD is negative, while positive values indicate a clockwise rotation of the simulated wind direction with respect to the observed records.

The performance of the simulated wind direction is evaluated through MBE, mean bias absolute (MBA), RMSE and relative root mean square error ($RMSE_{rel}$), according to Equations (3.6)–(3.9) (Salvação et al., 2018), where ΔWD is the difference between simulations and observations determined by Equation (3.5).

$$MBE = \frac{1}{n}\sum_{i=1}^{n}\Delta WD_i \quad (3.6)$$

$$MBA = \frac{1}{n}\sum_{i=1}^{n}|\Delta WD_i| \quad (3.7)$$

$$RMSE = \sqrt{\frac{\sum_{i=1}^{n}(\Delta WD_i)^2}{n}} \quad (3.8)$$

$$RMSE_{rel} = \frac{RMSE}{180°}\cdot 100 \quad (3.9)$$

3.2.5. Bias correction of wind speed

A temporal bias correction is performed to reduce the systematic deviations of the WRF simulated wind speeds at 80 m AGL with respect to observations. The bias correction methodology consists of two stages as displayed in Fig. 3-2.

The first stage focuses on the correction of a single site and follows three steps according to Li et al. (2019): (i) inferring correction terms using simulated and observed wind speed from a given time period, namely, the control period; (ii) applying the correction terms to the simulated wind speed from a different period, namely, the evaluation period; and (iii) comparing the bias-corrected data in the evaluation period with observations using different statistical metrics.

The control period is from November 2016 to October 2017. During this period, observations from sites A–D are used for the comparison. The evaluation period is from January to September 2015. During this period, the comparison is limited to observations from site D, since the other sites do not have data during that period.

The correction terms are inferred based on the difference between simulated and observed wind speeds in the control period. Instead of using a constant correction term, a specific term for a given hour and given month is determined. In this way, the diurnal and seasonal overestimation of the WRF simulated wind speed, which will be discussed in Section 3.3.1, is taken into account.

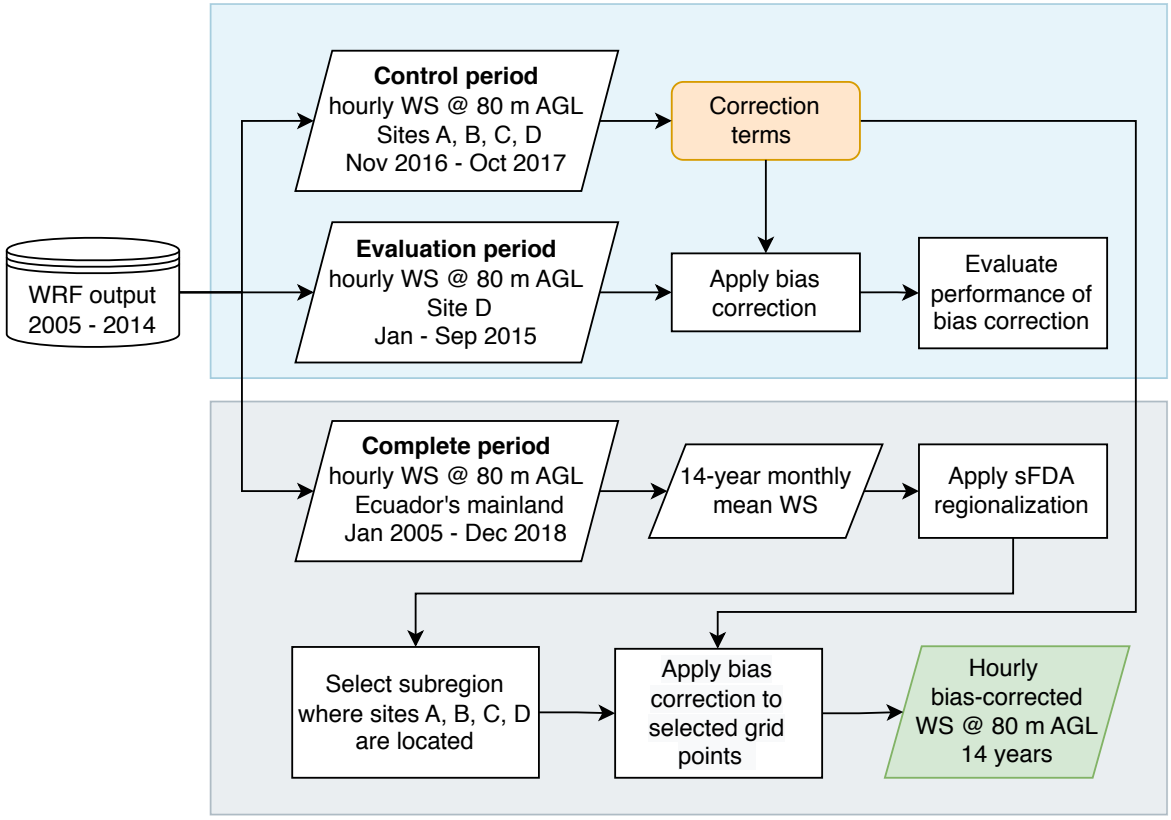

Fig. 3-2. Overview of the methodology for the bias correction of WRF simulated WS (wind speed). Source: Own representation.

In the second stage, the bias correction is applied to the hourly time series during the complete period (14 years) using the previously inferred correction terms. The correction is only applied to specific grid points of Ecuador's mainland, which are selected based on the results of the sFDA regionalization of wind speed (for detailed description of the sFDA regionalization method see Chapter 2, Section 2.2.2.1). In this way, the correction is applied to the grid points within a spatial region that share similar intra-annual variability patterns of wind speed to that of the four observation sites.

The bias correction methodology follows a linear scaling correction as applied in Lenderink et al. (2007). The correction terms are defined as the MBE during the control period weighted by the ratio of the hourly simulated wind speed at grid point x and time t to the long-term hourly mean wind speed at same grid point x. Thus, the bias-corrected hourly wind speed is calculated according Equation (3.10):

$$WS_{WRF}^{corrected}(t,x) = WS_{WRF}(t,x) - MBE_{(m,h)_{WRF-OBS}} \frac{WS_{WRF}(t,x)}{\overline{WS}_{WRF}(x)} \quad (3.10)$$

where,

$WS_{WRF}^{corrected}(t,x)$ is the bias-corrected hourly wind speed at grid point x and time t.

$MBE_{(m,h)_{WRF-OBS}}$ is a 12 × 24 matrix of the monthly and diurnal mean bias between simulated and observed wind speed during the control period (November 2016 to October 2017).

$WS_{WRF}(t,x)$ is the hourly simulated wind speed at grid point x and time t.

$\overline{WS}_{WRF}(x)$ is the long-term hourly mean simulated wind speed at the grid point x.

After the bias correction is applied, the Wilcoxon signed-rank test is used to determine if the improvements in the bias-corrected wind speed are statistically significant, following the approach used in Deppe et al. (2013). The significant level alpha is set at 0.05. This test is selected because it does not depend on the distribution of the data and is resistant to outliers (Wilks, 2006).

Note that the following assumptions are made to transfer the pointwise bias correction to any grid point. First, it is assumed that the bias at the selected grid points behaves similar to the calculated bias at the observation sites and is time-dependent, i.e., the bias varies depending on the month and time of the day. Second, the correction terms are inferred using present-day simulated and observed data, and it is assumed that the correction terms are a good estimate for past simulated data. Third, it is assumed that the correction terms remain unchanged for the complete 14-year period.

3.2.6. Spatio-temporal variability analysis of wind speed

The analysis of the spatio-temporal intra-annual and interannual variability of wind speed is conducted by applying the same methodology used for the solar resource dataset, which is explained in detail in Chapter 2, Section 2.2.2.

3.3. Results

3.3.1. Performance of WRF simulated wind speed

The monthly statistical scores of the comparison between observations, WRF, and ERA5 wind speed during the control period (November 2016 – October 2017) are presented in Table 3-2. It is evident from this table that the WRF model overestimates wind speed compared to observations, while ERA5 strongly underestimates wind speed compared to observations.

Table 3-2. Summary of monthly performance metrics between observations (OBS), WRF, and ERA5 wind speed averaged for the four observation sites during the control period (November 2016 – October 2017). (σ is the standard deviation).

Date	WRF–OBS			ERA5–OBS		
	MBE [m s^{-1}]	RMSE [m s^{-1}]	r_P [–]	MBE [m s^{-1}]	RMSE [m s^{-1}]	r_P [–]
2016–11	0.78	2.98	0.66	–3.53	4.77	0.57
2016–12	0.86	2.71	0.63	–2.99	4.09	0.47
2017–01	0.85	2.99	0.68	–3.30	4.33	0.55
2017–02	0.47	2.80	0.76	–2.93	4.03	0.58
2017–03	0.78	2.81	0.52	–2.25	3.20	0.41
2017–04	1.78	3.45	0.67	–3.48	4.62	0.52
2017–05	1.78	3.60	0.72	–3.47	4.89	0.56
2017–06	2.28	3.96	0.62	–4.44	5.68	0.47
2017–07	3.18	4.86	0.61	–7.37	8.42	0.50
2017–08	3.21	4.60	0.62	–5.21	6.40	0.52
2017–09	2.00	3.86	0.48	–6.24	7.21	0.45
2017–10	1.37	3.09	0.78	–5.19	6.48	0.60
Mean	**1.61**	**3.48**	**0.65**	**–4.20**	**5.34**	**0.52**
σ	**0.93**	**0.72**	**0.09**	**1.52**	**1.52**	**0.06**

The MBE between WRF and observations is 1.61 ± 0.93 m s^{-1} for all sites over all months, with higher values from June to September (2.00 to 3.21 m s^{-1}). RMSE between WRF and observations for all sites over all months is 3.48 ± 0.72 m s^{-1}, again with higher values from June to September (3.86 to 4.86 m s^{-1}). The overall correlation for the four sites is 0.65 ± 0.09.

The comparison of ERA5 and observations shows that the MBE is –4.20 ± 1.52 m s^{-1} for the whole control period. Larger negative biases are seen from July to October. RMSE between ERA5 and observations is also higher than that between WRF and observations, at 5.34 ± 1.52 m s^{-1}. Larger RMSE values are seen during July to October. The correlation coefficient for all sites over all months is 0.52 ± 0.06, which is lower than that of between WRF and observations.

A further breakdown of the MBE between WRF and observations by month and time of day for the four sites is displayed in Fig. 3-3. This plot reveals a trend of diurnal and monthly bias between WRF and observations. WRF overestimates nighttime wind speeds specially from 23:00 to 13:00 UTC (18:00 to 08:00 local time), which is more evident during July to September. The largest averaged bias of 4.59 m s^{-1} is seen in July at 08:00 UTC.

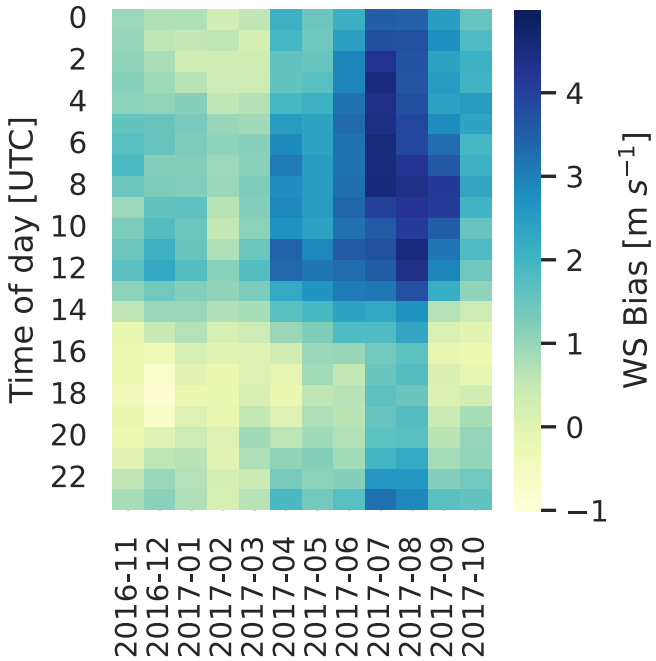

Fig. 3-3. Hourly and monthly variability of wind speed bias between WRF and observations at 80 m AGL averaged for the four sites during the control period (November 2016 – October 2017).

3.3.2. Performance of simulated wind direction

The monthly statistical scores of the comparison between observations, WRF, and ERA5 wind direction during the control period are presented in Table 3-3.

The MBE results indicate that WRF wind is rotated counterclockwise with respect to the observations (–6.95 ± 2.92°), with larger negative biases during April–July. The RMSE is 61.32 ± 13.5°, resulting in a relative RMSE of 34.07 ± 7.50% over all sites and months. ERA5 shows a positive (clockwise) wind direction bias of 24.84 ± 33.67° over all sites and months, with larger positive biases during July–September. The RMSE is 110.65 ± 6.77°, resulting in a relative RMSE of 61.47 ± 3.76% over all sites and months.

Table 3-3. Summary of monthly performance metrics between observations (OBS), WRF, and ERA5 wind direction averaged for the four observation sites during the control period (November 2016 – October 2017). (σ is the standard deviation).

Date	WRF–OBS				ERA5–OBS			
	MBE [°]	MBA [°]	RMSE [°]	$RMSE_{rel}$ [%]	MBE [°]	MBA [°]	RMSE [°]	$RMSE_{rel}$ [%]
2016–11	–5.10	46.71	69.32	38.51	2.76	94.30	105.26	58.48
2016–12	–7.97	45.74	68.75	38.20	2.50	98.55	108.62	60.34
2017–01	–4.80	45.90	68.86	38.26	2.82	93.17	102.79	57.10
2017–02	–1.22	49.87	72.75	40.42	–24.21	87.54	97.92	54.40
2017–03	–5.69	58.65	80.60	44.78	–11.60	92.26	103.92	57.73
2017–04	–11.51	42.74	66.42	36.90	20.40	105.83	113.65	63.14
2017–05	–9.28	50.16	72.02	40.01	15.82	102.73	112.21	62.34
2017–06	–9.63	38.65	58.52	32.51	39.59	109.12	116.06	64.48
2017–07	–9.44	25.80	40.82	22.68	84.34	114.93	118.26	65.70
2017–08	–7.60	31.00	46.36	25.76	63.99	112.53	117.34	65.19
2017–09	–7.31	28.30	40.89	22.72	66.99	113.22	117.31	65.17
2017–10	–3.82	33.39	50.56	28.09	34.62	107.55	114.45	63.59
Mean	**–6.95**	**41.41**	**61.32**	**34.07**	**24.84**	**102.64**	**110.65**	**61.47**
σ	**2.92**	**10.05**	**13.50**	**7.50**	**33.67**	**9.29**	**6.77**	**3.76**

Fig. 3-4 provides a visual comparison of the wind direction distribution of observations against WRF and ERA5 for each site during the control period. On the one hand, WRF tends to match the prevailing wind in sites A, B, C, where winds blow mostly from east / southeast directions. In site D, the observations indicate predominant west / northwest winds, while WRF is rotated counterclockwise. On the other hand, ERA5 matches the prevailing wind in sites A and C, while in site B ERA5 shows a counterclockwise rotation with respect to the observations. In site D, ERA5 does not display the predominant wind observed in this location, but it shows rather weaker breezes blowing from different directions. Overall, the results show that WRF simulated wind directions perform better than ERA5, which is reflected in the previously discussed statistics.

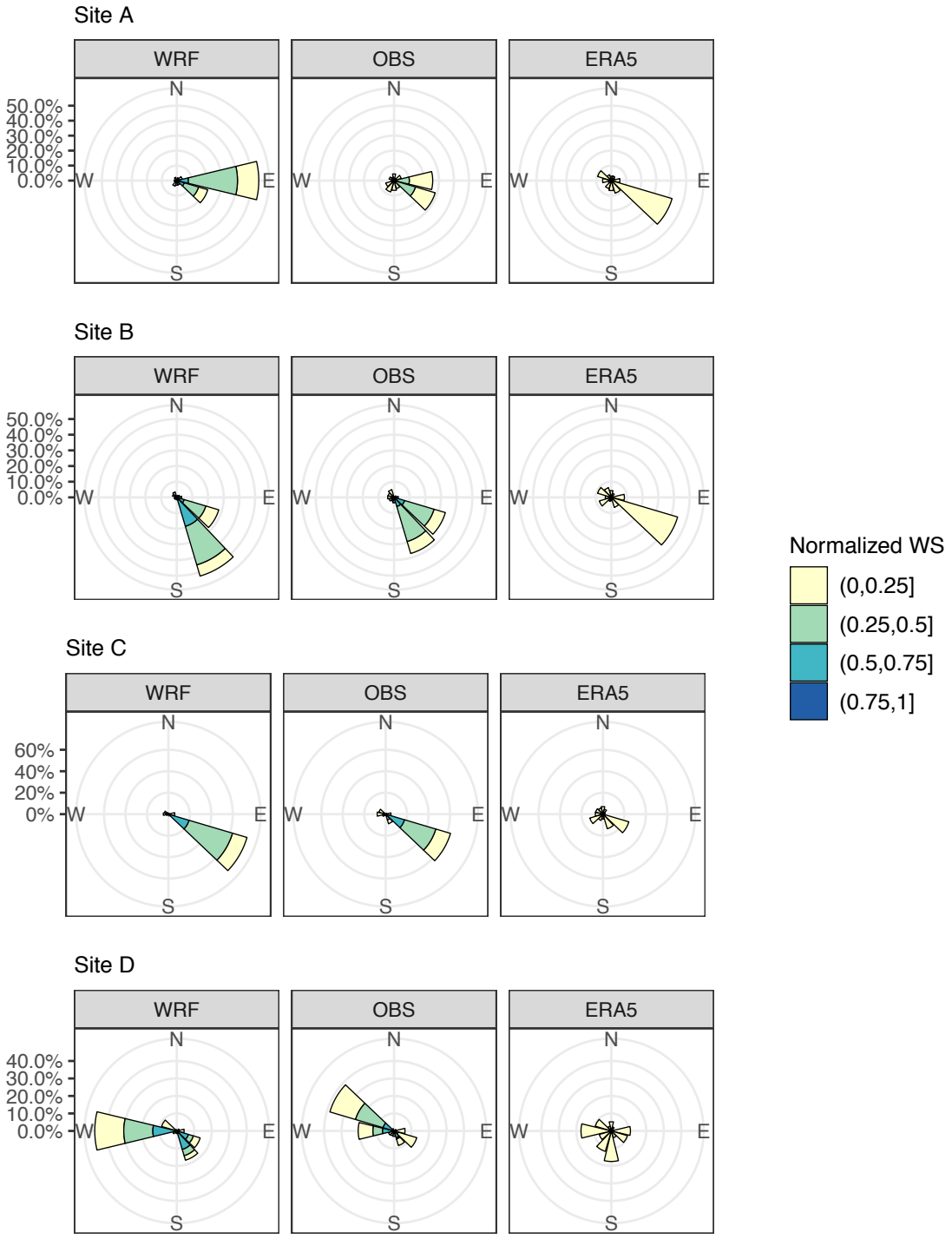

Fig. 3-4 Comparison of the distribution of wind speed and the varying wind directions from observations (OBS), WRF, and ERA5 during the control period (November 2016 – October 2017) for each observation sites. The concentric circles represent the probability of wind coming from a particular direction in percentage.

3.3.3. Bias correction of WRF simulated wind speed results

3.3.3.1. Bias correction at one observation site

According to the results in Section 3.3.1, there is a consistent trend of diurnal and monthly bias between WRF and observations (see Fig. 3-3). Therefore, the simulated wind speed at the observation site D during the evaluation period (January – September 2015) is corrected using a set of correction terms according to the month and time of day, which are inferred from the analysis during control period (see Equation (3.10)).

Table 3-4 shows the performance metrics for wind speed simulations before and after the bias correction at site D. Uncorrected simulated wind speeds show higher biases during June and July, a similar monthly pattern as previously seen in the control period.

After applying the correction, bias-corrected wind speeds show a significant improvement in comparison to the uncorrected values. MBE is reduced from 2.16 ± 0.94 to 0.36 ± 0.49 m s^{-1}, while the RMSE decreases from 4.28 ± 1.03 to 2.96 ± 0.55 m s^{-1}. The correlation coefficients also show an improvement from 0.57 ± 0.11 to 0.72 ± 0.06. Additionally, the Wilcoxon signed-rank test indicates that the bias correction is statistically significant with a p-value < 0.05.

Table 3-4. Performance metrics for wind speed simulations before and after the bias correction for site D during the evaluation period (January – September 2015). (σ is the standard deviation).

Date	WRF–OBS (Site D)			$WRF_{corrected}$–OBS (Site D)		
	MBE [m s^{-1}]	RMSE [m s^{-1}]	r_P [–]	MBE [m s^{-1}]	RMSE [m s^{-1}]	r_P [–]
2015–01	1.26	3.20	0.68	0.66	2.62	0.75
2015–02	0.92	2.98	0.70	0.44	2.50	0.78
2015–03	1.19	2.96	0.72	0.42	2.33	0.79
2015–04	2.36	4.42	0.43	0.58	2.56	0.72
2015–05	2.08	4.35	0.45	0.30	2.66	0.68
2015–06	2.99	5.19	0.60	0.71	3.69	0.70
2015–07	3.86	5.89	0.49	0.68	3.41	0.66
2015–08	2.34	4.81	0.50	–0.87	3.78	0.62
2015–09	2.47	4.75	0.56	0.36	3.12	0.75
Mean	**2.16**	**4.28**	**0.57**	**0.36**	**2.96**	**0.72**
σ	**0.94**	**1.03**	**0.11**	**0.49**	**0.55**	**0.06**

The improvement becomes clearer when comparing the MBE before and after the correction by month and time of the day. From Fig. 3-5, it is evident that the overestimation of WRF at nighttime from 23:00 to 13:00 UTC (18:00 to 08:00 local time) occurring from April to September is reduced when applying the time-dependent bias correction.

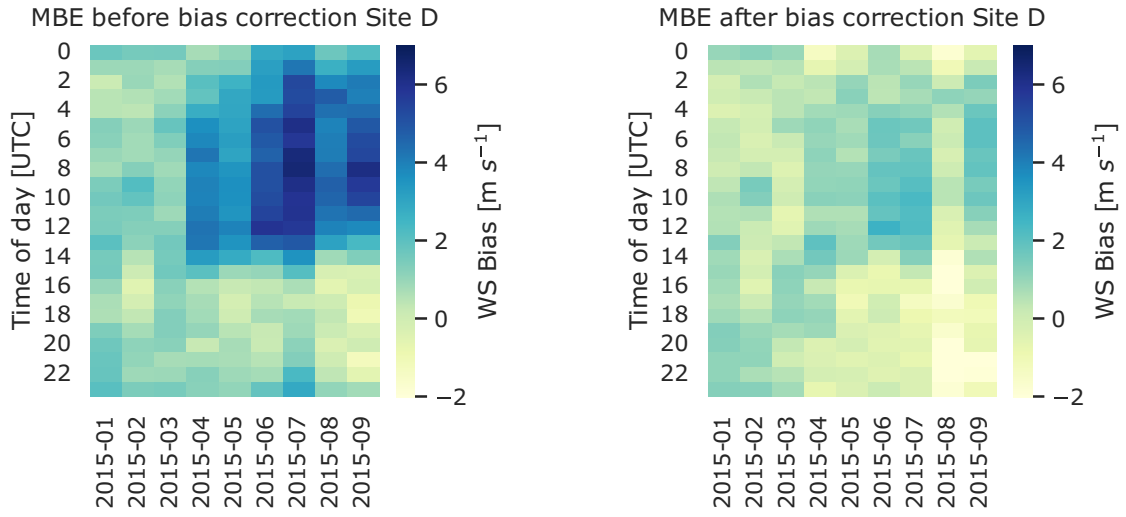

Fig. 3-5. Hourly and monthly variability of wind speed bias between WRF and observations at 80 m AGL for site D before (left) and after (right) applying the bias correction during the evaluation period (January to September 2015).

3.3.3.2. Bias correction at selected grid points

Based on the good performance in terms of MBE, RMSE, and correlation coefficient that the single point bias-correction methodology shows after being applied to WRF simulated wind speeds at site D (see Table 3-4), the second stage of the bias correction methodology is applied to selected grid points in Ecuador's mainland. As described in Section 3.2.5, the grid points for the application of the bias correction are selected based on the regionalization of the WRF simulated wind speed.

The regionalization results are shown in Fig. 3-6. From the map on the left, it can be seen that WRF simulated wind speeds in Ecuador's mainland are classified into three regions, named R1, R2, and R3. Remarkably, the four observation sites are located inside region R3, which is spatially distributed along the Andean highlands.

From the functional boxplot of region R3 displayed on the right side of Fig. 3-6, it is evident that the grid points of this region share a similar intra-annual variability. High wind speeds occur from June to September, similar to the intra-annual pattern seen in the observation sites.

Since the grid points in the region of interest (R3) share the same intra-annual variability pattern but differ in wind speed magnitude, a minimum threshold is set as constraint for the application of the bias correction. This is done to avoid negative wind speed values after applying the bias correction for those grid points that show a similar intra-annual variability pattern but have lower wind speed magnitude than the observations. As result, 1282 out of 2966 total grid points in region R3 satisfy the condition to have a higher or equal wind

speed magnitude to that at the four observation sites for all months. Therefore, these grid points are selected for the application of the bias correction methodology.

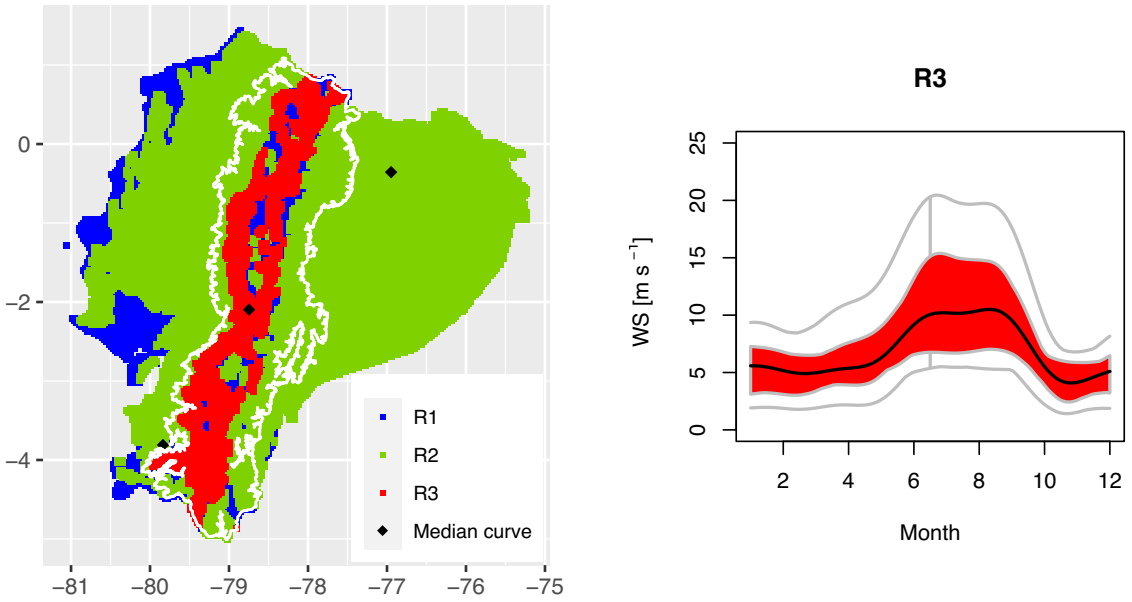

Fig. 3-6. Results of the regionalization of WRF simulated wind speed (not bias-corrected) in Ecuador's mainland. Left: Spatial distribution of the resulting regions after applying the sFDA regionalization method. The white line depicts the altitudinal contour at 1000 m.a.s.l. and the black points represent the location of the median curve of each region. Right: Functional boxplot of region R3, where the four observation sites are located. The colored shape represents the interquartile range, the gray external lines depict the minimum and maximum curves, the black line is the wind speed curve of the black point in R3 from the map on the left.

Once the subset of grid points is selected, the bias of the complete 14-year period wind speed time series of those grid points is corrected using Equation (3.10). Then, the bias-corrected dataset from the selected grid points is merged with the dataset of the remaining grid points in Ecuador's mainland, thus a new dataset of wind speed at 80 m AGL is generated.

Fig. 3-7 compares the probability density function of the original and corrected datasets from the selected grid points. As expected, the distribution of wind speed is shifted to the left, but the shape of the distribution is maintained. The correction effect is more evident from April to October, when the originally overestimations were higher.

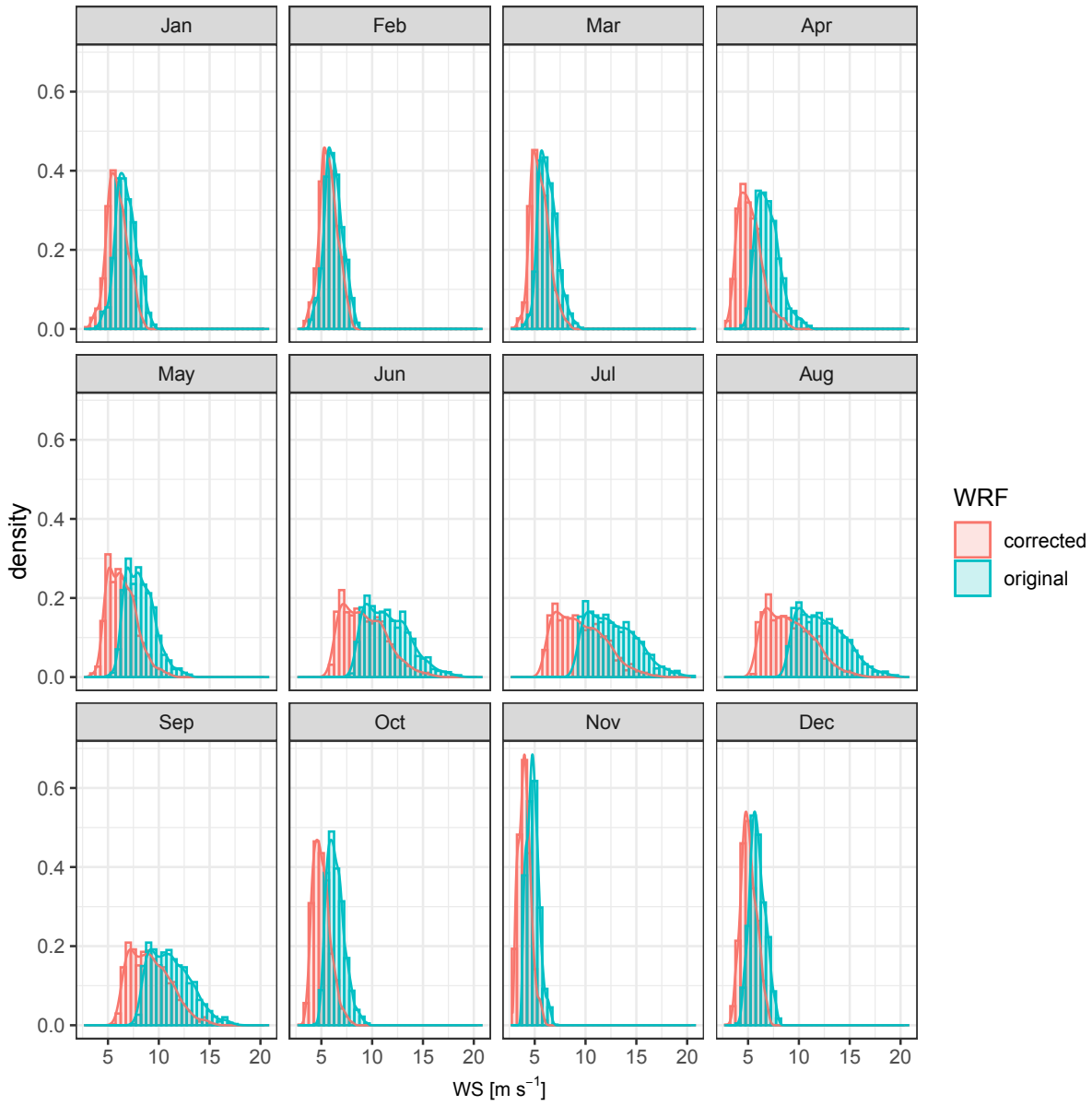

Fig. 3-7. Distribution of the 14-year monthly mean WRF simulated wind speed before (original) and after bias correction (corrected) at selected grid points inside region R3, where the four observation sites are located.

3.3.4. Spatio-temporal variability analysis of wind resources

After completing the validation and bias correction of WRF simulated wind speed, this section presents the results of the spatio-temporal variability analysis of the wind resources.

For the analysis, the long-term monthly mean wind speed datasets for Ecuador's mainland and the Galapagos Island are used, which are displayed in Fig. 3-8. These datasets are calculated using the complete 14-year period of the WRF simulated wind speed time series at 80 m AGL. Note that the dataset of Ecuador's mainland includes the bias-corrected time series of the selected grid points in the Andean highlands.

The results of the spatio-temporal variability analysis of wind resources are presented in a similar way as in the previous chapter for the variability analysis of solar resources. First, the results of the regionalization of wind speed in Ecuador's mainland and the Galapagos Islands are described and analyzed in relation to the climate characteristics of the resulting spatial areas in Section 3.3.4.1 and Section 3.3.4.2, respectively. Then, the results of the intra-annual variability analysis at yearly and monthly timescales are presented in Section 3.3.4.3.

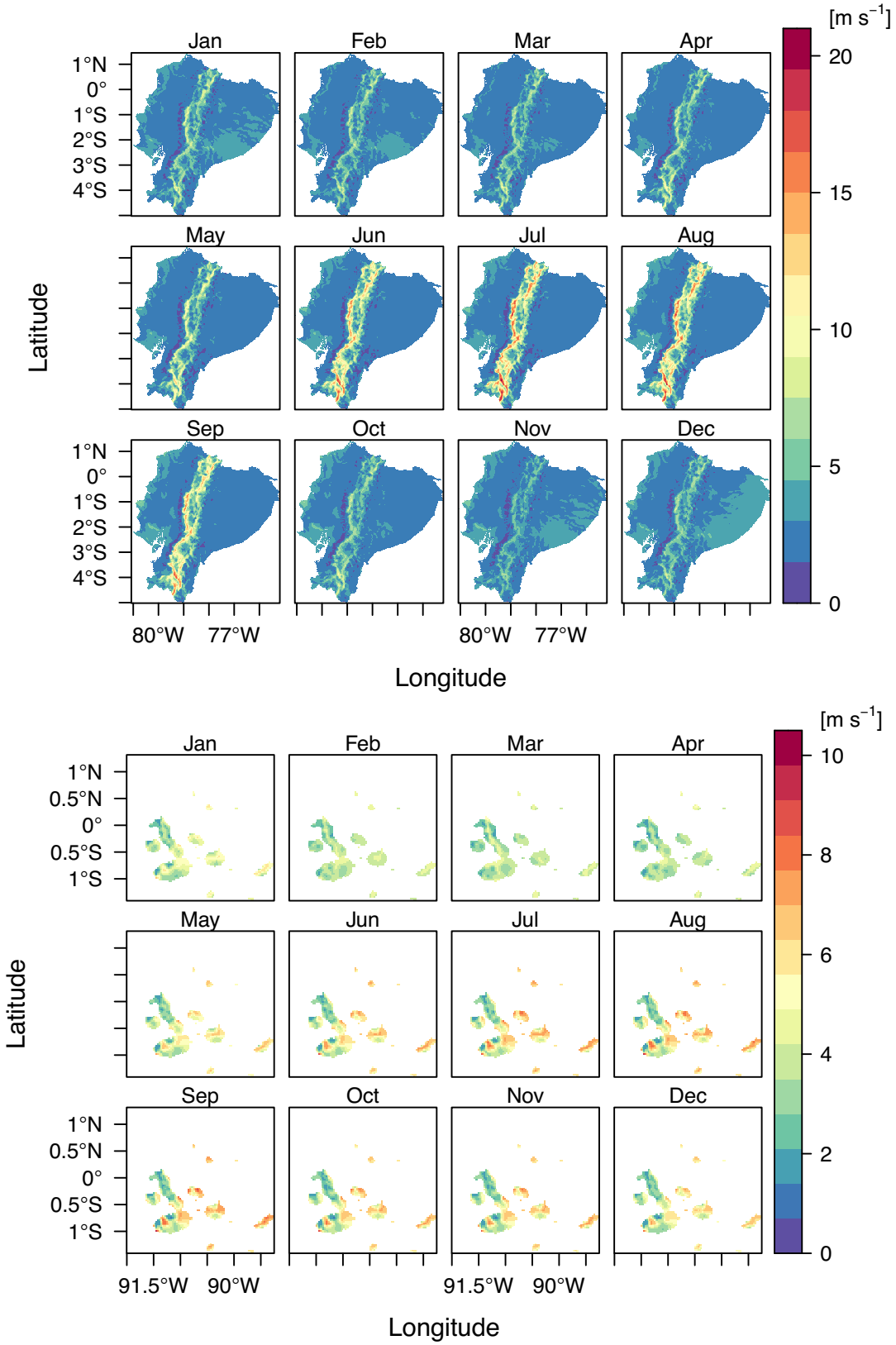

Fig. 3-8. Long-term monthly mean wind speed at 80 m AGL from 2005 to 2018 at a 3 x 3 km resolution on Ecuador's mainland (top) and the Galapagos Islands (bottom). Wind speeds are simulated using the WRF mesoscale model. Note that the maps for Ecuador's mainland include the bias-corrected wind speed applied to selected grid points in the Andean highlands (See Section 3.3.3.2).

3.3.4.1. Regionalization of wind speed in Ecuador's mainland

After applying the sFDA regionalization to the bias-corrected dataset, the resulting regions have a similar spatial classification pattern to that displayed on the left side of Fig. 3-6, although with some variations due to the bias-corrected wind speed values in the Andean highlands. To further analyze the difference in wind speed magnitude within each region, a second regionalization is applied using ten partitions (hereafter called subregions). The number of subregions is determined according to the cluster validity assessment explained in Appendix B.2. The spatial distribution of the three regions and their respective subregions is shown in Fig. 3-9. Regions R.1 and R.2 cover the coast and the Amazon lowlands, as well as scattered grid points along the Inter-Andean valleys. Region R.3 is a more compact region that is spatially distributed along the eastern and western Andean highlands.

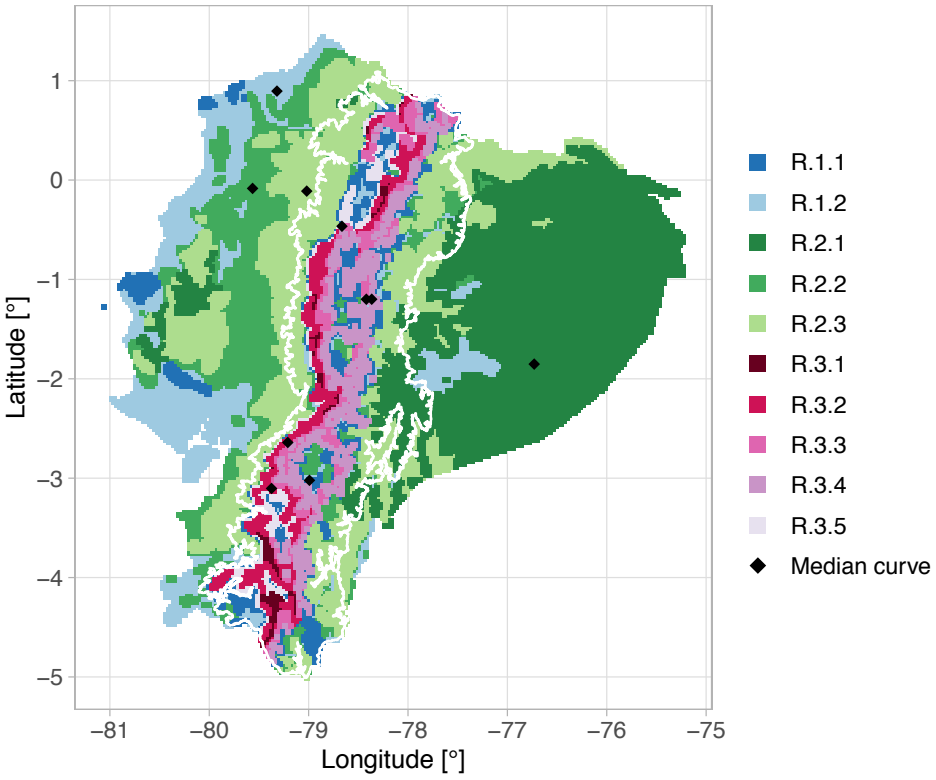

Fig. 3-9. Spatial distribution of the ten wind subregions in Ecuador's mainland after applying the sFDA regionalization method. The subregions are grouped and named according to their corresponding region: R1, R2, and R3. The black points represent the location of the median curve of each subregion.

Fig. 3-10 shows the spatial distribution and the intra-annual wind speed variability of the ten subregions grouped by their corresponding region. Here it is noticeable that the subregions in the corresponding region share similar seasonal patterns, but they differ in the magnitude of wind speed. This can also be seen in Table 3-5, which summarizes the long-term annual mean wind speed and wind power density per subregion.

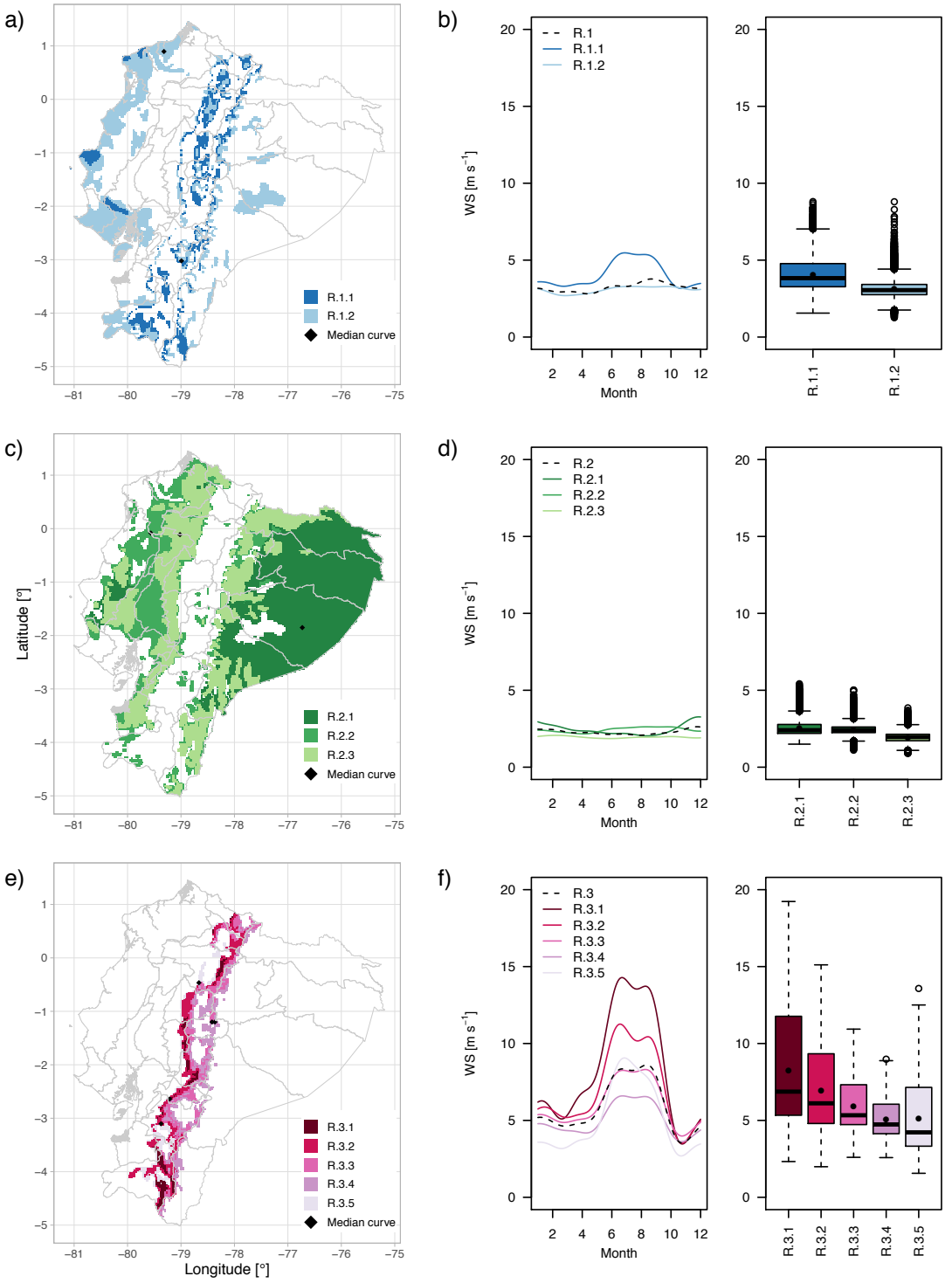

Fig. 3-10. Spatial distribution of the subregions in regions R.1, R.2, and R.3 and temporal variability of wind speed at 80 m AGL in each subregion in Ecuador's mainland. The maps on a), c) and e) show the spatial distribution of the subregions within each region (gray polygons depict the province boundaries. See Appendix D for provinces' names). The left sides of b), d) and f) show the comparison of the main wind speed seasonal patterns for the corresponding region (dotted black lines) and the median curves obtained from the functional boxplot of each subregion (Appendix B.3). The right sides of b), d) and f) show the dispersion of the annual mean wind speed for each subregion, where the black points represent the values of the median curve of each subregion.

Table 3-5. Long-term annual mean wind speed and wind power density at 80 m AGL, yearly coefficient of variation (CV_y), and mean elevation per wind subregion in Ecuador's mainland and the Galapagos Islands. Note that subregions are named and sorted in decreasing order according to the wind speed value in their respective region.

Wind Subregion	Wind speed [m s^{-1}]	Wind power density [W m^{-2}]	CV_y [%]	Mean Elevation [m.a.s.l]
R.1.1	4.1	84.9	6.6	2290.5
R.1.2	3.1	36.7	3.2	913.1
R.2.1	2.5	22.8	2.9	401.6
R.2.2	2.4	20.4	2.6	682.8
R.2.3	1.9	10.9	2.2	917.9
R.3.1	8.3	747.1	11.9	2992.5
R.3.2	6.9	400.7	10.8	3119.8
R.3.3	5.9	166.5	7.7	3538.8
R.3.4	5.1	106.5	6.5	3380.3
R.3.5	5.1	250.2	11.3	2473.9
R.4.1	5.7	157.9	4.8	138.0
R.4.2	4.7	95.2	5.5	176.5
R.4.3	3.8	59.2	6.3	294.2
R.5.1	2.8	36.3	7.0	453.9

The spatial and temporal variability of the wind resources over Ecuador's mainland is driven by the large-scale circulation systems in the Tropics, further influenced by changes in surface properties and elevation. The Andean highlands represent a strong divide for the lower tropospheric flow (Vuille et al., 2000). Accordingly, coastal areas and the lower western Andean flanks are mainly influenced by air masses originating in the Pacific, while the eastern part of the country is dominated by easterly trade winds originating over the tropical Atlantic and Amazon basin (Hastenrath, 1981). In the coastal area, the easterlies interact with two local circulation systems: (i) the breeze resulting from the temperature contrast between the continent and the ocean, and (ii) the valley-mountain winds due to the influence of the Andean highlands (MEER, 2013). This combination results in a higher spatial variability of wind speed with some areas showing stronger winds than those in the surrounding areas (MEER, 2013).

These characteristics are reflected in the spatial distribution of the resulting regions and subregions. Region R.1 comprises two subregions (R.1.1 and R.1.2). Subregion R.1.1 is mainly scattered along the Inter-Andean valleys. It also includes partitions along the coastline of Esmeraldas and Manta, and a small partition in the coastal Cordillera (Fig. 3-10a). This subregion shows a unimodal pattern with high winds from June to September and lower winds from October to May (Fig. 3-10b). The annual mean wind speed is 4.1 m s^{-1}.

Subregion R.1.2 covers the rest of the coastline, the Inter-Andean valleys and scattered partitions in the Amazon lowlands. The annual mean wind speed is 3.1 m s^{-1} and it is almost constant along the year. Regarding wind direction in these two subregions, R.1.1 shows scattered winds from southwest to east directions (Fig. 3-11); although, the higher winds during June to September come from east and southeast directions (Fig B-4 in Appendix B.4). In R.1.2, the predominant wind direction is from southwest and remain constant throughout the year (Fig. 3-11 and Fig B-5 in Appendix B.4).

Region R.2 comprises three subregions (R.2.1–R.2.3) that display low wind speed magnitudes over Ecuador's mainland. The largest area of R.2.1 is distributed over the Amazon lowlands. Wind speed in this subregion is low throughout the year, with an annual mean wind speed of 2.5 m s^{-1} (Fig. 3-10c and d). The predominant winds come from south and southeast (Fig. 3-11); however, during November to January, slightly higher winds (max. 5.4 m s^{-1}) come from the east (Fig B-6 in Appendix B.4).

Subregions R.2.2 and R.2.3 are distributed over the rest of the coast and Amazon areas, and scattered locations in the Inter-Andean Valleys. These two subregions have the lowest wind speed magnitude of all subregions in Ecuador's mainland, with annual mean wind speeds of 2.4 and 1.9 m s^{-1}, respectively. The predominant winds in R.2.2 come from southwest, while in R.2.3 weaker breezes blow from different directions ranging southeast and southwest (Fig. 3-11 and Fig B-7, Fig B-8 in Appendix B.4).

The most important wind resources are seen in Region R.3, which comprises five subregions (R.3.1–R.3.5) located over the Andean highlands (Fig. 3-10e). The intra-annual variability of wind speed in these subregions shows a unimodal pattern with higher magnitude from June to September and lower from October to May. Although a smaller peak is seen from November to January (Fig. 3-10f). The higher wind speeds observed in region R.3 correlate to the fact that the easterlies are stronger at elevations higher than ~1000 m.a.s.l. (Emck, 2007), and that the most intensive easterlies extend into the mid-troposphere over the Equator during June–September (Hastenrath, 1981). This behavior is also backed by observations at 4890 m.a.s.l. on *Antizana* volcano (eastern Andean highlands) where strong winds from July to September are observed (Favier et al., 2004). The observation sites A–D are located at elevations higher that 1000 m.a.s.l. and show strong winds during these months, as well.

Subregion R.3.1 shows the highest wind speed magnitude with an annual mean value of 8.3 m s^{-1}. This subregion is mainly scattered along the central part of the western Andean highlands and along the *Loja* province, but also a small partition and isolated grid points are seen in the northeastern Andean highlands (Fig. 3-10e). Subregion R.3.2 shows an annual mean wind speed of 6.9 m s^{-1}. It covers larger extensions of the western Andean highlands, as well as areas over the eastern Andes in the north and south of the country. Subregions R.3.3 and R.3.4 extend over the internal flanks of the highlands towards the valleys and show annual mean wind speeds of 5.9 and 5.1 m s^{-1}, respectively. Subregion R.3.5 is scattered throughout the outer flanks of the western Andean highlands and shows a similar temporal pattern to the previous subregions, but rather lower winds at the beginning and end of the year (Fig. 3-10f). The annual mean wind speed in subregion R.3.5 is 5.1 m s^{-1}.

The predominant winds throughout the year in subregions R.3.1–R.3.4 come from east and southeast directions (Fig. 3-11). In subregion R.3.5, weak winds from the south and southwest are also seen. Taking a more detailed look at wind direction in subregions R.3.1–R.3.5 per month (Fig B-9–Fig B-13 in Appendix B.4), it is observed that the stronger winds during June to September come from east and southeast, which is in agreement with the more pronounced easterlies.

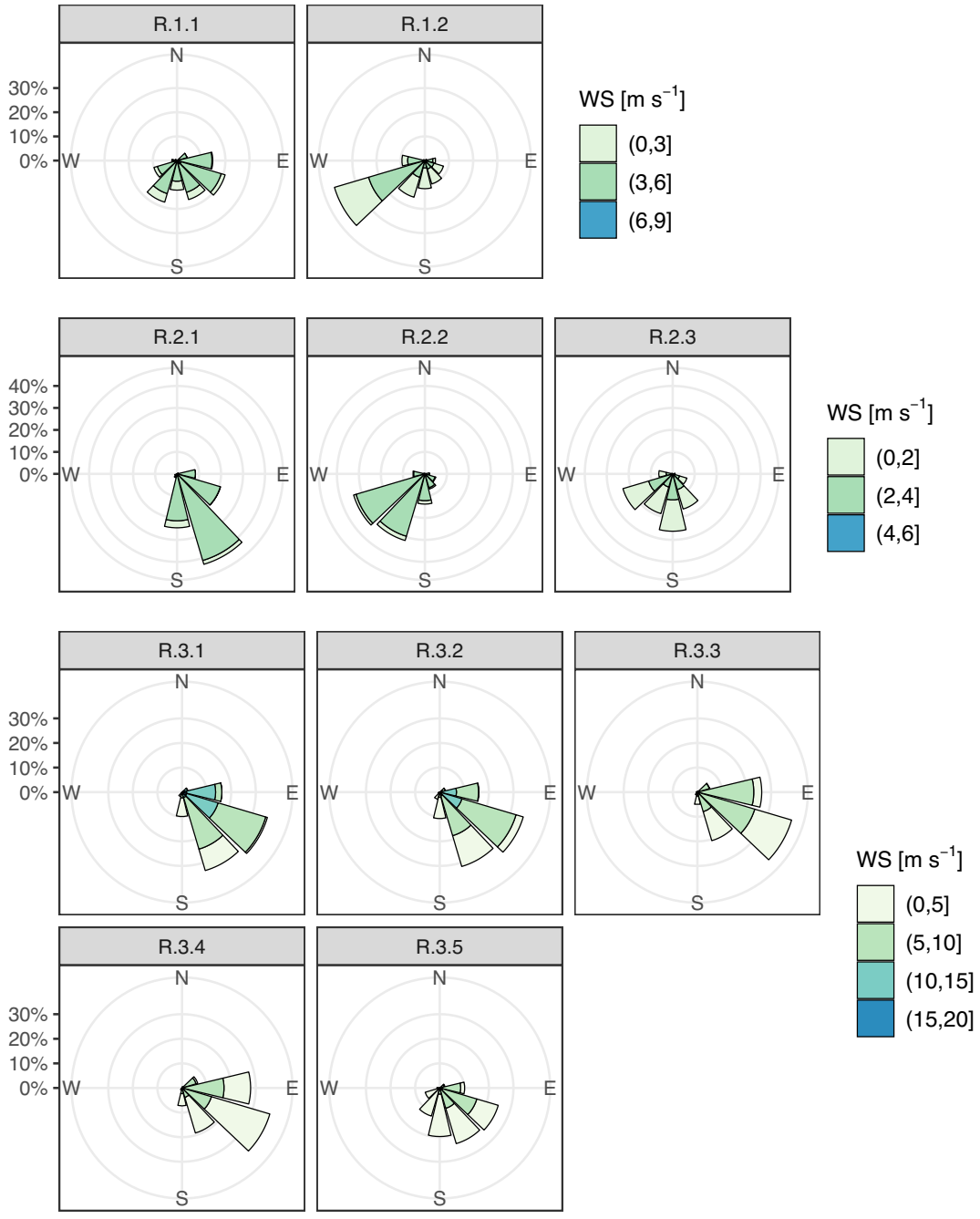

Fig. 3-11. Distribution of wind speed and the frequency of wind direction at 80 m AGL per subregion grouped by their respective region in Ecuador's mainland. The concentric circles represent the probability of wind coming from a particular direction in percentage.

3.3.4.2. Regionalization of wind speed in the Galapagos Islands

Four subregions are selected as the optimal partition for the Galapagos Islands according to the cluster validity assessment explained in Appendix B.2. The spatial distribution of the resulting four subregions R.4.1–R.4.3 and R.5.1 is displayed in Fig. 3-12a, while the intra-annual variability pattern of wind speed in each subregion is shown in Fig. 3-12b.

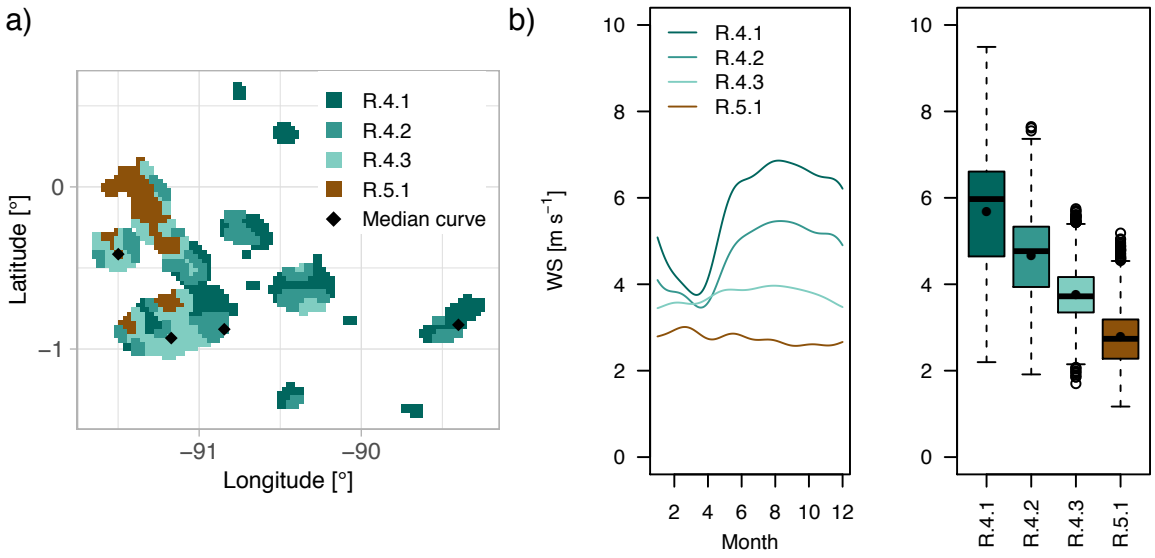

Fig. 3-12. Spatial and temporal variability of wind speed at 80 m AGL in the Galapagos Islands. The map on a) shows the spatial distribution of the subregions of regions R.4 and R.5 (See Appendix D for islands' names). The left side of b) shows the comparison of the median curves obtained from the functional boxplot of each subregion (Appendix B.3). The right side of b) shows the dispersion of the annual mean wind speed for each subregion, where the black points represent the values of the median curve of each subregion.

Subregions R.4.1–R.4.3 are spatially distributed over the islands located on the east side (*San Cristobal*, *Santa Cruz*, and *Floreana*) and scattered over the eastern and western side of the *Isabela* and *Fernandina* Islands.

Subregions R.4.1 and R.4.2 show a unimodal variability pattern with higher winds from June to December and lower winds from January to May. The annual mean wind speed in these subregions is 5.7 and 4.7 m s^{-1}, respectively. A similar pattern is seen in R.4.3 but to a lesser extent.

The marked seasonality in R.4.1 and R.4.2 corresponds to the two distinctive seasons in Galapagos that are influenced by the interaction of oceanic currents and winds, which in turn are governed by the north-south migration of the ITCZ (Trueman et al., 2010). From January to May, when the ITCZ is close to Galapagos, hot conditions with mild winds

prevail, while from June to December, when the ITCZ lies further north, cooler conditions with southeast trade winds predominate (Trueman et al., 2010). These dynamics are reflected in the intra-annual variability of wind speed (Fig. 3-12b) and wind direction in these subregions (Fig. 3-13 and Fig B-14–Fig B-16 in Appendix B.4).

A different intra-annual variability pattern is seen in subregion R.5.1 that is scattered over the western slopes of the volcanoes in *Isabela* and *Fernandina* Islands (Fig. 3-12a). In this subregion, wind speed is low and almost constant along the year with an annual mean of 2.8 m s^{-1}, except for a small peak in March (Fig. 3-12b). This subregion does not show the predominant southeast wind direction seen in the previous subregions, but rather weaker breezes coming from different directions between southwest and southeast (Fig. 3-13). The peak seen in March corresponds to higher winds (max. 5.1 m s^{-1}) coming from east and southeast directions (Fig B-17 in Appendix B.4).

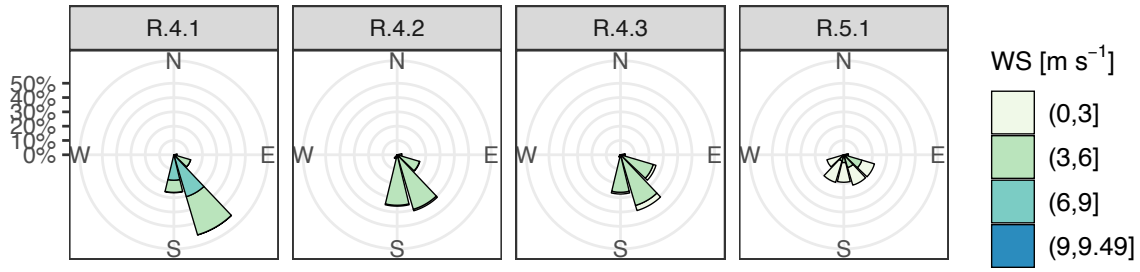

Fig. 3-13. Distribution of wind speed and the frequency of wind direction at 80 m AGL per subregion grouped by their respective region in the Galapagos Islands. The concentric circles represent the probability of wind coming from a particular direction in percentage.

3.3.4.3. Interannual spatial-temporal variability of wind speed

The coefficient of variation (CV) is used to analyze the interannual variability of wind speed at 80 m AGL during the 14-year period at yearly and monthly timescales. Fig. 3-14 shows the spatial distribution of the annual coefficient of variation CV_y.

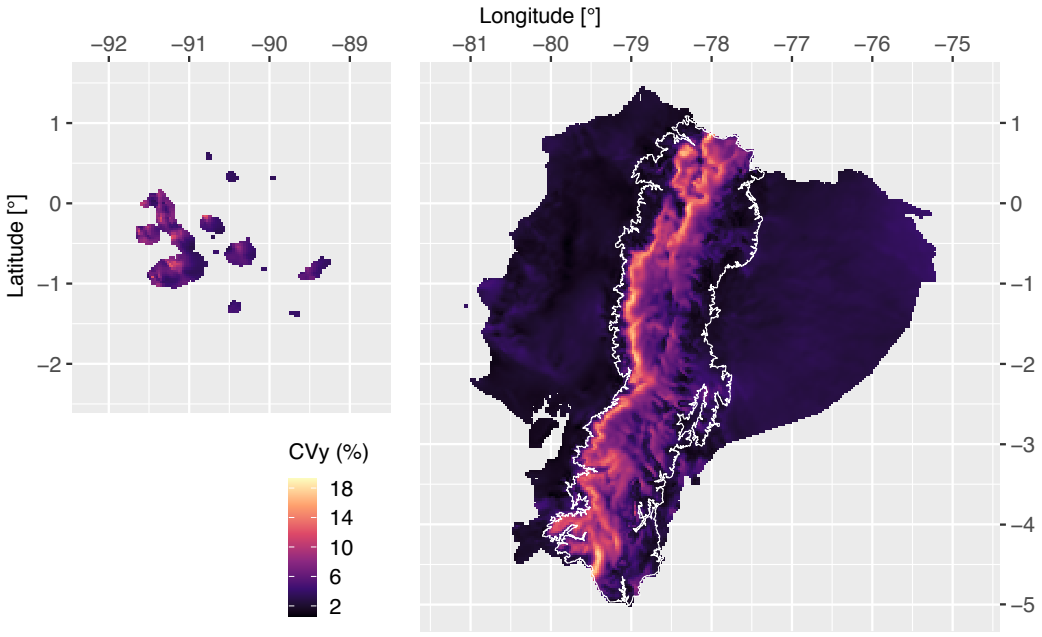

Fig. 3-14. Annual coefficient of variation CV_y (%) of wind speed at 80 m AGL during 2005–2018 over Ecuador's mainland and the Galapagos Islands. The white line over the continental part depicts the altitudinal contour at 1000 m.a.s.l.

The highest variabilities of wind speed are along the western Andean highlands, while the lowest variability is seen over the coast and Amazon areas, as well as in the Inter-Andean valleys. In Galapagos, the highest variabilities are seen over the northwest side of the islands, especially around the western slopes of the volcanoes in *Isabela* and *Fernandina* Islands.

The distribution of the CV_y values per subregion is shown in Fig. 3-15 and a summary of the mean values per subregion is given in Table 3-5. Subregions R.3.1, R.3.2, and R.3.5 have the highest mean CV_y values (>10%). The lowest mean CV_y values (<3.5%) are seen in R.1.2 and the subregions in region R.2. In Galapagos, subregion R.5.1 shows the highest mean CV_y values (7.0%), while subregion R.4.1 have the lowest values mean CV_y values (4.8%).

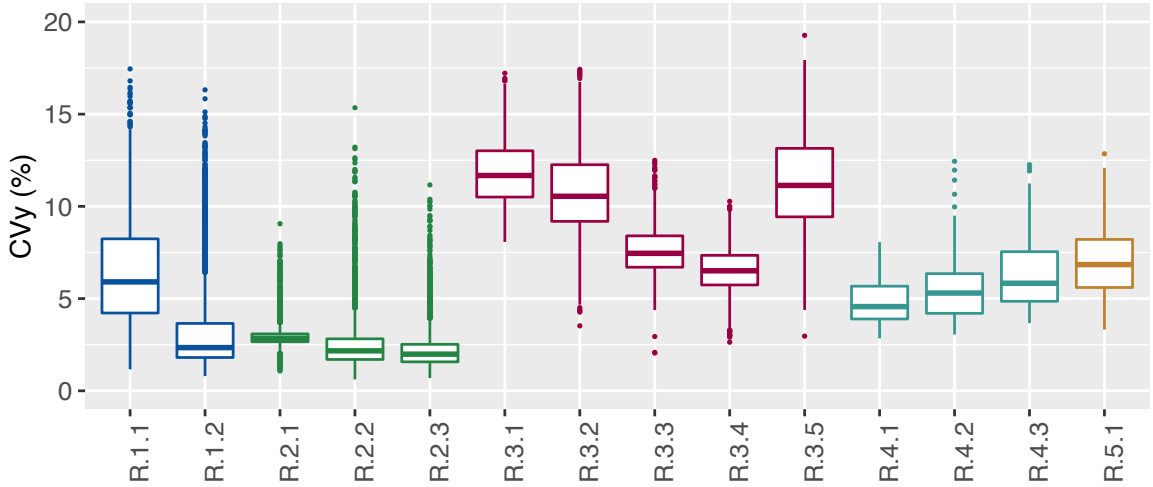

Fig. 3-15. Annual coefficient of variation CV_y (%) of wind speed at 80 m AGL during 2005–2018 per subregion and grouped by region in Ecuador's mainland (R.1–R.3) and in Galapagos (R.4–R.5).

At a monthly timescale, Fig. 3-16 shows that the monthly coefficient of variation CV_m over Ecuador's mainland reaches high values along the western Andean highlands throughout the year.

A further breakdown by subregion per month (Fig. 3-18) shows that the variability is seasonal rather than random. This is especially observed in subregions R.3.1, R.3.2, and R.1.1, which show high variability from October to May; however, during the months with stronger winds (June to September) the median CV_m is lower than 50%. This pattern is also observed in subregion R.3.5, but the CV_m value is higher than that observed in the aforementioned subregions (~50–60%) during the windy months. These results show that wind speed over the 14-year period in subregions R.3.1, R.3.2, and R.1.1 is less variable during the windy months. This finding may be of interest to power system planners, since the interannual variability of wind resources has significant implications for the cash flow of a wind farm operator (Watson, 2014).

Fig. 3-17 shows the monthly coefficient of variation CV_m over the Galapagos Islands. The highest variabilities throughout the year are around the western slopes of the volcanoes in *Isabela* and *Fernandina* Islands. This area corresponds to subregion R.5.1 that shows median CV_m values higher than 60% over all months (Fig. 3-18). Subregions R.4.1–R.4.3 show a similar seasonal variability pattern to that observed in Ecuador's mainland. During the windy months in Galapagos (June to December) the variability is lower (median $CV_m < 40\%$) compared to that during February to March (median $CV_m > 40\%$).

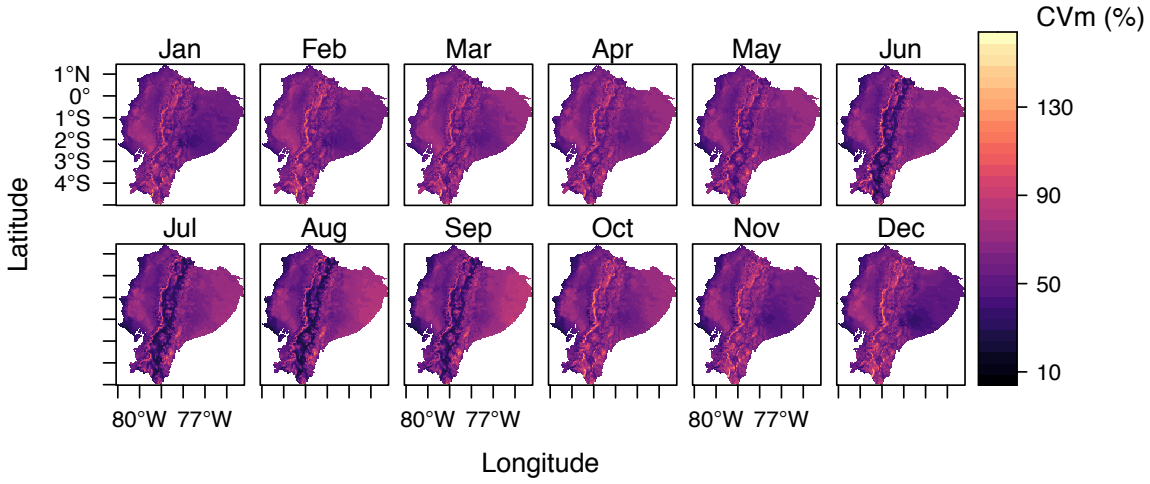

Fig. 3-16. Monthly coefficient of variation CV_m (%) of wind speed at 80 m AGL during 2005–2018 over Ecuador's mainland.

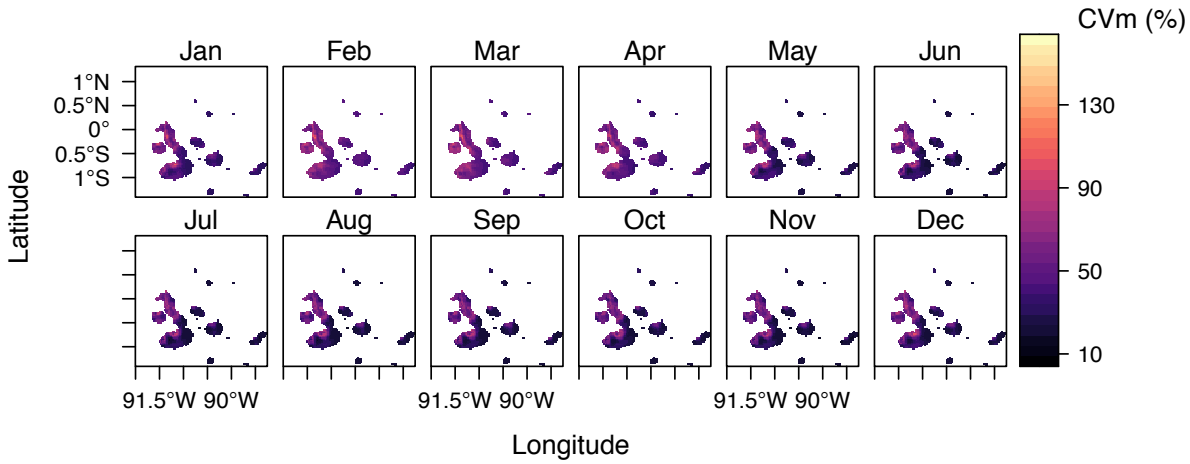

Fig. 3-17. Monthly coefficient of variation CV_m (%) of wind speed at 80 m AGL during 2005–2018 over the Galapagos Islands.

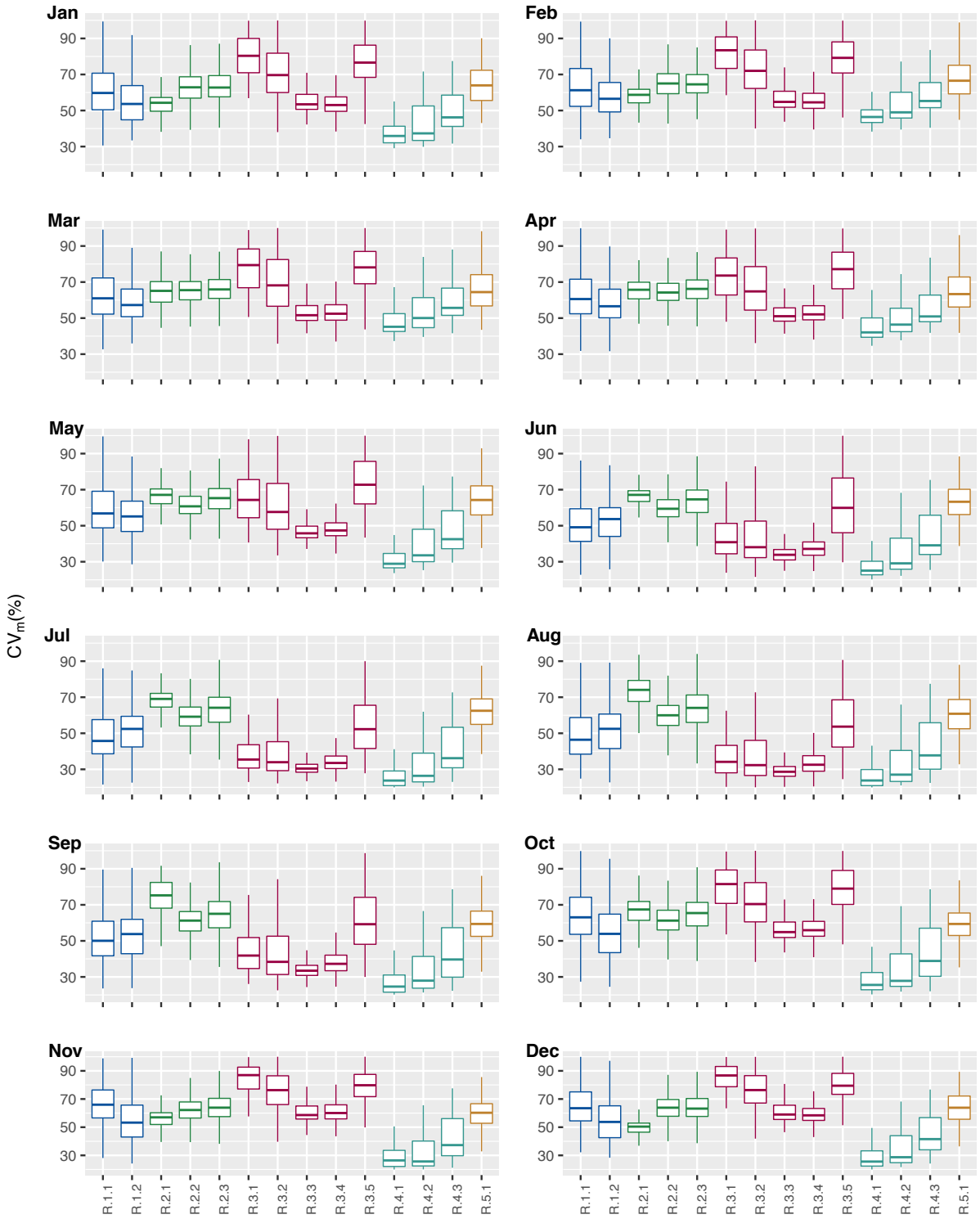

Fig. 3-18. Boxplots of the monthly coefficient of variation CV_m (%) of wind speed at 80 m AGL during 2005–2018 per subregion and grouped by region in Ecuador's mainland (R.1–R.3) and in Galapagos (R.4–R.5). Outliers are excluded for clarity.

3.4. Discussion

The lack of a validated, long-term, and high-resolved wind dataset for the study area was the motivation to simulate wind resources using the WRF mesoscale model. Wind speed measurements at 80 m AGL from four meteorological tall masts were made available to evaluate the performance of the model. Results indicate that WRF overestimates wind speed compared to observations, especially at nighttime and from June to September. All observation sites are located over complex terrain in the Andean highlands. According to previous studies, WRF seems to overestimate surface wind speeds in complex terrain due to unresolved orographic surface drag (Jiménez et al., 2012).

The nighttime overestimation is consistent with previous studies (Hahmann et al., 2010; Ngan et al., 2013; Zhang et al., 2004), which is probably due to excessive vertical mixing during nighttime hours. Normally, the sun heats the earth's surface during daytime, causing warm updrafts and vertical mixing, which results in an increase of wind speed during the day. Near sunset, a second temperature inversion starts to grow from the bottom surface as rapid radiative heat losses occur at the ground (Zhang et al., 2004). This dynamic corresponds to a change from an unstable daytime convective boundary layer to a stable nocturnal boundary layer (NBL) (Emeis, 2013).

The validation of WRF simulated wind speed performed by Ngan et al. (2013) found that the overestimation always began at sunset, which corresponds to the start of the growth of the NBL. The authors attributed the overestimation to the inaccuracy of WRF in capturing the thermal and mechanical dynamics that occur during the evening hours (Ngan et al., 2013). In another validation study of WRF simulated wind speed over Denmark, Hahmann and Peña (2010) found larger nighttime overestimations in October compared to those in June, which was attributed to the fact that stable conditions are more prevalent during fall and winter than during summer in this geographical area. In the Ecuadorian Andean highlands, clear skies generally occur during June to September (Hastenrath, 1981), which may explain the larger nighttime overestimation of the simulated winds at the observation sites during these months.

ERA5 is found to have significant negative biases compared to observations, which implies that the ERA5 reanalysis data may not be a reliable dataset to evaluate the wind power potential in the Ecuadorian Andean highlands. The underestimation of ERA5 might be attributed to the coarse resolution of the model and its inability to reproduce fluctuations at a local site, especially over complex terrain (Olauson, 2018). Nevertheless, based on the comparison of WRF simulated wind speed against observations, it can be inferred that

ERA5 is suitable as forcing data for the mesoscale model. One question that may arise is how WRF is able to input relatively inaccurate ERA5 data and produce more accurate wind speed simulations. This can be explain by the fact that the atmospheric processes not resolved by ERA5 (due to the coarse horizontal resolution) are considered in WRF with the aid of physical parameterization schemes (Carvalho et al., 2012). In addition, the nesting and nudging methods used in the WRF simulations provide better temporal detail at the nest boundary than driving it directly from linearly interpolated analyses, as well as better accounting for topographic and convective effects (Skamarock et al., 2019).

An improvement of WRF simulated wind speed forced by ERA5 compared to ERA5 data itself was also reported by Dörenkämper et al. (2020). The authors compared WRF simulations and ERA5 data against measurements from masts located in complex terrain in Greece. They found that ERA5 underestimates the mean wind speed by 2.5–4.0 m s^{-1}, while small underestimations were found between WRF and observations.

The evaluation of the sensitivity of the WRF model to changes in the configuration settings was outside the scope of this dissertation. For further research, a sensitivity analysis to test different initial and boundary forcing conditions, as well as other physical parametrization settings could be performed to determine the underlying factors of the model overestimations and evaluate different configurations to reduce WRF systematic biases.

The overestimation in wind speed translates to larger differences in wind power and capacity factors due the aforementioned cubic dependence. For a typical wind turbine, biases of 2 to 4 m s^{-1} can translate to the difference between 20% and 80% capacity factor (Staffell et al., 2016). Therefore, the correction of the bias is required for the assessment of wind power potential. The consistent trend of diurnal and monthly bias found between WRF simulated wind speeds and observations enables the definition of factors to correct the bias of the WRF simulations. According to the results, the bias correction increases the agreement of the WRF simulations to observations in terms of MBE, RSME, and correlation coefficients during the control and evaluation period. Thus, the resulting bias-corrected time series show a diurnal cycle that is more in phase with the observations during the control and evaluation period.

It is not possible, however, to evaluate the 14-year period of WRF simulated winds due to the lack of measurements covering this period. Nevertheless, the control period covers one year allowing the analysis of the performance of the simulation of wind speed and wind

direction. The evaluation period extents for nine extra months, allowing the evaluation of the performance of the pointwise bias correction approach.

The bias correction method combined with the sFDA regionalization method is found to be suitable for the adaptation of the pointwise bias correction to any other grid point in the dataset that has a similar wind speed temporal variability pattern to that of the observation sites. This approach denotes a significant advantage compared to other approaches to correct the bias of gridded datasets applied in previous studies. For instance, Heredia et al. (2018) used Voronoi diagrams to divide the study area into neighboring cells in such a way that each cell contains a measurement station. Such an approach is constrained by the number of observation sites. Therefore, its application would be restricted for the present work, since the observation sites are limited to four. In another study, Gruber et al. (2019) applied a bias correction method to grid points located within a certain distance from the nearest measurement station. Such an approach assumes that wind speeds at the selected grid points behave similar to that of the observation sites, without considering that wind speed may vary within a few kilometers, especially over complex terrain. This limitation is overcome by using the sFDA regionalization approach to select the grid points with a similar spatio-temporal variability of wind speed to that of the observation sites.

Due to the small number of available tall meteorological masts, the evaluation of the performance of WRF simulated wind speeds and the bias-correction is limited to grid points over the Andean highlands. Measurements in the Amazon, the coastal region, and the Galapagos Islands are not available, thus the validation in these areas is not possible. Nevertheless, the Andean highlands host the best wind resources and represent a key area for wind energy development. Therefore, the findings presented in this chapter provide new insights into the variability and availability of wind resources for a better deployment of wind power in the Ecuadorian Andes.

3.5. Conclusions

This chapter presents the first long-term wind resource dataset at a 3 × 3 km grid and hourly resolution for Ecuador's mainland and the Galapagos Islands. The dataset is generated using the Weather Research and Forecasting (WRF) mesoscale model forced by initial and boundary conditions from ERA5 reanalysis data.

Simulated wind speeds over the Andean highlands are bias-corrected based on the validation of the performance of the model using observational data from meteorological tall masts at 80 m AGL. Results shows that the bias correction method increases the agreement between WRF simulations and observations. MBE is reduced from 2.16 ± 0.94 to 0.36 ± 0.49 m s^{-1}, RMSE decreases from 4.28 ± 1.03 to 2.96 ± 0.55 m s^{-1}, and the correlation increases from 0.57 ± 0.11 to 0.72 ± 0.06. Moreover, the resulting bias-corrected time series shows a diurnal cycle that is more in phase with the observations.

Using the bias-corrected dataset, the intra-annual and interannual spatio-temporal variability of wind speed is characterized applying the methodology proposed in Chapter 2. The findings from this Chapter provide the first comprehensive spatio-temporal characterization of wind resources in Ecuador. The regionalization map and the variability statistics provide explicit information to identify optimal sites for the deployment of measurement networks and wind power plants. In Ecuador's mainland, subregion R.3.1, which is scattered over the Andean highlands, shows the highest long-term annual mean wind speed (8.3 m s^{-1}), with stronger winds (up to 19.2 m s^{-1}) between June and September coming from east and southeast direction. This subregion shows, however, the highest mean interannual variability (11.9%) compared to the other subregions. Nevertheless, a further breakdown of the coefficient of variation at monthly time scales reveals that the variability is seasonal rather than random, showing that wind speed over the 14-year period is less variable during the windy months. In the Galapagos Islands, the best wind resources are found in subregion R.4.1 that shows the highest long-term annual mean wind speed (5.7 m s^{-1}) and the lowest mean interannual variability (4.8%).

These findings contribute to the understanding of the spatio-temporal variability of wind resources in Ecuador, which is of particular relevance to support the optimal planning and deployment of wind power systems in the country. Furthermore, the generated wind resource dataset and the findings reported in this chapter support the achievement of the remaining research objectives of this dissertation, which are reported in the following chapters.

Chapter 4 Correlation analysis of renewable resources in Ecuador based on meteorological data with high spatial and temporal resolution

This chapter investigates for the first time to which extent solar and wind resources are complementary in time and space to water resources in Ecuador using correlation analysis. First, the spatio-temporal correlation is analyzed using the time series of GHI and wind speed at representative geographical locations obtained from the sFDA regionalization, and time series of river discharge records from gauging stations located near selected hydropower plants. Then, the temporal correlation of the different resources at each grid point over Ecuador is analyzed using GHI, wind speed, and precipitation gridded datasets. Results reveal that there are strong spatio-temporal complementarities between the different resources. This implies that solar and wind power have a high potential to compensate hydropower during the dry periods. Additionally, results from the temporal correlation analysis show a great potential for deploying complementary hydro-wind-solar hybrid power systems in Ecuador.

4.1. Introduction

The hydropower capacity in Ecuador could be reduced up to one-third of its installed capacity during the dry periods, or even more under severe drought events, which could lead to a significant expansion of fossil fuel thermal power to meet the country's electricity demand (Jara, 2018).

An alternative way to compensate hydropower during the dry periods is to use other renewable resources that show an anti-correlated (also called complementary) behavior to the hydrological regimes. Temporal complementarity can be observed when two or more energy sources have periods that complement each other over time in the same region (Bagatini et al., 2017), while spatial complementarity can be observed when energy sources from different regions complement each other. Spatio-temporal complementarity is considered for a single or multiple resources whose complementary nature is investigated simultaneously in time and space (Jurasz et al., 2020).

Recent studies evaluated the complementarities between solar, wind, and water resources in South American countries, such as in Brazil (Bagatini et al., 2017; Borba et al., 2017; de Oliveira Costa Souza Rosa et al., 2017, 2020; Schmidt et al., 2016), and in Colombia (Canales et al., 2020; Henao et al., 2020; Parra et al., 2020). These studies highlighted the potential of solar and wind resources to compensate hydropower during the dry seasons in the study areas. Spatio-temporal complementarities between different regions in Latin America have also been investigated recently (Gonzalez-Salazar et al., 2021; Viviescas et al., 2019).

In these studies, the assessment usually involved the complementarity to existing or planned hydropower plants (HPPs), using historical records of river discharge from gauging stations located near the selected plants. Energy yield records from HPPs in operation were also used in the case that the energetic complementarity was evaluated instead of the resource complementarity. Regarding solar and wind data for the complementarity analysis, some authors used measurements from meteorological stations or historical records of energy yield from existing solar or wind power plants. However, in sparsely monitored regions or where the number of installed solar and wind power plants is minimal, which is the case of Ecuador, such an approach would hinder an extended analysis that includes locations where observations are not available.

Other previous studies used solar and wind data from gridded reanalysis datasets that cover wider areas and longer time periods. This type of data is useful for the analysis of temporal complementarities, as demonstrated by Henao et al. (2020). The authors used precipitation, wind speed, and solar radiation data retrieved from the MERRA-2 reanalysis dataset (Gelaro et al., 2017) to assess the pairwise complementarities of the resources at each grid point over Colombia. However, a disadvantage of using this reanalysis dataset, which has a grid resolution of 50 km, may be that local variations in solar and wind resources are not captured due to the coarse horizontal resolution (Olauson, 2018).

Another issue of using reanalysis datasets for the assessment of spatio-temporal complementarities is regarding the selection of the representative sites for solar and wind power plants to be evaluated. A common approach is to use high-potential areas derived from a geographical potential assessment, which uses a set of criteria to exclude grid points considered unsuitable for solar and wind deployment (Gonzalez-Salazar et al., 2021; Viviescas et al., 2019). However, as revealed in Chapter 3, Section 3.3.1, reanalysis data significantly underestimates wind resources. Therefore, such an approach may exclude areas that eventually have larger potential than the one calculated using the reanalysis datasets.

This chapter assesses the temporal and spatio-temporal correlations between solar, wind, and water resources in Ecuador. Such an assessment has not been performed for this country yet and aims: (i) to investigate the potential of solar and wind resources to compensate in time and space existing and planned HPPs in Ecuador's mainland, and (ii) to assess the potential for the deployment of local hybrid and complementary renewable power systems in Ecuador's mainland and the Galapagos Islands.

The novelty of this chapter lies on the use of the sFDA regionalization method to select the representative solar and wind sites for the spatio-temporal correlation analysis in a country with limited and unevenly-distributed meteorological stations. In this way, the analysis is not limited to the geographical locations where the meteorological measurements are available, nor to their surroundings. Furthermore, the representative solar and wind sites are neither randomly selected, nor based on best geographical locations inferred from resource atlases or low-resolved reanalysis datasets, but rather they are selected based on the characterization of the spatio-temporal variability of solar and wind resources, which is reported in Chapter 2 and Chapter 3, respectively.

This chapter is structured as follows. Section 4.2 describes the methods and data used for the analysis. Section 4.3 presents the results of both the spatio-temporal correlation and temporal correlation analyses. Section 4.4 discusses the main findings and contributions. Finally, Section 4.5 presents the conclusions of this chapter.

4.2. Methods and data

4.2.1. Water resources

The Ecuadorian Andean highlands divide the country in two natural drainage basins: (i) the Pacific basin that comprises the watersheds located on the western side of the Andes conveying water to the Pacific Ocean, and (ii) the Amazon basin that comprises the watersheds located on the eastern side of the Andes draining to the Amazon River (Fernandez-Palomino et al., 2022). The hydropower technical potential of the Amazon and Pacific basins is 71% and 29%, respectively (CONELEC, 2013, p. 158).

For the spatio-temporal correlation analysis in this chapter, six large-scale HPPs are selected (Fig. 4-1a). Three are located in the Amazon basin (HA.1–HA.3) and three are located in the Pacific basin (HP.1–HP.3). Five of them are in operation and provided about 61% of the total electricity generated by hydropower in 2020 (CENACE, 2021).

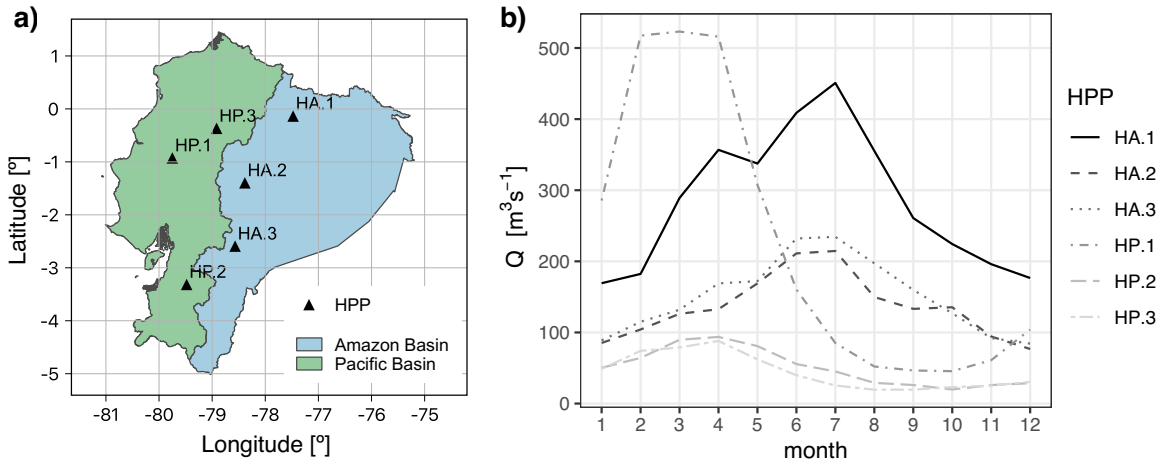

Fig. 4-1. Selected hydropower plants (HPPs) for the spatio-temporal correlation analysis. a) Geographical location of HPPs in the Amazon basin (HA.1–HA.3) and in the Pacific basin (HP.1–HP.3). b) Monthly mean river discharge (Q) at gauging stations near selected HPPs. Source: Own representation. Data retrieved from GRDC (2022).

To characterize the hydrological regime of each HPP, the records of mean daily river discharge (Q) from gauging stations located close to the selected HPPs are used. These records were retrieved from the Global Runoff Data Centre (GRDC) (GRDC, 2022). Table 4-1 shows the details of the selected HPPs and their related gauging station. Note that each station has a different period of records, however, due to the lack of further information it is assumed that the GRDC dataset provides the intra-annual characteristics of the respective river basin.

Table 4-1. Details of selected hydropower plants and the nearest gauging stations.

Hydropower plants						Gauging stations		
Basin	River basin	Name	Code name[1]	Installed capacity [MW] [2]	Type	River name	Station name	Period of records
Amazon	Napo	Coca Codo Sinclair	HA.1	1500.0	Run-of-river	Coca	San Rafael	1978–1982
Amazon	Pastaza	Agoyán	HA.2	154.0	Dam	Pastaza	Bannos	1970–1996
Amazon	Santiago	Paute Molino	HA.3	1100.0	Dam	Paute	D.J. Palmira	1970–1979
Pacific	Guayas	Marcel Laniado	HP.1	213.0	Dam	Quevedo	Quevedo	1962–2005
Pacific	Jubones	Minas San Francisco	HP.2	270.0	Run-of-river	Jubones	D.J. San Francisco	1970–2005
Pacific	Esmeraldas	Toachi-Pilatón[3]	HP.3	254.4	Run-of-river	Toachi	A.J. Pilaton	1964–2005

[1] Code name used in this dissertation. HA: Hydropower plant in Amazon basin, HP: Hydropower plant in Pacific basin.
[2] Source: (CENACE, 2021; MERNNR, 2018),
[3] Hydropower project under construction.

The seasonal hydrological regimes of the different gauging stations are displayed on Fig. 4-1b. It can be seen that the stations located in the Amazon basin show a marked seasonality with a peak in July and low values from November to February. Stations in the Pacific basin also show a unimodal variability pattern, with high values in March to April, and lower from August to November.

To assess the relationships between solar, wind, and water resources at the same geographical location measured or modeled river discharge data is required. However, as mentioned before, the study area is poorly monitored and hydrological modeling in the Andes is challenging due to large spatial variability of precipitation, specific soil properties, and very irregular topography (Buytaert et al., 2011). River discharge is determined by the balance among precipitation, surface and groundwater storage, and evapotranspiration (Heerspink et al., 2020). The relationship between precipitation and river discharge regimes in Ecuador was analyzed by Laraque et al. (2007), who found that there was no delay between the observed maximum precipitation and maximum river discharge in small to medium upper intra-Andean basins (i.e., *Santiago* river basin). However, the authors also found a delay between precipitation and discharge that varies from one to two months in larger basins (i.e., *Napo and Pastaza* river basins) (Laraque et al., 2007). No studies regarding the relationship between precipitation and river discharge in the Pacific basin were found in the literature. Consequently, due to the lack of long-term and validated river discharge data at high spatial resolution covering the study area, precipitation data is used for the temporal correlation analysis, assuming that the precipitation regime reflects the discharge regimes in small to medium river basins in the Amazon basin. For larger river basins, the spatio-temporal correlation analysis using the discharge records will prevail.

The gridded daily precipitation data from 1981 to 2019 for Ecuador's mainland was retrieved from the Climate Hazards Infrared Precipitation with Stations (CHIRPS) dataset version 2.0 (Funk et al., 2015). CHIRPS data is available at a $0.05° \times 0.05°$ grid resolution and has been successfully used to understand the precipitation variability over the tropical Andes (Segura et al., 2019). Two preprocessing steps were performed to the 39-year period CHIRPS dataset before applying the methodology described in Section 4.2.3. First, the spatial resolution was increased from the CHIRPS native resolution to 3×3 km, applying the first order conservative remapping method. This step was performed to match the grid resolution of the CHIRPS dataset with that of the solar and wind datasets generated in Chapter 2 and Chapter 3. Second, the long-term daily and monthly mean precipitation at each grid point was calculated.

4.2.2. Solar and wind resources

The datasets of solar irradiance and wind speed described in Chapter 2 and Chapter 3 are used for the temporal and spatio-temporal correlation analyses in this chapter.

For the spatio-temporal correlation analysis, the long-term monthly and daily mean GHI and wind speed time series of the grid points representing each solar or wind subregion are used. In Ecuador's mainland, the representative grid points of the 22 solar subregions (A.1, EH.1–EH.6, WH1–WH6, C.1.1–C.3.5) are used in the analysis, whose geographical location is displayed in Fig. 4-2a.

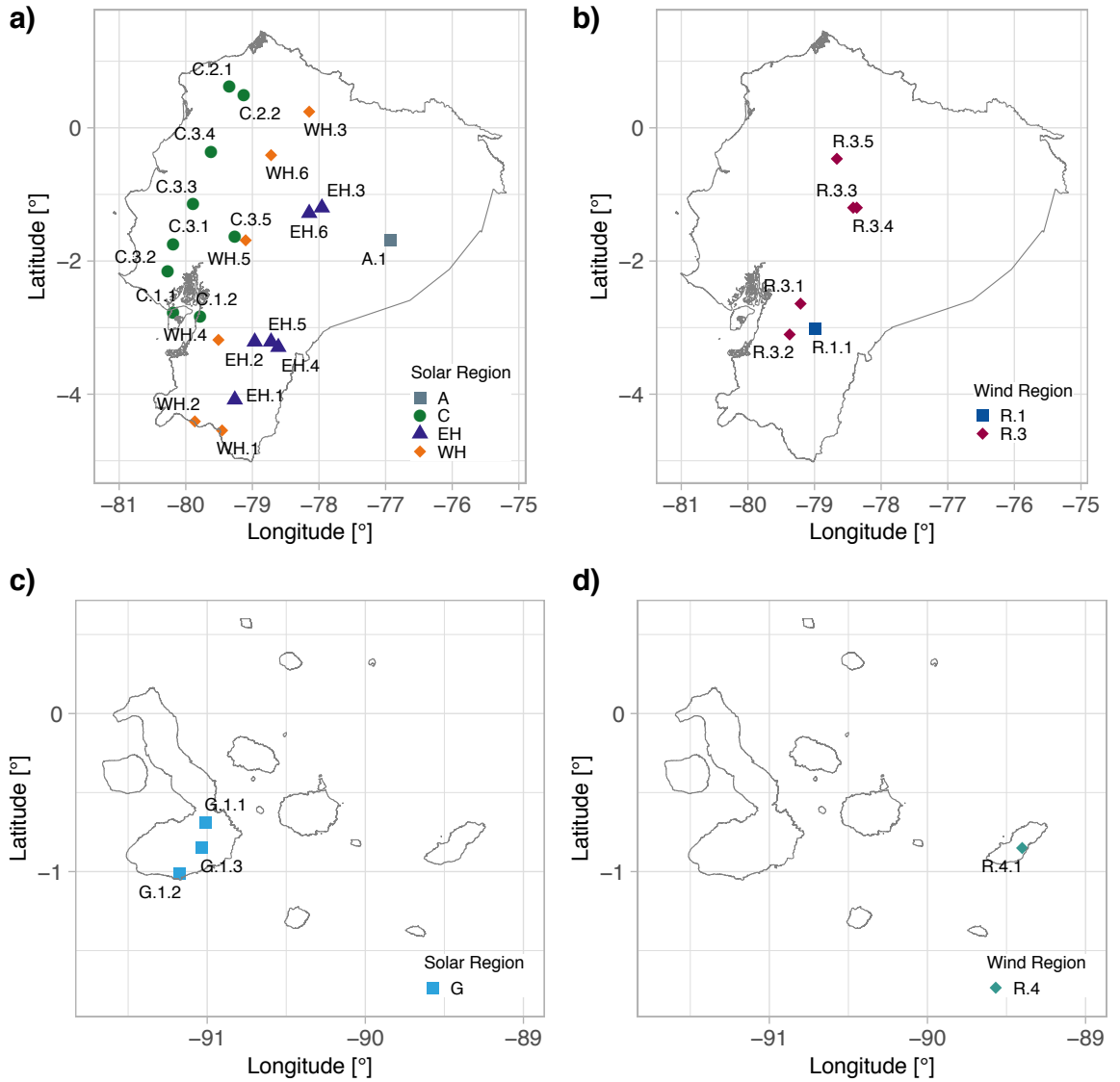

Fig. 4-2. Geographical location of the representative sites of solar and wind subregions used for the spatio-temporal correlation analysis. a) Representative sites of the solar subregions (A.1, EH.1–EH.6, WH1–WH6, C.1.1–C.3.5) in Ecuador' mainland. b) Representative sites of the wind subregions (R.1.1, R.3.1–R.3.5) in Ecuador' mainland. c) Representative sites of the solar subregions (G.1.1–G.1.3) in the Galapagos Islands. d) Representative site of the wind subregion (R.4.1) in the Galapagos Islands.

In the case of the wind resources, the representative grid points of subregions R.1.1 and R.3.1–R.3.5 are used for the analysis, whose geographical location is displayed in Fig. 4-2b. The other wind subregions are excluded from the correlation analysis because wind power densities (WPD) in those subregions are lower than 100 Wm^{-2}, which is considered too low to be exploited (Manwell et al., 2009).

In the Galapagos Islands, the three solar subregions (G.1.1–G.1.3) and the wind subregion R.4.1 (see geographical location in Fig. 4-2c and Fig. 4-2d) are included in the analysis. The other wind subregions in Galapagos are excluded from the correlation analysis for the same reason used for the mainland.

For the temporal correlation analysis, the long-term monthly and daily mean GHI and wind speed time series of all grid points of Ecuador's mainland (27,175) and of the Galapagos Islands (874) are used.

4.2.3. Correlation analysis methodology

In this study, correlation analysis is used to determine the pairwise relationship between the three renewable resources at monthly and daily timescales. The spatio-temporal correlation analysis uses the Pearson product-moment correlation coefficient (r_P) and the Spearman rank correlation coefficient (r_S), which are computed according to Equations (4.1) and (4.2), respectively (Wilks, 2006):

$$r_{P_{x_i y_j}} = \frac{Cov(x_i, y_j)}{\sigma_{x_i}\sigma_{y_i}} \tag{4.1}$$

$$r_{S_{x_i y_j}} = \frac{Cov(rg_{x_i}, rg_{y_j})}{\sigma_{rg_{x_i}}\sigma_{rg_{y_j}}} \tag{4.2}$$

where $Cov(x_i, y_j)$ is the covariance between the long-term monthly and daily mean time series of resources x and y at grid points i and j; and σ_{x_i}, σ_{y_i} is the standard deviation of the respective time series. In Equation (4.2), the Spearman correlation is defined as the Pearson correlation computed using the ranks rg_{x_i}, rg_{y_j} of the time series x_i, y_j; and $\sigma_{rg_{x_i}}$, $\sigma_{rg_{y_j}}$ are the standard deviation of the respective ranks. The Pearson correlation measures the strength of linear dependencies, while Spearman correlation reflects the strength of monotone relationships (Wilks, 2006).

The temporal correlation analysis between resources x and y at each grid point is calculated using the gridded long-term monthly and daily mean datasets of resources x and y as NetCDF files. The operator $timcor$ from the Climate Data

Operators (CDO) software is used for this purpose, which correlates each grid point of two NetCDF datasets over all time steps (Schulzweida, 2020).

4.3. Results

4.3.1. Spatio-temporal correlation of renewable resources

4.3.1.1. Spatio-temporal correlations of solar, wind, and water resources in Ecuador's mainland

The results of the Pearson and Spearman correlation coefficients using monthly time series are displayed in Fig. 4-3 and Fig. 4-4, respectively. The correlation coefficients are very similar, but it is found that $r_{P_{monthly}} \geq r_{S_{monthly}}$ in 74% of the pairs, suggesting a linear relationship between the monthly time series. Thus, the following sections will only refer to the Pearson correlation coefficient results.

According to the interpretation of the correlation coefficients (see Table 2-1), there are different levels of complementarity and similarity between the resources. Strong complementarities are seen between river discharge from stations in the Amazon basin and GHI in subregions EH.2, EH.4, EH.6 and C.1.1–C.1.2. In the Pacific basin, only HP.3 shows a very strong complementarity with GHI in subregion WH.3, while strong complementarities are seen between discharge in all three stations and GHI in subregions A.1, EH.1, EH.3, EH5, EH.6 and WH.1–WH.6. Remarkably, the correlation between discharge at stations in both basins is low ($-0.2 \leq r_{P_{monthly}} \leq 0.3$), implying that there is a very weak complementarity to a very weak similarity between both basins. This behavior is evident from the time series shown in Fig. 4-1, where it can be observed that between November and February water is limited in both basins.

Strong similarities are seen between discharge from stations in the Amazon basin and wind speed in subregions R.1.1 and R.3.1–R.3.5. In the Pacific basin, river discharge in HP.1 and HP.2 shows very strong similarities to GHI in subregions C.1.1–C.1.2, while a strong similarity is seen between the three stations and solar subregions C.2.1–C.2.2 and C.3.3–C.3.4. As expected, the correlation coefficients of river discharge between stations in the same basin are high ($0.9 \leq r_{P_{monthly}} \leq 1.0$), showing a very strong similarity.

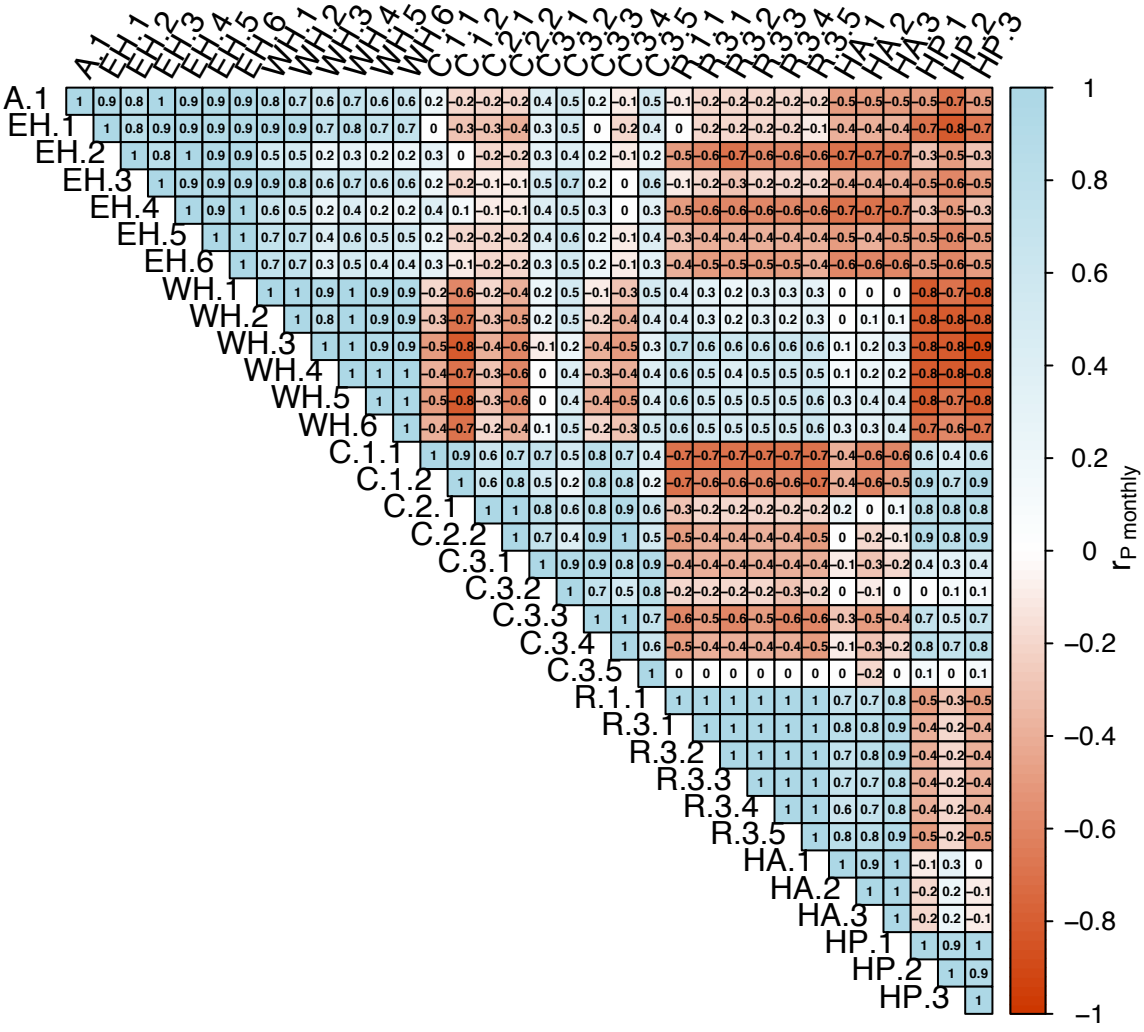

Fig. 4-3. Pearson correlation coefficient matrix of monthly time series of GHI at the representative sites of each solar subregions (A.1, EH.1–EH.6, WH1–WH6, C.1.1–C.3.5), wind speed at the representative sites of each wind subregions (R.1.1, R.3.1–R.3.5), and river discharge at gauging stations in the Amazon basin (HA.1–HA.3) and Pacific basin (HP.1–HP.3).

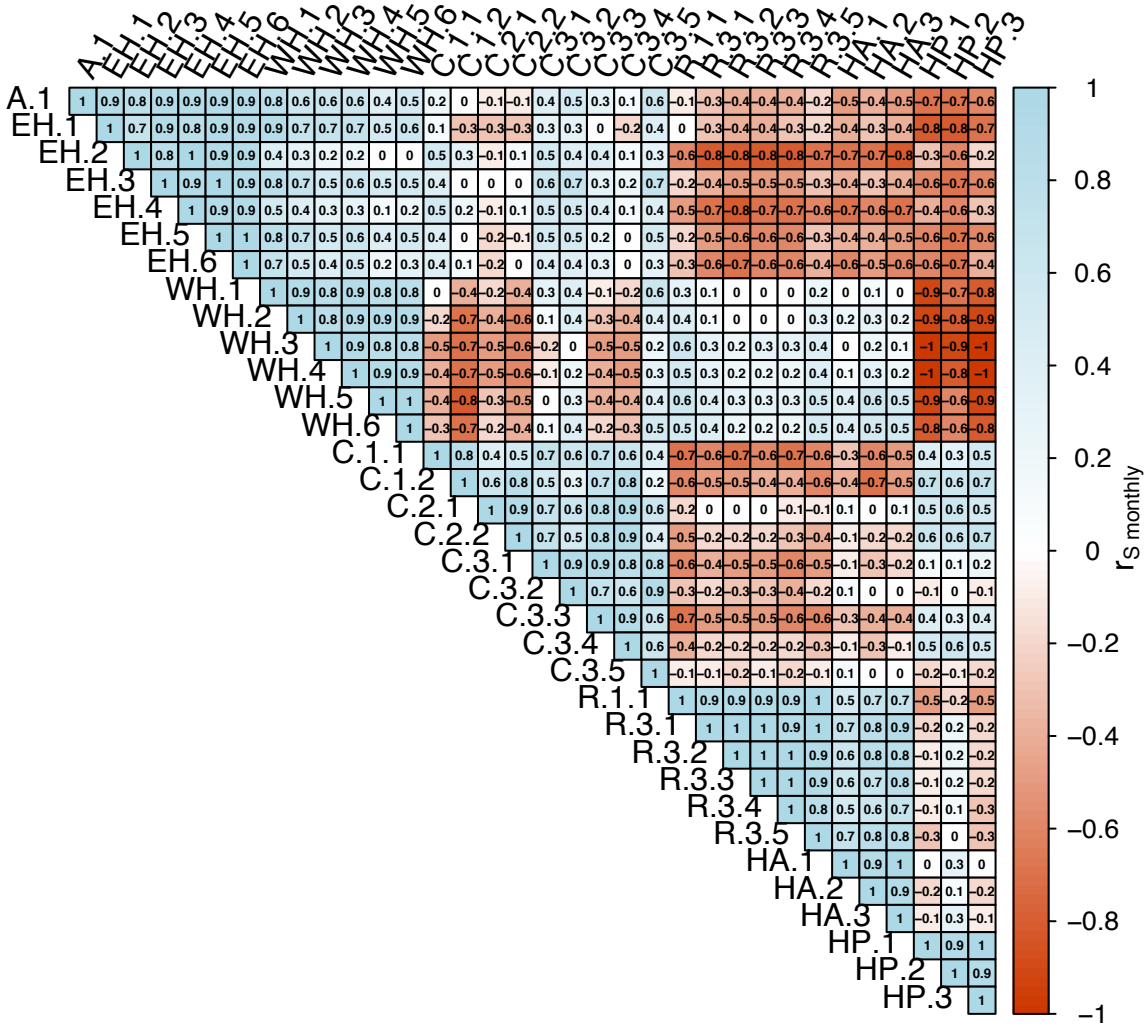

Fig. 4-4. Spearman correlation coefficient matrix of monthly time series of GHI at the representative sites of each solar subregions (A.1, EH.1–EH.6, WH1–WH6, C.1.1–C.3.5), wind speed at the representative sites of each wind subregions (R.1.1, R.3.1–R.3.5), and river discharge at gauging stations in the Amazon basin (HA.1–HA.3) and Pacific basin (HP.1–HP.3).

Taking a look into the normalized monthly time series, the intra-annual complementarity and similarity between the different resources is more evident. Note that the time series are normalized by dividing them by the mean value. From Fig. 4-5, it is clear that the low availability of water resources in the Amazon basin during October–March can be compensated with solar resources from subregions on the coast (C.1.1–C.1.2) that show high GHI values during November–April and in September, or from subregions in the Eastern Andean highlands (EH.2, EH.4, EH.6) that show high GHI values during September–December.

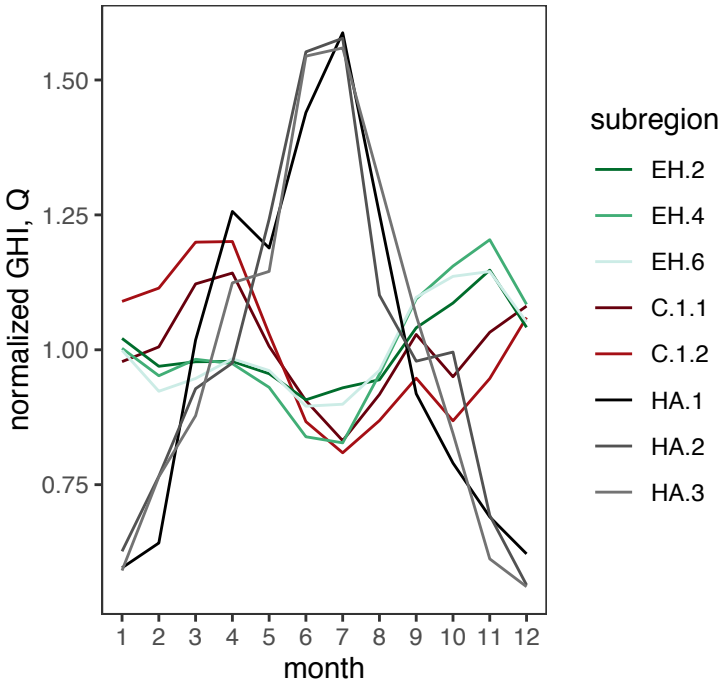

Fig. 4-5. Normalized monthly time series of strong complementary pairs between river discharge (Q) at stations in the Amazon basin and global horizontal irradiance (GHI) at the representative sites of each solar subregion.

In the case of the Pacific basin, river discharge at HP.3, located in the eastern highlands, shows an almost perfect complementarity to GHI in WH.3, located in the western highlands, since both time series are six months lagged (Fig. 4-6a). The time series of the subregions with a strong complementarity to river discharge in the Pacific basin are shown in Fig. 4-6b. From this figure, it can be observed that the low availability of water resources during June–November can be compensated with solar resources in both sides of the Andean highlands and in the Amazon (A.1, EH.1, EH.3, EH5, EH.6 and WH.1–WH.6). From Fig. 4-6c, it is observed that wind speed from all wind subregions have a moderate complementarity to water resources in the Pacific basin. The compensation occurs from June to October, while during November and December both wind and water resources are low.

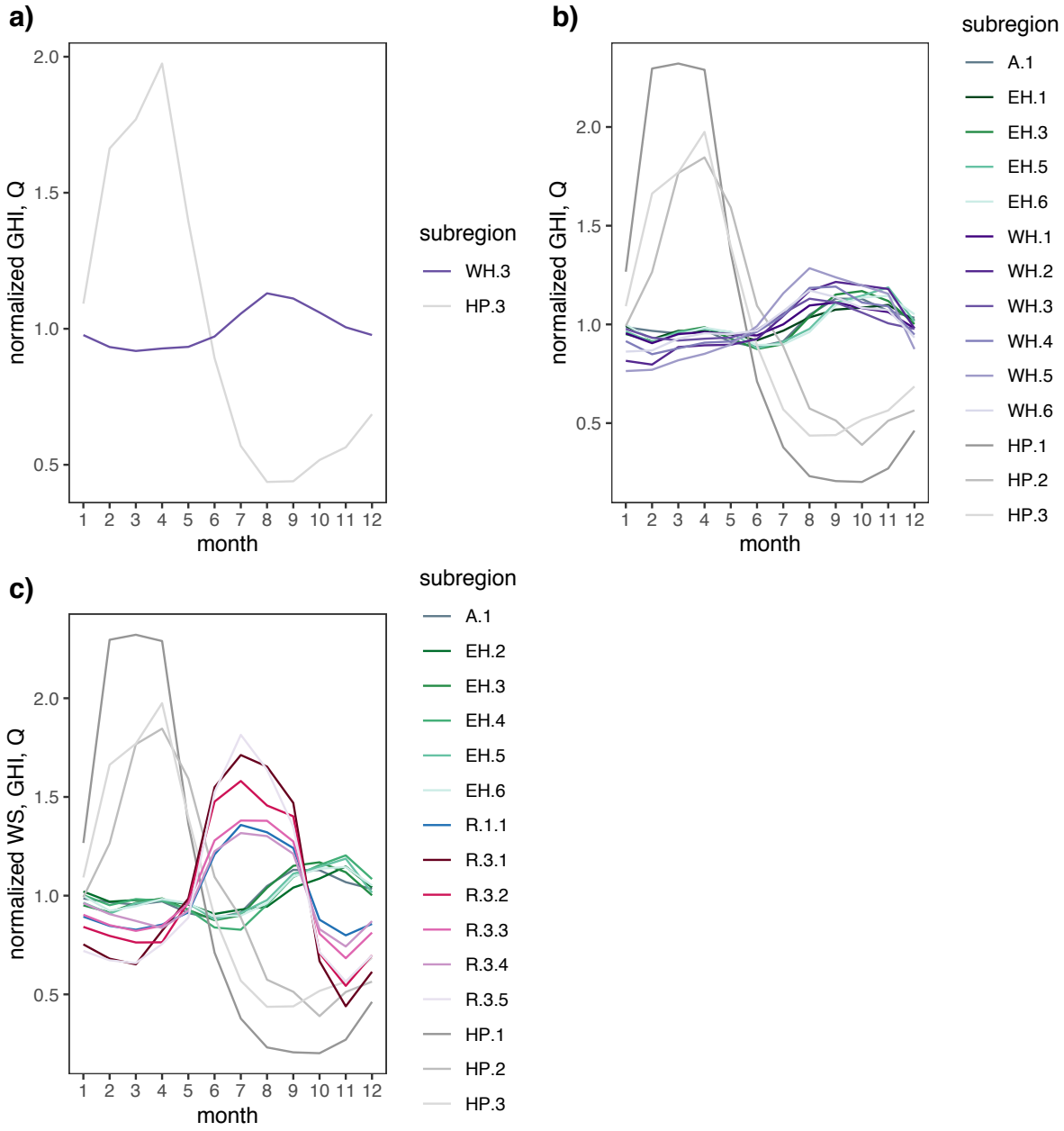

Fig. 4-6. Normalized monthly time series of river discharge (Q) at stations in the Pacific basin, global horizontal irradiance (GHI) and wind speed (WS) at the representative sites of each solar and wind subregion. a) Very strong complementary pairs, b) strong complementary pairs, and c) moderate complementary pairs.

Regarding the complementarity and similarity of wind and solar resources among the different subregions, it is found that wind speed in subregions R.1.1 and R.3.1–R.3.5 has a strong complementarity with GHI in subregions EH.2, EH.4, C.1.1, C.1.2, and C.3.3 (Fig. 4-7a). The low availability of wind resources during November–May can be compensated with solar resources from the aforementioned subregions. Strong similarities are seen between wind speed in subregions R.1.1 and R.3.1–R.3.5 and GHI in subregions WH.3–WH.6 (Fig. 4-7b).

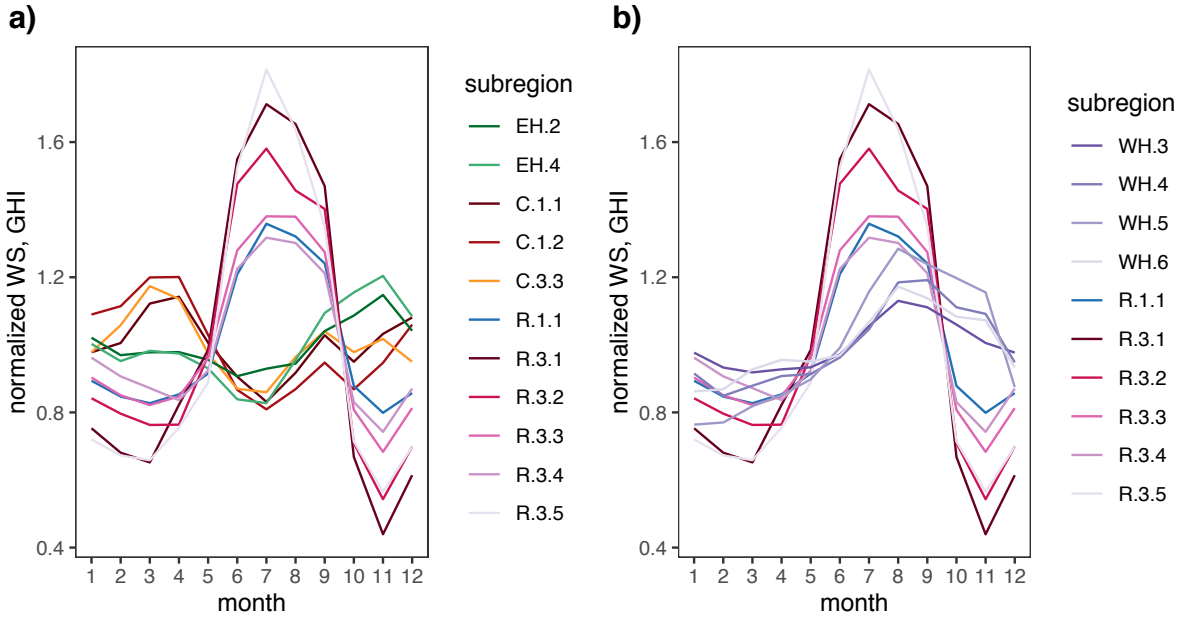

Fig. 4-7. Normalized monthly time series of global horizontal irradiance (GHI) and wind speed (WS) at the representative sites of each solar and wind subregion, showing: a) strong complementary pairs and b) strong similarity pairs.

Another important complementary behavior, as previously seen in Chapter 2, Section 2.3.3, is that GHI from subregions C.1.2 and C.2.2 on the coast shows a strong complementarity with GHI in subregions WH.1–WH.6 in the western Andean highlands, as displayed in Fig. 4-8.

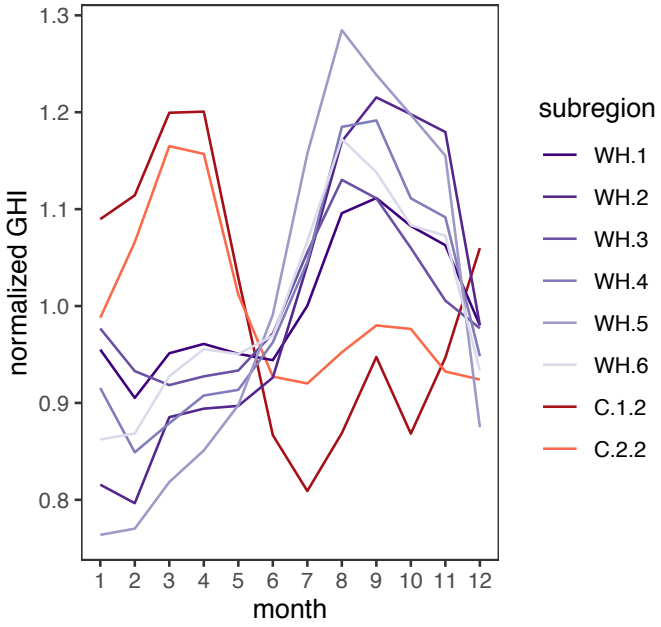

Fig. 4-8. Normalized monthly time series of strong complementary pairs among global horizontal irradiance (GHI) at the representative sites of each solar subregion.

Turning now to the results of the correlation analysis using daily time series, displayed in Fig. 4-9 and Fig. 4-10, it is seen that the Pearson and Spearman correlation coefficients slightly change compared to the resulting values using the monthly time series. Nevertheless, there are still marked complementarities and similarities between the different resources. Similar to the analysis at monthly timescale, the relationship between the time series seems to be linear, since for 84% of the pairs $r_{P_{daily}} \geq r_{S_{daily}}$. Thus, the following sections will only refer to the Pearson correlation coefficient results.

Strong complementarities at daily timescale are seen between river discharge at stations HA.2 and HA.3 in the Amazon basin and GHI in subregion EH.4. In the Pacific basin, strong complementarities are seen between river discharge at HP.1–HP.3 stations and GHI in subregions WH.1–WH.6. Similar to the analysis of the monthly time series, the correlation coefficient between daily time series of river discharge at gauging stations in both basins is low ($-0.2 \leq r_{P_{daily}} \leq 0.2$).

Strong similarities are seen between discharge at stations in the Amazon basin and wind speed in subregions R.1.1 and R.3.1–R.3.5. The similarity level between discharge at stations in the Pacific basin decreases compared to that at monthly timescale. Nevertheless, strong similarities are seen between discharge at the three stations and GHI in subregions C.1.1, C.2.1–C.2.2 and C.3.3–C.3.4. The correlation between discharge at stations of the same basin also decreases compared to that at monthly timescale and range between $0.7 \leq r_{P_{daily}} \leq 1$, still showing a strong similarity.

Regarding the correlation of wind and solar resources at daily timescale, wind speed in subregions R.1.1, R.3.1–R.3.2 and R.3.5 shows a strong complementarity to GHI in subregions EH.4 and C.1.1–C.1.2. Strong similarities are only seen between wind speed in subregion R.1.1 and GHI in subregion WH.5.

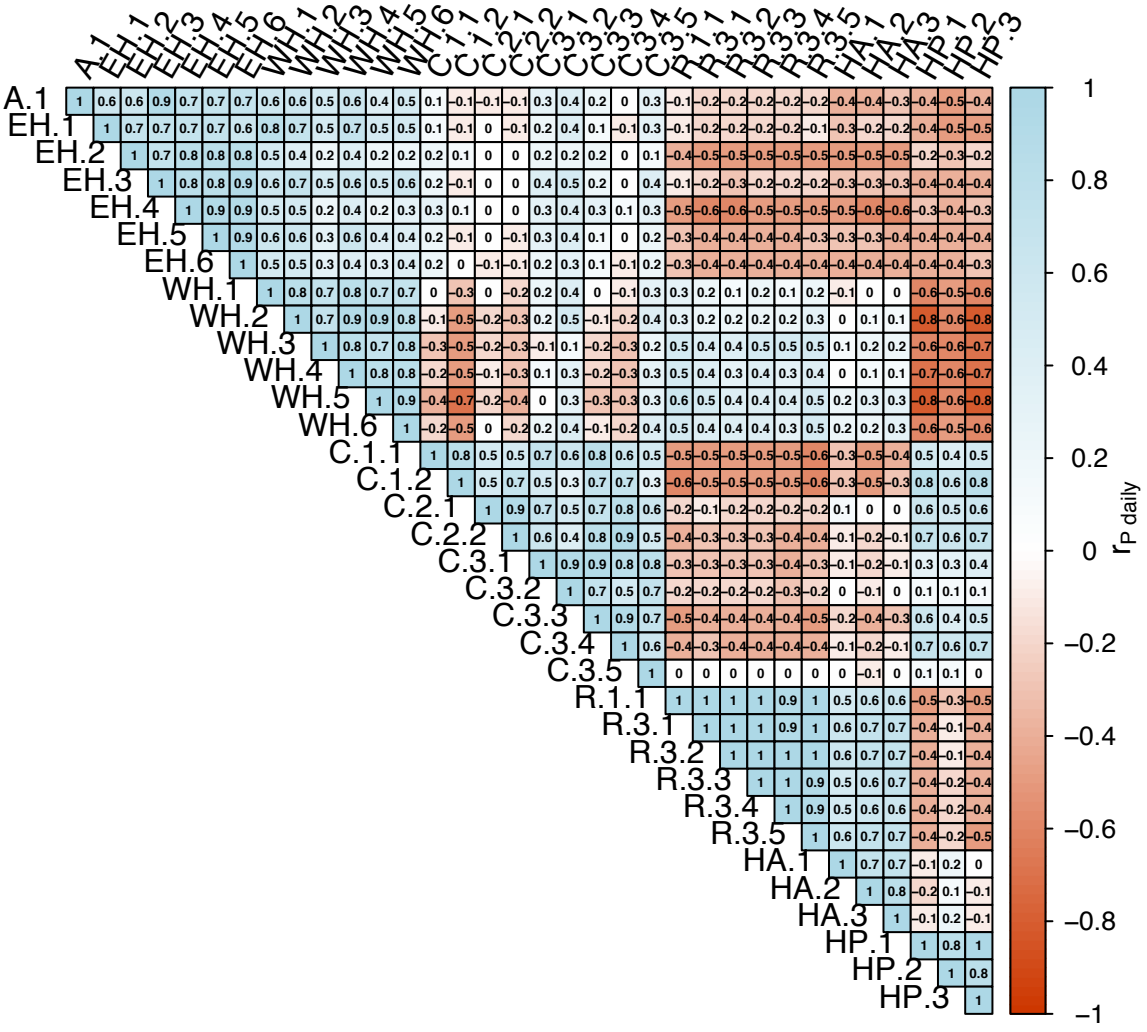

Fig. 4-9. Pearson correlation coefficient matrix of daily time series of GHI at the representative sites of each solar subregions (A.1, EH.1–EH.6, WH1–WH6, C.1.1–C.3.5), wind speed at the representative sites of each wind subregions (R.1.1, R.3.1–R.3.5), and river discharge at gauging stations in the Amazon basin (HA.1–HA.3) and Pacific basin (HP.1–HP.3).

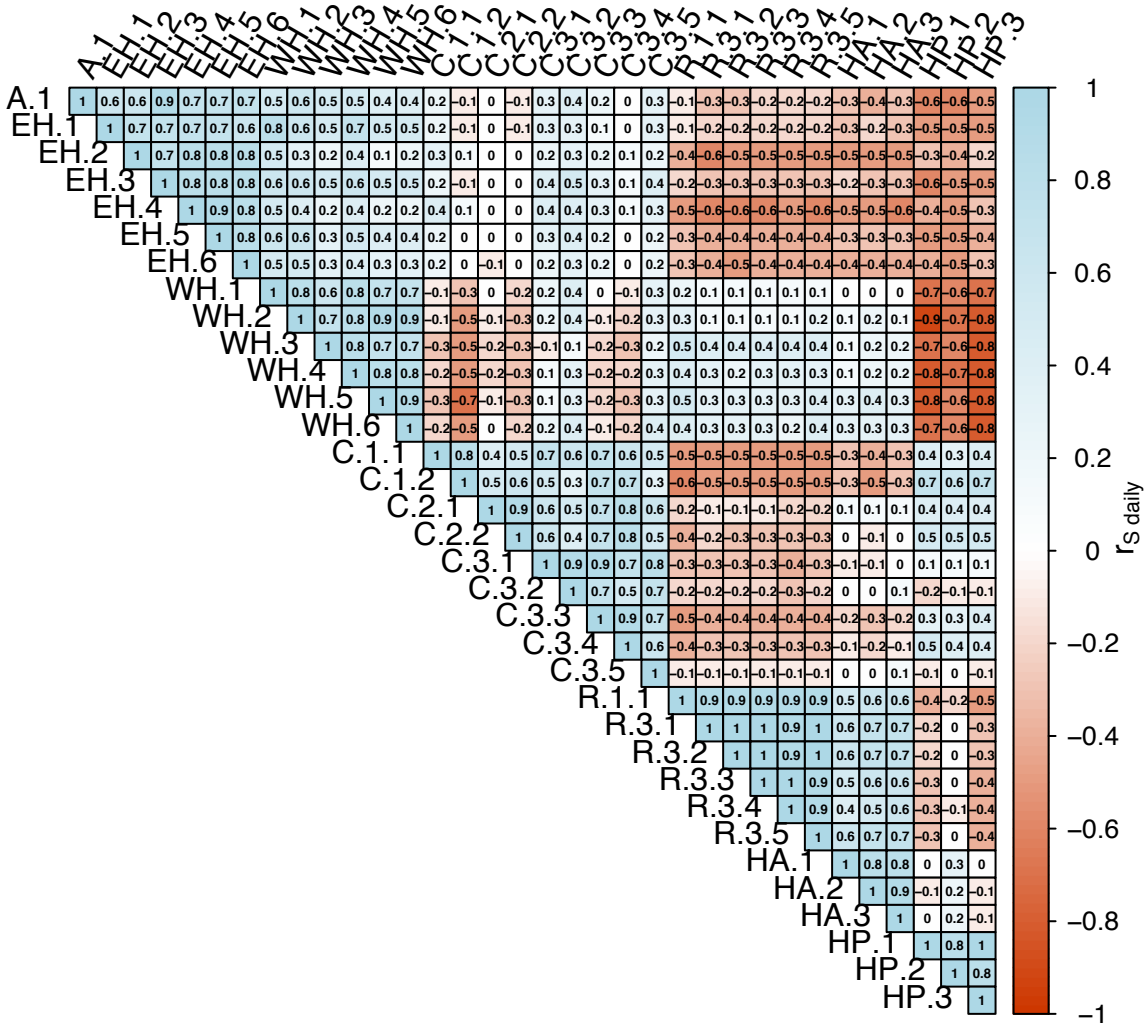

Fig. 4-10. Spearman correlation coefficient matrix of daily time series of GHI at the representative sites of each solar subregions (A.1, EH.1–EH.6, WH1–WH6, C.1.1–C.3.5), wind speed at the representative sites of each wind subregions (R.1.1, R.3.1–R.3.5), and river discharge at gauging stations in the Amazon basin (HA.1–HA.3) and Pacific basin (HP.1–HP.3).

4.3.1.2. Spatio-temporal correlations of solar and wind resources in the Galapagos Islands

For the Galapagos Islands, only the spatio-temporal correlations between solar and wind resources at the representative grid points of the solar and wind subregions are evaluated, because there is no hydropower capacity installed in the islands. The results of the Pearson and Spearman correlation coefficients using monthly time series are shown in Fig. 4-11a and Fig. 4-11b. Strong and moderate complementarities are observed between GHI in subregions G.1.2–G.1.3 and wind speed in subregion R.4.1. From the monthly time series displayed in Fig. 4-11c, it is clear that wind and solar resources compensate each other during January–May and June–August, while during the other months both resources have a similar behavior.

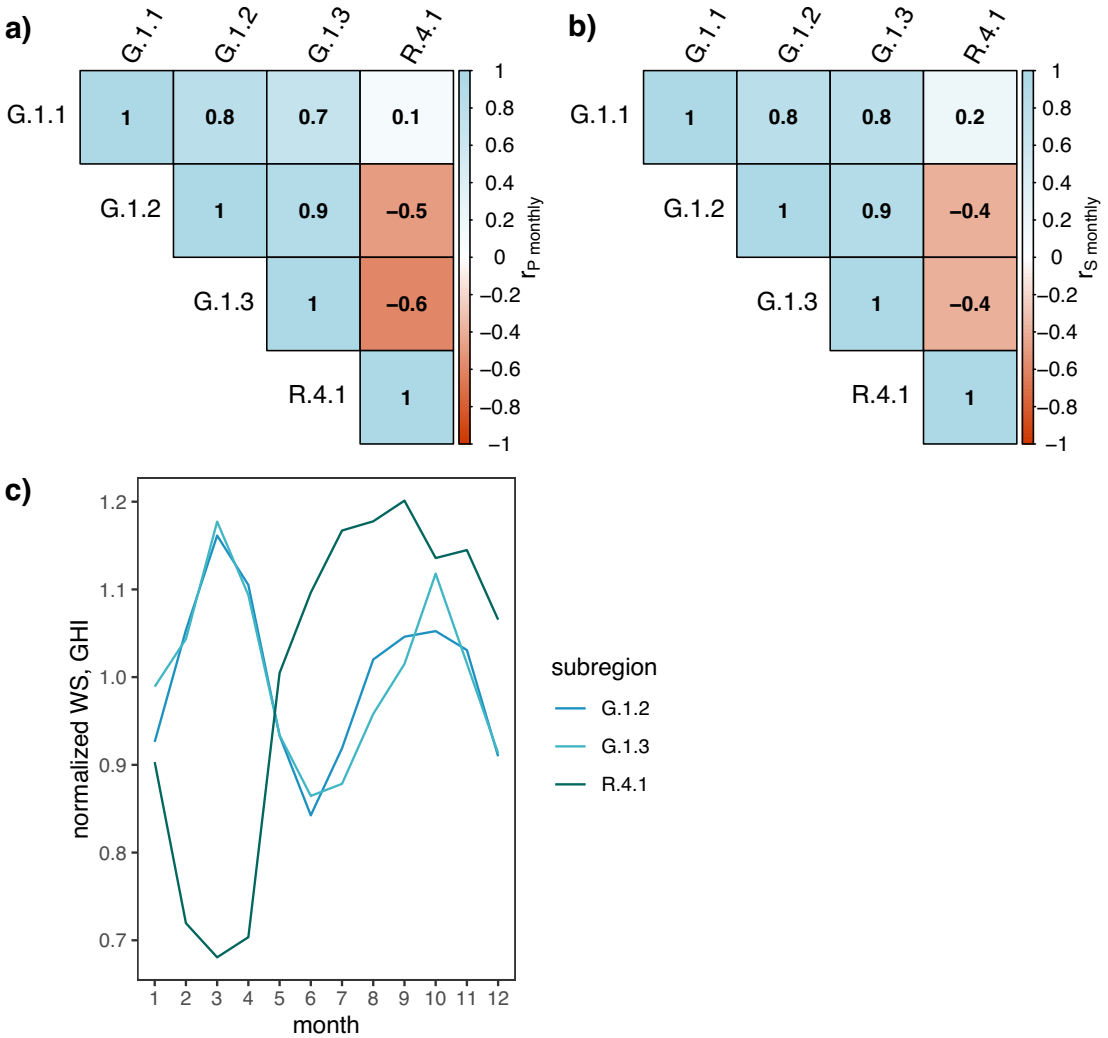

Fig. 4-11. Spatio-temporal correlations of solar and wind resources in the Galapagos Islands. a) Pearson correlation coefficient $r_{P_{monthly}}$ and b) Spearman correlation coefficient $r_{S_{daily}}$ matrices of monthly time series of global horizontal irradiance (GHI) and wind speed (WS) at the representative sites of each solar subregions (G.1.1–G.1.3) and the wind subregion R.4.1 in the Galapagos Islands. c) Normalized monthly time series of GHI and WS at the representative sites of solar subregions (G.1.1–G.1.3) and the wind subregion R.4.1.

4.3.2. Temporal correlation of renewable resources

This next section presents the results of the pairwise correlations at the same grid point. In Ecuador's mainland the pairwise correlation between GHI, wind speed, and precipitation is calculated, while in the Galapagos Islands only the correlation between GHI and wind speed is calculated.

4.3.2.1. Temporal correlation of solar, wind, and water resources in Ecuador's mainland

The spatial distribution of the correlation coefficients between GHI and precipitation at monthly and daily timescales is shown in Fig. 4-12a-b. Similar patterns are observed in both maps with the only difference that correlation values at a daily timescale are lower than the values at a monthly timescale. A marked longitudinal gradient is observed from the coastal lowlands (positive correlations) towards the western flanks of the Andes up to 1000 m.a.s.l. (negative correlations). Another gradient is observed from the western highlands (negative correlations) towards the drainage divide between the Pacific and Amazon basins along the Intra-Andean valleys (positive correlations). Then, negative correlations continue from the eastern highlands towards the Amazon lowlands. Translating the negative correlations into complementarity levels shows that a strong complementarity ($-0.75 \leq r \leq -0.6$) exists between GHI and precipitation along the western Andean highlands, which corresponds to the Pacific basin and to the solar subregions WH.1–WH.6. This pattern is reflected in the correlation values from the spatio-temporal correlation analysis that uses river discharge at gauging stations HP.1–HP.3 in the Pacific basin (see Fig. 4-9).

The spatial distribution of the correlation coefficients between wind speed and precipitation at monthly and daily timescales is shown in Fig. 4-12c-d. Again, similar patterns are observed in both maps with the only difference that correlation values at a daily timescale are lower than the values at a monthly timescale. From the maps, it is observed that a large percentage of Ecuador's mainland (82.5 %) has negative correlation values. Translating the negative correlations into complementarity levels shows that a strong complementarity ($-0.85 \leq r \leq -0.6$) between wind speed and precipitation is observed over the coastline, the coastal inland low valley, and the northwestern highlands, which corresponds to the Pacific basin and to the wind subregions R.1.1 and R.3.5. This pattern is reflected in the correlation values from the spatio-temporal correlation analysis that uses river discharge at gauging stations HP.1–HP.3 in the Pacific basin (see Fig. 4-9). Surprisingly, the strong similarity observed between wind speed at

representative grid points in subregions R.1.1 and R.3.1–R.3.4 and discharge at gauging stations in the Amazon basin from the spatio-temporal correlation analysis, previously seen in Fig. 4-9, is not reflected in the temporal correlation analysis displayed in Fig. 4-12c. This may be due to the fact that there is a delay between precipitation and discharge that varies from one to two months in larger basins in the Amazon (Laraque et al., 2007). As mentioned before, the correlation analysis using the river discharge records is preferred for these areas.

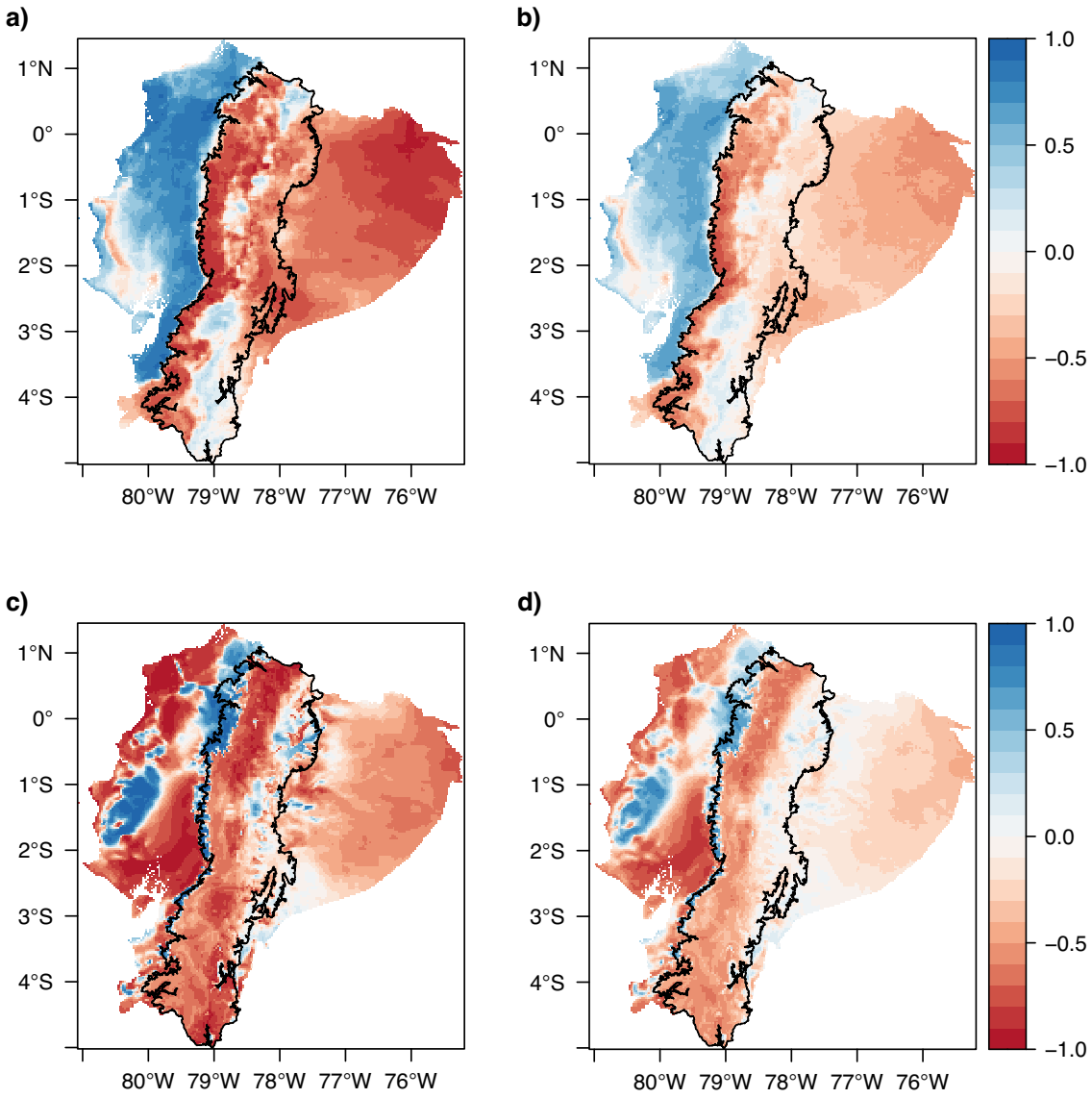

Fig. 4-12. Spatial distribution of correlation coefficients between GHI and precipitation at each grid point in Ecuador's mainland at monthly (a) and daily (b) timescales. Likewise, spatial distribution of correlation coefficients between wind speed and precipitation at each grid point in Ecuador's mainland at monthly (c) and daily (d) timescales. Grid resolution 3 × 3 km. The black line depicts the altitudinal contour at 1000 m.a.s.l.

The results of the temporal correlation analysis between GHI and wind speed at monthly and daily timescales are shown in Fig. 4-13a-b. Similar to previous figures, same patterns are observed with the only difference that correlation values at a daily timescale are lower than the values at a monthly timescale.

It is found that 40.5 % of the area in Ecuador's mainland shows negative correlations. However, excluding grid points with WPD lower than 100 Wm^{-2}, the area is reduced to 4.7% (11,430 km^2), located over the Andean highlands.

Another notable result is that there exists an overlap of grid points with negative correlation between wind speed and precipitation (Fig. 4-12c-d) and grid points with negative correlation between wind speed and GHI (Fig. 4-13a-b), especially over the coastline and the coastal inland low valley. This implies that wind speed at the grid points in these areas is complementary in time with both precipitation and GHI. Nevertheless, it must be noted that WPD over the coastal area is lower than 100 Wm^{-2}, which means that wind resources are too low to be exploited.

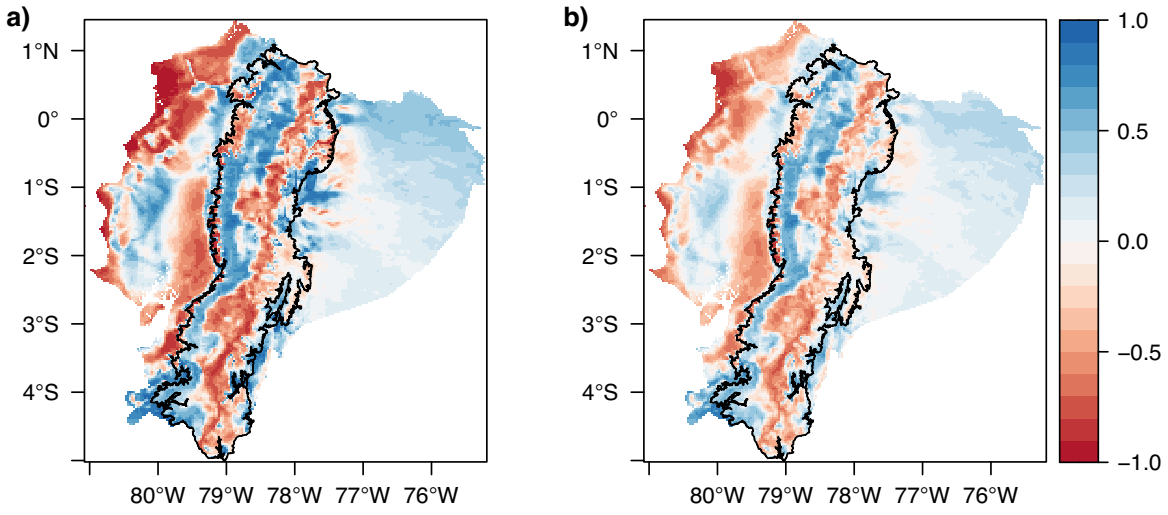

Fig. 4-13. Spatial distribution of correlation coefficients between GHI and wind speed at each grid point in Ecuador's mainland at monthly (a) and daily (b) timescales. Grid resolution 3 × 3 km. The black line depicts the altitudinal contour at 1000 m.a.s.l.

4.3.2.2. Temporal correlations of solar and wind resources in the Galapagos Islands

The spatial distribution of the correlation coefficients between GHI and wind speed at monthly and daily timescales is shown in Fig. 4-14a-b. Similar patterns are observed with the only difference that correlation values at a daily timescale are lower than at a monthly timescale. Negative correlations are observed over the volcanoes, as well as over the eastern side of the islands. However, excluding grid points with WPD lower than 100 Wm^{-2}, the area with negative correlation values is reduced to 26.5% (2088 km^2). This area corresponds to wind subregion R.4.1 (see Fig. 3-12 in Chapter 3). The complementarity behavior is driven by the intra-annual variability of wind speed and GHI, as seen in Fig. 4-11.

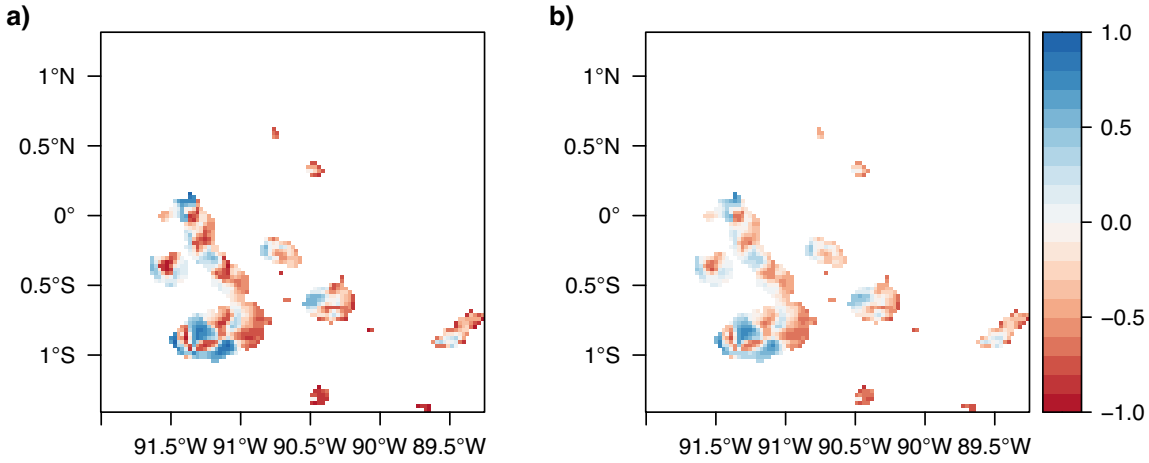

Fig. 4-14. Spatial distribution of correlation coefficients between GHI and wind speed at each grid point in the Galapagos Islands at monthly (a) and daily (b) timescales. Grid resolution 3 × 3 km.

4.4. Discussion

This chapter demonstrates the advantage of using the sFDA regionalization method to select the representative solar and wind sites for the correlation analysis between different renewable resources in a country with limited and unevenly-distributed meteorological stations.

The sFDA regionalization method applied to the long-term gridded datasets of GHI and wind speed identifies subregions that share similar intra-annual variability patterns of each resource. The geographical location of the median curve of each subregion, which is considered the most characteristic temporal pattern of the subregion (see Fig. 2-5, Fig. 2-6,

Fig. 2-7, Fig. 3-10, and Fig. 3-12), is selected as representative site for the spatio-temporal correlation analysis. In this way, even if the number of correlation pairs is reduced, the solar and wind resources over the complete study area are considered, since each representative site already characterizes the temporal variability of the resource over a specific spatial area.

This approach has a significant advantage compared to previous studies. For instance, Cantão et al (2017) evaluated the complementarity between water and wind resources in Brazil by means of correlation maps elaborated from Voronoi diagrams. The authors used the geographical location of meteorological stations from a widespread measurement network to divide the study area into Voronoi cells. However, the limitation of such an approach is that assuming that the time series of the meteorological station "could represent all the points inside its corresponding Voronoi cell is a strong approximation" (Cantão et al., 2017, p. 1217). A similar approach was used by Jara (2018) to analyze the complementarity of solar and water resources in Ecuador. The author used the geographical location of existing and hypothetical PV plants to generate the Voronoi cells. However, due to the uneven spatial distribution of the considered PV plants, some of the resulting Voronoi cells covered large spatial areas from the Ecuadorian coast to the Amazon, without reflecting the spatial variability of the solar resource in the country. In contrast, as described in Chapter 2 and Chapter 3, the data-driven sFDA regionalization method captures the variabilities of GHI and wind speed due to microclimate and topographical effects, consequently, all points inside the resulting subregions share similar temporal variability patterns. Furthermore, the analysis performed in this chapter is not limited to the solar and wind resources of the specific geographical location of existing meteorological stations or power plants, but by using the sFDA regionalization method, the solar and wind resources of the entire study area are considered.

The methodology outlined in this chapter is used to achieve two objectives: (i) to investigate the potential of solar and wind resources to compensate in time and space existing and planned hydropower plants in Ecuador's mainland, and (ii) to assess the potential for the deployment of local hybrid and complementary renewable power systems in Ecuador's mainland and the Galapagos Islands.

Concerning the first objective, the results suggest that the deployment of solar and wind power over geographically-dispersed sites that show complementary variability patterns can smooth out the seasonal variability of water resources to a large degree. This finding has significant implications for developing strategies to expand the solar and wind power capacity that could compensate hydropower during the dry periods in both basins. Thus,

displacing the current – and planned – fossil fuel thermal power capacity that is used to meet the electricity demand during the dry periods.

The spatio-temporal correlation analysis also reveals that the complementarity level between water resources in the Pacific and Amazon basins is very low. Water resources from both basins complement each other only during February–April and May–August. This aspect has been already taken into account in previous Ecuadorian generation capacity expansion plans (CONELEC, 2013). The government planned to increase the hydropower capacity in the Pacific basin to take advantage of the so called "quasi-complementary" behavior of water resources in both basins (CONELEC, 2013, p. 178). Two of the planned projects have already started operations: *Manduriacu* (50 MW) in 2016 and *Minas San Francisco* (275 MW) in 2018 (ARCERNNR, 2020). However, the third planned hydropower project in the Pacific basin, *Toachi-Pilatón* (254.4 MW), is still on hold due to technical and financial problems (CGE, 2020; IHA, 2022), consequently, delaying the important expected contribution of this project to supply electricity during the dry season in the Amazon basin.

Another important finding concerns the similar temporal variability patterns between solar, wind, and water resources found in Ecuador's mainland. This characteristic suggests that solar and/or wind power projects could be planned instead of hydropower projects. Large hydropower projects generally imply environmental and social impacts (Anderson et al., 2018). Additionally, these kind of projects may also experience serious delays and cost overruns (Ansar et al., 2014; Sovacool et al., 2014), as mentioned above. Therefore, these issues could be prevented by expanding the solar and/or wind power capacity in sites that have similar intra-annual variability patterns to the hydrological regime in both basins.

Regarding the second objective, the pairwise correlation maps between GHI, wind speed, and precipitation show the great extent of the complementarity between the resources. This finding suggests that the potential to develop local hydro-solar-wind hybrid and complementary power systems could be further explored. It is important to bear in mind that although gridded precipitation data is found to be useful for analyzing the relationships to solar and wind resources at each grid point, hydropower potential is not available in all grid points, since it depends on effective inflow and available head. Thus, a hydrological model that converts precipitation to streamflow in selected catchments would be necessary for further analysis.

4.5. Conclusions

This chapter assesses for the first time the temporal and spatio-temporal correlations between renewable resources in Ecuador for two objectives: (i) to investigate the potential of solar and wind resources to compensate in time and space existing and planned hydropower plants in Ecuador's mainland, and (ii) to assess the potential for the deployment of local hybrid and complementary renewable power systems in Ecuador's mainland and the Galapagos Islands.

Results show that there are strong spatio-temporal complementarities between solar, wind, and water resources in Ecuador's mainland. This implies that geographically-dispersed solar and wind power plants can compensate hydropower during the dry periods. The low availability of water resources in the Amazon basin during October–March can be compensated with solar resources from subregions on the coast (C.1.1–C.1.2) that show high GHI values during November–April and in September, or from subregions in the Eastern Andean highlands (EH.2, EH.4, EH.6) that show high GHI values during September–December. In the case of the Pacific basin, the low availability of water resources during June–November can be compensated with solar resources in both sides of the Andean highlands and the Amazon (A.1, EH.1, EH.3, EH5, EH.6 and WH.1–WH.6). It is also found that wind resources over the Andean highlands (R.1.1 and R.3.1–R.3.4) have a moderate complementarity to water resources in the Pacific basin.

In the Galapagos Islands, results show that wind and solar resources compensate each other during January–May and June–August, while during the other months both resources have a similar behavior.

The temporal correlation analysis reveals that local hybrid and complementary power systems have a great potential to be explored. Excluding grid points where wind resources are too low to be exploited, solar and wind resources show a complementary behavior over 4.7% (11,430 km^2) of Ecuador's mainland, and over 26.5% (2088 km^2) of the Galapagos Islands.

The new understanding of the complementarity of renewable resources in Ecuador gained in this chapter will be useful for power sector planners and operators. The regionalization maps, correlation matrixes, and time series plots provide explicit information regarding the spatio-temporal correlations between the different renewable resources. The findings can be used for generation capacity expansion plans, as well as to optimize the operation of water reservoirs and back-up systems.

Sites inside the solar and wind subregions that show strong complementary behavior to water resources can be selected as candidates for further capacity expansion planning. The temporal correlation maps also provide the tools to explore the potential for deploying hybrid and complementary power systems.

From the methodological point of view, this chapter demonstrates the advantages of using the sFDA approach to assess the spatio-temporal correlations between different renewable resources in a country with limited and unevenly-distributed meteorological stations. This approach can be applied to other countries or regions to explore the complementarity of renewable resources or energy yield for a better capacity expansion.

Chapter 5 Spatio-temporal synergies of renewable power generation

While the previous chapter focuses on the spatial and temporal complementarity between solar, wind, and water resources, this chapter further evaluates the power generation complementarity of geographically-dispersed renewable resources. The evaluation focuses on the benefits that the spatio-temporal synergies between PV, wind, and hydropower could provide to the Ecuadorian power supply system. The benefits are assessed in terms of reliability and stability. Results show that the joint operation of wind and solar power systems from different subregions could provide at least up to 5.5% of the combined capacity for 87.5% of the time in a year. It is also found that wind power stabilizes PV output at diurnal timescales during the windy months, suggesting that both technologies could serve as baseload during these months. These findings indicate that generation capacity expansion plans should focus on exploiting the spatio-temporal synergies between renewable resources, which may provide the economic incentive for the deployment of PV and wind power, thus increasing the diversity and enhancing the resilience of the power supply system in Ecuador.

5.1. Introduction

Diversity, redundancy, geographical dispersion, and decentralization of power supply sources are all key resilience-enhancing design principles, which aim at helping the power supply system to be prepared for and to cope with uncertain disturbances (Brand et al., 2017; Gleich et al., 2019; Gößling-Reisemann, 2016; Gößling-Reisemann et al., 2019).

The diversification of the Ecuadorian power mix is mentioned as an important strategy in the latest government generation capacity expansion plan (MERNNR, 2018). However, diversity is more than the number of power supply sources. Diversity is defined as “an evenly balanced reliance on a variety of mutually disparate options” (Stirling, 2010, p. 1625). Thus, diversity includes three interrelated and distinct components: variety (how many different elements), balance (how many of each element), and disparity (how different the elements are from each other) (Biggs et al., 2012; Stirling, 1994, 2007).

Looking at the historical power generation capacity in Ecuador from 2008 to 2020 disaggregated by source in Fig. 5-1, it is noticeable that in spite of the different power supply sources (*variety*), there exists an imbalance due to the high dependence on thermal and hydropower (*balance*). Non-hydro renewables play only a marginal role for the electricity supply. The same tendency is expected to continue in the mid- and long-term (MERNNR, 2018; MICSE, 2016).

Furthermore, there is a high degree of centralization of power generation, since three large-scale hydropower facilities (namely, *Mazar–Paute–Sopladora, Agoyán–San Francisco,* and *Coca Codo Sinclair*) generate a large share of the total electricity in the country (71.5% in 2020 (CENACE, 2021)).

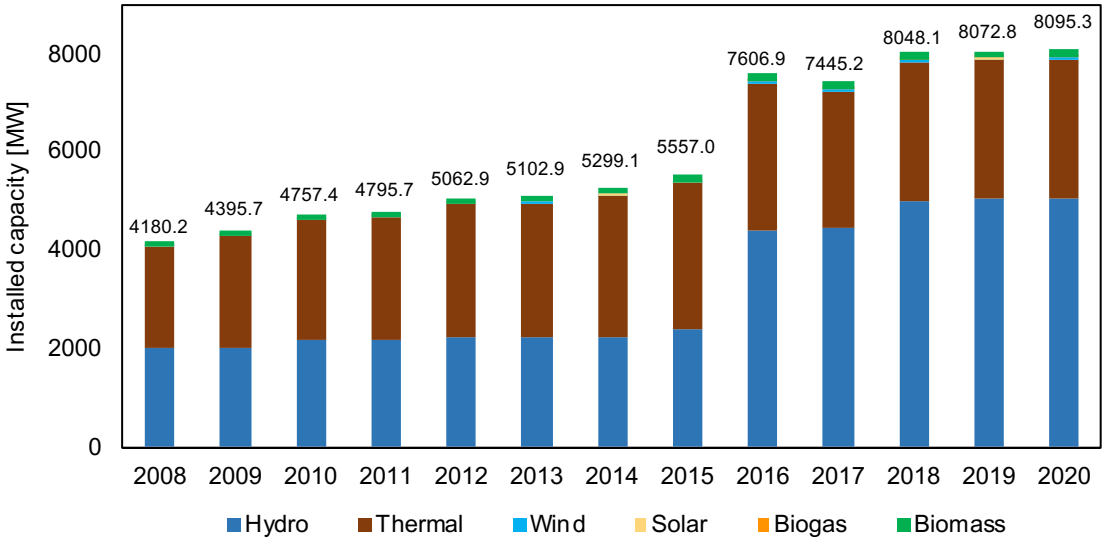

Fig. 5-1. Historical power generation capacity in Ecuador from 2008 to 2020 disaggregated by supply source. Source: Own representation, data from ARCERNNR (2022a).

Disparity is an inherently qualitative attribute that "requires consideration of options in terms such as the similarities of their technical characteristics, the degrees to which they are dependent on each other's infrastructures and the mutual elasticities (or covariance) in the costs of their fuels" (Stirling, 1994, p. 198). In this respect, Fig. 5-2 illustrates the similarities and dissimilarities among the power supply options regarding the type of resource. From the figure, it can be seen that there is already a broad portfolio of power supply options in the Ecuadorian power mix, implying that the challenge is to increase the balance among them. From a resilience perspective, a low balance potentially leads to a higher stability of the system, but at the same time to a lower degree of flexibility and potential for adaptability (Binder et al., 2017).

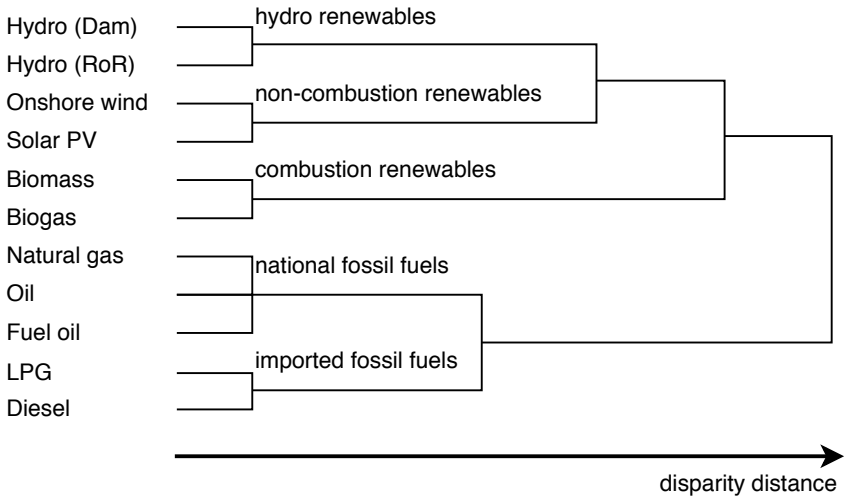

Fig. 5-2. Illustration of the disparity of electricity supply sources of the Ecuadorian power mix in respect to the type of resource. RoR is run-of-river hydropower, Dam is hydropower with reservoir capacity, LPG is liquefied petroleum gas. Source: Own representation based on Stirling (2010)*. Data from* (ARCERNNR, 2021)*.*

The geographical dispersion of power supply options also plays an important role for the resilience of the power system. When system elements are geographically-dispersed, localized stressors, ranging from weather and climate-related events to terrorist attacks, have a relatively smaller attack surface (Gößling-Reisemann et al., 2019). In this regard, the deployment of hydropower plants in both the Amazon and the Pacific basins, which have anticorrelated hydrological regimes, have shown the beneficial effect of the use of geographically-dispersed water resources in Ecuador to reduce the power output variability, at least for some months (see Fig. 4-1 in Chapter 4). However, the potential benefits of the joint operation of geographically-dispersed PV and/or wind power systems across the country has not been evaluated yet.

An important question that arises is, what is the potential to increase the share of geographically-dispersed wind and solar power in the Ecuadorian power mix to achieve a more diversified and decentralized power system? As an initial point to tackle this question, this chapter aims at assessing – from an energy meteorology perspective – the spatial and temporal synergies of geographically-dispersed PV and wind power systems. The assessment focuses on the benefits that these synergies could provide to the Ecuadorian power system in terms of reliability and stability. The ability of the combined PV and wind power to complement the intra-annual power output variability of existing hydropower plants is also evaluated.

To capture the benefits associated with geographical smoothing of aggregated wind or PV power outputs, spatially and temporally resolved solar and wind resource datasets are required. For this reason, the results from the previous chapters are the basis for the

assessment. First, the hourly time series of solar and wind resources at selected sites with high potential in each solar and wind subregion are converted into power output. Then, the benefits of the joint operation of geographically-dispersed PV and wind power systems are assessed by looking at two metrics: (i) reliability, in terms of the amount of firm capacity that the joint operation could provide for a certain percentage of hours per year, and (ii) stability, in terms of the reduction of the power output variability of a combined system as compared to a system comprising only one technology. The latter metric is assessed at two different timescales: intra-day for the case of the joint operation of PV with wind power and intra-annual for the case of the combination of PV or wind power with hydropower.

This chapter is structured as follows. Section 5.2 describes the methods and data used in this chapter in different subsections: (5.2.1) describes the methodology used for the selection of the sites with high potential in each solar and wind subregion; (5.2.2) and (5.2.3) describe the power modeling tools used to simulate PV and wind power output at each site; (5.2.4) presents the hydropower data used for the assessment; and (5.2.5) describes the methodology for the analysis of the joint operation of renewable power plants. Then, Section 5.3 presents the results of the analysis, which are then discussed in Section 5.4. Finally, Section 5.5 presents the conclusions of this chapter.

5.2. Methods and data

5.2.1. Geographical assessment of wind and solar potential

A Geographic Information System (GIS) approach is used to determine the geographical area available for the deployment of utility-scale solar and wind power farms. This approach consists of applying a set of restriction criteria with buffer distances to exclude non-suitable areas. For simplicity, this study is limited to restrictions concerning safety and ecological constraints that are grouped into three categories: infrastructure, water bodies, and protected areas (Table 5-1). The GIS datasets used for this purpose were retrieved as vector layers from publicly available sources (see Table C-1 in Appendix C).

The software QGIS version 3.16 (QGIS Association, 2022) is used for the processing of the GIS datasets. First, the buffer distances are added to each vector feature (point, line or polygon) and then the vector layers are converted into raster layers with a binary logic for each grid cell to represent suitable and non-suitable areas.

The grid resolution of each raster layer is then set at 3×3 km, which is determined by the solar and wind resource datasets described in Chapter 2 and Chapter 3. Next, a binary

overlapping of the processed layers is applied to obtain a raster map comprising those grid cells suitable for the deployment of utility-scale solar and wind power farms.

The resulting suitable grid cells from the raster map are then grouped by the solar and wind subregions to select a representative site for each subregion. Since the interest of this chapter is to assess the PV and wind power that could be generated at sites with high resources, the selected grid cells are those showing the highest long-term annual mean daily total GHI within each solar subregion and the highest long-term annual mean wind power density within each wind subregion.

Table 5-1. Constraint layers and buffer distance applied to select suitable areas for the deployment of utility-scale solar and wind power plants. Sources: see Table C-1 in Appendix C.

Category	Constraint	Buffer distance [m]	Reference
Infrastructure	Urban areas	500, 1000 or 1500 [1]	Latinopoulos and Kechagia (2015)
	Roads	100 [2]	Lütkehus et al. (2013)
	Railways	250 [2]	Lütkehus et al. (2013)
	Airports	1760 or 5000 [3]	Lütkehus et al. (2013)
	Transmission grid	120	Lütkehus et al. (2013)
	Archeological sites	–	Villacreses et al. (2017)
Water bodies	Rivers	65	Lütkehus et al. (2013)
	Lakes	65	Lütkehus et al. (2013)
	Mangroves	65	Lütkehus et al. (2013)
	Reservoirs	65	Lütkehus et al. (2013)
Protected areas	Natural reserves	250	Villacreses et al. (2017)
	Protected forest	250	Villacreses et al. (2017)
	Intangible areas	250	Villacreses et al. (2017)
	Protected biosphere	250	Villacreses et al. (2017)

[1] Latinopoulos and Kechagia (2015) set the buffer distance depending on the population size of the urban area. This criterion is applied to Ecuador based on the type of urban area; thus, the buffer distances are set as follows: for country, province or canton capitals: 1500 m; for parish capitals: 1000 m; and for towns: 500 m.
[2] Distance measured from the center of roads or railways, which are considered as objects of 6 m width.
[3] A radial distance of 1760 m and 5000 m around the runaway is considered for small airfields and big airports, respectively.

5.2.2. Solar PV power model

The *pvlib-python* package (Holmgren et al., 2018) is used to simulate the power output of a solar PV system at each selected solar subregion's site. The input dataset for the simulation comprises hourly time series from 1998 to 2018 of global horizontal irradiance (GHI), diffuse horizontal irradiance (DHI), and direct normal irradiance (DNI) in $[Wm^{-2}]$, wind speed at 10 m AGL in $[m\,s^{-1}]$, and ambient temperature in [℃], which are retrieved from the NSRDB and downscaled to 3 × 3 km (see Chapter 2).

For each site, a solar PV farm of 10 MW DC capacity is simulated. Each PV farm consists of mono-crystalline silicon modules (SPR 220 BLK-U from SunPower) mounted on an open rack. The surface azimuth is set at 90º respect to due north and the tilt angle is

set at 10º, which is the optimal module orientation according to a previous sensitivity analysis of the rooftop PV technical potential in three cities of Ecuador's mainland, reported in Tapia et al. (2022). To account for the system losses, the factor f_{loss} is set at 14%, which is a typical value representing losses due to soiling, shading, mismatch, wiring, connections, light induced degradation, nameplate rating, and operational availability (Dobos, 2014), as well as cable and inverter losses (Bódis et al., 2019). Note that losses due to temperature are not included in f_{loss}, since *pvlib-python* uses a thermal model to predict the associated operating temperature of the PV modules based on the given meteorological dataset (King et al., 2004).

After setting the technical parameters, the simulation of the PV system power output is performed using the object-oriented modeling paradigm of *pvlib-python* (pvlib, 2022). The `PVSystem` object is instantiated with the selected PV module and the predefined tilt and azimuth angles. The Sandia Array Performance Model (SAPM) (King et al., 2004) is selected to model the electrical performance of the PV modules. The temperature of the PV modules and cells are modeled assuming an open rack mounting configuration (King et al., 2004). The Hay-Davies model (Hay et al., 1980) is selected as the irradiance transposition model to get the plane of array irradiance components.

Then, an instance of the `ModelChain` class is created with the geographical coordinates of the site (s) and the previously defined `PVSystem` object. Next, the model is run with the hourly meteorological data of site (s). In this step, the SAPM model simulates the characteristic current-voltage (*I-V*) curve that determines the output power of a single PV module under the specific meteorological conditions of the site (s). The output is a time series that includes short-circuit current (I_{sc}), open-circuit voltage (V_{oc}), and current, voltage, and power at maximum power point (I_{mp}, V_{mp}, P_{mpp}, respectively).

Subsequently, the total PV power output $P_{PV_{(s)}}(t)$ produced by the PV farm at site (s) and time (t) is calculated according to Equation (5.1):

$$P_{PV_{(s)}}(t) = N_m \cdot P_{mpp_{(s)}}(t) \cdot (1 - f_{loss}) \qquad (5.1)$$

where $P_{mpp_{(s)}}$ is the hourly output power at the maximum power point from the SAPM model, simulated using the meteorological data of site (s) at time (t); N_m is the number the PV modules, and the factor f_{loss} accounts for the system losses.

Then, the hourly PV capacity factors (CF_{PV}) are calculated as the ratio between the hourly PV power output $P_{PV_{(s)}}(t)$ and the total installed capacity of each PV farm at site (s). The process described above is repeated for each solar subregion's site.

5.2.3. Wind power model

The python package *windpowerlib* (Haas et al., 2021) is used to simulate the power output of a 10 MW wind farm at each selected wind subregion's site. The input dataset comprises the hourly time series for the period 2005–2018 from the mesoscale WRF model (see Chapter 3), which includes wind speed in $[m\ s^{-1}]$ and temperature in $[K]$ both at 80 m AGL, surface air density in $[kg\ m^{-3}]$, surface pressure in $[Pa]$, and surface roughness length in $[m]$.

Depending on the long-term annual mean wind speed of each site, one of the three commercial wind turbines listed in Table 5-2 is used to simulate the power output of the wind farm. The power output curves of each wind turbine type are directly retrieved from the turbine type database of *windpowerlib*, then the power output curves are corrected according to the site's specific air density at 80 m AGL using the ideal gas equation (Haas, 2019).

Table 5-2. Long-term annual mean wind speed and wind power density at selected sites in each wind subregion and specifications of the wind turbines used to simulate the power output of a wind farm at each site.

Subregion	Mean wind speed [m s^{-1}]	Mean wind power density [W m^{-2}]	Turbine model (Wind class)	Manufacturer
R.3.1	10.95	1420.06	V112-3.45 (IEC IA)	Vestas
R.3.2	8.63	821.57	V117-3.45 (IEC IIA – IB)	Vestas
R.3.3	5.91	258.34	GE 3.2-130 (IEC IIIA)	General Electric
R.3.4	5.23	186.37	GE 3.2-130 (IEC IIIA)	General Electric
R.3.5	6.54	336.58	GE 3.2-130 (IEC IIIA)	General Electric
R.1.1	4.60	148.72	GE 3.2-130 (IEC IIIA)	General Electric

No height corrections are performed for wind speed or temperature, since the mesoscale WRF model directly provides the data at hub height. The design of the layout of the wind turbines within each site is outside the scope of this study. Nevertheless, the power reduction due to wake losses is estimated in the form of a wind farm efficiency (Haas, 2019). In this study, the wind farm efficiency is set at 90%.

The calculation of the wind power output is performed using the object-oriented modeling paradigm of *windpowerlib* (Haas, 2019). The object `WindFarm` is instantiated with the corresponding wind turbine type and the total installed capacity of the wind farm. Then, an instance of the `TurbineClusterModelChain` class is created with the aforementioned parameters for wake losses and density correction. Next, the model is run with the meteorological data at each site (s). The output is a time series of the wind power output $P_{W_{(s)}}(t)$ of each wind farm located at site (s) and time (t). Then, the hourly wind capacity

factors (CF_W) are calculated as the ratio between the hourly wind power output $P_{W_{(s)}}(t)$ and the total installed capacity of each wind farm at site (s).

5.2.4. Hydropower data

The monthly energy yield records for the period 2005–2018 of two representative hydropower plants are used for the analysis in this chapter. The selected HPPs are: *Agoyán* (named HA.2) of 154 MW capacity, which is located in the Amazon basin, and *Marcel Laniado* (named HP.1) of 213 MW capacity, which is located in the Pacific basin. The records are retrieved from ARCERNNR (2022b). These HPPs are selected because they were in operation during the selected period and their capacity was not expanded during the same time. The other HPPs listed in Table 4-1 in Chapter 4 either started operations later, increased their capacity, or are still under construction.

The monthly hydropower capacity factors (CF_H) of each HPP are calculated as the ratio between the monthly energy yield record and the maximum possible energy that would have been produced operating at its installed capacity over the number of hours of the corresponding month.

5.2.5. Analysis of joint operation of renewable power plants

The benefits that the joint operation of complementary and geographically-dispersed PV and wind power could bring to the power system are assessed using two metrics identified in the literature: firm capacity and stability coefficient.

5.2.5.1. Firm capacity

Firm capacity provides an additional metric of complementarity by quantifying the minimum amount of power output that can be guaranteed for a given percentile of hours per year (Slusarewicz et al., 2018). Following Archer and Jacobson (2007), the percentile threshold is set at 87.5%, which is the average time that coal-fired power plants are operating free from unscheduled or scheduled maintenance in a year. In this sense, the firm capacity metric quantifies the fraction of the combined PV and wind capacity for each pair of sites that could be online to provide renewable power generation at the same probability as that of a coal-fired power plant.

5.2.5.2. Stability coefficient

The stability coefficient C_{stab} (Sterl et al., 2018) is used to quantify the reduction of the power output variability of a hybrid system composed by two renewable energy technologies (x and y) as compared to a system comprising only one technology. This measure considers the strength of the resources through capacity factors CF and is calculated according to Equation (5.2) (Sterl et al., 2018):

$$C_{stab} = 1 - \frac{CV_{CF_{x,y}}}{CV_{CF_x}} = 1 - \frac{\sqrt{\sum_{i=1}^{T}\left(CF_{x,y_i} - \overline{CF}_{x,y}\right)^2}\Big/\overline{CF}_{x,y}}{\sqrt{\sum_{i=1}^{T}\left(CF_{x_i} - \overline{CF}_x\right)^2}\Big/\overline{CF}_x} \tag{5.2}$$

$$CF_{x,y} = \frac{nCF_x + mCF_y}{n+m} \tag{5.3}$$

where, CV_{CF_x} and $CV_{CF_{x,y}}$ are the coefficient of variation of the capacity factors of technology x and combined technologies x and y, respectively; T is the total number of time intervals; $CF_{x,y}$ is the capacity factor of combined technologies; and $\overline{CF}_{x,y}$ denotes the average of the combined capacity factors. $CF_{x,y}$ is calculated according to Equation (5.3), where CF_x and CF_y are the capacity factors of each technology with an installed capacity of n and m, respectively.

By definition, $C_{stab} \leq 1$, with $C_{stab} = 0$ meaning that the hybrid system does not provide benefits in terms of power generation stability compared to the output of only one technology, and $C_{stab} = 1$ denotes that the power output of the combined operation is constant over time (perfect synergy) (Sterl et al., 2018).

In this study, C_{stab} is applied to investigate if wind power from the selected sites could provide diurnal stability to geographically-dispersed combined PV-wind power systems. Thus, the simulated hourly PV and wind power output time series at each site is used. Technologies x and y in Equation (5.2) are PV and wind, respectively.

Additionally, the coefficient C_{stab} is applied to investigate if PV or wind power from the different sites could provide stability to the hydropower output. Since hourly records of hydropower production are not publicly available, the analysis uses the monthly energy yield records of the two selected HPPs and the monthly time series of simulated energy yield of PV and wind power. In this case, technology x in Equation (5.2) is hydropower, and technology y can be PV or wind power.

5.3. Results

5.3.1. Geographical wind and PV potential

After applying the set of restriction criteria described in Section 5.2.1, a total of 15,750 grid cells (out of 27,175) are found to be suitable for the deployment of utility-scale wind and PV power farms. This represents a geographical area of 141,750 km^2, which is about 58% of the total surface area of Ecuador's mainland.

The spatial distribution of the long-term annual mean daily total GHI over the suitable grid cells is shown in Fig. 5-3. This figure also displays the geographical location of the sites that have the highest value within each subregion. It is worth noting that within the subregions A.1 and EH.3 the grid cells with the highest solar radiation are located in remote areas in the Amazon. Since this chapter focuses on assessing the renewable energy potential of geographically-dispersed power plants that could operate together, an additional constraint is applied. This additional constraint allows the identification of the grid cells within subregion A.1 and EH.3 that have high resource potential and are located closer to the interconnected transmission network. The grid cells in these subregions that satisfy the additional constraint are those displayed in Fig. 5-3.

The spatial distribution of the long-term annual mean wind power density (WPD) over the suitable grid cells is shown in Fig. 5-4. This figure also displays the geographical location of the sites that have the highest value within each subregion. Note that the wind subregions included in the analysis are R.1.1 and R.3.1–3.5, since the long-term annual mean WPD of the grid points in these subregions is higher than 100 Wm^{-2}. Another remark is that only suitable grid cells in which the bias of simulated wind speed was corrected (see Chapter 3, Section 3.3.3.2) are included in the selection of the representative sites within the aforementioned subregions. A total of 575 grid cells meets these two conditions (i.e., suitable and bias-corrected) and out of them the sites with the highest wind resource are selected and displayed in Fig. 5-4.

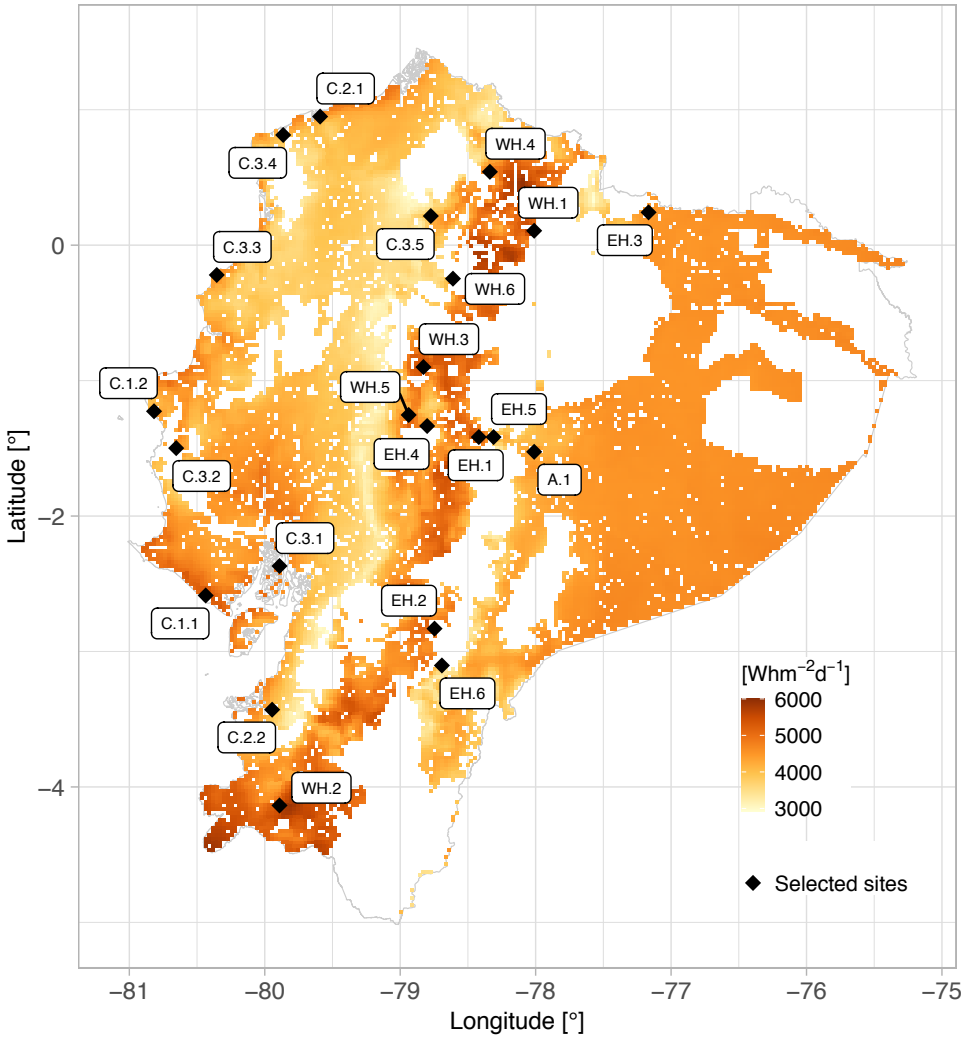

Fig. 5-3. Long-term annual mean daily total GHI of suitable grid cells (3 x 3 km) over Ecuador's mainland for the deployment of utility-scale PV farms after applying the GIS-based selection approach using the constraint layers. The grid cells that have the highest value within each solar subregion are marked in black and labeled according to the subregion's name.

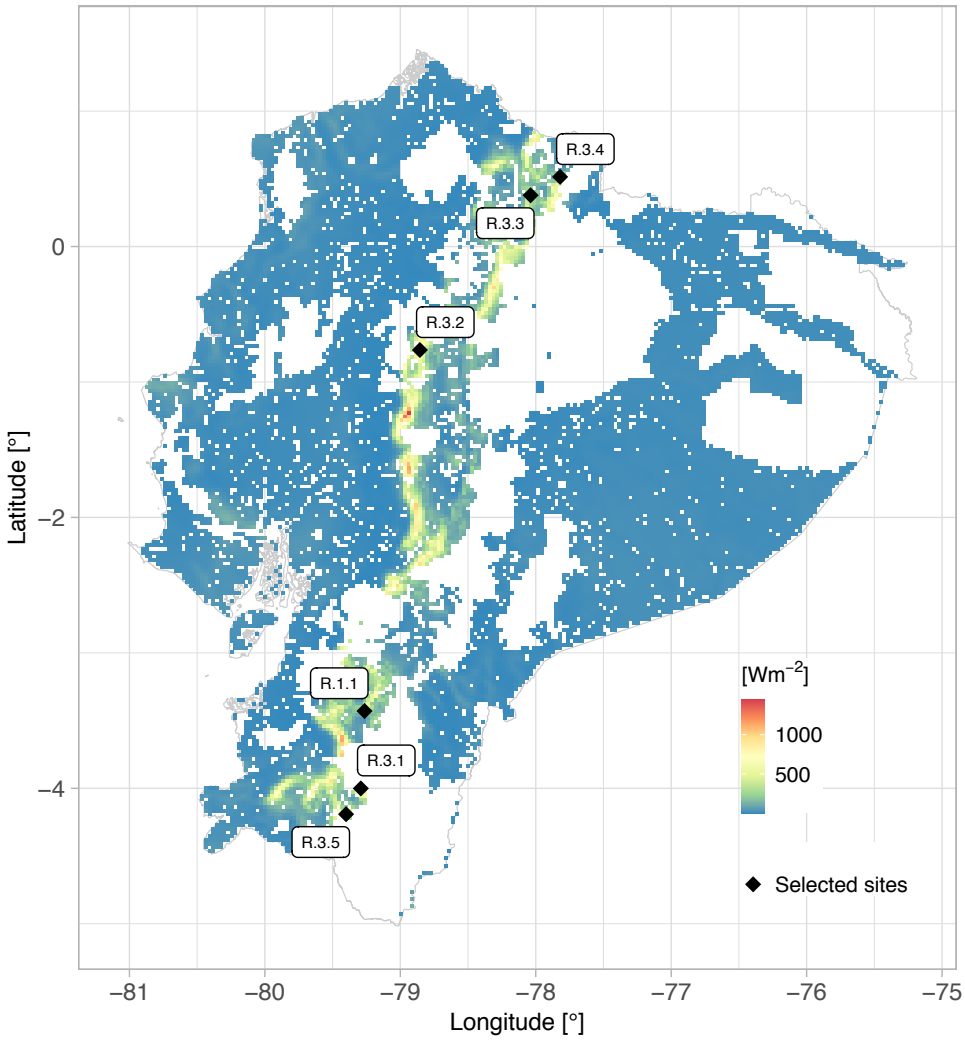

Fig. 5-4. Long-term annual mean wind power density of suitable grid cells (3 x 3 km) over Ecuador's mainland for the deployment of utility-scale wind power farms after applying the GIS-based selection approach using the constraint layers. The grid cells that have the highest value within each wind subregion are marked in black and labeled according to the subregion's name.

5.3.2. PV and wind power output simulation

The hourly time series of meteorological data of the selected sites are used to simulate the power output of a 10 MW solar or wind power farm according to the methods explained in Sections 5.2.2 and 5.2.3.

Table 5-3 provides a summary of the annual mean CF_{PV} and CF_{W} of the simulated PV and wind farms at each subregion's site. What stands out in the table is the high annual mean CF of the wind farm in subregion R.3.1 (52.1 %), which is aligned to the high winds seen in this subregion and already discussed in Chapter 3, Section 3.3.4.1. Regarding the PV farms, the highest annual mean CF_{PV} is seen in WH.1 and EH.1 (~20% both), while the lowest value (12.7%) is seen in subregion C.2.2. These results are also aligned to the difference of GHI magnitude in each solar subregion as discussed in Chapter 2, Section 2.3.1.1.

Table 5-3. Annual mean capacity factors (CF) of simulated PV and wind farms of 10 MW at each solar and wind subregion's site.

Solar								Wind	
Subregion	**CF_{PV} [%]**	**Subregion**	**CF_{PV} [%]**	**Subregion**	**CF_{PV} [%]**	**Subregion**	**CF_{PV} [%]**	**Subregion**	**CF_{W} [%]**
A.1	14.5	EH.1	20.0	WH.1	20.3	C.1.1	16.9	R.1.1	15.9
		EH.2	17.4	WH.2	17.0	C.1.2	14.5	R.3.1	52.1
		EH.3	14.2	WH.3	18.7	C.2.1	13.6	R.3.2	36.8
		EH.4	15.6	WH.4	17.3	C.2.2	12.7	R.3.3	21.9
		EH.5	14.9	WH.5	15.9	C.3.1	15.6	R.3.4	17.5
		EH.6	12.8	WH.6	15.7	C.3.2	14.4	R.3.5	28.6
						C.3.3	14.7		
						C.3.4	12.8		
						C.3.5	13.1		

Looking at the diurnal cycle of CF_{PV} and CF_{W} per month at each site in Fig. 5-5, a noticeable intra-annual variability pattern of wind power is observed. High CF_{W} values are seen during June–September, which is in agreement to the high wind speed in this period, while during the rest of the year CF_{W} values remain low.

Another remarkable observation in Fig. 5-5 is that wind farms in subregions R.3.1 and R.3.2 (also in R.3.5, but to a lesser degree) have CF_{W} values almost constant and high throughout the day during June–September. This fact reveals an intra-day complementary behavior between PV and wind power in these subregions, which will be further quantified in the Section 5.3.4. During the same period, CF_{W} of wind farms in subregions R.1.1 and R.3.3 is high during local daytime (from 10:00 to 23:00 UTC) and decreases at local nighttime.

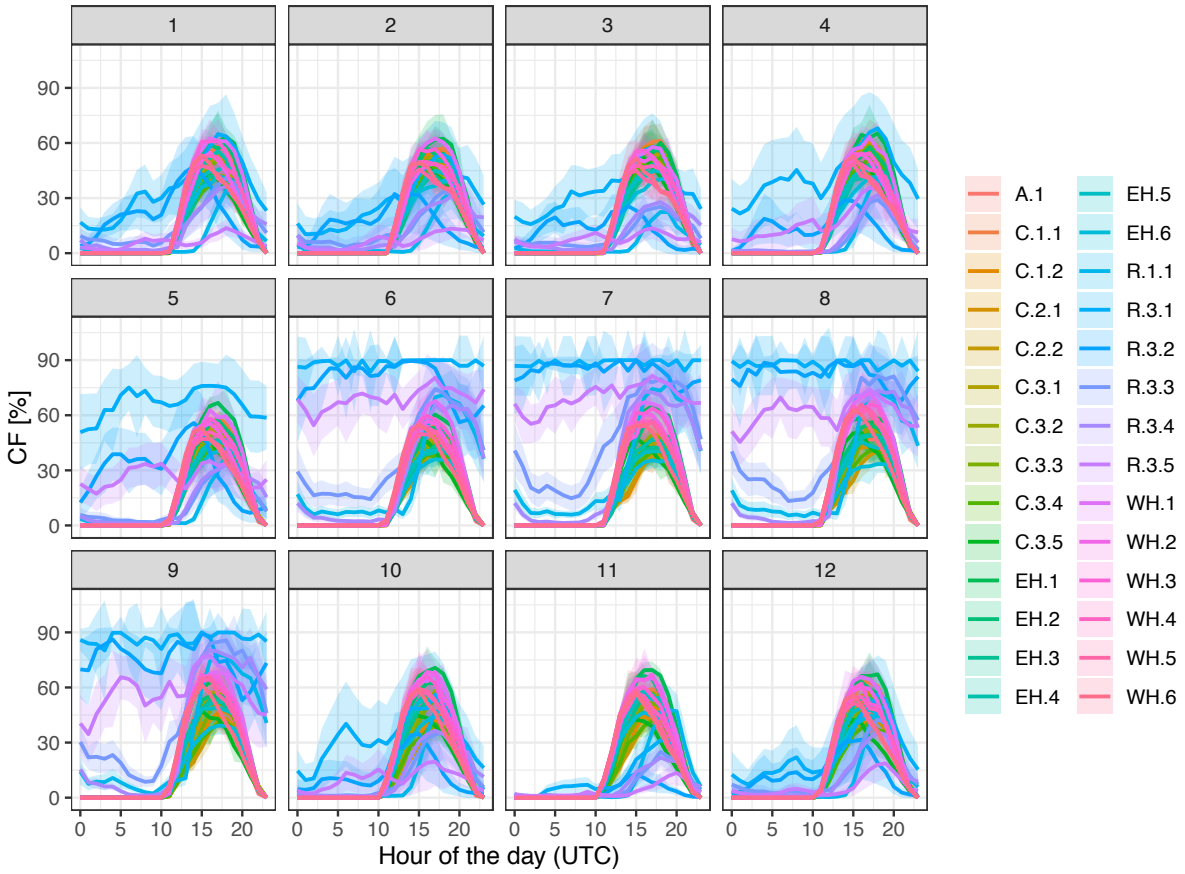

Fig. 5-5. Diurnal cycle of PV and wind capacity factors (CF) per month of simulated PV and wind farms of 10 MW at each solar and wind subregion's site. Bold lines are the mean values and the shaded ribbons represent the standard deviation.

Taking a closer look at the duration curves of CF_{PV} and CF_W at each site in Fig. 5-6, the frequency distribution of the PV and wind power output in a year can be observed. Each point on the x axis represents the probability (in terms of number of hours in a year) of PV or wind capacity factors greater or equal to the corresponding y value on the curve. Note that the PV and wind farms are assumed to be down during 2% of the time to account for unplanned maintenance.

As expected, PV is off for 50% of the time, since it only generates power during daytime. Nevertheless, solar farms in subregions WH.1 and EH.2 show CF_{PV}≥50% for ~23% of the time. In the case of wind power, CF_W of wind farms in subregions R.3.1 and R.3.2 is above 85% for 34% and 20% of the time, respectively, while in subregions R.1.1 and R.3.4 are above this value only ~0.3% of the time.

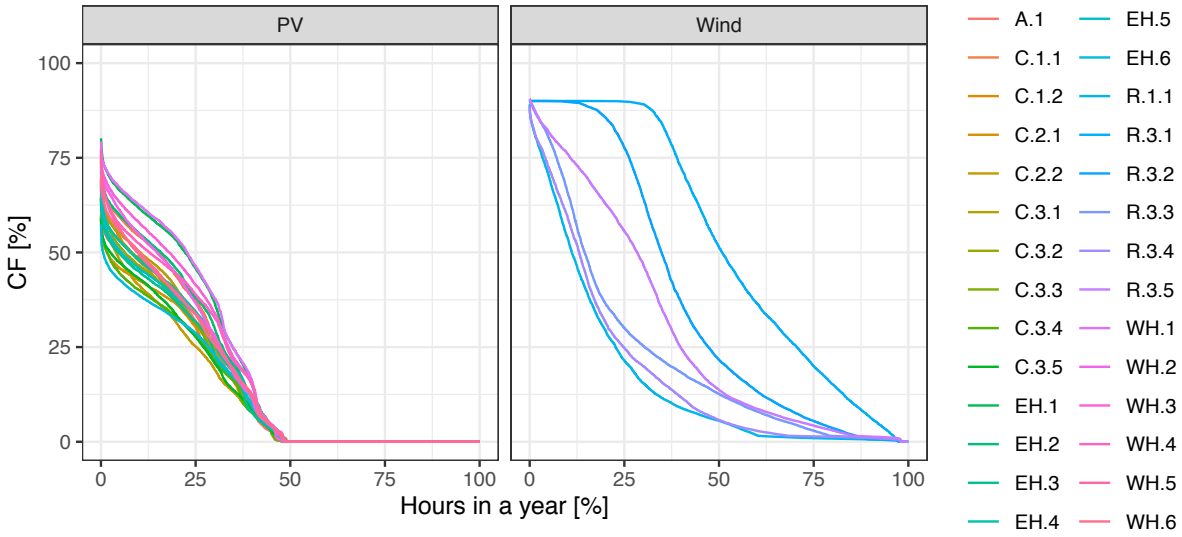

Fig. 5-6. Duration curves of capacity factors (CF) of simulated PV and wind farms of 10 MW at each solar and wind subregion's site.

5.3.3. Firm Capacity

When analyzing the power output of combined PV and wind farms (total capacity of 20 MW) operating in pairs, the benefits of the complementary behavior between the resources is more evident. Fig. 5-7 shows the power output percentage of paired PV and wind farms that could be available for 87.5% of the time in a year. This figure reveals that the contribution to firm capacity is ruled by the magnitude of the wind resource at the subregion's site. Thus, it is observed that combining the wind farm in R.3.1 (the site with the best wind resource) with PV farms in any solar subregion results in a firm capacity of 5.2–5.5% of the combined capacity. The combination of wind farms in subregions R.3.2 or R.3.5 with PV farms in any solar subregion could provide a firm capacity of 1.1–1.8%. The lowest firm capacity (0.4 to 0.7%) is provided by the combination of wind farms in subregions R.3.4, R.3.3 or R.1.1 with PV farms in any solar subregion, which is not surprising because the wind resources in these subregions are lower compared to the previous ones.

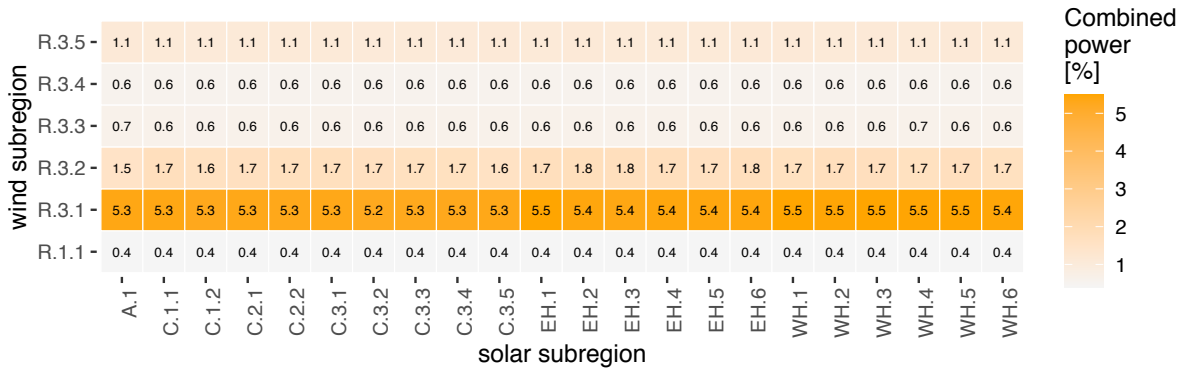

Fig. 5-7. Power output percentage of paired PV and wind farms (20 MW total) that could be online for 87.5% of the time in a year.

Fig. 5-8 provides a graphical representation of the increase in firm capacity for three sample pairs. The figure displays the duration curves of PV power output at one site (WH.1) and wind power output at three different sites (R.3.1, R.3.2, R.1.1), and the duration curve of the combined PV and wind farms. It is noticeable that more power could be delivered when PV and wind operates in combination compared to the firm capacity levels they could provide when they operate separately. The left and middle panels show that due to the better wind resources in R.3.1 and R.3.2 higher firm capacity levels could be achieved, while the right panel shows the low contribution of R.1.1 to the firm capacity.

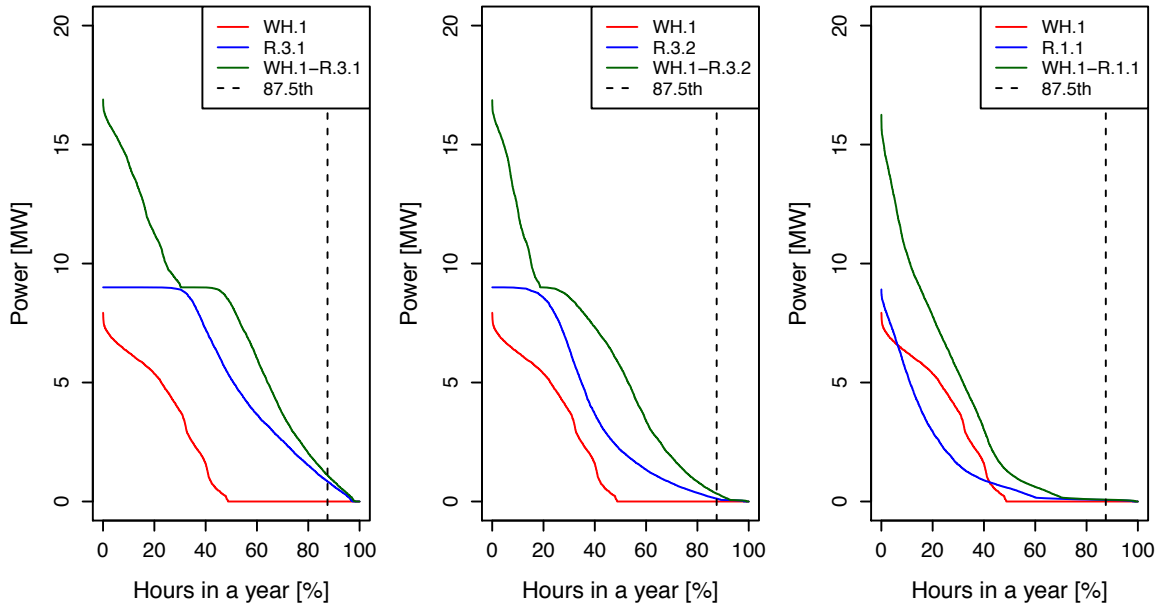

Fig. 5-8. Duration curves of the simulated power output of PV and wind farms and the power output of the combined operation (20 MW total) for three sample pairs (WH.1–R.3.1, WH.1–R.3.2, WH.1–R.1.1). The dashed vertical line represents the 87.5% availability threshold.

Comparing the duration curves of the capacity factor for the same sample pairs, two different patterns are observed. First, the left panel of Fig. 5-9 shows that CF_W of the wind farm in R.3.1 is higher when operates separately than when it operates in combination with the solar farm in WH.1, which is expected due to the large CF_W of the farm in this subregion. Second, the middle panel shows that although the capacity factor of the combined operation is lower for ~40% of the hours than the values of CF_{PV} and CF_W operating separately, this is compensated by a higher average capacity factor over the remaining 60% of the time. The same pattern is observed in the right panel, although to a lesser degree due to the lower wind resources in R.1.1.

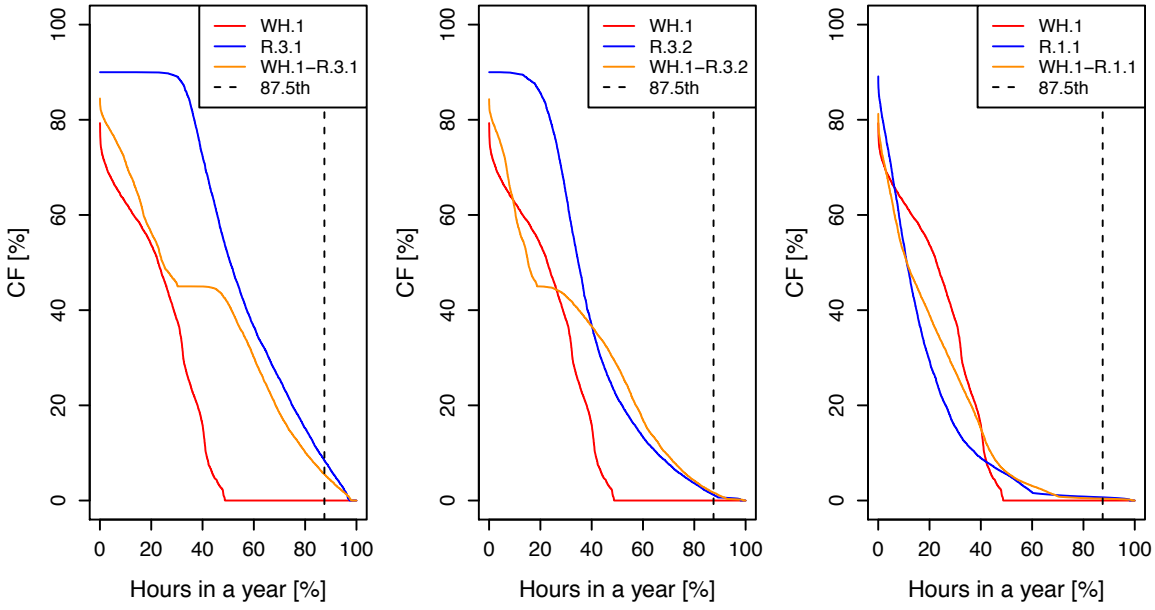

Fig. 5-9. Duration curves of the capacity factor (CF) of the simulated PV and wind farms and the capacity factor of the combined operation (20 MW total) for three sample pairs (WH.1–R.3.1, WH.1–R.3.2, WH.1–R.1.1). The dashed vertical line represents the 87.5% availability threshold.

As mentioned in Chapter 4, water resources in the Amazon and Pacific basins are limited from November to February (see Fig. 4-1), for this reason it is important to assess the firm capacity that combined PV and wind power could provide during these months. Fig. 5-10 shows that the combination of the wind farm in subregion R.3.1 with PV farms in any solar subregion could provide 1.93–1.97% of the total capacity (20 MW) for 87.5% of the time during the dry months, while the other combinations could provide between 0.30 to 0.65% of the total capacity.

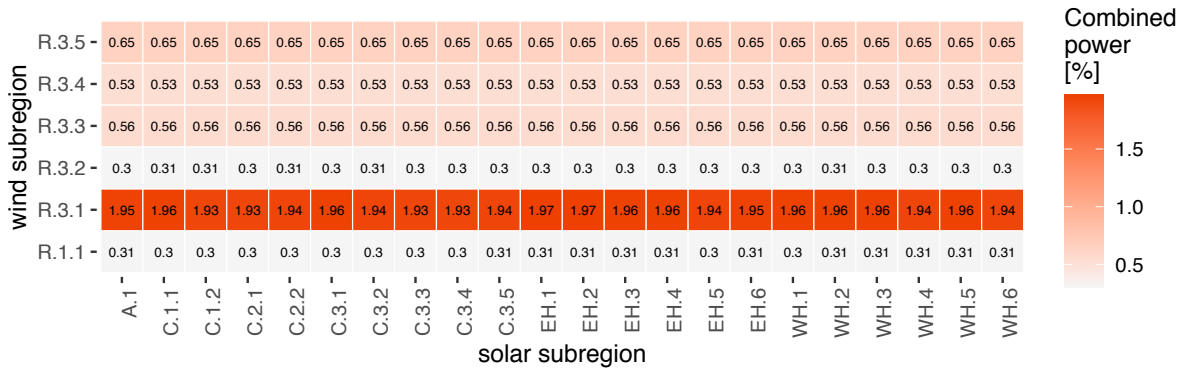

Fig. 5-10. Power output percentage of paired PV and wind farms (20 MW total) that could be online 87.5% of the time during November–February.

Looking at the duration curves of the combined power output from November to February, it is observed that the power output increases compared to that when the PV and wind farms operate separately. Fig. 5-11 displays the duration curves of PV power output at one site (EH.1) and wind power output at three different sites (R.3.1, R.3.5, R.1.1), and the duration curve of the combined PV and wind farms. Note that EH.1 is selected this time for the comparison because this subregion shows higher radiation levels from November to January compared to those in WH.1. From the figure, it is noticeable that the number of hours of high wind power output decreases, which is driven by the lower wind resources in the subregions during these months. Contrary, PV delivers half of its capacity for at least ~30% of the time during these months. This pattern leads to higher power that could be delivered when PV and wind operates together.

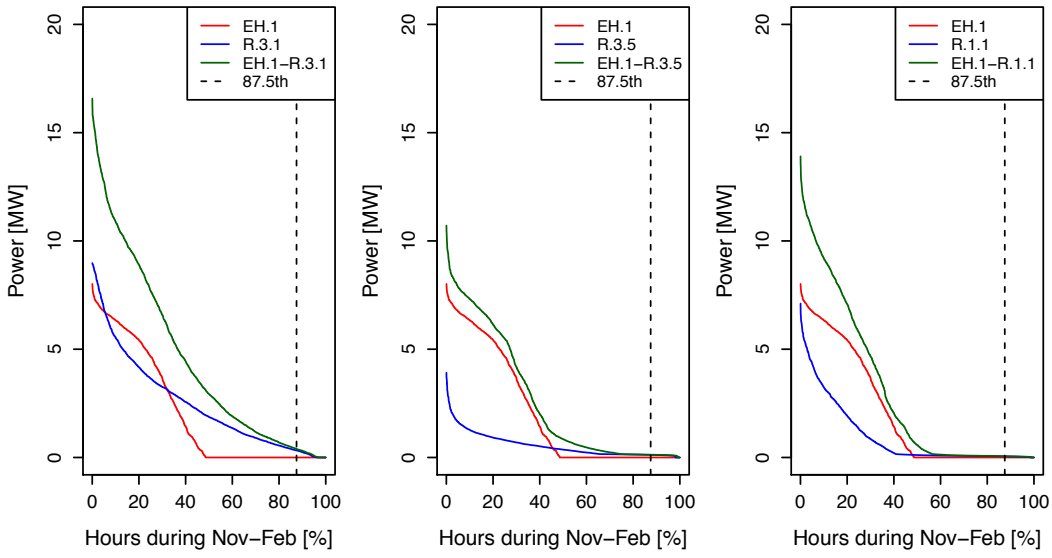

Fig. 5-11. Duration curves during November–February of the simulated power output of PV and wind farms and the power output of the combined operation (20 MW total) for three sample pairs (EH.1–R.3.1, EH.1–R.3.5, EH.1–R.1.1). The dashed vertical line represents the 87.5% availability threshold.

Regarding the capacity factor of the PV and wind farms during the dry months, the duration curves depicted in Fig. 5-12 show that when operating separately, the PV farm in subregion EH.1 performs better than the wind farms in the three wind subregions. Additionally, from the left panel in Fig. 5-12 it can be observed that although the capacity factor of the combined operation is lower for ~35% of the hours during November to February than the values of CF_{PV}, this is compensated by a higher average capacity factor over the remaining 65% of the time, which PV alone would not be able to provide. A similar pattern is seen in the middle and right panels, except that CF_{PV} is higher than CF_W for a longer time, which implies that the time when the combined average capacity is higher will be reduced.

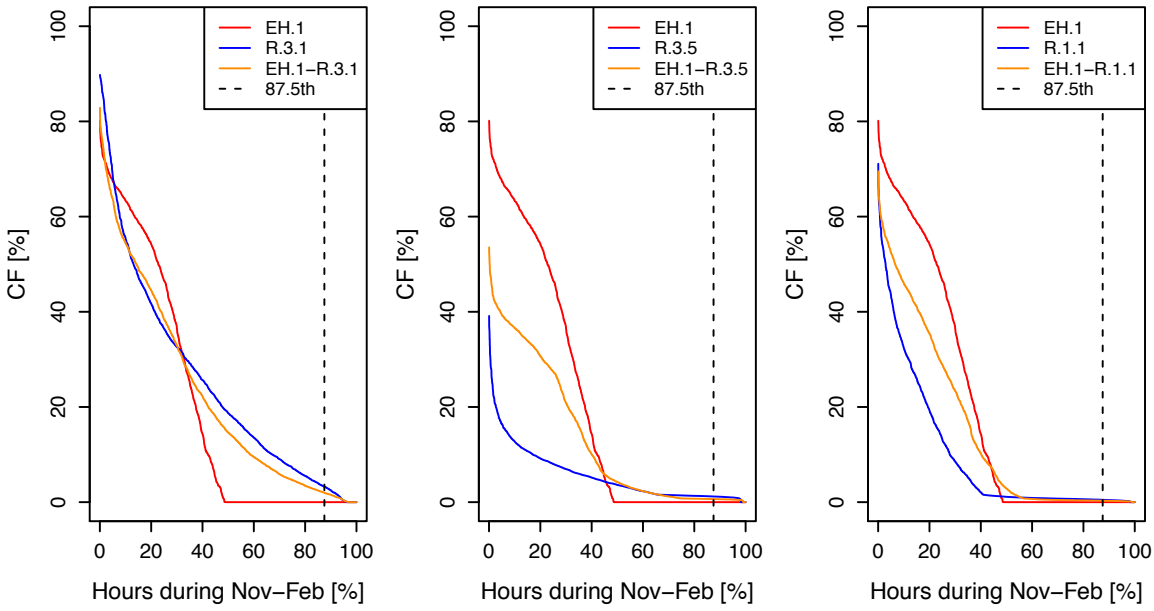

Fig. 5-12. Duration curves during November–February of the capacity factor (CF) of the simulated PV and wind farms and the CF of the combined operation (20 MW total) for three sample pairs (EH.1–R.3.1, EH.1–R.3.5, EH.1–R.1.1). The dashed vertical line represents the 87.5% availability threshold.

5.3.4. Stability coefficient

The stability coefficient C_{stab} is calculated for each pair of PV and wind farms and the annual mean value is mapped in Fig. 5-13. The combination of wind farms in subregions R.3.1, R.3.2 or R.3.5 with PV farms in any solar subregion results in the highest annual mean C_{stab} values (0.4–0.6), implying that wind power could provide diurnal stability to PV when they both operate combined. As expected, due to the low CF_W of the wind farm in

R.1.1, the lowest average C_{stab} values (~0.1) are seen in the combination of R.1.1 with PV farms in any solar subregion.

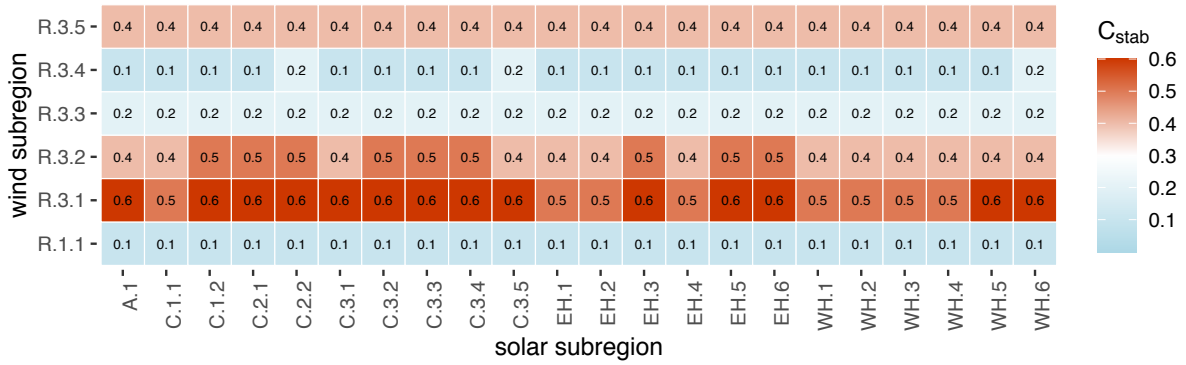

Fig. 5-13. Annual mean stability coefficient C_{stab} of paired PV and wind farms (20 MW total, capacity ratio 1:1).

As already mentioned, from the monthly plots of CF_{PV} and CF_W (see Fig. 5-5), it is evident that the best intra-day complementary behavior occurs during June–September. This is now confirmed and quantified using the stability coefficient metric. Fig. 5-14 displays the dispersion of C_{stab} values for all pairs per month, showing higher values that occur during June–September, when wind speed is almost constant and high throughout the day, thus complementing PV output at diurnal timescales.

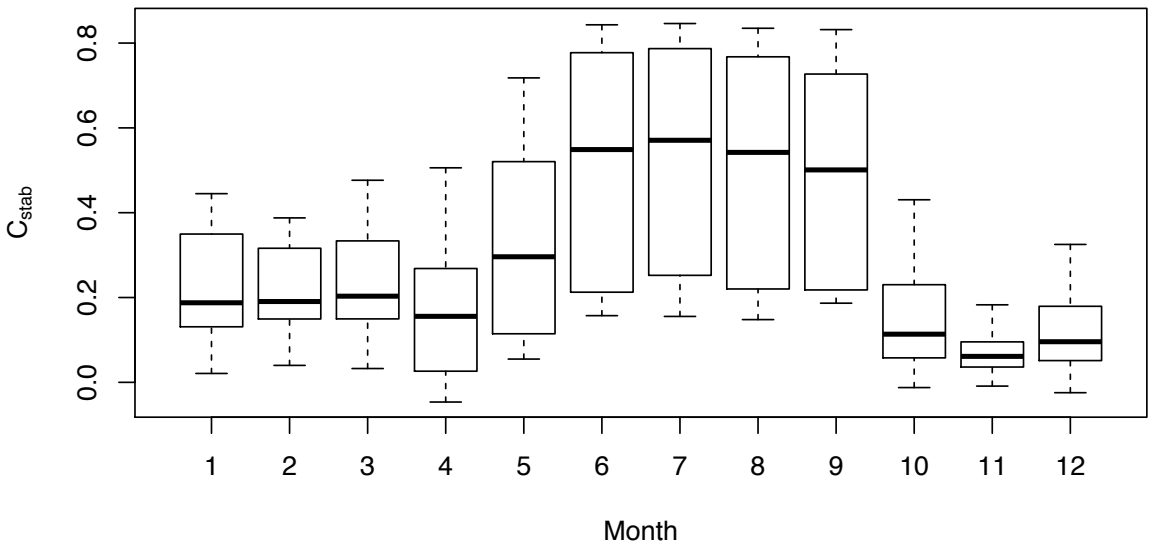

Fig. 5-14. Boxplots of the monthly stability coefficient C_{stab} for each pair of combined PV and wind power plants (assuming a capacity ratio 1:1).

The coefficient C_{stab} is also applied to assess if the PV or wind farms in different subregions could provide intra-annual stability to hydropower output from the two selected HPPs. Fig. 5-15 shows the C_{stab} results for the pairwise combinations of PV farms and HPPs, assuming a capacity ratio 1:1. A higher C_{stab} value (0.4) results from the combination of the hydropower plant in the Pacific basin, HP.1, with PV farms in subregions WH1–WH.5, which are located in the western Andean highlands. In the case of the hydropower plant in the Amazon basin, HA.2, the higher C_{stab} values (0.3) are observed with the combination of PV farms in subregions A.1, and EH (except for EH.3), which are located in the Amazon lowlands and the eastern Andean highlands, respectively.

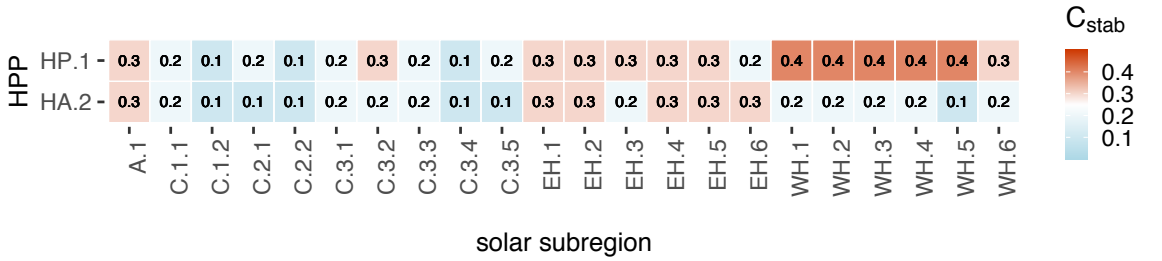

Fig. 5-15. Annual mean stability coefficient C_{stab} for each pair of combined PV farms and selected hydropower plants (assuming a capacity ratio 1:1).

Regarding the combination of the HPPs with wind farms in different subregions shown in Fig. 5-16, it can be observed that the joint operation of the HP.1 in the Pacific basin with the wind farms in subregion R.1.1 or R.3.4 results in the highest C_{stab} values (0.3). The other combinations result in C_{stab} values below zero, implying that wind farms in those subregions could not provide intra-annual stability to hydropower of the HPPs in both basins.

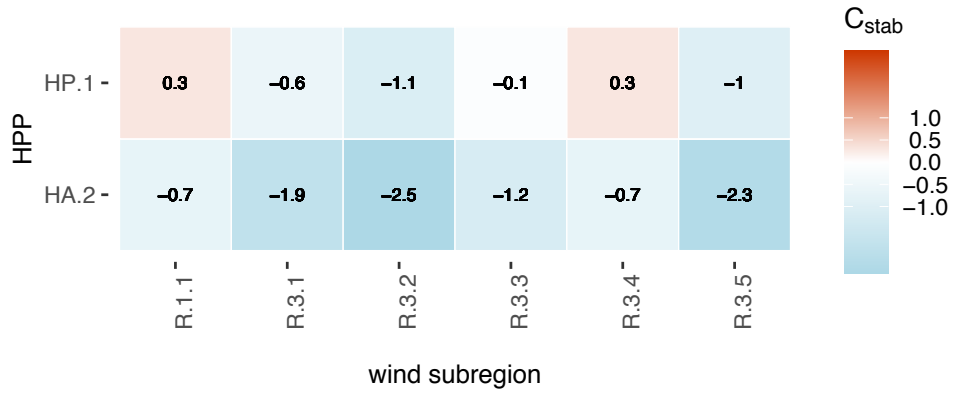

Fig. 5-16. Annual mean stability coefficient C_{stab} for each pair of combined wind farms and selected hydropower plants (assuming a capacity ratio 1:1).

5.4. Discussion

This chapter investigates the ability of geographically-dispersed and combined solar PV and wind power farms to reduce their power output variability and provide a reliable power generation, while complementing the intra-annual power output variability of existing hydropower plants. This is assessed by the firm capacity and stability coefficient C_{stab}, which are additional quantitative metrics to evaluate the complementarity of renewable power generation.

The results using the coefficient C_{stab} to assess the potential of PV or wind power to provide stability to the intra-annual hydropower variability (Fig. 5-15 and Fig. 5-16) are consistent with the results of the correlation analysis of renewable resources. As described in Chapter 4, Section 4.3.1.1, solar resources have a stronger complementary behavior with water resources in both basins, while water resources in the Pacific basin have a moderate complementarity with wind resources. Nevertheless, the coefficient C_{stab} represents an additional metric for the better understanding of the effectiveness of the joint operation of complementary power plants, since it takes into account the strength of the resources (i.e., by using capacity factors) (Sterl et al., 2018). Thus, the coefficient C_{stab} results reveal that PV generation from complementary solar subregions could provide intra-annual stability to hydropower in the case of the PV capacity is similar to that of the HPP. When testing different capacity ratios, the coefficient C_{stab} decreases accordingly. This suggests that the joint operation of PV and hydropower would not provide additional benefits in terms of intra-annual stability, unless PV and hydropower have similar installed capacities. The same applies to the joint operation of wind and hydropower in the Pacific basin. Therefore, an increase of the PV and wind power installed capacity is needed to take advantage of the stability benefits. This capacity can be built by aggregating several power systems within the same subregion or other subregions where solar irradiance or wind speed has similar intra-annual variability patterns. For instance, the additional PV capacity needed to stabilize hydropower could be distributed among subregions WH.1–WH.6, which share similar temporal variability patterns (see Fig. 2-5).

The assessment in this chapter focuses on the supply-side of the power system aiming to establish a starting point for further exploration of planning and operation strategies. The two metrics used, firm capacity and stability coefficient, are found to be useful to assess the reliability and stability of the power system, without explicitly considering electricity demand profiles. The main reason for this is the lack of publicly available demand data. Further work should focus on assessing the ability of complementary and geographically-dispersed PV and wind power systems to balance demand and supply. Synthetic hourly

load data that considered the spatial variability of demand in the study area could be useful for this purpose.

Overall, the findings in this chapter demonstrate that the joint operation of geographically-dispersed PV and wind power farms in Ecuador provide reliable and stable power output. Therefore, these technologies can play an important role in the displacement of the fossil-fuel thermal power capacity that is used to compensate the intra-annual variability of hydropower generation, especially during the dry months. These findings are contrary to the general assumption among energy planners in some Latin American countries that consider that solar and wind power do not contribute to the firm capacity (Campo, 2015; Levy et al., 2021). One reason for this assumption is the lack of hourly historical data of wind and solar resources, which makes it difficult to assess in more detail the contribution of these technologies to firm capacity (IRENA, 2017; Levy et al., 2021). Similarly, the spatio-temporal synergies of PV and wind power are not captured by long-term generation expansion planning models that use coarse meteorological datasets as input data for modeling PV and wind power outputs (e.g., Carvajal et al. (2019), Godoy et al. (2021)). Other studies completely ignored these synergies when aggregating solar and wind data at the country level by technology (e.g., Heredia and Gardumi (2022), Rivera-González et al. (2019). A coarse spatial and temporal resolution is necessary to keep the models solvable within reasonable time and to reduce calibration and other input data requirements (Pfenninger et al., 2014). However, the low temporal and spatial resolution of PV and wind power data may explain that the optimization models used in some of these studies result in an optimal power mix favoring thermal power generation with natural gas to compensate the variability of hydropower in Ecuador (e.g., Carvajal et al. (2019)). The spatio-temporal synergies among renewables in Ecuador may provide economic incentives, making the investment in solar and wind power projects more economically attractive. This eventually could lead to alternative development pathways with higher participation of wind and PV power in long-term generation capacity expansion optimization models.

In the end, a higher share of geographically-dispersed PV and wind power – and other non-hydro renewables – in the Ecuadorian power mix will reduce the existing imbalance among current power supply options in the country. By doing so, the diversity of the system (with its three interdependent attributes: variety, balance, and disparity) will increase, thus, enhancing the resilience of the system for responding to changes and disturbances (Biggs et al., 2012). Although the design of operating strategies will be necessary to cope with the mismatch between electricity supply and demand, from a resilience perspective,

as argued by Binder et al., (2017), a high balance implies that a more even distribution of technologies might potentially provide a higher degree of flexibility and adaptability to the system.

Nevertheless, power systems are not only technical systems, but rather socio-technical systems. Thus, the social dimension – including different actors involved in the governance structure of the national energy system (e.g., politics, industry, research, society, or media), and their complex interactions (Binder et al., 2017) – should be part of the analysis of the transformation towards a more sustainable and resilient power system in Ecuador. The ability of the different actors to learn, anticipate, and plan is integral to the resilience of socio-technical systems (Ruth et al., 2019). The findings of this dissertation lay the foundations for the technical aspects of the analysis; yet, the social aspects and a holistic analysis approach should be the direction for further research.

5.5. Conclusions

This chapter assesses the benefits that the spatio-temporal synergies between PV, wind, and hydropower could provide to the Ecuadorian power supply system in terms of reliability and stability. For this purpose, the power output of PV and wind farms located at high potential sites within each solar and wind subregion is simulated using hourly time series from the meteorological datasets generated in the previous chapters.

Results indicate that the joint operation of geographically-dispersed PV and wind power systems can smooth out the variability of the power output when compared to that of individual resources. This joint operation can provide at least 0.4 to 5.5% of the combined capacity for 87.5% of the time in a year (7665 hours), which differs from the general assumption among energy planners that wind and solar power do not contribute to the firm capacity. The higher the wind potential at the site, the higher the firm capacity that could be provided by the joint operation. From November to February, when water resources in both basins are limited, the joint operation can provide at least about 2% of the combined capacity for 87.5% of the time in these months (2520 hours). PV generation from subregions over the eastern Andean highlands (EH.1–EH.5) is important to provide reliable power generation during these months, since the high solar resources in these subregions complement the limited water resources in both basins.

Another important finding is that wind power from subregions with high wind resources (R.3.1, R.3.2, and R.3.5) stabilizes PV power output at diurnal timescales during the windy months (June–September), which suggests that these technologies could serve as baseload in these months, thus reducing the requirements for energy storage.

The potential of PV and wind power systems to reduce the intra-annual variability of existing hydropower plants is assessed using the stability coefficient, which provides an additional metric to better understand the effectiveness of the joint operation of complementary power plants. The results are consistent with the findings of the correlation analysis of renewable resources (Chapter 4), but it is additionally found that PV and wind power generation from complementary subregions could provide stability to hydropower in the case that the PV and hydropower capacities are similar. The required PV and wind power capacities can be built by aggregating geographically-dispersed power systems with similar intra-annual variability patterns. The regionalization maps and the spatio-temporal variability analysis of solar and wind resources reported in Chapter 2 and Chapter 3 are useful tools for solving the siting problem.

The identified complementary behavior and the operational benefits of the spatio-temporal synergies between renewables in the country demonstrate that solar and wind power can play an important role in shaping a more sustainable, decentralized, and diversified power system. Generation capacity expansion planning in Ecuador should be focused on exploiting the identified spatio-temporal synergies for the design of a more robust and precaution-oriented power supply system. This will enhance the resilience of the Ecuadorian power system to cope with weather and climate-related variabilities, and other uncertain stressors.

Chapter 6 Conclusions and outlook

6.1. Conclusions

This dissertation systematically investigates the spatio-temporal variabilities and synergies of renewable resources in the complex terrain of Ecuador for the optimal planning of a more sustainable and resilient power system in the country. The main findings and contributions of this dissertation grouped by each research objective are presented below.

Research Objective 1: To generate long-term and high-resolved solar and wind resource datasets for Ecuador.

Long-term, high-quality measurements of solar irradiance and wind speed at relevant heights for wind applications are generally scarce and sparsely distributed, which challenges the spatio-temporal characterization of solar and wind resources at a country level, especially over complex terrain. To tackle this challenge, this dissertation generates two long-term meteorological datasets at a 3 × 3 km grid resolution covering Ecuador's mainland and the Galapagos Islands.

The first dataset comprises a 21-year period (1998–2018) of hourly satellite-derived solar irradiance and other meteorological data, which is compiled from the widely used National Solar Radiation Database (NSRDB) (Sengupta et al., 2018). This dataset was previously validated against ground measurements from 53 stations in Ecuador's mainland (Ordoñez et al., 2019). In addition, a statistical check of the 21-year period dataset is performed in this dissertation. Results reveal that few grid points over the eastern Andean highlands show anomalies that might be attributed to satellite artifacts. Thus, the nearest-neighbor interpolation method is applied to the identified grid points to reduce these anomalies.

The second dataset comprises a 14-year period (2005–2018) of hourly wind speed and wind direction data at several heights. This dataset is generated using the Weather Research and Forecast (WRF) mesoscale model forced by initial and boundary conditions from ERA5 reanalysis data. The lack of a validated, long-term, and high-resolved wind resource dataset for the study area was the motivation to produce the mesoscale model

simulations. The number of simulation years is limited due to time and computational constraints. The comparison between WRF simulated wind speed and observations at 80 m above ground level from four meteorological tall masts located over the Andes shows that the WRF model overestimates wind speed, especially at nighttime and during the windy months (June to September). This overestimation is consistent with previous studies. However, since the overestimation in wind speed translates to larger differences in wind power, a bias correction is applied to the simulated WRF wind speed. The correction factors are defined based on the consistent trend of diurnal and monthly bias found between WRF and observations. According to the results, the bias correction method increases the agreement between the WRF simulations and observations in terms of MBE, RSME, and correlation coefficients during the control and evaluation period. Therefore, the resulting bias-corrected time series show a diurnal cycle that is more in phase with the observations.

The solar and wind resource datasets constitute a core element of this dissertation, since they are necessary for the achievement of the remaining research objectives. Moreover, this is the first time that such long-term and high-resolved solar and wind resource datasets have been compiled and generated for the study area, providing the groundwork for future research in energy meteorology and energy system modeling.

Research Objective 2: To develop a new methodology based on spatial functional data analysis for the characterization of the spatio-temporal variability of solar and wind resources.

A new methodology to characterize the spatio-temporal variability of gridded solar and wind resource datasets using spatial functional data analysis (sFDA) is proposed and demonstrated. The methodology comprises multiple steps. First, a hierarchical regionalization method for spatial functional data is used to identify homogeneous areas (called subregions in this dissertation) with similar intra-annual variability patterns. Second, the characterization of the interannual variability is performed using the coefficient of variation. Finally, the spatio-temporal complementarity between the resulting subregions from the regionalization is analyzed through correlation coefficients.

Results indicate that the sFDA regionalization method identifies coherent subregions with similar intra-annual variability patterns of solar radiation and wind speed, effectively capturing the variability due to microclimate and topographic effects in the complex terrain of Ecuador. This is the first time that the sFDA regionalization method is used for this purpose and the results indicate that it provides an appropriate basis for the interannual

variability and complementarity analyses. In general, it is concluded that the proposed methodology can be applied to other regions or countries and adapted to analyze the spatio-temporal variability of other renewables resources or energy yield.

Furthermore, the sFDA regionalization method is found to be useful for adapting the pointwise wind speed bias correction to any grid point that has similar wind speed temporal variability patterns to that of the observation stations. This implies that such an approach can be applied to correct the bias of other gridded wind resource datasets.

From a practical perspective with respect to Research Objective 2, this dissertation provides the first comprehensive spatio-temporal characterization of solar radiation and wind speed in Ecuador's mainland and the Galapagos Islands. The regionalization maps and the variability statistics provide explicit information to identify optimal sites for the deployment of meteorological measurement networks, as well as for the construction of solar and wind power facilities in the country. These results are of particular relevance to support planners and decision-makers for the optimal planning and deployment of solar and wind power systems in the country.

Research Objective 3: To analyze the spatio-temporal correlation between solar, wind, and water resources in Ecuador based on long-term and high-resolved meteorological datasets.

The most significant finding from the spatio-temporal correlation analysis of renewable resources in the study area is that solar and wind resources have strong spatio-temporal complementarities to water resources in the Amazon and Pacific basins. The low availability of water resources in the Amazon basin during October–March can be compensated by solar resources from subregions on the coast and along the Eastern Andean highlands. In the case of the Pacific basin, the low availability of water resources during June–November can be compensated by solar resources from subregions in both sides of the Andean highlands and in the Amazon. Wind resources over the Andean highlands are also complementary to water resources in the Pacific basin, although to a moderate level. Furthermore, strong complementarities of solar resources between the coastal area and the Western Andean highlands are also identified.

The intra-annual variability patterns of solar and wind resources in some subregions are also found to be similar to the hydrological regimes in both basins. This aspect suggests that solar and/or wind power projects could be planned instead of hydropower plants. Such a strategy could prevent serious environmental and social impacts related to the

deployment of large-scale hydropower projects in the Amazon basin, where most of the untapped hydropower potential of the country resides.

The temporal correlation analysis reveals that there exists a great potential for deploying hydro-solar-wind hybrid systems. Although gridded precipitation data is found to be useful for analyzing the pairwise correlation to solar and wind resources at each grid point, hydropower potential is not available in all grid points, as it depends on effective inflow and available head. To further explore the potential of hybrid power systems, a hydrological model that converts precipitation to streamflow in selected catchments would be needed.

The newly identified seasonal complementary behavior between solar, wind, and water resources in Ecuador lays the foundation for the optimal planning and siting of new geographically-dispersed solar and wind power capacities to compensate hydropower during the dry periods.

Research Objective 4: To analyze the opportunity of wind and solar power to enhance the resilience of the power supply system by accounting the spatio-temporal synergies of renewable power generation.

The benefits that the spatio-temporal synergies of renewable power generation could provide to the power system are quantified in terms of reliability and stability. Results reveal that the joint operation of geographically-dispersed PV and wind power systems from different subregions reduces the intrinsic variability of each resource and provides certain levels of firm capacity to be available at a given time. This finding differs from the general assumption among energy planners that wind and solar power do not contribute to the firm capacity. Another important finding is that wind power from subregions with high resources stabilizes PV power output at diurnal timescales during the windy months, suggesting that both technologies could serve as baseload during this period, thus reducing the requirements for energy storage. The identified operational benefits of the spatio-temporal synergies of renewable power generation may provide economic incentives to support the deployment of PV and wind power, thus displacing fossil fuel thermal power generation.

From the findings of this dissertation, it can be concluded that solar and wind power can play an important role in shaping a more sustainable and resilient power system in the country. Generation capacity expansion planning in Ecuador should be focused on exploiting the identified spatio-temporal synergies for the design of a more robust and precaution-oriented power supply system. A higher share of geographically-dispersed PV and wind power – and eventually other non-hydro renewables – in the power mix will

reduce the existing imbalance among current power supply options in the country. By doing so, the diversity of the power system, which involves variety, balance, and disparity, will increase. Likewise, similar power generation profile patterns translate into redundancy of power supply sources, which is another precautionary measure. Therefore, taking these design elements into account for capacity expansion planning can help in enhancing the resilience of the current hydro-thermal power system to cope with weather and climate related variabilities, uncertainties of fossil fuel prices due to geopolitical conditions, and other uncertain stressors.

6.2. Outlook

The methodology and data developed in this dissertation open up a plethora of options for further research. A natural progression of this work is to assess the optimal sizing and relative share among PV and wind power needed to meet the electricity demand, while displacing fossil fuel thermal power. For this purpose, the results from this dissertation can be integrated into both operational power system models and long-term generation expansion planning models.

The hourly datasets will support operational power system models to assess the flexibility of the power system with an increasing contribution of solar and wind generation. Long-term generation expansion planning models can be used to explore different scenarios for 100% renewable energy, optimizing the spatio-temporal complementarity between resources.

The sFDA regionalization method will enable the incorporation of better spatial details into the models. In this way, the computational requirements to solve the optimization problems can be reduced, while accounting for the spatio-temporal synergies among renewable power generation. Such an approach will capture the benefits associated with spatial smoothing of variable renewable energy generation, which is a challenge in long-term planning models (Collins et al., 2017).

Considering that power systems are complex socio-technical systems, the modeling of the power system transformation should not focus only on the rationale of techno-economic optimization, but should also take into account human behavior and interaction of different stakeholders. The findings of this dissertation provide the groundwork for the technical aspects of the analysis; yet, the social dimension and the development of a holistic analysis

approach, using for instance agent-based models, should be the direction for further research.

Further studies should also focus on investigating the impact of weather and climate on the energy sector in both a retrospective and prospective way. The generated long-term meteorological datasets will support further research on different topics in this respect, e.g., the assessment of the sensitivity of the power system to interannual climate variability, the impacts of El Niño–Southern Oscillation (ENSO) on solar and wind resources, and the analysis of the degree to which the complementarity between renewable resources in Ecuador could mitigate the impacts of ENSO on hydrological resources.

Bibliography

Anderson, E. P., Jenkins, C. N., Heilpern, S., Maldonado-Ocampo, J. A., Carvajal-Vallejos, F. M., Encalada, A. C., Rivadeneira, J. F., Hidalgo, M., Cañas, C. M., Ortega, H., Salcedo, N., Maldonado, M., and Tedesco, P. A. (2018). Fragmentation of Andes-to-Amazon connectivity by hydropower dams. *Science Advances*, *4*(1), 1–7. https://doi.org/10.1126/sciadv.aao1642

Ansar, A., Flyvbjerg, B., Budzier, A., and Lunn, D. (2014). Should we build more large dams? The actual costs of hydropower megaproject development. *Energy Policy*, *69*, 43–56. https://doi.org/10.1016/j.enpol.2013.10.069

Apolo, H. I., Escobar-Segovia, K., and Arcentales-Bastidas, D. (2019). Santa cruz, galapagos electricity sector towards a zero fossil fuel Island. *Proceedings of the LACCEI International Multi-Conference for Engineering, Education and Technology*. https://doi.org/10.18687/LACCEI2019.1.1.170

ARCERNNR. (2020). *Estadística anual y multianual del sector eléctrico ecuatoriano 2019*. https://www.controlrecursosyenergia.gob.ec/wp-content/uploads/downloads/2020/11/Estadística-2019-nuevologo-small.pdf

ARCERNNR. (2021). *Estadística anual y multianual del sector eléctrico ecuatoriano 2020*. https://www.controlrecursosyenergia.gob.ec/wp-content/uploads/downloads/2021/09/Estadistica-2020-baja.pdf

ARCERNNR. (2022a). *Estadísticas del sector eléctrico ecuatoriano buscar – Agencia de Regulación y Control de Energía y Recursos Naturales no Renovables*. https://www.controlrecursosyenergia.gob.ec/estadisticas-del-sector-electrico-ecuatoriano-buscar/

ARCERNNR. (2022b). *Reportes de información estadística del sector eléctrico*. http://reportes.controlrecursosyenergia.gob.ec

Archer, C. L., and Jacobson, M. Z. (2007). Supplying baseload power and reducing transmission requirements by interconnecting wind farms. *Journal of Applied Meteorology and Climatology*, *46*(11), 1701–1717. https://doi.org/10.1175/2007JAMC1538.1

Ascencio-Vásquez, J., Brecl, K., and Topič, M. (2019). Methodology of Köppen-Geiger-Photovoltaic climate classification and implications to worldwide mapping of PV system performance. *Solar Energy*, *191*(September), 672–685. https://doi.org/10.1016/j.solener.2019.08.072

Bagatini, M., Benevit, M. G., Beluco, A., and Risso, A. (2017). Complementarity in Time between Hydro, Wind and Solar Energy Resources in the State of Rio Grande do Sul, in Southern Brazil. *Energy and Power Engineering*, *09*(09), 515–526. https://doi.org/10.4236/epe.2017.99036

Ballari, D., Giraldo, R., Campozano, L., and Samaniego, E. (2018). Spatial functional data analysis for regionalizing precipitation seasonality and intensity in a sparsely monitored region: Unveiling the spatio-temporal dependencies of precipitation in

Ecuador. *International Journal of Climatology*, *38*(8), 3337–3354. https://doi.org/10.1002/joc.5504

Bendix, A., and Bendix, J. (2006). Heavy rainfall episodes in Ecuador during El Niño events and associated regional atmospheric circulation and SST patterns. *Advances in Geosciences*, *6*, 43–49. https://doi.org/10.5194/adgeo-6-43-2006

Bendix, J., Rollenbeck, R., Göttlicher, D., and Cermak, J. (2006). Cloud occurrence and cloud properties in Ecuador. *Climate Research*, *30*(2), 133–147. https://doi.org/10.3354/cr030133

Biggs, R., Schlüter, M., Biggs, D., Bohensky, E. L., Burnsilver, S., Cundill, G., Dakos, V., Daw, T. M., Evans, L. S., Kotschy, K., Leitch, A. M., Meek, C., Quinlan, A., Raudsepp-Hearne, C., Robards, M. D., Schoon, M. L., Schultz, L., and West, P. C. (2012). Toward principles for enhancing the resilience of ecosystem services. *Annual Review of Environment and Resources*, *37*, 421–448. https://doi.org/10.1146/annurev-environ-051211-123836

Binder, C., Mühlemeier, S., and Wyss, R. (2017). An Indicator-Based Approach for Analyzing the Resilience of Transitions for Energy Regions. Part I: Theoretical and Conceptual Considerations. *Energies*, *10*, 36. https://doi.org/10.3390/en10010036

Bódis, K., Kougias, I., Jäger-Waldau, A., Taylor, N., and Szabó, S. (2019). A high-resolution geospatial assessment of the rooftop solar photovoltaic potential in the European Union. *Renewable and Sustainable Energy Reviews*, *114*. https://doi.org/10.1016/j.rser.2019.109309

Borba, E. M., and Brito, R. M. (2017). An Index Assessing the Energetic Complementarity in Time between More than Two Energy Resources. *Energy and Power Engineering*, *09*(09), 505–514. https://doi.org/10.4236/epe.2017.99035

Brand, U., Giese, B., Gleich, A. von, Heinbach, K., Petschow, U., Schnülle, C., Stührmann, S., Stührmann, T., Thier, P., Wachsmuth, J., and Wigger, H. (2017). *Resiliente Gestaltung des Energiesystems am Beispiel der Transformationsoptionen „EE-Methan-System“ und „Regionale Selbstversorgung“: Schlussbericht des vom BMBF geförderten Projektes RESYSTRA (FKZ: 01UN1219A-B)*. Universität Bremen. https://doi.org/10.2314/KXP:1667649884

Burton, T., Jenkins, N., Sharpe, D., and Bossanyi, E. (2021). Wind Energy Handbook. In *Wind Energy Handbook* (Third). John Wiley & Sons Ltd. https://doi.org/10.1002/9781119992714

Buytaert, W., and Beven, K. (2011). Models as multiple working hypotheses: Hydrological simulation of tropical alpine wetlands. *Hydrological Processes*, *25*, 1784–1799. https://doi.org/10.1002/hyp.7936

Buytaert, W., Celleri, R., Willems, P., Bièvre, B. De, and Wyseure, G. (2006). Spatial and temporal rainfall variability in mountainous areas: A case study from the south Ecuadorian Andes. *Journal of Hydrology*, *329*, 413–421. https://doi.org/10.1016/j.jhydrol.2006.02.031

Campo, R. (2015). *Estudio comparativo de modelos de mercado eléctrico, estructura institucional, metódos de regulación y estructuras tarifarias*. Latin American Energy Organization (OLADE). http://www.olade.org/wp-content/uploads/2015/08/Estudio-Comparativo-modelos-mercado-eléctrico-metodos-de-regulación-y-estructura-tarifaria-6-paises.pdf

Canales, F. A., Jurasz, J., Kies, A., Beluco, A., Arrieta-Castro, M., and Peralta-Cayón, A. (2020). Spatial representation of temporal complementarity between three variable energy sources using correlation coefficients and compromise programming.

MethodsX, *7*. https://doi.org/10.1016/j.mex.2020.100871

Cantão, M. P., Bessa, M. R., Bettega, R., Detzel, D. H. M., and Lima, J. M. (2017). Evaluation of hydro-wind complementarity in the Brazilian territory by means of correlation maps. *Renewable Energy*, *101*, 1215–1225. https://doi.org/10.1016/J.RENENE.2016.10.012

Carvajal, P. E., Anandarajah, G., Mulugetta, Y., and Dessens, O. (2017). Assessing uncertainty of climate change impacts on long-term hydropower generation using the CMIP5 ensemble—the case of Ecuador. *Climatic Change*, *144*, 611–624. https://doi.org/10.1007/s10584-017-2055-4

Carvajal, P. E., Li, F. G. N., Soria, R., Cronin, J., Anandarajah, G., and Mulugetta, Y. (2019). Large hydropower, decarbonisation and climate change uncertainty: Modelling power sector pathways for Ecuador. *Energy Strategy Reviews*, *23*, 86–99. https://doi.org/10.1016/J.ESR.2018.12.008

Carvalho, D., Rocha, A., Gómez-Gesteira, M., and Santos, C. (2012). A sensitivity study of the WRF model in wind simulation for an area of high wind energy. *Environmental Modelling and Software*, *33*, 23–34. https://doi.org/10.1016/j.envsoft.2012.01.019

Carvalho, D., Rocha, A., Gómez-Gesteira, M., and Silva Santos, C. (2014). WRF wind simulation and wind energy production estimates forced by different reanalyses: Comparison with observed data for Portugal. *Applied Energy*, *117*, 116–126. https://doi.org/10.1016/j.apenergy.2013.12.001

CELEC. (2016). *Central eólica villonaco genera el 152% de lo planificado*. https://www.celec.gob.ec/gensur/noticias/central-eolica-villonaco-genera-el-152-de-lo-planificado/

Celleri, R., Willems, P., Buytaert, W., and Feyen, J. (2007). Space–time rainfall variability in the Paute basin, Ecuadorian Andes. *Hydrological Processes*, *21*, 3316–3327. https://doi.org/10.1002/hyp.6575

CENACE. (2021). *Informe Anual 2020*. Operador Nacional de Electricidad. http://www.cenace.gob.ec/informe-anual-2020/

Cevallos-Sierra, J., and Ramos-Martin, J. (2018). Spatial assessment of the potential of renewable energy: The case of Ecuador. *Renewable and Sustainable Energy Reviews*, *81*, 1154–1165. https://doi.org/10.1016/j.rser.2017.08.015

CGE. (2020). *Contraloria General Del Estado :: Energía: Fallas en la construcción del Proyecto Hidroeléctrico Toachi Pilatón*. https://www.contraloria.gob.ec/SalaDePrensa/NoticiasPorSectores/23961

Chiew, F. H. S., and McMahon, T. A. (2002). Global ENSO-streamflow teleconnection, streamflow forecasting and interannual variability. *Hydrological Sciences Journal*, *47*, 505–522. https://doi.org/10.1080/02626660209492950

Collins, S., Deane, J. P., Poncelet, K., Panos, E., Pietzcker, R. C., Delarue, E., and Ó Gallachóir, B. P. (2017). Integrating short term variations of the power system into integrated energy system models: A methodological review. *Renewable and Sustainable Energy Reviews*, *76*, 839–856. https://doi.org/10.1016/j.rser.2017.03.090

Coltorti, M., and Ollier, C. D. (2000). Geomorphic and tectonic evolution of the Ecuadorian Andes. *Geomorphology*, *32*, 1–19. https://doi.org/10.1016/S0169-555X(99)00036-7

CONELEC. (2012). *Plan Maestro de Electrificación 2012-2021*. Consejo Nacional de Electricidad.

CONELEC. (2013). *Plan Maestro de Electrificación 2013-2022. Vol. 4. Aspectos de*

sustentabilidad y sostenibilidad social y ambiental. Consejo Nacional de Electricidad.

de Oliveira Costa Souza Rosa, C., Costa, K. A., da Silva Christo, E., and Bertahone, P. B. (2017). Complementarity of hydro, photovoltaic, and wind power in Rio de Janeiro State. *Sustainability (Switzerland)*, *9*, 1–12. https://doi.org/10.3390/su9071130

de Oliveira Costa Souza Rosa, C., da Silva Christo, E., Costa, K. A., and Santos, L. dos. (2020). Assessing complementarity and optimising the combination of intermittent renewable energy sources using ground measurements. *Journal of Cleaner Production*, *258*, 120946. https://doi.org/10.1016/j.jclepro.2020.120946

Deppe, A. J., Gallus, W. A., and Takle, E. S. (2013). A WRF ensemble for improved wind speed forecasts at turbine height. *Weather and Forecasting*, *28*, 212–228. https://doi.org/10.1175/WAF-D-11-00112.1

Dobos, A. (2014). PVWatts Version 5 Manual - Technical Report NREL/TP-6A20-62641. In *National Renewable Energy Laboratory* (Issue September).

Dörenkämper, M., Olsen, B. T., Witha, B., Hahmann, A. N., Davis, N. N., Barcons, J., Ezber, Y., Garciá-Bustamante, E., Fidel González-Rouco, J., Navarro, J., Sastre-Marugán, M., Sile, T., Trei, W., Žagar, M., Badger, J., Gottschall, J., Rodrigo, J. S., and Mann, J. (2020). The Making of the New European Wind Atlas - Part 2: Production and evaluation. *Geoscientific Model Development*, *13*, 5079–5102. https://doi.org/10.5194/gmd-13-5079-2020

Echegaray-Aveiga, R. C., Masabanda, M., Rodriguez, F., Toulkeridis, T., and Mato, F. (2018). Solar Energy Potential in Ecuador. *2018 5th International Conference on EDemocracy and EGovernment, ICEDEG 2018*, 46–51. https://doi.org/10.1109/ICEDEG.2018.8372318

Emck, P. (2007). *A Climatology of South Ecuador - With special focus on the major Andean ridge as Atlantic-Pacific climate divide* [Friedrich-Alexander-Universität Erlangen-Nürnberg (FAU)]. https://opus4.kobv.de/opus4-fau/frontdoor/index/index/docId/477

Emeis, S. (2013). *Wind energy meteorology. Atmospheric physics for wind power generation* (1st ed.). Springer-Verlag Berlin Heidelberg.

Erazo, B., Bourrel, L., Frappart, F., Chimborazo, O., Labat, D., Dominguez-Granda, L., Matamoros, D., and Mejia, R. (2018). Validation of satellite estimates (Tropical Rainfall Measuring Mission, TRMM) for rainfall variability over the Pacific slope and Coast of Ecuador. *Water*, *10*, 1–23. https://doi.org/10.3390/w10020213

Favier, V., Wagnon, P., Chazarin, J. P., Maisincho, L., and Coudrain, A. (2004). One-year measurements of surface heat budget on the ablation zone of Antizana Glacier 15, Ecuadorian Andes. *Journal of Geophysical Research Atmospheres*, *109*, 1–15. https://doi.org/10.1029/2003JD004359

Fernandez-Palomino, C. A., Hattermann, F. F., Krysanova, V., Lobanova, A., Vega-Jácome, F., Lavado, W., Santini, W., Aybar, C., and Bronstert, A. (2022). A Novel High-Resolution Gridded Precipitation Dataset for Peruvian and Ecuadorian Watersheds: Development and Hydrological Evaluation. *Journal of Hydrometeorology*, *23*, 309–336. https://doi.org/10.1175/JHM-D-20-0285.1

Fernández Peruchena, C. M., Ramírez, L., Silva-Pérez, M. A., Lara, V., Bermejo, D., Gastón, M., Moreno-Tejera, S., Pulgar, J., Liria, J., Macías, S., Gonzalez, R., Bernardos, A., Castillo, N., Bolinaga, B., Valenzuela, R. X., and Zarzalejo, L. F. (2016). A statistical characterization of the long-term solar resource: Towards risk assessment for solar power projects. *Solar Energy*, *123*, 29–39. https://doi.org/10.1016/j.solener.2015.10.051

Funk, C., Peterson, P., Landsfeld, M., Pedreros, D., Verdin, J., Shukla, S., Husak, G., Rowland, J., Harrison, L., Hoell, A., and Michaelsen, J. (2015). The climate hazards infrared precipitation with stations - A new environmental record for monitoring extremes. *Scientific Data*, *2*, 1–21. https://doi.org/10.1038/sdata.2015.66

García de Fonseca, L., Parikh, M., and Manghani, R. (2019). *Evolución futura de costos de las energías renovables y almacenamiento en América Latina* (Juan Paredes (Ed.)). Banco Interamericano de Desarrollo División de Energía. https://doi.org/10.18235/0002101

Gelaro, R., McCarty, W., Suárez, M. J., Todling, R., Molod, A., Takacs, L., Randles, C. A., Darmenov, A., Bosilovich, M. G., Reichle, R., Wargan, K., Coy, L., Cullather, R., Draper, C., Akella, S., Buchard, V., Conaty, A., da Silva, A. M., Gu, W., … Zhao, B. (2017). The modern-era retrospective analysis for research and applications, version 2 (MERRA-2). *Journal of Climate*, *30*, 5419–5454. https://doi.org/10.1175/JCLI-D-16-0758.1

Giler-Ormaza, A. (2018). A province with several climates: What knowledge of hydrology can be useful? A literature review. *Maskana*, *9*(2), 41–51. https://doi.org/10.18537/mskn.09.02.06

Giraldo, R., Dabo-Niang, S., and Martínez, S. (2018). Statistical modeling of spatial big data: An approach from a functional data analysis perspective. *Statistics & Probability Letters*, *136*, 126–129. https://doi.org/https://doi.org/10.1016/j.spl.2018.02.025

Giraldo, R., Delicado, P., and Mateu, J. (2011). Ordinary kriging for function-valued spatial data. *Environmental and Ecological Statistics*, *18*, 411–426. https://doi.org/10.1007/s10651-010-0143-y

Giraldo, R., Delicado, P., and Mateu, J. (2012). Hierarchical clustering of spatially correlated functional data. *Statistica Neerlandica*, *66*(4), 403–421. https://doi.org/10.1111/j.1467-9574.2012.00522.x

Giraldo, R., Mateu, J., and Delicado, P. (2012). geofd: An R package for function-valued geostatistical prediction. *Revista Colombiana de Estadistica*, *35*(3), 383–405.

Gleich, A. von, and Giese, B. (2019). Resilient systems as a biomimetic guiding concept. In M. Ruth and S. Goessling-Reisemann (Eds.), *Handbook on Resilience of Socio-technical Systems* (pp. 89–98). Edward Elgar Publishing Limited.

Gleich, A. von, Gößling-Reisemann, S., Stührmann, S., Woizeschke, P., and Lutz-Kunisch, B. (2010). Resilienz als Leitkonzept – Vulnerabilität als analytische Kategorie. In K. Fichter, A. von Gleich, R. Pfriem, and B. Siebenhüner (Eds.), *Theoretische Grundlagen für erfolgreiche Klima- anpassungsstrategien* (pp. 13–49). Projektkonsortium ‚nordwest2050'.

Global Wind Atlas. (2022). https://globalwindatlas.info/

Godoy, J. C., Villamar, D., Soria, R., Vaca, C., Hamacher, T., and Ordóñez, F. (2021). Preparing the Ecuador's power sector to enable a large-scale electric land transport. *Energies*, *14*, 1–22. https://doi.org/10.3390/en14185728

Gonzalez-Salazar, M., and Poganietz, W. R. (2021). Evaluating the complementarity of solar, wind and hydropower to mitigate the impact of El Niño Southern Oscillation in Latin America. *Renewable Energy*, *174*, 453–467. https://doi.org/10.1016/j.renene.2021.04.048

Gößling-Reisemann, S. (2016). Resilience – Preparing Energy Systems for the Unexpected. In I. Link and V. Florin (Eds.), *IRGC Resource Guide on Resilience*. EPFL International Risk Governance Center (IRGC).

Gößling-Reisemann, S., and Thier, P. (2019). On the difference between risk management and resilience management for critical infrastructures. In M. Ruth and S. Goessling-Reisemann (Eds.), *Handbook on Resilience of Socio-technical Systems* (pp. 117–135). Edward Elgar Publishing Limited.

GRDC. (2022). *GRDC: Long-Term Statistics and Annual Characteristics of GRDC Time Series Data / Online provided by the Global Runoff Data Centre of WMO*. Koblenz: Federal Institute of Hydrology (BfG).

Gruber, K., Klöckl, C., Regner, P., Baumgartner, J., and Schmidt, J. (2019). Assessing the Global Wind Atlas and local measurements for bias correction of wind power generation simulated from MERRA-2 in Brazil. *Energy*, *189*, 116212. https://doi.org/10.1016/j.energy.2019.116212

Gueymard, C. A., and Wilcox, S. M. (2011). Assessment of spatial and temporal variability in the US solar resource from radiometric measurements and predictions from models using ground-based or satellite data. *Solar Energy*, *85*, 1068–1084. https://doi.org/10.1016/j.solener.2011.02.030

Gutiérrez, C., Gaertner, M. Á., Perpiñán, O., Gallardo, C., and Sánchez, E. (2017). A multi-step scheme for spatial analysis of solar and photovoltaic production variability and complementarity. *Solar Energy*, *158*, 100–116. https://doi.org/https://doi.org/10.1016/j.solener.2017.09.037

Haas, S. (2019). *Implementation and validation of an open source model for generating wind feed-in time series* [Technische Universität Berlin]. https://reiner-lemoine-institut.de/wp-content/uploads/2019/01/MasterThesis_SabineHaas.pdf

Haas, S., Krien, U., Schachler, B., Bot, S., Kyri-petrou, Zeli, V., Shivam, K., and Bosch, S. (2021). *windpowerlib v0.2.1*.

Habte, A., Sengupta, M., Gueymard, C., Golnas, A., and Xie, Y. (2020). Long-term spatial and temporal solar resource variability over America using the NSRDB version 3 (1998–2017). *Renewable and Sustainable Energy Reviews*, *134*. https://doi.org/10.1016/j.rser.2020.110285

Habte, A., Sengupta, M., Lopez, A., Xie, Y., and MacLaurin, G. (2018). Assessment of the National Solar Radiation Database (NSRDB 1998-2016). *2018 IEEE 7th World Conference on Photovoltaic Energy Conversion, WCPEC 2018 - A Joint Conference of 45th IEEE PVSC, 28th PVSEC and 34th EU PVSEC*, 2305–2308. https://doi.org/10.1109/PVSC.2018.8547589

Hahmann, A. N., and Peña, A. (2010). Validation of boundary-layer winds from WRF mesoscale forecasts over Denmark. *European Wind Energy Conference and Exhibition 2010, EWEC 2010*, *2*.

Hahmann, A. N., Sile, T., Witha, B., Davis, N. N., Dörenkämper, M., Ezber, Y., Garciá-Bustamante, E., Fidel González-Rouco, J., Navarro, J., Olsen, B. T., and Söderberg, S. (2020). The making of the New European Wind Atlas - Part 1: Model sensitivity. *Geoscientific Model Development*, *13*, 5053–5078. https://doi.org/10.5194/gmd-13-5053-2020

Hastenrath, S. (1981). *The glaciation of the Ecuadorian Andes*. Balkema.

Hay, J. E., and Davies, J. A. (1980). Calculation of the solar radiation incident on a inclined surface. In J. E. Hay and T. K. Won (Eds.), *Proceedings of the 1st Canadian Solar Radiation Data Workshop, Toronto, Canada* (pp. 59–72). Canadian Atmospheric Environment Service.

Heerspink, B. P., Kendall, A. D., Coe, M. T., and Hyndman, D. W. (2020). Trends in

streamflow, evapotranspiration, and groundwater storage across the Amazon Basin linked to changing precipitation and land cover. *Journal of Hydrology: Regional Studies*, *32*(March), 100755. https://doi.org/10.1016/j.ejrh.2020.100755

Henao, F., Viteri, J. P., Rodríguez, Y., Gómez, J., and Dyner, I. (2020). Annual and interannual complementarities of renewable energy sources in Colombia. *Renewable and Sustainable Energy Reviews*, *134*. https://doi.org/10.1016/j.rser.2020.110318

Heredia, M. B., Junquas, C., Prieur, C., and Condom, T. (2018). New statistical methods for precipitation bias correction applied to WRF model simulations in the Antisana Region, Ecuador. *Journal of Hydrometeorology*, *19*, 2021–2040. https://doi.org/10.1175/JHM-D-18-0032.1

Heredia, R., and Gardumi, F. (2022). Assessing the impact of applying individual discount rates in power system expansion of Ecuador using OSeMOSYS. *International Journal of Sustainable Energy Planning and Management*, *33*, 35–52. https://doi.org/10.5278/ijsepm.6820

Hersbach, H., Bell, B., Berrisford, P., Biavati, G., Horányi, A., Muñoz Sabater, J., Nicolas, J., Peubey, C., Radu, R., Rozum, I., Schepers, D., Simmons, A., Soci, C., Dee, D., and Thépaut, J.-N. (2018). *ERA5 hourly data on pressure levels from 1959 to present. Copernicus Climate Change Service (C3S) Climate Data Store (CDS).* 10.24381/cds.bd0915c6

Hersbach, H., Bell, B., Berrisford, P., Hirahara, S., Horányi, A., Muñoz-Sabater, J., Nicolas, J., Peubey, C., Radu, R., Schepers, D., Simmons, A., Soci, C., Abdalla, S., Abellan, X., Balsamo, G., Bechtold, P., Biavati, G., Bidlot, J., Bonavita, M., … Thépaut, J. N. (2020). The ERA5 global reanalysis. *Quarterly Journal of the Royal Meteorological Society*, *146*, 1999–2049. https://doi.org/10.1002/qj.3803

Holmgren, W. F., Hansen, C. W., and Mikofski, M. A. (2018). pvlib python: a python package for modeling solar energy systems. *Journal of Open Source Software*, *3*(29), 884. https://doi.org/10.21105/joss.00884

IEA. (2021a). *Hydropower Special Market Report: Analysis and forecast to 2030*. OECD Publishing. https://doi.org/10.1787/07a7bac8-en

IEA. (2021b). *IEA Wind TCP Annual Report 2020*.

IGM. (2021). *Geoportal IGM*. http://www.geoportaligm.gob.ec

IHA. (2017). *Hydropower Status Report 2017*. International Hydropower Association. https://www.hydropower.org/resources/publications

IHA. (2022). *Hydropower status report 2022*. International Hydropower Association. https://www.hydropower.org/status-report

Ilbay-Yupa, M., Lavado-Casimiro, W., Rau, P., Zubieta, R., and Castillón, F. (2021). Updating regionalization of precipitation in Ecuador. *Theoretical and Applied Climatology*, *143*, 1513–1528. https://doi.org/10.1007/s00704-020-03476-x

IRENA. (2016). *Renewable Energy Market Analysis: Latin America*. https://www.irena.org/-/media/Files/IRENA/Agency/Publication/2016/IRENA_Market_Analysis_Latin_America_2016.pdf

IRENA. (2017). *Exchanging best practices to incorporate variable renewable energy into long-term energy/power sector planning in South America*. https://www.irena.org/-/media/Files/IRENA/Agency/Events/2017/Aug/Summary-Report---IRENA-Regional-Workshop-on-Long-term-Energy-Planning---Buenos-Aires-2017.pdf?la=en&hash=0FA13A0D0A9F67E354EA27652FD190A24EEED3CB

IRENA. (2021). *Renewable Energy Capacity Highlights*. https://www.irena.org/publications/2021/March/Renewable-Capacity-Statistics-2021

IRENA. (2022). *Renewable Power Generation Costs in 2021*. https://irena.org/publications/2022/Jul/Renewable-Power-Generation-Costs-in-2021

Jacques, J., and Preda, C. (2014). Functional data clustering: A survey. *Advances in Data Analysis and Classification*, *8*, 231–255. https://doi.org/10.1007/s11634-013-0158-y

Jara, J. (2018). *Solar photovoltaic potential to complement hydropower in Ecuador : a GIS-based framework of analysis* [Lund University]. https://lup.lub.lu.se/student-papers/search/publication/8962977

Jijón, D., Constante, J., Villacreses, G., and Guerrero, T. (2018). Estimación del rendimiento de aerogeneradores de 2 MW en el Ecuador: Potencial Eolo-Eléctrico. *Revista Técnica "Energía,"* *15*(1), 62–69. https://doi.org/10.37116/revistaenergia.v15.n1.2018.324

Jiménez, P. A., and Dudhia, J. (2012). Improving the representation of resolved and unresolved topographic effects on surface wind in the wrf model. *Journal of Applied Meteorology and Climatology*, *51*(2), 300–316. https://doi.org/10.1175/JAMC-D-11-084.1

Jiménez, P. A., and Dudhia, J. (2013). On the ability of the WRF model to reproduce the surface wind direction over complex terrain. *Journal of Applied Meteorology and Climatology*, *52*, 1610–1617. https://doi.org/10.1175/JAMC-D-12-0266.1

Jung, C., Taubert, D., and Schindler, D. (2019). The temporal variability of global wind energy – Long-term trends and inter-annual variability. *Energy Conversion and Management*, *188*, 462–472. https://doi.org/10.1016/j.enconman.2019.03.072

Jurasz, J., Canales, F. A., Kies, A., Guezgouz, M., and Beluco, A. (2020). A review on the complementarity of renewable energy sources: Concept, metrics, application and future research directions. *Solar Energy*, *195*, 703–724. https://doi.org/10.1016/j.solener.2019.11.087

King, D. L., Boyson, W. E., and Kratochvil, J. A. (2004). *Photovoltaic array performance model. Tech. Rep. SAND2004-3535*. https://www.osti.gov/biblio/919131

Kottek, M., Grieser, J., Beck, C., Rudolf, B., and Rubel, F. (2006). World map of the Köppen-Geiger climate classification updated. *Meteorologische Zeitschrift*, *15*(3), 259–263. https://doi.org/10.1127/0941-2948/2006/0130

Laguarda, A., Alonso-Suárez, R., and Terra, R. (2020). Solar irradiation regionalization in Uruguay: Understanding the interannual variability and its relation to El Niño climatic phenomena. *Renewable Energy*, *158*, 444–452. https://doi.org/https://doi.org/10.1016/j.renene.2020.05.083

Laraque, A., Ronchail, J., Cochonneau, G., Pombosa, R., and Guyot, J. L. (2007). Heterogeneous distribution of rainfall and discharge regimes in the Ecuadorian Amazon basin. *Journal of Hydrometeorology*, *8*, 1364–1381. https://doi.org/10.1175/2007JHM784.1

Latinopoulos, D., and Kechagia, K. (2015). A GIS-based multi-criteria evaluation for wind farm site selection. A regional scale application in Greece. *Renewable Energy*, *78*, 550–560. https://doi.org/10.1016/j.renene.2015.01.041

Lave, M., Kleissl, J., and Arias-Castro, E. (2012). High-frequency irradiance fluctuations and geographic smoothing. *Solar Energy*, *86*, 2190–2199. https://doi.org/https://doi.org/10.1016/j.solener.2011.06.031

Lenderink, G., Buishand, A., and Van Deursen, W. (2007). Estimates of future discharges of the river Rhine using two scenario methodologies: Direct versus delta approach. *Hydrology and Earth System Sciences*, *11*(3), 1145–1159. https://doi.org/10.5194/hess-11-1145-2007

Levy, A., Messina, D., and Contreras Lisperguer, R. (2021). *Definiciones del sector eléctrico para la incorporación de las energías renovables variables y la integración regional en América Latina y el Caribe*. Comisión Económica para América Latina y el Caribe (CEPAL). https://repositorio.cepal.org/bitstream/handle/11362/47656/1/S2100738_es.pdf

Li, D., Feng, J., Xu, Z., Yin, B., Shi, H., and Qi, J. (2019). Statistical Bias Correction for Simulated Wind Speeds Over CORDEX-East Asia. *Earth and Space Science*, *6*, 200–211. https://doi.org/10.1029/2018EA000493

Lohmann, S., Schillings, C., Mayer, B., and Meyer, R. (2006). Long-term variability of solar direct and global radiation derived from ISCCP data and comparison with reanalysis data. *Solar Energy*, *80*, 1390–1401. https://doi.org/10.1016/j.solener.2006.03.004

Lütkehus, I., Salecker, H., and Adlunger, K. (2013). *Potenzial der Windenergie an Land*. https://www.umweltbundesamt.de/sites/default/files/medien/378/publikationen/potenzial_der_windenergie.pdf

Manwell, J. F., McGowan, J. G., and Rogers, A. L. (2009). *Wind energy explained Theory, design and application* (Second). John Wiley & Sons, Ltd.

Marcos, J., Marroyo, L., Lorenzo, E., and García, M. (2012). Smoothing of PV power fluctuations by geographical dispersion. *Progress in Photovoltaics: Research and Applications*, *20*, 226–237. https://doi.org/https://doi.org/10.1002/pip.1127

McKenna, R., Pfenninger, S., Heinrichs, H., Schmidt, J., Staffell, I., Bauer, C., Gruber, K., Hahmann, A. N., Jansen, M., Klingler, M., Landwehr, N., Larsén, X. G., Lilliestam, J., Pickering, B., Robinius, M., Tröndle, T., Turkovska, O., Wehrle, S., Weinand, J. M., and Wohland, J. (2022). High-resolution large-scale onshore wind energy assessments: A review of potential definitions, methodologies and future research needs. *Renewable Energy*, *182*, 659–684. https://doi.org/10.1016/j.renene.2021.10.027

MEER. (2013). *Atlas Eólico del Ecuador con fines de generación eléctrica*. Ministerio de Electricidad y Energía Renovable.

MERNNR. (2018). *Plan Maestro de Electricidad 2018-2027*. Ministerio de Energía y Recursos Naturales no Renovables.

MICSE. (2016). *Agenda nacional del energía 2016-2040*. Ministerio Coordinador de Sectores Estrategicos. https://biblioteca.olade.org/opac-tmpl/Documentos/cg00362.pdf

Mills, A., Ahlstrom, M., Brower, M., Ellis, A., George, R., Hoff, T., Kroposki, B., Lenox, C., Miller, N., Stein, J., and Wan, Y. (2009). *Understanding Variability and Uncertainty of Photovoltaics for Integration with the Electric Power System*. https://www.osti.gov/biblio/979812

Morán-Tejeda, E., Bazo, J., López-Moreno, J. I., Aguilar, E., Azorín-Molina, C., Sanchez-Lorenzo, A., Martínez, R., Nieto, J. J., Mejía, R., Martín-Hernández, N., and Vicente-Serrano, S. M. (2016). Climate trends and variability in Ecuador (1966–2011). *International Journal of Climatology*, *36*, 3839–3855. https://doi.org/10.1002/joc.4597

Mortensen, N. G., Davis, N., Badger, J., and Hahmann, A. N. (2017). *Global Wind Atlas – validation and uncertainty*.

https://backend.orbit.dtu.dk/ws/portalfiles/portal/132511681/Global_Wind_Atlas_validation_DTU_Wind_Energy.pdf

Moya, R. (2006). *Climas Del Ecuador*. http://www.serviciometeorologico.gob.ec/gisweb/TIPO_DE_CLIMAS/PDF/CLIMAS DEL ECUADOR 2016.pdf

Ng, J. Y., Turner, S. W. D., and Galelli, S. (2017). Influence of El Niño Southern Oscillation on global hydropower production. *Environmental Research Letters*, *12*. https://doi.org/10.1088/1748-9326/aa5ef8

Ngan, F., Kim, H., Lee, P., Al-Wali, K., and Dornblaser, B. (2013). A study of nocturnal surface wind speed overprediction by the WRF-ARW model in Southeastern Texas. *Journal of Applied Meteorology and Climatology*, *52*, 2638–2653. https://doi.org/10.1175/JAMC-D-13-060.1

Olauson, J. (2018). ERA5: The new champion of wind power modelling? *Renewable Energy*, *126*, 322–331. https://doi.org/10.1016/j.renene.2018.03.056

Oliver, M. A., and Webster, R. (2015). *Basic steps in geostatistics: the variogram and kriging*. Springer International Publishing. https://doi.org/10.1007/978-3-319-15865-5

Ordoñez, F., Vaca-Revelo, D., and Lopez-Villada, J. (2019). Assessment of the Solar Resource in Andean Regions by Comparison between Satellite Estimation and Ground Measurements: Study Case of Ecuador. *Journal of Sustainable Development*, *12*, 62. https://doi.org/10.5539/jsd.v12n4p62

Paredes, J. R., and Ramírez, J. (2017). *Variable Renewable Energies and Their Contribution to Energy Security: Complementarity in Colombia*. https://publications.iadb.org/en

Parra, L., Gómez, S., Montoya, C., and Henao, F. (2020). Assessing the Complementarities of Colombia's Renewable Power Plants. *Frontiers in Energy Research*, *8*. https://doi.org/10.3389/fenrg.2020.575240

Peel, M. C., Finlayson, B. L., and McMahon, T. A. (2007). Updated world map of the Köppen-Geiger climate classification. *Hydrology and Earth System Sciences*, *11*, 1633–1644. https://doi.org/10.5194/hess-11-1633-2007

Pfenninger, S., Hawkes, A., and Keirstead, J. (2014). Energy systems modeling for twenty-first century energy challenges. *Renewable and Sustainable Energy Reviews*, *33*, 74–86. https://doi.org/10.1016/j.rser.2014.02.003

Pickering, B., Grams, C. M., and Pfenninger, S. (2020). Sub-national variability of wind power generation in complex terrain and its correlation with large-scale meteorology. *Environmental Research Letters*, *15*. https://doi.org/10.1088/1748-9326/ab70bd

Pourrut, P. (Ed.). (1995). *El Agua en el Ecuador: Clima, precipitaciones, escorrentía*. Corporación Editora Nacional, Colegio de Geógrafos del Ecuador. https://horizon.documentation.ird.fr/exl-doc/pleins_textes/pleins_textes_7/divers2/010014823.pdf

pvlib. (2022). *pvlib python*. https://pvlib-python.readthedocs.io/en/stable/index.html

QGIS Association. (2022). *QGIS Geographic Information System*. http://www.qgis.org/

R Core Team. (2020). *R: A language and environment for statistical computing*. www.R-project.org

Ramsay, J. O., Graves, S., and Hooker, G. (2020). *fda: Functional Data Analysis* (5.1.4). https://cran.r-project.org/package=fda

Ramsay, J. O., Hooker, G., and Graves, S. (2009). *Functional data analysis with R and MATLAB* (R. Gentleman, K. Hornik, and G. Parmigiani (Eds.)). Springer-Verlag New York. https://doi.org/10.1007/978-0-387-98185-7

Ramsay, J. O., and Silverman, B. W. (2005). *Functional Data Analysis* (Second). Springer Science + Business Media.

Rivera-González, L., Bolonio, D., Mazadiego, L. F., and Valencia-Chapi, R. (2019). Long-Term Electricity Supply and Demand Forecast (2018–2040): A LEAP Model Application towards a Sustainable Power Generation System in Ecuador. *Sustainability*, *11*, 5316. https://doi.org/10.3390/su11195316

Rodríguez-Benítez, F. J., Arbizu-Barrena, C., Santos-Alamillos, F. J., Tovar-Pescador, J., and Pozo-Vázquez, D. (2018). Analysis of the intra-day solar resource variability in the Iberian Peninsula. *Solar Energy*, *171*, 374–387. https://doi.org/10.1016/j.solener.2018.06.060

Rollenbeck, R., and Bendix, J. (2011). Rainfall distribution in the Andes of southern Ecuador derived from blending weather radar data and meteorological field observations. *Atmospheric Research*, *99*, 277–289. https://doi.org/10.1016/j.atmosres.2010.10.018

Romano, E., Mateu, J., and Giraldo, R. (2015). On the performance of two clustering methods for spatial functional data. *AStA Advances in Statistical Analysis*, *99*, 467–492. https://doi.org/10.1007/s10182-015-0253-9

Rose, S., and Apt, J. (2015). What can reanalysis data tell us about wind power? *Renewable Energy*, *83*, 963–969. https://doi.org/10.1016/j.renene.2015.05.027

Rousseeuw, P. J. (1987). Silhouettes: A graphical aid to the interpretation and validation of cluster analysis. *Journal of Computational and Applied Mathematics*, *20*, 53–65. https://doi.org/10.1016/0377-0427(87)90125-7

Ruth, M., and Goessling-Reisemann, S. (2019). Introduction to resilience of socio-technical systems. In M. Ruth and S. Goessling-Reisemann (Eds.), *Handbook on Resilience of Socio-technical Systems*. Edward Elgar Publishing Limited.

Sachs, J. P., and Ladd, S. N. (2002). 21st Century : expected changes and research needs. *Galápagos Research*, *67*, 50–54.

Salvação, N., and Guedes Soares, C. (2018). Wind resource assessment offshore the Atlantic Iberian coast with the WRF model. *Energy*, *145*, 276–287. https://doi.org/10.1016/j.energy.2017.12.101

Santos-Alamillos, F. J., Pozo-Vázquez, D., Ruiz-Arias, J. A., Lara-Fanego, V., and Tovar-Pescador, J. (2014). A methodology for evaluating the spatial variability of wind energy resources: Application to assess the potential contribution of wind energy to baseload power. *Renewable Energy*, *69*, 147–156. https://doi.org/10.1016/j.renene.2014.03.006

Santos-Alamillos, F. J., Pozo-Vázquez, D., Ruiz-Arias, J. A., Von Bremen, L., and Tovar-Pescador, J. (2015). Combining wind farms with concentrating solar plants to provide stable renewable power. *Renewable Energy*, *76*, 539–550. https://doi.org/10.1016/j.renene.2014.11.055

Sathyajith, M. (2006). *Wind Energy : Fundamentals, Resource Analysis and Economics*. Springer Berlin / Heidelberg.

Schaeffer, R., Szklo, A., Frossard Pereira De Lucena, A., Soria, R., and Chavez-Rodriguez, M. (2013). The Vulnerable Amazon: The Impact of Climate Change on the Untapped Potential of Hydropower Systems. *IEEE Power and Energy Magazine*, *11*, 22–31.

https://doi.org/10.1109/MPE.2013.2245584

Schmidt, J., Cancella, R., and Pereira, A. O. (2016). The role of wind power and solar PV in reducing risks in the Brazilian hydro-thermal power system. *Energy*, *115*, 1748–1757. https://doi.org/10.1016/J.ENERGY.2016.03.059

Schulzweida, U. (2020). *CDO User Guide version 2.0.0*. https://doi.org/10.5281/zenodo.3539275

Segura, H., Junquas, C., Espinoza, J. C., Vuille, M., Jauregui, Y. R., Rabatel, A., Condom, T., and Lebel, T. (2019). New insights into the rainfall variability in the tropical Andes on seasonal and interannual time scales. *Climate Dynamics*, *53*, 405–426. https://doi.org/10.1007/s00382-018-4590-8

Sengupta, M., Habte, A., Kurtz, S., Dobos, A., Wilbert, S., Lorenz, E., Stoffel, T., Renné, D., Gueymard, C., Myers, D., Wilcox, S., Blanc, P., and Perez, R. (2015). *Best Practices Handbook for the Collection and Use of Solar Resource Data for Solar Energy Applications*. https://doi.org/10.18777/ieashc-task46-2015-0001

Sengupta, M., Xie, Y., Lopez, A., Habte, A., Maclaurin, G., and Shelby, J. (2018). The National Solar Radiation Data Base (NSRDB). *Renewable and Sustainable Energy Reviews*, *89*, 51–60. https://doi.org/10.1016/J.RSER.2018.03.003

Skamarock, C., Klemp, B., Dudhia, J., Gill, O., Liu, Z., Berner, J., Wang, W., Powers, G., Duda, G., Barker, D. M., and Huang, X. (2019). *A Description of the Advanced Research WRF Model Version 4*.

Slusarewicz, J. H., and Cohan, D. S. (2018). Assessing solar and wind complementarity in Texas. *Renewables: Wind, Water, and Solar*, *5*. https://doi.org/10.1186/s40807-018-0054-3

Sovacool, B. K., Gilbert, A., and Nugent, D. (2014). Risk, innovation, electricity infrastructure and construction cost overruns: Testing six hypotheses. *Energy*, *74*, 906–917. https://doi.org/10.1016/j.energy.2014.07.070

Staffell, I., and Pfenninger, S. (2016). Using bias-corrected reanalysis to simulate current and future wind power output. *Energy*, *114*, 1224–1239. https://doi.org/10.1016/j.energy.2016.08.068

Sterl, S., Liersch, S., Koch, H., Lipzig, N. P. M. V., and Thiery, W. (2018). A new approach for assessing synergies of solar and wind power: Implications for West Africa. *Environmental Research Letters*, *13*. https://doi.org/10.1088/1748-9326/aad8f6

Stirling, A. (1994). Diversity and ignorance in electricity supply investment. Addressing the solution rather than the problem. *Energy Policy*, *22*, 195–216. https://doi.org/10.1016/0301-4215(94)90159-7

Stirling, A. (2007). A general framework for analysing diversity in science, technology and society. *Journal of the Royal Society Interface*, *4*, 707–719. https://doi.org/10.1098/rsif.2007.0213

Stirling, A. (2010). Multicriteria diversity analysis: A novel heuristic framework for appraising energy portfolios. *Energy Policy*, *38*, 1622–1634. https://doi.org/10.1016/J.ENPOL.2009.02.023

Sun, X., Bright, J. M., Gueymard, C. A., Acord, B., Wang, P., and Engerer, N. A. (2019). Worldwide performance assessment of 75 global clear-sky irradiance models using Principal Component Analysis. *Renewable and Sustainable Energy Reviews*, *111*, 550–570. https://doi.org/10.1016/j.rser.2019.04.006

Tapia, M., Ramos, L., Heinemann, D., and Zondervan, E. (2022). Power to the city:

Assessing the rooftop solar photovoltaic potential in multiple cities of Ecuador. *Physical Sciences Reviews*. https://doi.org/doi:10.1515/psr-2020-0061

Trenberth, K. E. (2019). El Niño southern oscillation (ENSO). In *Encyclopedia of Ocean Sciences* (pp. 420–432). Elsevier. https://doi.org/10.1016/B978-0-12-409548-9.04082-3

Trueman, M., and D'Ozouville, N. (2010). Characterizing the Galapagos terrestrial climate in the face of global climate change. *Galapagos Research*, *67*, 26–37.

Vignola, F., Grover, C., Lemon, N., and McMahan, A. (2012). Building a bankable solar radiation dataset. *Solar Energy*, *86*, 2218–2229. https://doi.org/10.1016/j.solener.2012.05.013

Villacreses, G., Gaona, G., Martínez-Gómez, J., and Jijón, D. J. (2017). Wind farms suitability location using geographical information system (GIS), based on multi-criteria decision making (MCDM) methods: The case of continental Ecuador. *Renewable Energy*, *109*, 275–286. https://doi.org/10.1016/J.RENENE.2017.03.041

Vincent, C. L., and Hahmann, A. N. (2015). The impact of grid and spectral nudging on the variance of the near-surface wind speed. *Journal of Applied Meteorology and Climatology*, *54*, 1021–1038. https://doi.org/10.1175/JAMC-D-14-0047.1

Vindel, J. M., Valenzuela, R. X., Navarro, A. A., and Polo, J. (2020). Temporal and spatial variability analysis of the solar radiation in a region affected by the intertropical convergence zone. *Meteorological Applications*, *27*, 1–10. https://doi.org/10.1002/met.1824

Viviescas, C., Lima, L., Diuana, F. A., Vasquez, E., Ludovique, C., Silva, G. N., Huback, V., Magalar, L., Szklo, A., Lucena, A. F. P., Schaeffer, R., and Paredes, J. R. (2019). Contribution of Variable Renewable Energy to increase energy security in Latin America: Complementarity and climate change impacts on wind and solar resources. *Renewable and Sustainable Energy Reviews*, *113*. https://doi.org/10.1016/j.rser.2019.06.039

Vuille, M., Bradley, R. S., and Keimig, F. (2000). Climate Variability in the Andes of Ecuador and Its Relation to Tropical Pacific and Atlantic Sea Surface Temperature Anomalies. *Journal of Climate*, *13*, 2520–2535. https://doi.org/10.1175/1520-0442(2000)013<2520:CVITAO>2.0.CO;2

Ward, J. H. (1963). Hierarchical Grouping to Optimize an Objective Function. *Journal of the American Statistical Association*, *58*(301), 236–244. https://doi.org/10.2307/2282967

Watkins, D. (2021). *30-Meter SRTM Tile Downloader*. https://dwtkns.com/srtm30m/

Watson, S. (2014). Quantifying the variability of wind energy. *Wiley Interdisciplinary Reviews: Energy and Environment*, *3*, 330–342. https://doi.org/10.1002/wene.95

Wilks, D. S. (2006). *Statistical methods in the atmospheric sciences* (Second). Academic Press.

Zagouras, A., Inman, R. H., and Coimbra, C. F. M. M. (2014). On the determination of coherent solar microclimates for utility planning and operations. *Solar Energy*, *102*, 173–188. https://doi.org/10.1016/j.solener.2014.01.021

Zagouras, A., Kazantzidis, A., Nikitidou, E., and Argiriou, A. A. (2013). Determination of measuring sites for solar irradiance, based on cluster analysis of satellite-derived cloud estimations. *Solar Energy*, *97*, 1–11. https://doi.org/10.1016/j.solener.2013.08.005

Zagouras, A., Pedro, H. T. C., and Coimbra, C. F. M. (2014). Clustering the solar resource

for grid management in island mode. *Solar Energy*, *110*, 507–518. https://doi.org/10.1016/j.solener.2014.10.002

Zambrano-Barragan, P. (2012). *The role of the state in large-scale hydropower development Perspectives from Chile, Ecuador and Peru*. Massachussets Institute of Technology.

Zhang, D.-L., and Zheng, W.-Z. (2004). Diurnal Cycles of Surface Winds and Temperatures as Simulated by Five Boundary Layer Parameterizations. *Journal of Applied Meteorology*, *43*, 157–169. https://doi.org/10.1175/1520-0450(2004)043<0157:DCOSWA>2.0.CO;2

Appendix A Supplementary material to Chapter 2

A.1. Overview of studies on the analysis of spatio-temporal variability of the solar resource

Table A-1. Overview of studies on the analysis of spatio-temporal variability of the solar resource at a regional scale that used gridded satellite-derived datasets (GHI: Global horizontal irradiance, DNI: Direct normal irradiance, NA: not available)

Reference	Objective	Region	Dataset	Time period	Temporal resolution	Spatial resolution	Number of grid points	Classification method
Habte et al. (2020)	To assess the long-term spatial and temporal solar resource variability at a regional scale	America (land surfaces only)	gridded satellite data (GHI, DNI)	20 years	30 min, then aggregated to seasonal, annual and long-term averages	4 x 4 km	2 million (approx.)	Köppen-Geiger climate classification
Gutierrez et al. (2017)	To analyze the variability and complementarity of the solar resource and photovoltaic production among sub-regions of a wide area	Iberian Peninsula	gridded satellite data (GHI)	30 years	daily	0.05 x 0.05 degrees	NA	k-means initialized with a complete linkage hierarchical clustering solution of a dimension-reduced dataset by principal component analysis
Laguarda et al. (2020)	To understand the impact of El Niño South Oscillation on the solar resource over a region of Southeastern South America	southeastern South America (containing Uruguay)	gridded satellite data (GHI)	15 years	hourly, then aggregated to long-term monthly averages	1 x 1 degrees	31	k-means initialized with a Ward hierarchical clustering solution after reducing the dimensionality of the dataset by principal component analysis

Table A-1. Cont.

Reference	Objective	Region	Dataset	Time period	Temporal resolution	Spatial resolution	Number of grid points	Classification method
Vindel et al. (2020)	To analyze the spatial and temporal variability of solar irradiance over a region affected by the intertropical convergence zone	Zambia and surrounding zones	gridded satellite data (GHI)	9 years	daily	0.1 x 0.1 degrees	14,500	Principal component analysis to obtain temporal variability patterns and k-means based on the interquartile range to analyze the spatial variability
Zagouras et al. (2013)	To determine the location of measuring sites for solar irradiance	Greece	gridded satellite data (Cloud modification factor)	2 years	daily	0.05 x 0.05 degrees	28,800	k-means after reducing the dimensionality of the dataset by principal component analysis
Zagouras , Inman, et al. (2014)	To determine coherent zones of global horizontal irradiance for a utility-scale territory	California	gridded satellite data (GHI)	2 years	30 min	0.01 x 0.01 degrees	NA	k-means initialized with a deterministic scheme after reducing the dimensionality of the dataset by principal component analysis
Zagouras, Pedro, et al. (2014)	To select candidate locations for solar power plants that take into account solar variability and geographical smoothing effect	Lanai Island (Hawaii)	gridded satellite data (GHI)	15 years	30 min	0.01 x 0.01 degrees	411	k-means initialized by Affinity propagation method applied to a dimensionally reduced dataset through principal component analysis

A.2. Anomalies in NSRDB dataset

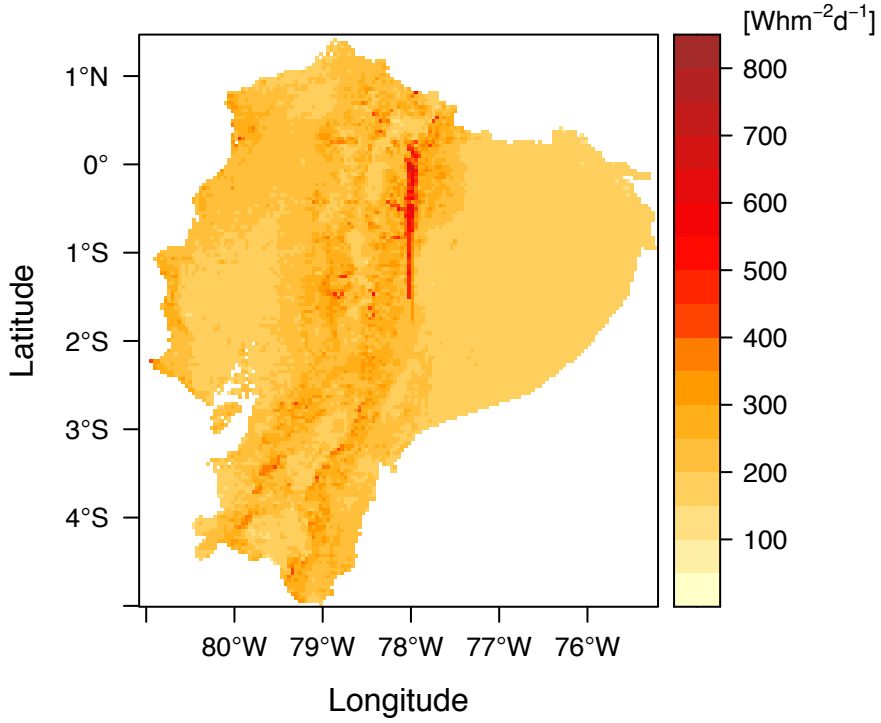

Fig A-1. Spatial distribution of the standard deviation of the annual mean daily total GHI during 1998–2018 over Ecuador's mainland at a 4 × 4 km spatial resolution. Grid points at longitudes 78.02ºW and 77.98ºW between latitudes 0.13ºN and 1.71ºS showed anomalies during the period 24-11-2008 to 31-12-2017. Source: Own representation, data from the NSRDB.

A.3. List of NSRDB variables

Table A-2. List of variables retrieved from the National Solar Radiation Database.

Short name	Long name	Units	Dimensions
DHI	Diffuse horizontal irradiance	W m^{-2}	3
DNI	Direct normal irradiance	W m^{-2}	3
GHI	Global horizontal irradiance	W m^{-2}	3
T	Air temperature	°C	3
WS	Wind speed	m s^{-1}	3
Lon	Center longitude of grid cell	°	2
Lat	Center latitude of grid cell	°	2
Times	Time	UTC	1

A.4. Cluster validity assessment for GHI regionalization

The optimal number of clusters for the regionalization of the GHI dataset is selected based on both the analysis of the average silhouette width (ASW), and the analysis of the functional boxplots of the resulting clusters.

For the regionalization of GHI in Ecuador's mainland, twenty-two clusters are selected as optimal partition because the AWS value decreases significantly for higher number of partitions (Fig A-2). In addition, as seen in Fig A-4, the functional boxplots of the 22 subregions display a uniform dispersion of the functional curves with a minimum number of outliers curves, which suggests a coherent spatial classification.

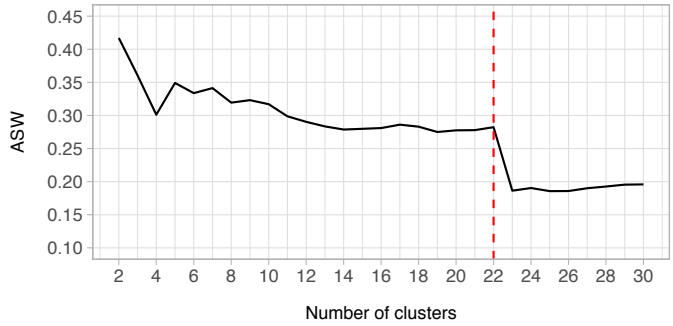

Fig A-2. Average silhouette width (AWS) values against the number of clusters for the regionalization of GHI in Ecuador's mainland.

For the regionalization of GHI in the Galapagos Islands, three clusters are selected as optimal partition. Although the AWS value at 2 is higher (Fig A-3), three clusters are selected because the spatial distribution of the clusters is aligned to the climatic zones described in Trueman et al. (2010). In addition, as seen in Fig A-4, the functional boxplots of the three subregions in the Galapagos Islands display a uniform dispersion of the functional curves without outlier curves, which suggests a coherent spatial classification.

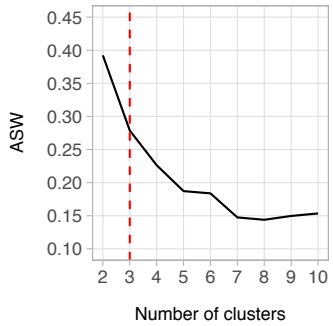

Fig A-3. Average silhouette width (AWS) values against the number of clusters for the regionalization of GHI in the Galapagos Islands.

A.5. Functional boxplots regionalization GHI

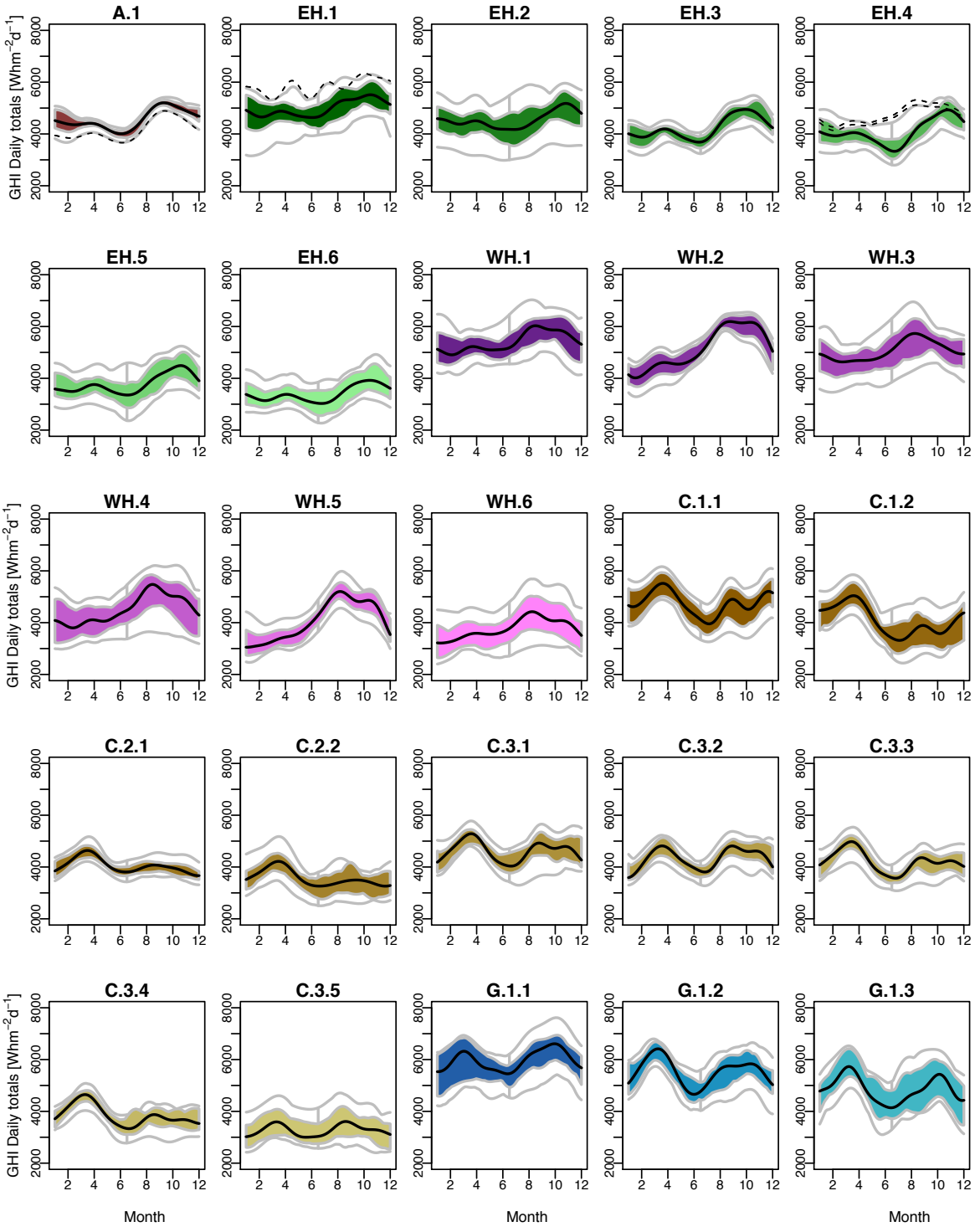

Fig A-4. Functional boxplots that show the dispersion of the GHI functional curves per subregion in Ecuador's mainland and the Galapagos Islands, named according to their corresponding region: Amazon (A), Eastern highlands (EH), Western highlands (WH), Coast (C), and Galapagos (G). The colored shapes represent the interquartile range, the gray external lines depict the minimum and maximum curves, the black lines are the median curves interpreted as the representative temporal pattern of each subregion. The black dotted lines in A.1, EH.1, EH.4 represent the outlier curves.

Appendix B Supplementary material to Chapter 3

B.1. Output variables from the WRF simulations

Table B-1. List of output variables from the WRF simulations. The four-dimensional variables are given at: 30, 40, 50, 60, 70, 80, and 100 m AGL. These variables are obtained following the post-processing procedure performed by Dörenkämper et al. (2020).

Short name	Long name	Units	Dimensions
WS	Wind speed	$m\ s^{-1}$	4
WD	Wind direction	°	4
PD	Power density	$W\ m^{-2}$	4
T	Air temperature	K	4
TKE	Turbulent kinetic energy	$m^2 s^{-2}$	4
Q	Humidity mixing ratio	1	4
HFX	Surface sensible sensible heat flux	$W\ m^{-2}$	3
PBLH	PBL height	m	3
PSFC	Surface pressure	Pa	3
Q2	Specific humidity at 2 m	1	3
RHO	Air density at surface	$kg\ m^{-3}$	3
T2	Air temperature at 2 m	K	3
TSK	Surface skin temperature	K	3
UST	Friction velocity	$m\ s^{-1}$	3
WD10	Wind direction at 10 m	°	3
WS10	Wind speed at 10 m	$m\ s^{-1}$	3
ZNT	Surface aerodynamic roughness length	m	3
ALPHA	Map projection distortion	°	2
HGT	Surface elevation	m	2
XLAT	Center latitude of grid cell	°	2
XLON	Center longitude of grid cell	°	2
Times	Time	UTC	1
Z	Height above ground	m	1

B.2. Cluster validity assessment for wind speed regionalization

The optimal number of clusters for the regionalization of the wind speed dataset is selected based on both the analysis of the average silhouette width (ASW), and the analysis of the functional boxplots of the resulting clusters.

For the regionalization of wind speed in Ecuador's mainland, ten clusters are selected because the AWS value decreases significantly for higher number of partitions (Fig B-1). In addition, as seen in Fig B-3, the functional boxplots of the 10 subregions display a uniform dispersion of the functional curves with a minimum number of outliers curves, which suggests a coherent spatial classification.

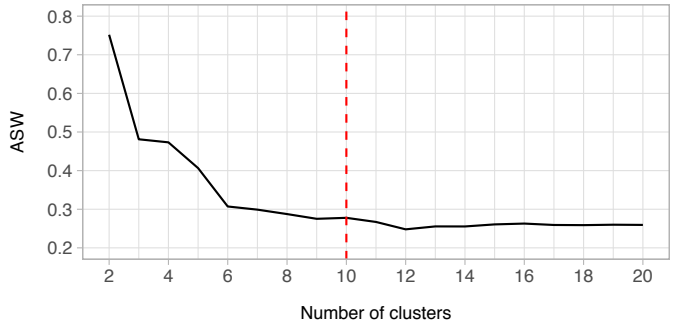

Fig B-1. Average silhouette width (AWS) values against the number of clusters for the regionalization of wind speed in Ecuador's mainland.

For the regionalization of GHI in the Galapagos Islands, four clusters are selected as optimal partition. Although the AWS value at 2 is higher (Fig B-2), four clusters are selected because the spatial distribution of the clusters is aligned to the analysis of wind speed described in Trueman et al. (2010). In addition, as seen in Fig B-3, the functional boxplots of the four subregions in the Galapagos Islands display a uniform dispersion of the functional curves without outlier curves, which suggests a coherent spatial classification.

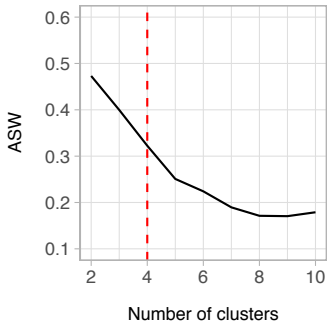

Fig B-2. Average silhouette width (AWS) values against the number of clusters for the regionalization of wind speed in the Galapagos Islands.

B.3. Functional boxplots regionalization wind speed

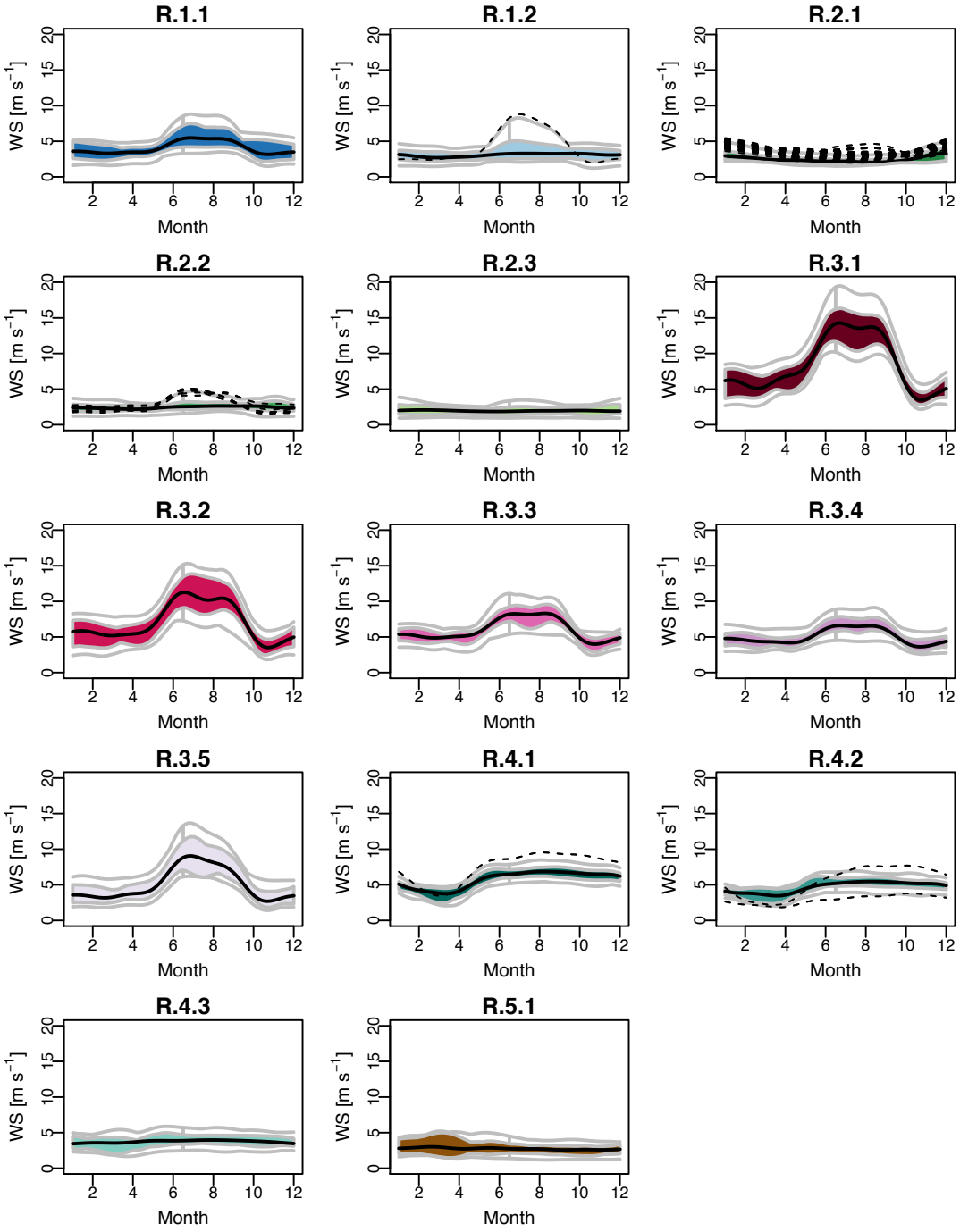

Fig B-3. Functional boxplots that show the dispersion of the wind speed functional curves per subregion in Ecuador's mainland and the Galapagos Islands. The colored shapes represent the interquartile range, the gray external lines depict the minimum and maximum curves, the black lines are the median curves interpreted as the representative temporal pattern of each subregion. The black dotted lines in R.1.2, R.2.1, R.2.2, R.4.1, and R.4.2 represent the outlier curves.

B.4. Monthly wind direction in subregions

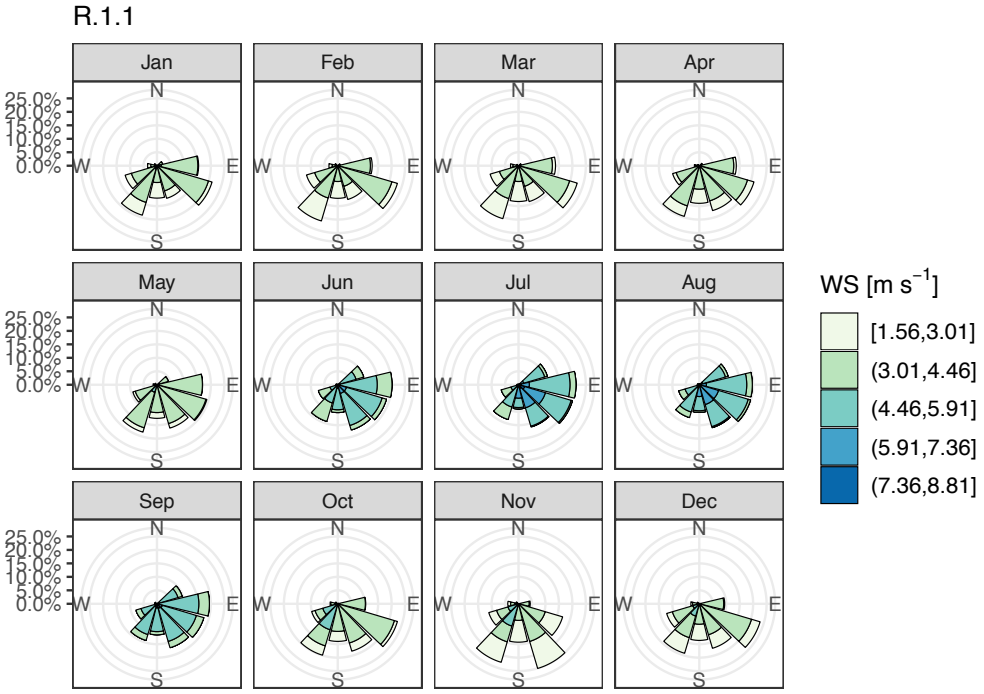

Fig B-4. Distribution of monthly wind speed and the frequency of wind direction at 80 m AGL in subregion R.1.1 in Ecuador's mainland.

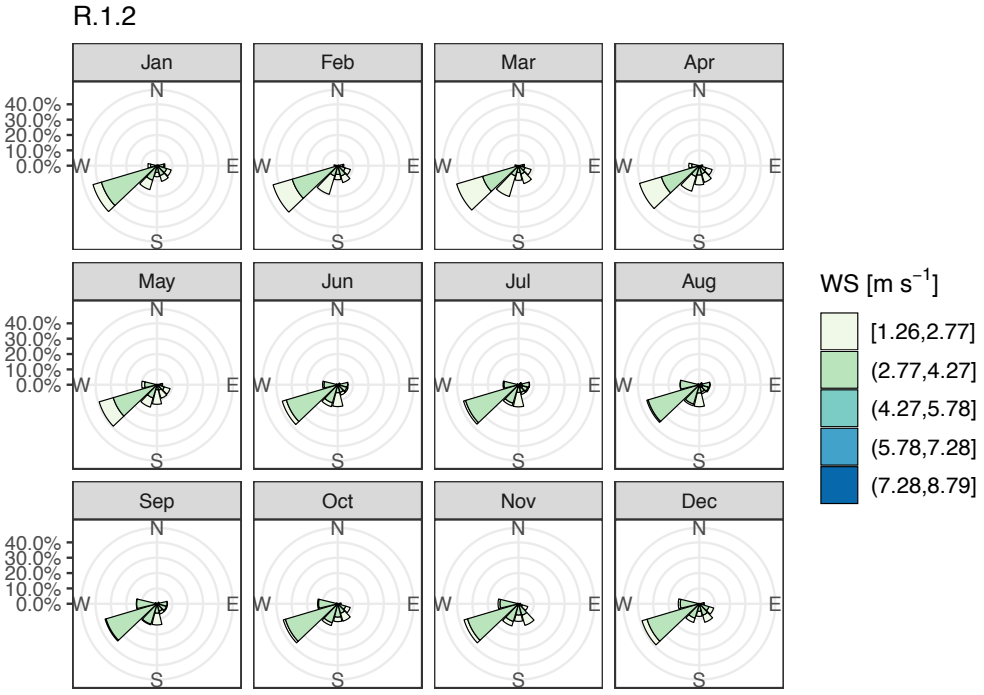

Fig B-5. Distribution of monthly wind speed and the frequency of wind direction at 80 m AGL in subregion R.1.2 in Ecuador's mainland.

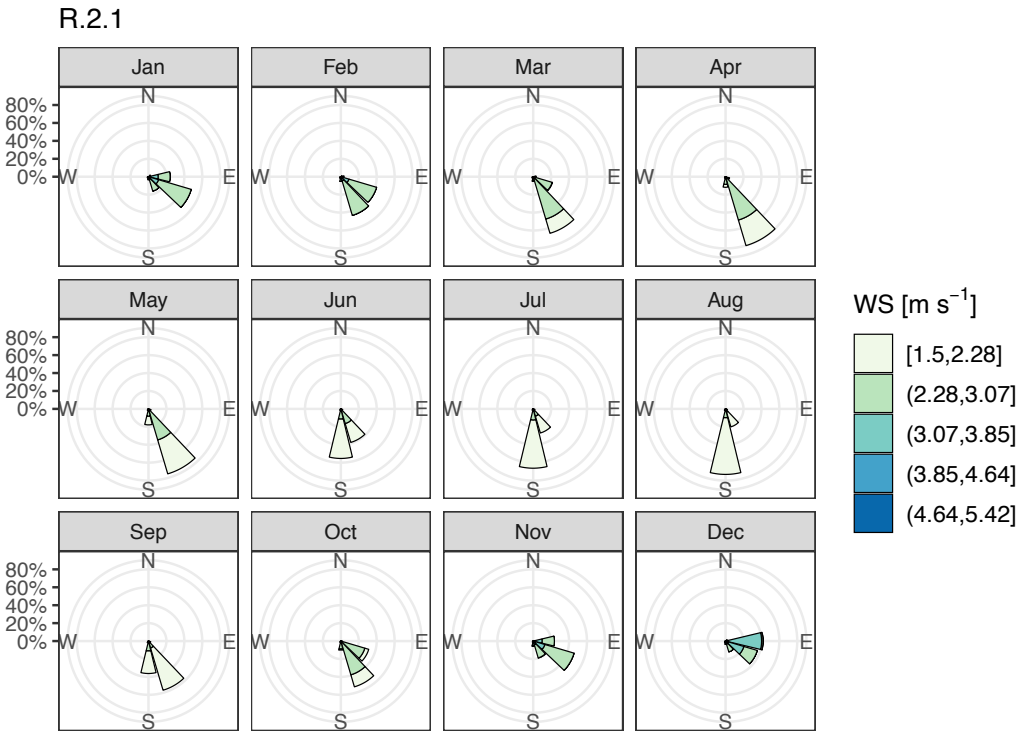

Fig B-6. Distribution of monthly wind speed and the frequency of wind direction at 80 m AGL in subregion R.2.1 in Ecuador's mainland.

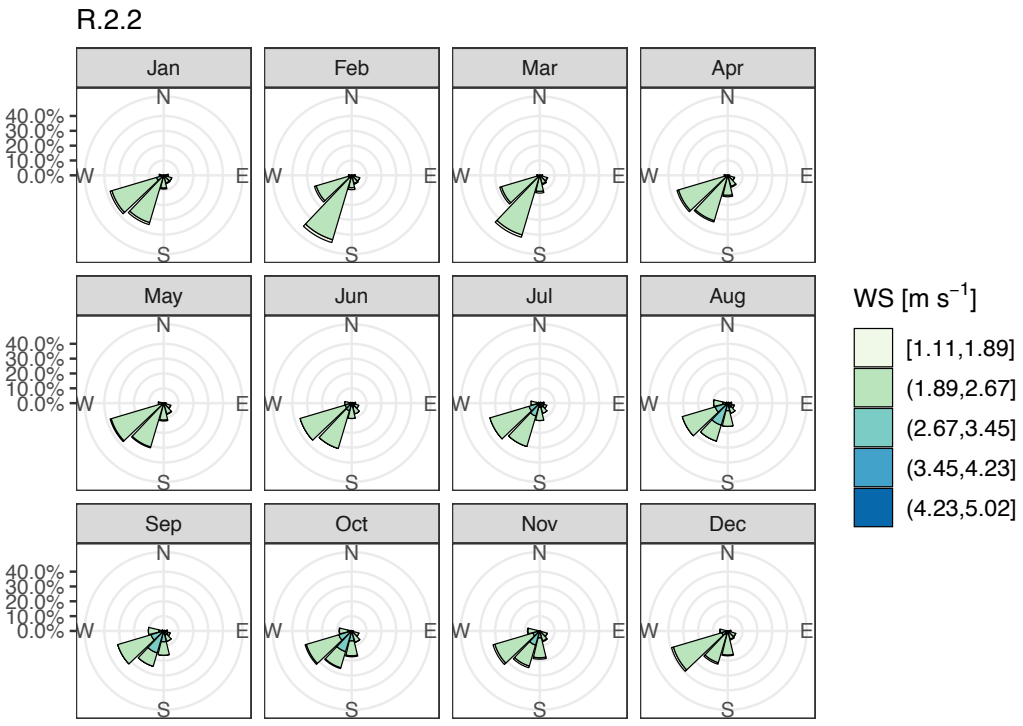

Fig B-7. Distribution of monthly wind speed and the frequency of wind direction at 80 m AGL in subregion R.2.2 in Ecuador's mainland.

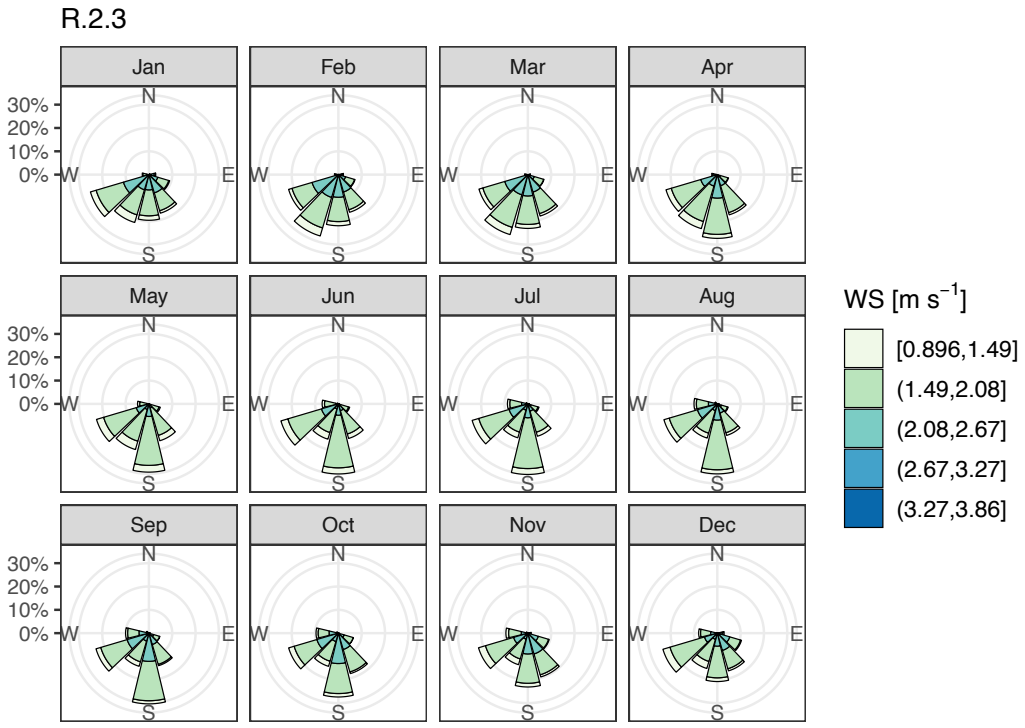

Fig B-8. Distribution of monthly wind speed and the frequency of wind direction at 80 m AGL in subregion R.2.3 in Ecuador's mainland.

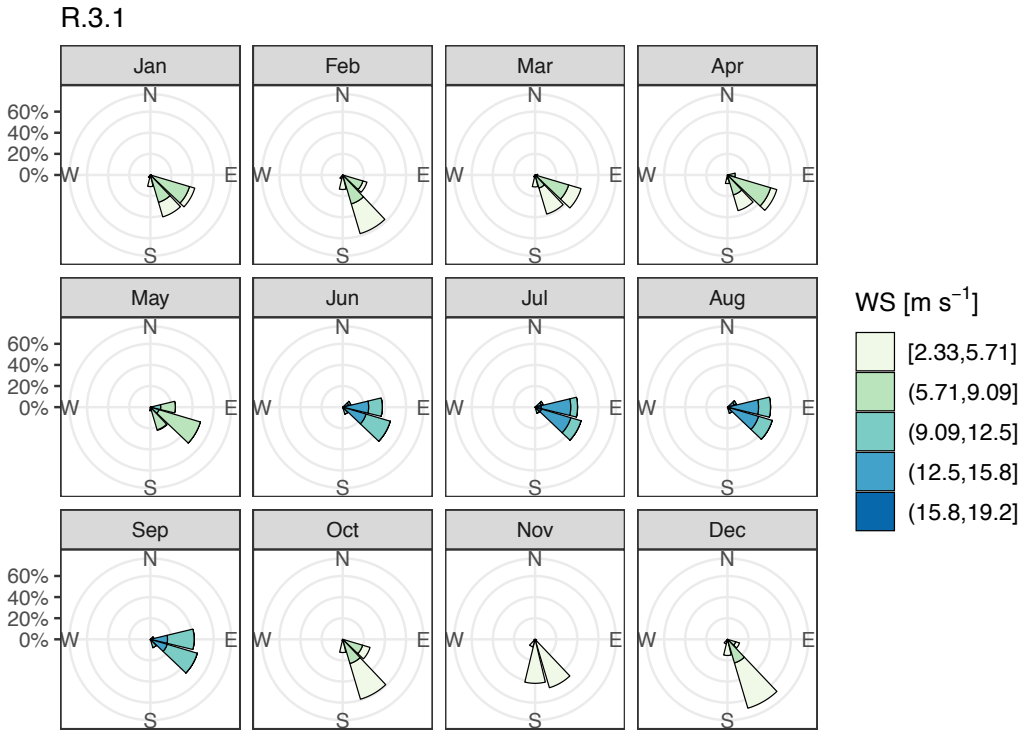

Fig B-9. Distribution of monthly wind speed and the frequency of wind direction at 80 m AGL in subregion R.3.1 in Ecuador's mainland.

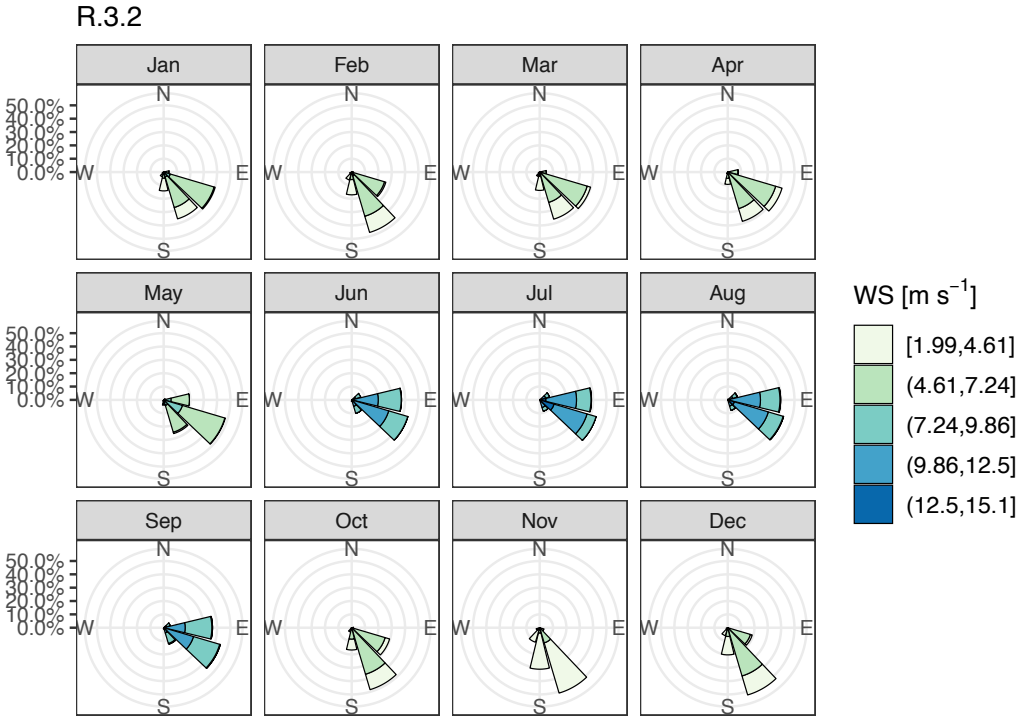

Fig B-10. Distribution of monthly wind speed and the frequency of wind direction at 80 m AGL in subregion R.3.2 in Ecuador's mainland.

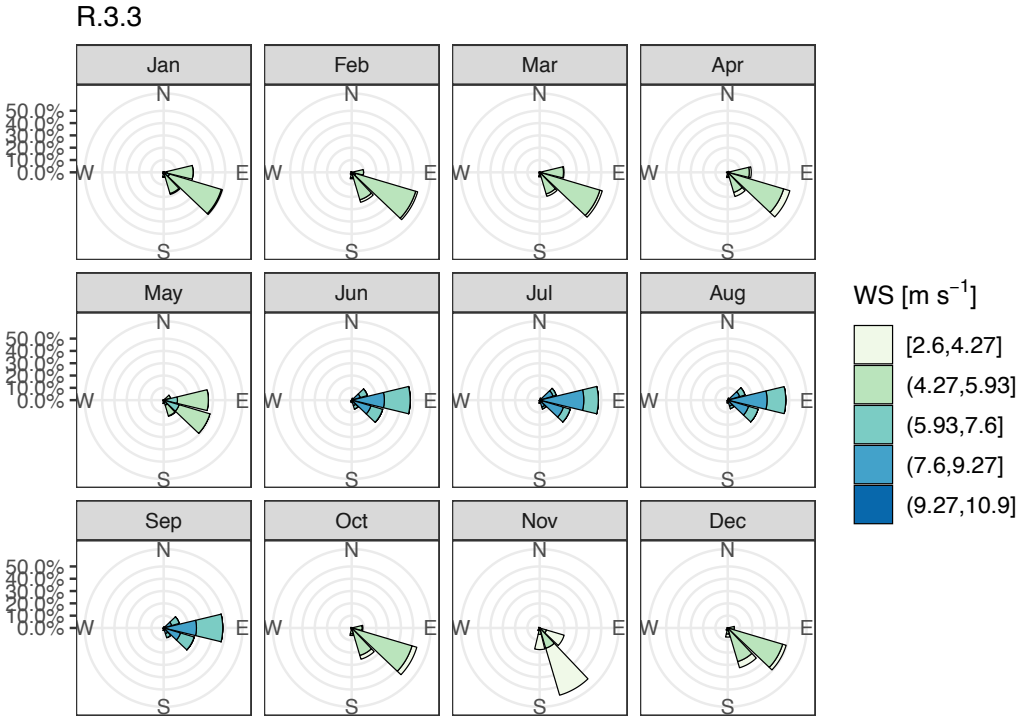

Fig B-11. Distribution of monthly wind speed and the frequency of wind direction at 80 m AGL in subregion R.3.3 in Ecuador's mainland.

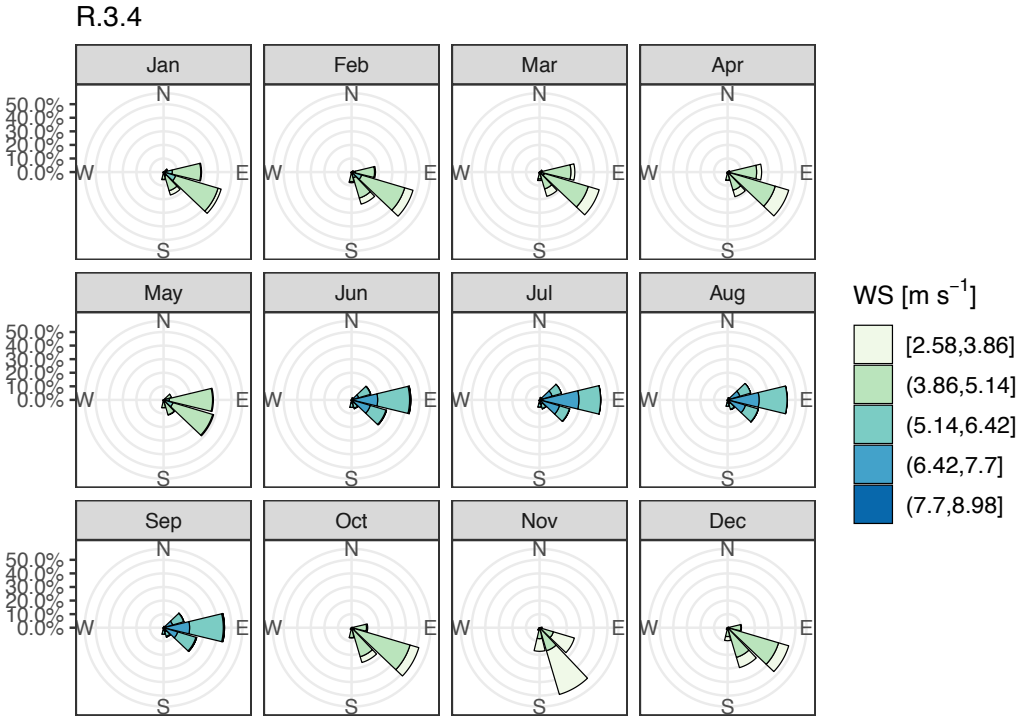

Fig B-12. Distribution of monthly wind speed and the frequency of wind direction in at 80 m AGL subregion R.3.4 in Ecuador's mainland.

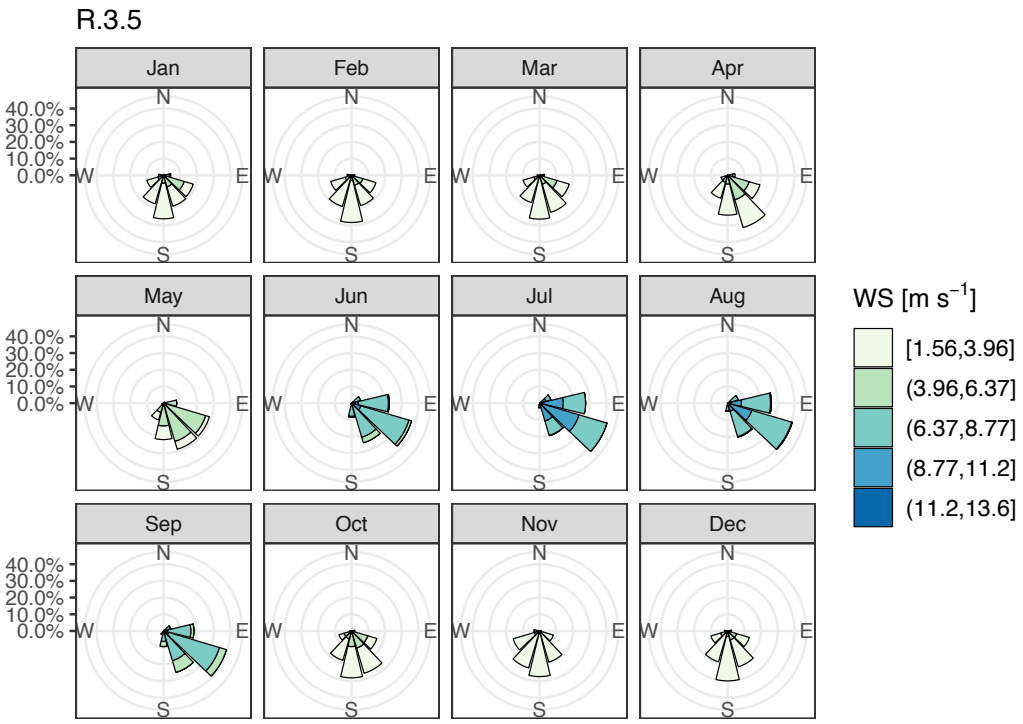

Fig B-13. Distribution of monthly wind speed and the frequency of wind direction in at 80 m AGL subregion R.3.5 in Ecuador's mainland.

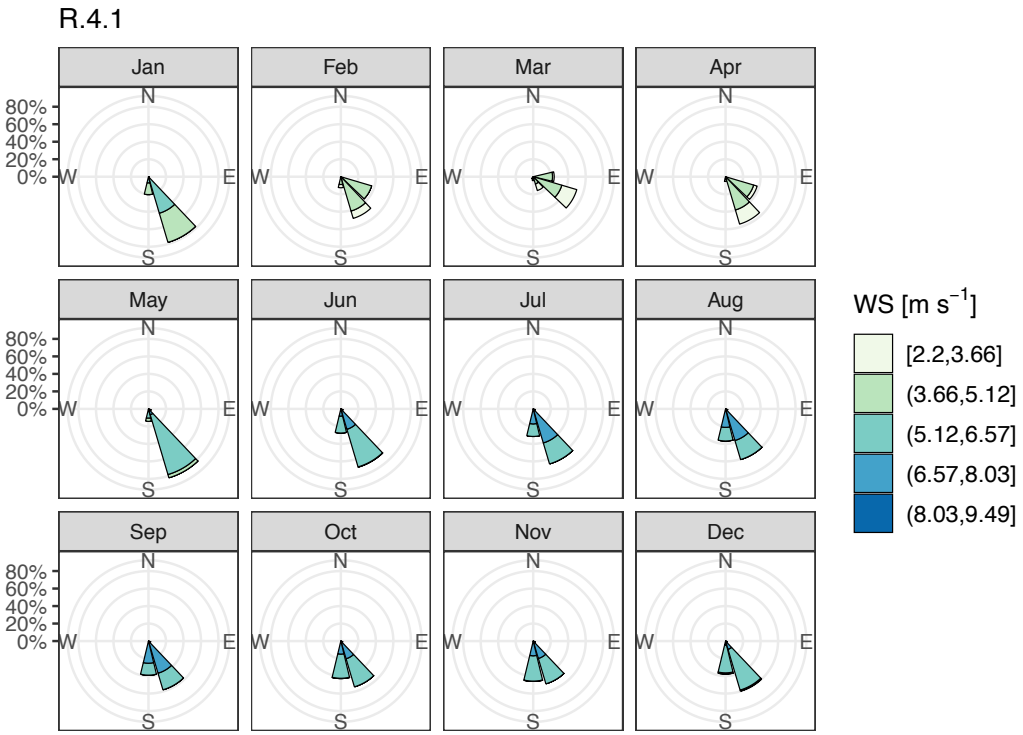

Fig B-14. Distribution of monthly wind speed and the frequency of wind direction at 80 m AGL in subregion R.4.1 in the Galapagos Islands.

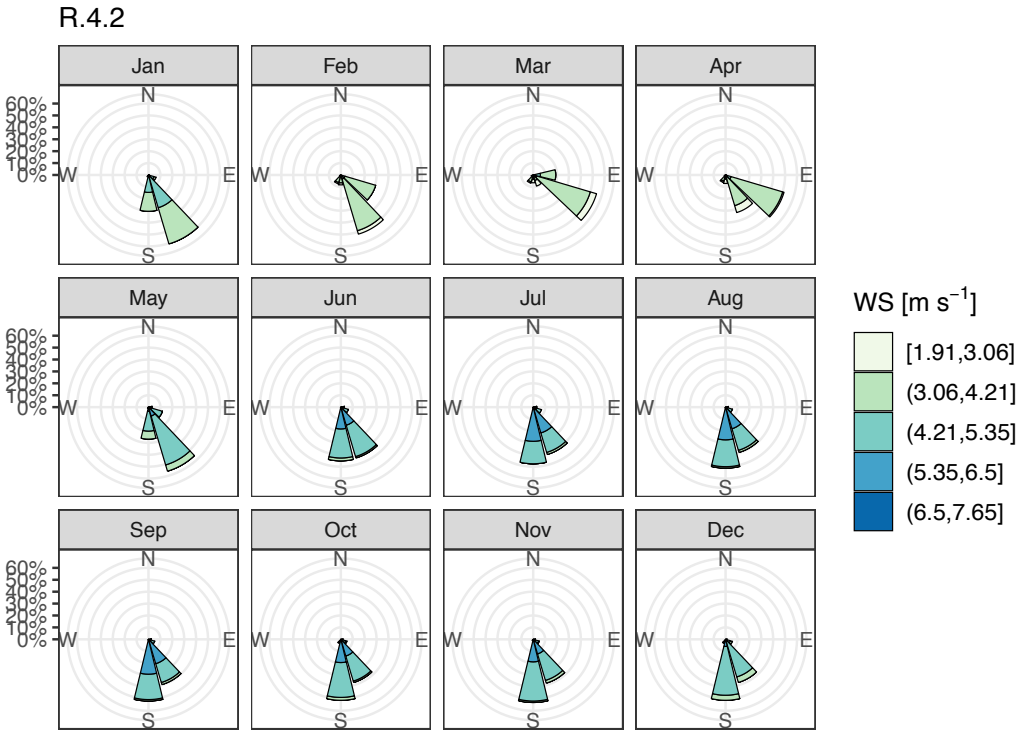

Fig B-15. Distribution of monthly wind speed and the frequency of wind direction at 80 m AGL in subregion R.4.2 in the Galapagos Islands.

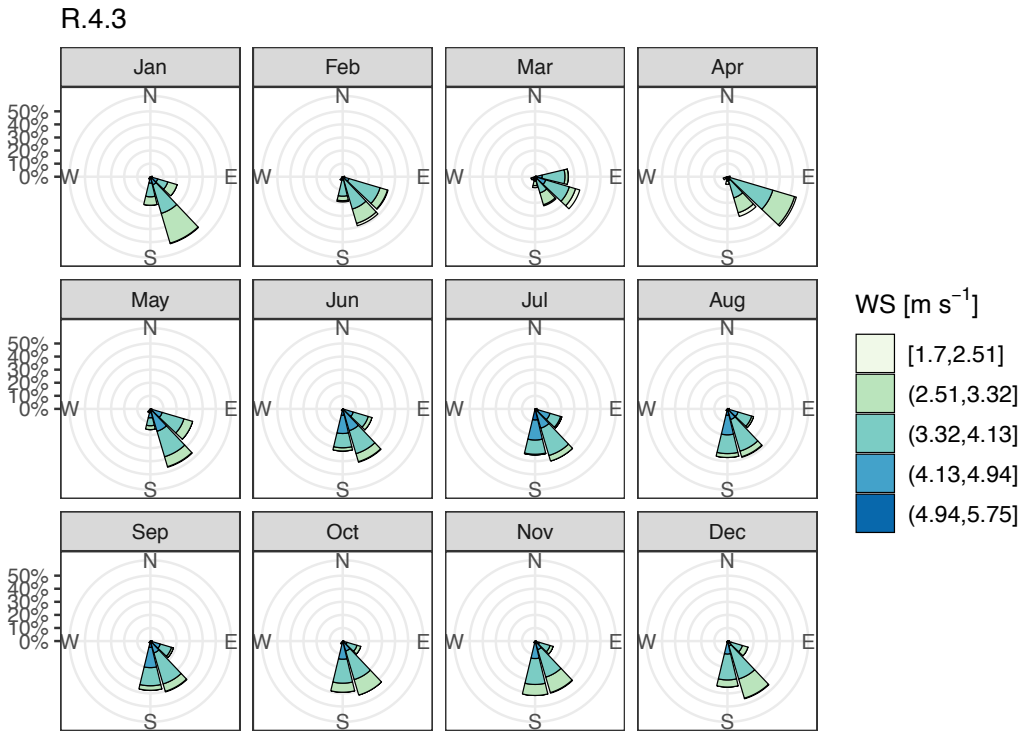

Fig B-16. Distribution of monthly wind speed and the frequency of wind direction at 80 m AGL in subregion R.4.3 in the Galapagos Islands.

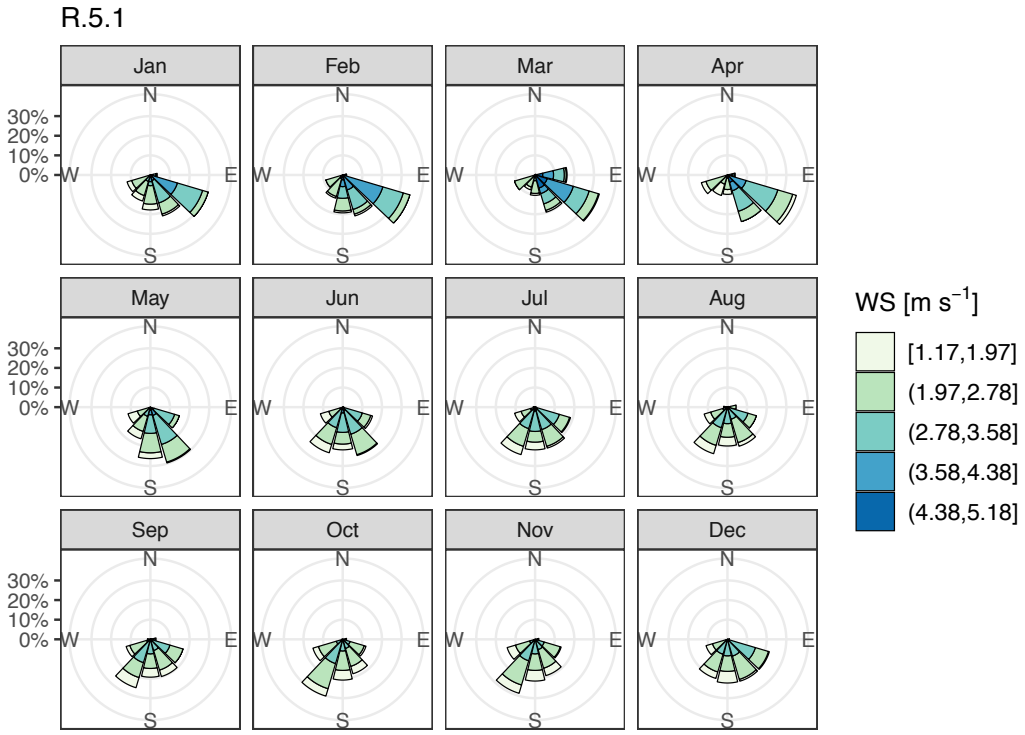

Fig B-17. Distribution of monthly wind speed and the frequency of wind direction at 80 m AGL in subregion R.5.1 in the Galapagos Islands.

Appendix C Supplementary material to Chapter 5

C.1. GIS datasets for geographical wind and PV potential assessment

Table C-1. Data sources of constraint layers used to determine the geographical area available for the deployment of utility-scale solar and wind farms.

Category	Constrain	Date accessed	Data source	Website
Infrastructure	Urban areas	08/07/2019	Military Geographic Institute	http://www.geoportaligm.gob.ec/portal/index.php/cartografia-de-libre-acceso-escala-50k/
	Roads	03/01/2019	Military Geographic Institute	http://www.igm.gob.ec/work/files/downloads/trans.zip
	Railways	03/01/2019	Military Geographic Institute	http://www.igm.gob.ec/work/files/downloads/trans.zip
	Airports	08/07/2019	Military Geographic Institute	http://www.geoportaligm.gob.ec/portal/index.php/cartografia-de-libre-acceso-escala-50k/
	Transmission grid	03/01/2019	CONELEC	http://app.sni.gob.ec/sni-link/sni/PORTAL_SNI/PORTAL/AIG/68_linea_transmision.rar
	Archeological sites	08/07/2019	Military Geographic Institute	http://www.geoportaligm.gob.ec/portal/index.php/cartografia-de-libre-acceso-escala-50k/
Water bodies	Rivers	08/07/2019	Ministry of Environment	http://www.geoportaligm.gob.ec/portal/index.php/cartografia-de-libre-acceso-escala-50k/
	Lakes	08/07/2019	Ministry of Environment	http://www.geoportaligm.gob.ec/portal/index.php/cartografia-de-libre-acceso-escala-50k/
	Mangroves	08/07/2019	Ministry of Environment	http://mapainteractivo.ambiente.gob.ec/
	Reservoirs	08/07/2019	Ministry of Environment	http://www.geoportaligm.gob.ec/portal/index.php/cartografia-de-libre-acceso-escala-50k/
Protected areas	Natural reserves	03/01/2019	Ministry of Environment	http://mapainteractivo.ambiente.gob.ec/
	Protected forest	03/01/2019	Ministry of Environment	http://mapainteractivo.ambiente.gob.ec/
	Intangible areas	08/07/2019	Ministry of Environment	http://mapainteractivo.ambiente.gob.ec/
	Protected biosphere	03/01/2019	Ministry of Environment	http://mapainteractivo.ambiente.gob.ec/

Appendix D Ecuador map

Fig D-1. Political map of Ecuador. The map of the continental area shows the provincial boundaries and provinces' names. The map of Galapagos shows the name of the bigger islands. Source: Own representation, data from IGM (2021).

Appendix E Student contributions

In this dissertation the results from the supervision of the following students' works are included:

- Jonathan L Chu, *Mesoscale modelling of wind resources over complex tropical terrain in Ecuador using the ERA5 reanalysis dataset*. Bachelor's Thesis, Carl von Ossietzky Universität Oldenburg, 2019.
- Leonard Ramos Perez, *Geospatial assessment of rooftop solar photovoltaic potential for multiple cities in Ecuador*. Master's Thesis, Carl von Ossietzky Universität Oldenburg, 2022.